

Transcriptional similarities of non-lymphoid tissue regulatory T cells in health, acute inflammation and cancer

Dissertation

zur Erlangung des Grades

„Doktor der Naturwissenschaften“

(Dr. rer. nat.)

Am Fachbereich Biologie

der Johannes Gutenberg-Universität Mainz

Sara Salome Clara Helbich

████████████████████
Mainz, 2025

Aus dem Institut für Immunologie der
Universitätsmedizin der Johannes Gutenberg-Universität Mainz

Dekan: Prof. Dr. Eckhard Thines

Berichterstatter:

Berichterstatter:

Tag der mündlichen Prüfung: 28.04.2025

Declaration

Parts of this work have already been published, while others are currently being prepared for publication. The scRNA/TCR-seq workflows were established by our group and described in a methods article, which explains the respective techniques. Additionally, some of the figures in this thesis are based on that publication. We are currently in the process of publishing the data presented in the results section of this thesis.

Directory

1.	Introduction.....	1
1.1.	The Immune System – Guardian of Health and Balance	1
1.1.1.	The innate immune system – First line of defense.....	1
1.1.2.	The adaptive immune system – Tailored defense against pathogens.....	2
1.2.	T Cells – Immune defense and regulation	3
1.2.1.	Foxp3 is crucial for regulatory T cell development and function	4
1.2.2.	Immunosuppressive function and tissue-specific roles of Treg cells.....	7
1.2.3.	Non-lymphoid regulatory T Cells (NLT Treg cells) arise in a two-step progenitor program	8
1.2.4.	NLT Treg cells support tissue regeneration.....	11
1.3.	The TME is a complex network	13
1.3.1.	Hallmarks of Cancer: Understanding Tumor Behavior	13
1.3.2.	Cancer Immunotherapies	16
1.4.	Treg cells during acute, chronic and latent infection diseases.....	18
1.5.	Aim of this project.....	19
2.	Material	23
	Table 1: Consumables.....	23
	Table 2: Chemicals and Reagents	23
	Table 3: Enzymes	24
	Table 4: Antibodies.....	24
	Table 5: Biological Material	25
	Table 6: Kits	25
	Table 7: Laboratory software and Equipment	26
	Table 8: Buffer and Cell Culture Media	27
	Table 9: Software and Packages.....	28
3.	Methods	31

3.1.	Mouse Models	31
3.1.1.	Healthy mice	31
3.1.2.	MC38: subcutaneous colorectal carcinoma model	31
3.1.3.	Skin Cancer: subcutaneous B16-F10 melanoma model	32
3.1.4.	Tumor cell line cultivation (B16-F10 and MC38).....	33
3.1.5.	Tumor cell injection (MC38 and B16-F10).....	33
3.1.6.	Colitis-Associated Cancer: AOM/DSS-induced colitis model	34
3.2.	Immune Cell Isolation for phenotype and transcriptome analysis	35
3.2.1.	Isolation of immune cells from murine secondary lymphoid environment (SLE)	37
3.2.2.	Isolation of immune cells from murine tissue – skin	37
3.2.3.	Isolation of immune cells from murine tissue – colon	38
3.2.4.	Isolation of immune cells from murine tissue – subcutaneous tumor tissue	38
3.2.5.	Isolation of immune cells from murine tissue – lung	38
3.3.	Characterization of Treg cells from different tissue by scRNA/TCR-seq analysis	39
3.3.1.	Magnetic Activated Cell Sorting (MACS).....	39
3.3.2.	FACS.....	40
3.3.3.	Single droplet barcoding of T cells, amplification and library preparation	41
3.3.4.	Next Generation Sequencing (NGS) strategy	43
3.3.5.	Computation.....	43
3.3.6.	Alignment of reads to the reference genome	43
3.3.7.	Creating the count matrix from CellRanger Multi output	47
3.3.8.	Gene level annotation and linking TCR information.....	47
3.3.9.	Per sample quality control and doublet detection	48
3.3.10.	Normalisation and feature selection.....	49
3.3.11.	Data integration and Batch Correction.....	49
3.3.12.	Dimensionality reduction and clustering.....	49

3.3.13.	Cell-type annotation and reassignment of clusters	50
3.3.14.	Defining gene expression signatures.....	50
3.3.15.	Differential gene expression (DGE) analysis	55
3.3.16.	Functional enrichment analysis	56
3.3.17.	Cell Interaction Analysis	56
3.3.18.	Pseudo-time analysis	57
3.3.19.	TCR repertoire diversity analysis.....	57
3.4.	Investigation the transcriptional profiles of tumor and healthy tissue using bulk RNA-seq.....	58
3.4.1.	Sample preparation for RNA-seq of cells from tumor and healthy tissue.....	58
3.4.2.	Analysis of bulk RNA-seq data.....	58
3.5.	Flow cytometry analysis of immune cells in healthy and tumor- bearing mice.....	59
4.	Results	61
4.1.	Treg cells across lymphoid and non-lymphoid tissues show distinct marker gene expression	61
4.2.	Treg cells from non-lymphoid tissue show shared gene expression pattern but have a tissue-specific signature	64
4.3.	Pseudo-time analysis reveals trajectory of Treg cells	67
4.4.	Functional Treg signatures are shared across various tissues	68
4.5.	Treg cells from NLT are higher in clonal expansion.....	70
4.6.	Tissue-dependent TCR overlaps among Treg cell populations.....	71
4.7.	Shared TCR clonotypes across different tissues exhibit tissue- specific gene signatures.....	74
4.8.	Acute colitis is induced by AOM/DSS	75
4.9.	Colon pTreg and tTreg cells express cell-type specific signatures.....	76
4.10.	Inflamed colon Treg cells express more suppressive and regenerative genes.....	79

4.11.	Precursor NLT-like Treg cells share TCR with inflamed colon Treg cells	83
4.12.	CAC is induced by AOM/DSS treatment	86
4.13.	Colon tumor and NAT pTreg cells express more tTreg signature genes	87
4.14.	DGE revealed highly shared gene expression pattern of tumor and NAT Treg cells	90
4.15.	TCR from NLT-like Treg cells in SLE are highly overlapping with tumor tTreg cells.....	93
4.16.	Treg cells infiltrate the TME of MC38 tumors in high frequency	97
4.17.	Tumor-infiltrating Treg cells share more genes with colon Treg cells	98
4.18.	MC38 tumor Treg cells show enhanced roles in immune response and cytokine signaling.....	102
4.19.	MC38 tumor Treg cells show overlap in TCR usage with SLE and colon Treg cells.....	105
4.20.	scRNA analysis of CD45 ⁺ immune cells revealed strong immune cell interaction within the TME.....	109
4.21.	Treg cell infiltration in a B16-F10 melanoma skin model.....	113
4.22.	B16-F10 tumor Treg cells show co-expression of skin- and colon-specific genes	114
4.23.	B16-F10 tumor Treg cells express genes involved in response to biotic stimuli and innate immune response.....	117
4.24.	TCR repertoire in tumor-associated Treg cells show limited tissue overlaps	120
4.25.	Tumor-specific Treg marker genes as potential targets for immunotherapy	123
4.26.	bulkRNA-seq reveals strong tissue specificity in healthy and tumor tissues	126
5.	Discussion.....	129
5.1.	NLT-Treg cells show tumor-type-dependent alteration in the Treg cell phenotype.....	129

5.2.	Treg cells modulate immune responses within both the SLE and TME.....	132
5.3.	Treg cell show tissue-plasticity and adaptation in the TME.....	135
5.4.	Recruitment of Treg cells into the TME is highly dependent on the tumor type.....	137
5.5.	Outlook	140
6.	Abstract.....	142
7.	Zusammenfassung	143
8.	Appendix	145
8.1.	Supplementary Figures	145
8.2.	List of Abbreviations	147
8.3.	List of Figures	151
8.4.	List of Tables	165
8.5.	List of References	166
9.	Marker genes for gene expression signatures.....	187
9.1.	Skin Treg signature.....	187
9.2.	Colon tTreg signature.....	187
9.3.	Colon pTreg signature	188
9.4.	SLE NLT-like Treg signature	189
9.5.	Core Treg signature.....	190
9.6.	Regenerative Treg signature	191
9.7.	Suppressive Treg signature.....	192
9.8.	Genes upregulated in all tumor tissue.....	193
9.9.	Genes upregulated in the overall DGE analysis and BioMart Database	193
10.	Curriculum vitae	195
11.	Acknowledgment	197
12.	Eidesstaatliche Erklärung	199

1. Introduction

1.1. The Immune System – Guardian of Health and Balance

Every day, our body wages an invisible war: millions of tiny invaders, such as viruses, bacteria or fungi, attack it. At the same time, there are harmless visitors that wander through our airways or food. Interestingly, the body's own cells can lose their loyalty and can grow uncontrollably or trigger diseases. That's why it is important to have an intelligent safety system that detects, checks and, if necessary, eliminates these many potential pathogens. This system is our body's own immune system, which is a highly sophisticated network of cells, tissues and organs. The mammalian immune system consists of two lines of defenses, the innate and the adaptive immune system, in each of humoral and cellular processes are involved [1].

1.1.1. The innate immune system – First line of defense

The innate immune system serves as the body's first line of defense and as an immediate, non-specific protection. It remains active throughout life. The skin and mucosa already represent an effective physical barrier defense at the surface of the body. If a pathogen breaches these anatomical barriers, various cellular and soluble components immediately respond, either killing or weakening the invaders. The various cells involved in innate immunity include monocytes or their mature form, macrophages, granulocytes, natural killer (NK) cells and innate lymphoid cells (ILC). It also contains soluble recognition molecules such as natural antibodies, pentraxin and the complement system [2].

In the detection of microbial infection, toll-like receptors (TLR) play an important role. Most mammalian species have 10-13 types of TLRs which recognize conserved pathogen-associated molecular pattern (PAMPs), such as conserved bacterial cell wall components or viral structures. This recognition triggers a broad inflammatory response, including the release of cytokines, chemokines, major histocompatibility

Introduction

complex (MHC) molecules, and co-stimulatory molecules [3, 4]. Additionally, TLRs regulate DC maturation and the differentiation of CD4⁺ T helper cells. (CD4⁺ Th cells) [4, 5].

The innate immune system responds rapidly, reaching full activation within minutes to hours and recognizes a broad range of organisms or molecules [6]. However, if a pathogen manages to bypass the non-specific immune response and persists for a certain time in the body, a specific immune reaction becomes necessary. This is where the adaptive immune system, mediated by B and T cells, comes into play, as these cells are capable of recognizing and specifically targeting pathogens for elimination. DCs are involved in this process, as they connect innate and adaptive immunity by presenting antigens to T cells [7].

1.1.2. The adaptive immune system – Tailored defense against pathogens

In contrast to the innate immune defense, the adaptive immune response is highly adaptable and specifically targets antigens, enabling the body to mount a precise response against pathogens. Although this process takes time, ranging from days to weeks, it is long-lasting due to immunological memory and the system's ability to recognize antigens with high specificity, differentiate between self and non-self, and respond to a vast array of foreign molecules [8].

B and T lymphocytes are responsible for both humoral and cellular immunity [9]. Both cell types originate from the bone marrow, where B cells remain for maturation and differentiation. Meanwhile CD34⁺ precursors T cells entering the thymus from the bone marrow and undergo a tightly regulated process involving TCR rearrangement, and positive and negative selection [10]. The thymus, besides the bone marrow, is a primary lymphoid organ and an important part of the lymphatic system. The mammalian thymus, located in the upper chest above the heart, consists of two lobes with a medullary and cortical part [11]. The cortico-medullary

Introduction

junction (CMJ) is a blood vessel-rich region where T precursor cells enter and mature T cells exit.

The T cell development process includes multiple checkpoints that monitor the VDJ rearrangement of the T cell. Crucial steps in T cell development occur after entering the double positive (DP) stage, where positive and negative selection determine which cells leave the thymus. After TCR rearrangement, TCR $\alpha\beta$ affinity for self-peptide-MHC complexes on thymic epithelial cells is essential for survival; otherwise, cells undergo apoptosis. Positive selection promotes cells that bind to MHC molecules, the site of antigen presentation [12]. Negative selection is crucial to prevent responses to self-antigens [13].

T cells leave the thymus as either helper T cells (CD4⁺ T cells) or cytotoxic T cells (CD8⁺ T cells). Before their first encounter with an antigen, T cells are considered naïve and often require antigen-presenting cells (APCs) for activation. APCs include dendritic cells (DCs), macrophages, and B cells, each of which triggers different immune responses. B and T cells can be activated simultaneously and often work cooperatively. If the B and T cells recognize a specific antigen via their B cell receptor (BCR) or T cell receptor (TCR), respectively, they get activated. This leads to a clonally expansion to one and the same BCR/TCR which provides an antigen specific-response [9].

1.2. T Cells – Immune defense and regulation

T lymphocytes are a specialized type of immune cell essential for maintaining a finely tuned immune system. These cells originate from progenitor cells in the bone marrow and gain their full immunocompetence after migrating to the thymus. Within the thymus, they undergo a maturation process that includes the development of their unique TCR. This receptor, in complex with the surface molecule CD3, enables T cells to recognize and bind antigens presented on cell surfaces in conjunction with major histocompatibility complex (MHC) molecules [9]. This recognition is the product of multiple TCR rearrangements that occur in the thymus during T cell development, which result in $\sim 10^8$ unique T cell clones.

Introduction

Afterwards T cells undergo thymic selection, where self-reactive T cells can be eliminated. The mature T cell migrate to lymphoid tissue and can be activated by DCs, leading to clonal expansion of one T cell with the same TCRs. Each of these clones are having different antigen specificities being present in the body at any given time [14]. There are two phenotypically and functionally distinct subgroups of $\alpha\beta$ T cells: CD8⁺ cytotoxic T cells and CD4⁺ T helper cells [15].

CD8⁺ T cells rely on MHC class I molecules for antigen recognition. Since MHC class I molecules are expressed on nearly all nucleated cells, this subpopulation of T cells has the ability to monitor a vast array of potential targets. Once activated, CD8⁺ T cells compel their target cells to undergo cytolysis and apoptosis, effectively neutralizing threats. This process is initiated through the targeted release of granzyme B and perforin, which together trigger a proteolytic cascade mediated by caspases. Additionally, intrinsic apoptosis pathways lead to mitochondrial membrane disruption and the release of proapoptotic molecules, increasing the cell's programmed demise [16].

In contrast to CD8⁺ T cells, helper T (Th) cells express CD4 molecules and recognize antigens presented by MHC class II molecules. These MHC molecules are exclusively produced by APCs such as B cells, macrophages, and DCs. Upon activation, Th cells secrete cytokines that drive the activation of B cells, T cells, and other components of the innate immune response, effectively coordinating a robust and multifaceted defense [9].

Naive CD4⁺ T cells possess remarkable flexibility, differentiating into distinct subtypes based on cytokine signals in their environment. One subtype are Regulatory T cells (Treg cells) which are pivotal for counteracting excessive immune activation and maintaining immune homeostasis [17, 18].

1.2.1. Foxp3 is crucial for regulatory T cell development and function

Regulatory T (Treg) cells are an anti-inflammatory subset of CD4⁺ T cells. These cells play a crucial role in engaging the maintenance of peripheral tolerance to self-antigens and controlling excessive inflammation [19]. In 2000, Sakaguchi and his

Introduction

team demonstrated that naturally occurring Treg cells are defined by the expression of the transcription factor forkhead box protein 3 (Foxp3), which is a critical regulator of Treg development and for coordinating the immunosuppressive functions of Treg cells [17, 19, 20]. The importance of Foxp3 can be seen in the Scurfy mouse strain which consists in loss-of function mutation in the *Foxp3* gene and leads to hyperactivation of CD4⁺ T cells as well as overexpression of proinflammatory cytokines [21]. Mutations of the human gene *FOXP3* are causing the genetic immunodysregulation polyendocrinopathy enteropathy X-linked (IPEX) syndrome, which can be seen as the human counterpart of Scurfy [22]. IPEX typically presents with early-onset, persistent diarrhea, type 1 diabetes (T1D), and eczema. As a monogenic autoimmune disorder, it often leads to additional autoimmune issues, including hepatitis, thyroiditis, hemolytic anemia, and nephropathy [23]. Certain *FOXP3* mutations may be linked to specific manifestations, but the genotype alone does not fully account for the severity of IPEX, indicating that environmental or other genetic factors may also play a role in determining the disease outcome [24].

This complexity in disease manifestation highlights the critical role of Foxp3 in Treg cell function. Foxp3 transduction in naive T cells upregulates surface molecules such as CD25, which is the Interleukin 2 (IL-2) receptor alpha chain. Additionally, the TF Foxp3 also orchestrates the cellular and molecular program involved in Treg function by interacting with several transcription factors. It acts as a homo-oligomer and can associate with other transcription factors such as NFAT (nuclear factor of activated T cells), AML1 (acute myeloid leukemia-1)/Runx1 (runt-related transcription factor 1) and HAT (histone acetyl transferase)/HDAC (histone deacetyl transferase) to regulate the transcription of Treg specific target genes [25]. However, Foxp3 expression alone is insufficient to fully establish the Treg cell phenotype. For suppressive functionality, lineage stability, and specific gene expression in Treg cells also depend on a unique methylation pattern, which is

Introduction

developed independently of *Foxp3* expression. This methylation pattern is initiated in the thymus and maintained in peripheral tissues, relying on TCR signaling [26].

Treg cells can be further classified into two subgroups based on their development and side of induction: thymus-derived Treg cells (tTreg cells) and peripheral-induced Treg cells (pTreg cells). Treg cells predominantly originate in the thymus, where their development follows two distinct pathways involving CD25⁺ *Foxp3*⁻ and CD25⁻ *Foxp3*^{low} progenitors. These progenitors emerge from an initial agonist-activated state, which progresses through a transitional stage before differentiating into mature Treg cells [27]. The development of Treg cells is driven by signals transmitted through the TCR and co-stimulatory receptors such as CD28, LFA-1, and CD27 [28-31]. Cytokines, particularly IL-2 and IL-15, also play a crucial role in Treg development. These cytokines are primarily produced by DCs and medullary thymic epithelial cells (mTECs). Their absence results in reduced intrathymic Treg development and appears to influence the TCR repertoire expressed by developing Treg cells in mice [28, 32].

Additionally, a significant proportion of thymic Treg cells are recirculating from the periphery. These recirculating cells regulate the Treg development process by competing for IL-2, thereby limiting the generation of new thymic Treg cells. This population is characterized by the expression of CD73⁺ and encompasses multiple subsets with a highly diverse TCR repertoire [27].

pTreg cells arise from naïve T cells in the periphery and can acquire *Foxp3* expression and Treg function during antigenic stimulation [33, 34]. Treg cells can also be induced from naïve T cells (iTreg) by the induction of TGF- β (Transforming Growth Factor Beta) and IL-2 in vitro. However, these iTreg cells are phenotypically functionally unstable in mice, due to the less widely demethylation in the regulatory regions of the *Foxp3* gene [35, 36]. Moreover, *Foxp3* seems not to just suppress the function of other T cell populations, but may also act as an intrinsic brake to the further activation of antigen-stimulated effector T cells in the human counterpart [37].

Introduction

1.2.2. Immunosuppressive function and tissue-specific roles of Treg cells

Treg cells can suppress various different immune cells such as B cells, NK cells, natural killer T (NKT) cells, CD4⁺ and CD8⁺ T cells, monocytes and DCs. The functional mechanisms of suppressing immune tolerance by Treg cells is already well-studied [19, 38, 39]. These mechanisms, demonstrated in **Figure 1**, include the secretion of immunosuppressive and anti-inflammatory cytokines like IL-10, IL-35 and TGF- β as well as the induction of apoptosis via secretion of perforin and granzyme-A and -B [40]. Moreover, Treg cells can kill effector T cells or APC through Tumor Necrosis Factor (TNF)-related cell-cell-contact with Tumor Necrosis Factor Related Apoptosis Inducing Ligand (TRAIL), Fas ligand (FAS-L), Galectin-9 and mucin domain 3 (TIM-3) [41]. One of the core Treg signature marker genes in human and mice include the cytotoxic T cell-associated antigen-4 (Ctla4), which is an co-inhibitory molecule of Treg cells and a key molecule for Treg-mediated immune-suppressive functions. It binds to the CD80/CD86 surface molecule on APCs and leads to a very effectively suppression of effector T cells. On a metabolic level Treg cells could function via the degradation of extracellular adenosine triphosphate (ATP) via their ectoenzymes CD39/CD73 or gap junction-transferred cyclic adenosine monophosphate (cAMP) [42].

Additionally, Treg cells have been also found in non-lymphoid tissues, where they can accumulate and exhibit a lot of different tissue-specific and tissue-regenerative functions. Research has highlighted the unique tissue-specific functions of these non-lymphoid tissue (NLT) Treg cells, demonstrating their roles beyond immune suppression [28–31], demonstrated in **Figure 1**.

Introduction

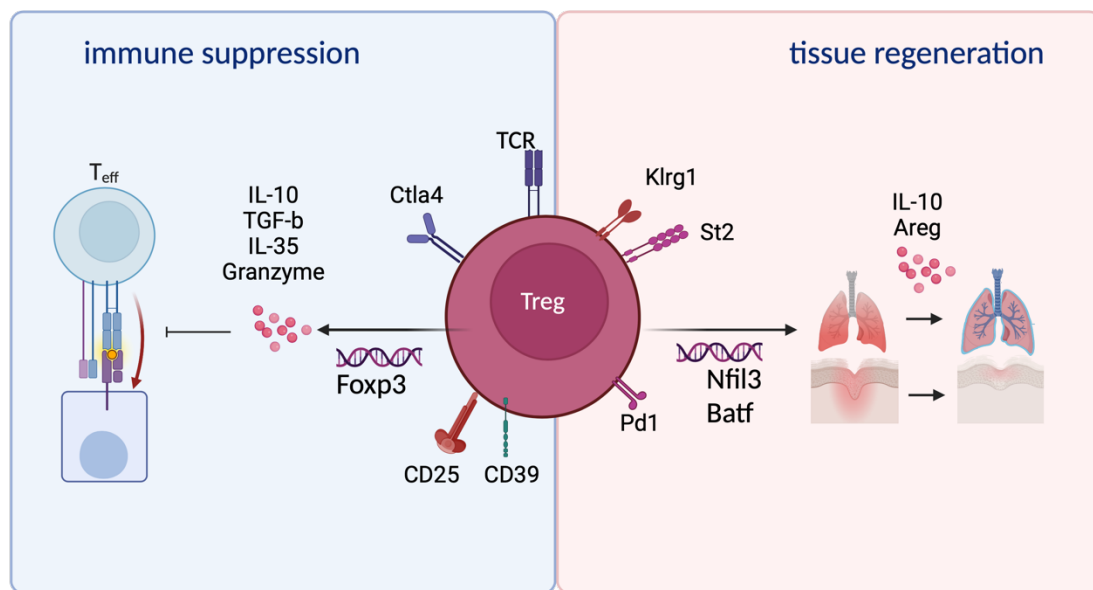


Figure 1: Treg cells regulate the immune system and repair tissue damage. Left: Immune suppression - Treg cells suppress effector T cells (T_{eff}) by secretion of immunosuppressive and anti-inflammatory cytokines, induction of apoptosis via granzyme secretion, via Ctl4 or metabolic disruption via CD39. Right: Tissue regeneration – Treg cells mediate tissue repair program and upregulate surface molecules like Killer cell lectin-like receptor G1 (KlrG1). Effector programs are activated via IL-10 and murine Amphiregulin (Areg) and support wound healing and epithelial regeneration in the murine lung. Created with Biorender.

1.2.3. Non-lymphoid regulatory T Cells (NLT Treg cells) arise in a two-step progenitor program

Recent studies have shown that Treg cells can be found not only within lymphoid tissue and the site of inflammation, but almost every mouse tissue [43]. In secondary lymphoid organs (SLOs), Treg cells get primed by DCs presenting tissue-specific self-antigens which Treg cells can recognize via their specific TCR. Based on specific recognition, Treg cells also migrate into inflamed-tissue, the TME or infectious sites. Furthermore, Treg cells express different homing receptors, which include adhesion molecules and chemokine receptors and control their trafficking and localization in the body [44]. The development of NLT Treg cells has been described in a nuclear factor interleukin-3 regulated (Nfil-3) reporter mouse line which describes this program in two steps: in the SLO, early precursor Treg cells (Nfil3(GFP)⁻KlrG1⁻) further develop in late precursor (Nfil3 (GFP)⁺KlrG1⁻) towards

Introduction

more mature (Nfil3 (GFP)⁺ KlrG-1⁺) NLT Treg cells [45], which is illustrated in Figure 2. Additionally, global chromatin profiling of these mature NLT Treg cells and the precursor stages revealed a stepwise chromatin accessibility and reprogramming. These findings were further corroborated by a pseudo-time analysis of single-cell RNA sequencing (scRNA-seq) data from various tissues. scRNA-seq allowed the detailed examination of complex cellular processes at single-cell resolution within the biologically diverse tissues and cell populations. The pseudo-time analysis used in the study computationally placed Treg cells along a pseudo-temporal trajectory based on their progressively changing transcriptomes [45].

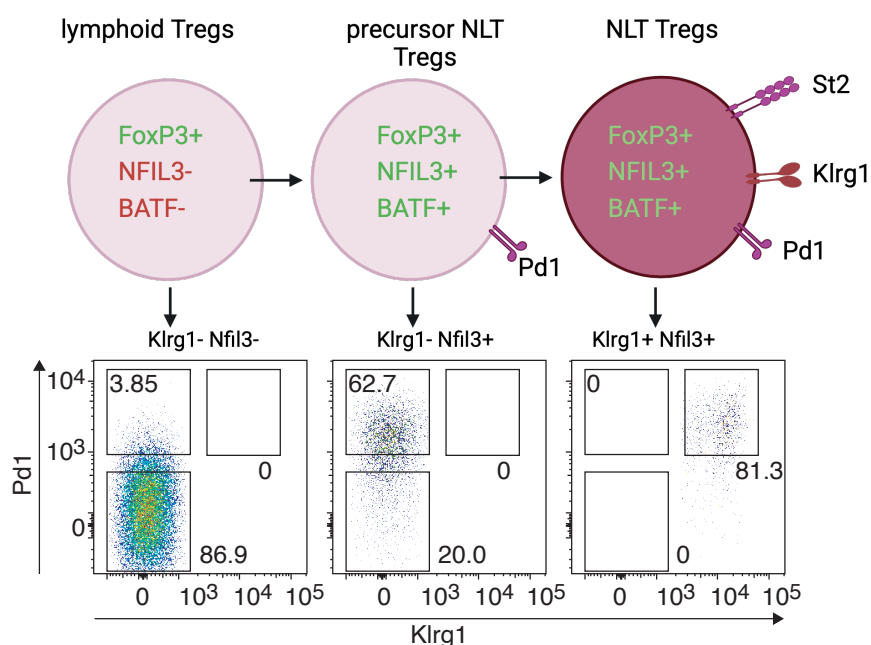


Figure 2: Development of NLT Treg cells and their expression of Foxp3, Nfil3, Batf and their surface receptors programmed cell death protein 1 (PD-1), Killer Cell Lectin Like Receptor G1 (KlrG1) and ST2 (IL-33 receptor); created with Biorender, adapted from Delacher et al., 2020 [45].

By analyzing the enrichment of differential binding motifs from various transcription factor (TF) families between Nfil3(GFP)⁻ KlrG1⁻ and Nfil3(GFP)⁻ KlrG1⁺ Treg cells, the TF basic leucine zipper transcription factor (Batf) was identified as a key regulator of the tissue-specific Treg cell program. scRNA-seq data revealed more than 60 genes either positively or negatively correlated with Batf expression. Positively

Introduction

correlated genes included TNF superfamily member 4 (Tnfsf4), Klrp1, and programmed cell death 1 (Pdc1), while negatively correlated genes included B-cell lymphoma 2 (Bcl2), selectin L (Sell), Ccr7, SATB homeobox 1 (Satb1), and inhibitor of desoxyrinonucleic acid (DNA) binding 3 (Id3) [28]. The critical role of Batf in NLT Treg development was further validated using Batf-deficient mice. These mice lacked both early and late NLT Treg precursors and were unable to develop mature NLT Treg cells in non-lymphoid tissues [28]. This underscores the importance of Batf in orchestrating the specialized functions of Treg cells in tissue environments [45].

Further studies have revealed NLT-specific Treg gene signatures that reflect their distinct roles in various tissue environments. By analyzing the scRNA landscape of Treg cells from colon, skin, and SLOs, researchers identified several defining characteristics of NLT Treg cells. These included the expression of key components of the TNFRSF-NF- κ B pathway, such as transducers (Traf1, Traf4, Traf2b), effectors (Nfkb1, Nfkb2, Rel, Rela, Relb), and inhibitors (Nfkbib, Nfkbid, Nfkbie). Additionally, tissue-specific chemokine receptors were identified: Ccr4, Ccr8, and Cxcr4 were prominent in both skin and colon Treg cells, while Ccr1 and Ccr5 were more specific to the colon, and Ccr6 was distinctive for skin NLT Treg cells [46].

This raises an important question: Does the gene expression and function of NLT Treg cells differ significantly depending on the tissue of origin? While there are tissue-specific features, evidence suggests that NLT Treg cells share a common phenotype across different non-lymphoid tissues. Recent findings propose a pan-tissue model of the NLT Treg population, characterized by a shared capacity for circular migration among various tissues [47]. In this model, NLT Treg cells are capable of entering tissues and being retained when antigen recognition occurs. Treg cells with TCRs that recognize antigens across multiple tissues likely migrate through different environments over their lifespan. In contrast, rare Treg clones with tissue-restricted antigen recognition exhibit a more specialized migratory pattern, with their presence and activity largely confined to a single tissue. This duality

Introduction

highlights the dynamic nature of Treg cells in balancing broad immunoregulatory functions with tissue-specific specialization [47].

1.2.4. NLT Treg cells support tissue regeneration

The first evidence of this novel, non-classical function of NLT Treg cells, such as the regulation of insulin sensitivity, was observed in studies on murine visceral adipose tissue (VAT). In this context, metabolic homeostasis and the regulation of insulin sensitivity was linked to VAT-resident regulatory T cells, which utilize signaling through the IL-33 receptor (ST2) [48].

Similarly, in the skin, Treg cells contribute to wound healing by modulating local immune responses and promoting tissue repair mechanisms. They interact with various cell-types, including keratinocytes and fibroblasts, to enhance re-epithelialization and tissue remodeling [49]. A key effector molecule of NLT Treg cells in mice is the epidermal growth factor receptor (EGFR) ligand amphiregulin (Areg), which plays a critical role in wound healing and also in epithelial regeneration in the murine lung [50, 51]. Areg-dependent processes help resolve inflammation and promote the restoration of normal lung architecture, thereby preventing chronic lung diseases. The mechanisms involve the secretion of anti-inflammatory cytokines and direct interactions with lung epithelial cells [52]. Within the central nervous system (CNS), Treg cells promote IL-10-dependent repair after ischemic brain injury and suppress neurotoxic astrogliosis via Areg [53, 54]. They also enhance myelin regeneration and oligodendrocyte differentiation in experimental autoimmune encephalomyelitis (EAE), a model of multiple sclerosis [55]. In skeletal muscle, Treg cells accumulate in response to injury, facilitating repair through the secretion of growth factors such as Areg, which promotes the proliferation and differentiation of muscle satellite cells, essential for muscle regeneration [56, 57]. Similarly, in the heart, Treg cells facilitate recovery after myocardial infarction by modulating monocyte differentiation [58]. Furthermore, Treg cells suppress pulmonary responses to allergens and maintain liver homeostasis by regulating bile acid synthesis, protecting against cholestatic injury

Introduction

[59, 60]. However, during non-alcoholic steatohepatitis (NASH), a condition of chronic liver injury, Areg-producing Treg cells activate pro-fibrotic transcriptional programs via EGFR signaling. This also reveals a maladaptive role for NLT Treg cell-mediated tissue repair functions in chronic liver disease and links liver damage to NASH-dependent glucose intolerance [61]. This duality of NLT Treg cells can be found not only in the inflamed tissue but also during cancer progression. An overview of the function of NLT Treg cells within different organs is illustrated in Figure 3.

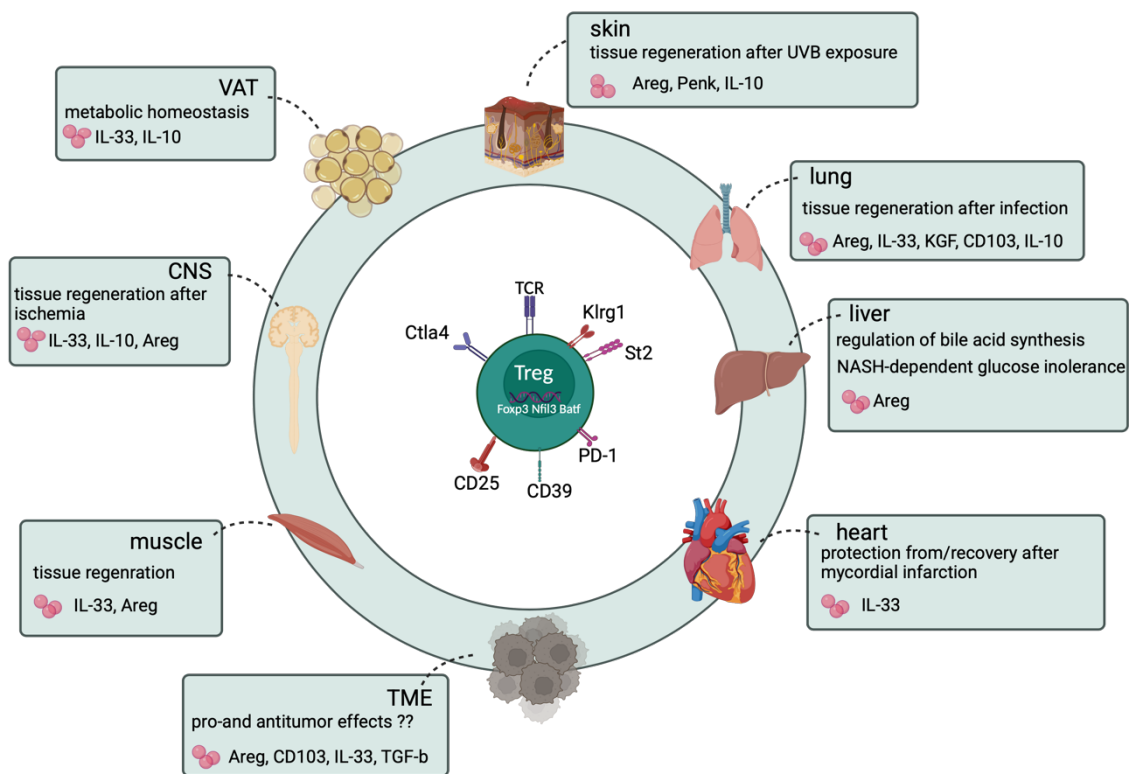


Figure 3: Overview of NLT Treg-mediated regeneration in murine tissues. NLT Treg cells are characterized by the expression of the transcription factors Foxp3, Batf and Nfil3. They exhibit surface markers such as Klrp1, St2 (IL-33R), PD-1, CD39, CD25 and Ctl4-4, along with a T cell receptor (TCR). Across various tissues - including visceral adipose tissue (VAT), skin, lung, liver, heart, muscle, and the central nervous system (CNS) - NLT Tregs facilitate tissue regeneration through effector molecules such as amphiregulin (Areg), proenkephalin (Penk), IL-10, IL-33, IL-13, and CD103. In the tumor microenvironment (TME), these cells not only produce regenerative factors but also contribute to immunosuppression, notably through TGF- β . Created with Biorender.

Introduction

All of these different studies have shown the important role of NLT Treg cells in tissue regeneration and repair in many different settings. They are operating through diverse mechanisms tailored to specific organ environments. Moreover, NLT Treg cells can be also found in high numbers in the TME of different types of malignancies. Treg cells hinder the immunological surveillance of tumors in healthy individuals and diminish the anti-tumor immune response in cancer patients, potentially contributing to tumor development and progression [62]. Additionally, Treg cells support tumor cell survival by releasing growth factors and interacting with stromal cells [63]. An increased presence of tumor-infiltrating Treg cells has been associated with poorer patient survival across various types of malignant tumors [64, 65]. Specifically, Treg infiltration correlates with reduced recurrence-free survival (RFS) in patients with non-small cell lung cancer (NSCLC) [66]. However, the underlying mechanisms on the pro- and antitumor effects of Treg cells in various TME remain poorly understood.

1.3. The TME is a complex network

The interaction and communication between the tumor and its microenvironment are essential for its differentiation, proliferation, invasion and metastasis as well as for the development of drug resistance [67]. The surrounding cells, also known as tumor stroma, define the non-neoplastic area of the TME. In addition to the extracellular matrix (ECM), the stroma consists of cells from the innate and adaptive immune system, endothelial cells, cancer-associated fibroblasts (CAF) and pericytes. Essential functions of the tumor stroma include neoangiogenesis, the supply of growth factors and cytokines as well as the remodeling of the ECM [63, 68].

1.3.1. Hallmarks of Cancer: Understanding Tumor Behavior

The interaction between cancer cells and the TME plays a crucial role in driving tumor growth, invasion, immune evasion, and response to cancer therapies. In 2000, Hanahan and Weinberg introduced the six "Hallmarks of Cancer," which

Introduction

remain the gold standard for describing cancer's complex development [69]. These hallmarks were later updated in 2011 and represent essential traits that allow cancer cells to survive, proliferate, and disseminate, as well as the enabling characteristics that support their emergence [70].

1. Self-sufficiency in growth signals: Cancer cells exhibit uncontrolled growth due to mutations or dysregulation in genes responsible for cell cycle control and growth factor signaling pathways.
2. Insensitivity to anti-growth signals: Tumor cells evade the inhibitory signals that normally regulate cell growth or induce cell death, allowing them to continue proliferating despite adverse conditions.
3. Evading apoptosis: Cancer cells resist programmed cell death by developing mechanisms to survive even in the presence of cellular stress or damage.
4. Limitless replicative potential: By maintaining telomere length through telomerase activation or alternative mechanisms, cancer cells can bypass normal cellular lifespan limits and divide indefinitely.
5. Sustained angiogenesis: Tumors promote the formation of new blood vessels to supply oxygen and nutrients, facilitating their growth and ability to metastasize.
6. Tissue invasion and metastasis: Cancer cells acquire the ability to invade nearby tissues and migrate to distant sites, leading to metastasis and contributing to cancer progression.
7. Reprogramming energy metabolism: Cancer and malignant cells reprogram their metabolism to support rapid growth through aerobic glycolysis, which produces lactate and is known as the Warburg effect [71].
8. Evading immune destruction: Tumor development has been shown to improve in immunodeficient mice lacking both types of T cells as well as NK cells. This mechanism is triggered by downregulating antigen presentation or creating an immunosuppressive microenvironment [72].

Recently, in the 2022 review, two additional emerging hallmarks were presented: "unlocking phenotypic plasticity" and "senescent cells". Current research introduced two new enabling characteristics, "nonmutational epigenetic reprogramming" and "polymorphic microbiomes" [73]. Taken together, the evolving understanding of the hallmarks of cancer underscores the complexity of cancer development and the critical role of TME. An overview of the hallmarks of cancer is shown in **Figure 4**.

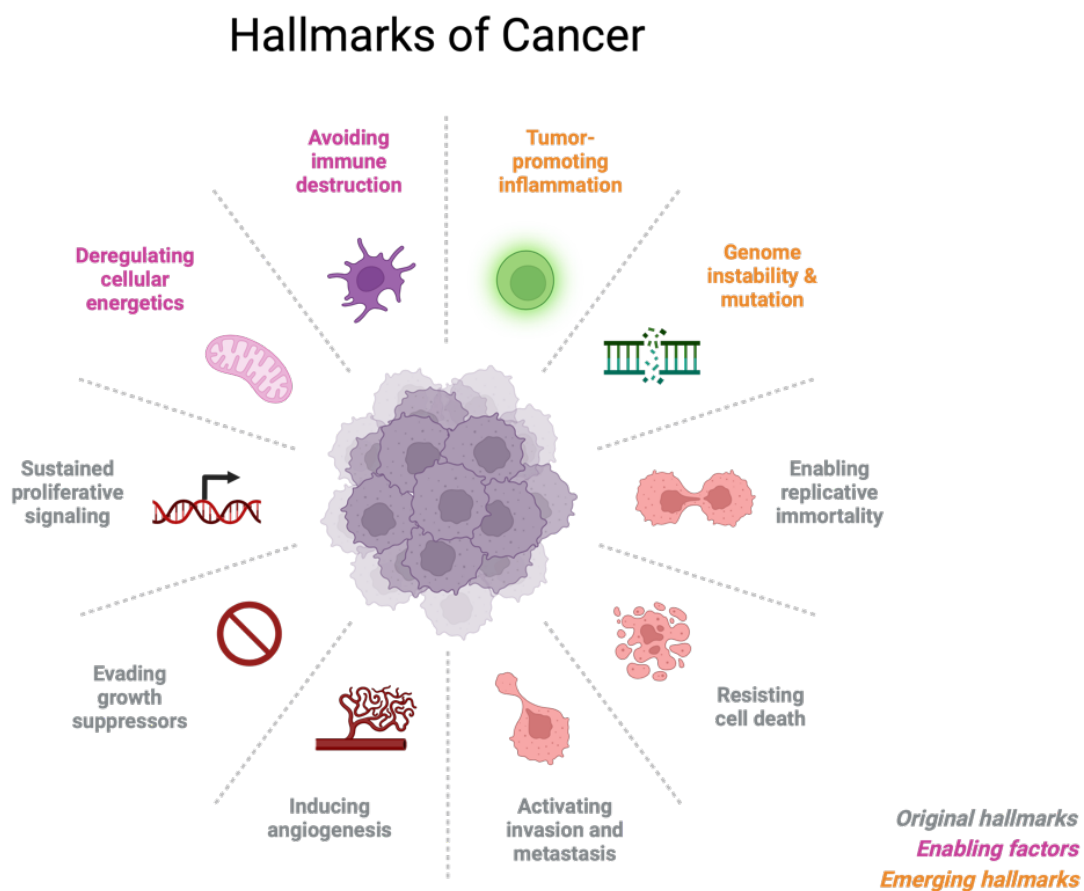


Figure 4: Hallmarks of Cancer – Six classical hallmarks of cancer defined by Hanahan and Weinberg in 2000 marked in grey, two enabling factors colored in pink and two emerging hallmarks colored in yellow. Created with Biorender, adapted from Hanahan and Weinberg, 2010 [69].

Introduction

1.3.2. Cancer Immunotherapies

One focus for fighting tumor development and progression is the role of T cells to engage the immune system [74]. Normally, the cancer immune surveillances help to identify and eliminate malignant cells by recognizing tumor-associated antigens (TAAs). Nevertheless, tumor cells have developed mechanisms to trigger peripheral immune tolerance and evade destruction by an immune attack. This immune escape can take place through four different mechanisms, including down-regulation of antigen expression on their surface, up-regulating of immune checkpoints to suppress CD8⁺ T cell activity, recruiting suppressor immune cells such as Treg cells and release cytokines to form an immune suppressive environment [75, 76].

Cancer immunotherapies aim to stimulate, enhance or suppress the immune system to reshape the tumor microenvironment and prevent tumorigenesis [77]. Various approaches to immunotherapies have already been tested, ranging from cytokine therapy, treatment with tumor-specific vaccines and immune checkpoint inhibitors to adoptive T cell therapy. However, despite the promise, these therapies face challenges such as immune resistance and limited response rates, necessitating deeper understanding and further innovation in the field [78, 79].

Cancer vaccines are one subset of immunotherapy approaches and aim to stimulate the immune system to prevent cancer development or recurrence. Preventative vaccines, such as those targeting virus-induced cancers, have shown success in preventing cancer initiation but remain less effective in eliminating established tumors due to the complex TME and mechanisms of immune evasion [80]. Consequently, these vaccines are limited to addressing viral infections rather than directly targeting tumorigenesis.

Immunotherapies can also use small molecules targeting immune pathways that provide additional tools for cancer treatment. This includes for example the PD-1/PD-L1 interaction to enhancing T cell activity in the TME as well as stimulators of interferon genes (STING), which activate innate immunity and promote antitumor responses, particularly in combination with other therapies [81, 82].

Introduction

Moreover, monoclonal antibodies (mAbs) have become a milestone of cancer immunotherapy due to their specificity and versatility. Approaches include targeting of cancer-specific antigens to inhibit tumor growth, bi-specific mAbs which bind two different antigens, enhancing immune system-targeted tumor destruction and the Immune Checkpoint Inhibitors (ICI) [83]. The latter block proteins like PD-1/PD-L1 or cytotoxic T-lymphocyte antigen-4 (CTLA-4) to reinvigorate exhausted T cells and overcome immune suppression [84]. In 2018, the Nobel Prize was awarded to two immunologists for the development of immune checkpoint inhibitors of the PD-1 and CTLA-4 on T cells [85].

Another alternative to reactivate the immune system are adoptive cell therapies, which involve the transfer of autologous or engineered immune cells to enhance antitumor immunity. Key approaches include Chimeric Antigen Receptor (CAR) T cells therapy, TCR-T cell therapy and the use of Tumor-Infiltrating Lymphocytes (TILs). CAR T cell therapy uses genetically engineered T cells to target specific TAAs. These modified cells are reintroduced into the patient, where they exert potent antitumor effects. While highly effective in hematological malignancies, CAR T cell therapy faces challenges in solid tumors due to the immunosuppressive TME and antigen heterogeneity [86, 87]. TCR-engineered therapies modify T cells to recognize TAAs in an MHC-dependent manner. Enhancing the affinity of TCRs to TAAs can improve tumor-specific responses [88]. Moreover, TIL therapy involves isolating and expanding lymphocytes from tumor tissues. These cells exhibit natural specificity for TAAs and have shown promising results in metastatic melanoma, though their broader applicability remains under investigation [89].

Treg cells play a key role in resistance to ICIs, making them a focus of research for depletion strategies within the TME. However, systemic Treg depletion risks triggering severe autoimmunity. Clinical and preclinical studies highlight Treg cells as significant barriers to effective antitumor immunity and contributors to tumor progression [90]. Thus, targeting Treg cells is essential for improving cancer immunotherapy outcomes. Several therapies, often combined with ICIs, aim to directly or indirectly target Treg cells. A deeper understanding of Treg

Introduction

characteristics in cancer could enable disease-specific therapies, enhancing efficacy while minimizing immune-related adverse effects [91, 92].

1.4. Treg cells during acute, chronic and latent infection diseases

Infectious diseases can be categorized into acute, chronic, and latent types based on their progression, pathogen behavior and immune response. Acute infections can be caused by a variety of microorganisms, including viruses, bacteria, fungi, protozoa or worms [93]. It is characterized by a sudden or rapid onset of disease and short duration, typically clearing up within a month. The immune system responds robustly, aiming to eliminate the pathogen swiftly and effectively [94].

Treg cells play a complex role in the immune response during acute infections, influencing outcomes for both the host and pathogens. In acute infections, Treg cells prevent immune overactivation, reducing the risk of excessive tissue damage while modulating effector responses to pathogens [72, 73]. They accumulate at infection sites, expanding in response to various pathogens and shaping immune responses in ways that can benefit both the host and the microorganism. In contrast to acute infections, chronic infections persist for extended periods, often months to years, due to the pathogen's ability to evade or modulate the immune response [95]. In chronic infections, Treg cells contribute to pathogen persistence, primarily through the secretion of IL-10 [74]. This immunosuppressive mechanism can help pathogens evade immune clearance, prolonging infection. Treg cells also play a role in latent infections, which, alongside chronic infections, represent another common mechanism by which viruses persist for extended periods in an infected host [96]. Latent infections can be characterized by asymptomatic persistence of pathogens which can reactivate under conditions like immune suppression, malnutrition, stress, or certain medical treatments. For instance, studies indicate that Treg cells facilitate the establishment and reactivation of latent infections, such as Herpes simplex virus 1 (HSV-1), with stress-induced Treg cells promoting viral reactivation [75].

Introduction

Understanding the characteristics of Treg cells and exploring Treg-depleting therapies could enhance effector T cell function, offering potential benefits in the treatment of acute, chronic, and latent infectious diseases [75].

1.5. Aim of this project

Recent studies have highlighted the convergent mechanisms utilized by tumors and infectious diseases to evade the immune system. Both conditions share overlapping strategies of immune evasion and pathogenesis, revealing potential targets for therapeutic intervention. For example, one common mechanism involves evading recognition of stress-induced surface markers such as natural killer group 2 member D (NKG2D) ligands. These ligands activate NK and CD8⁺ T cell-mediated immune responses, and their suppression represents a shared evolutionary strategy in viral infections and malignant transformations [97].

As antitumor immunity leads to immune escape the question remains whether Treg cells from healthy tissues, TME or infection sites exhibit similar transcriptomic and genomic characteristics. Additionally, the identification of shared TCR clonotypes could give a hint of common molecular mechanisms across these different settings. Emerging evidence suggests a pan-tissue Treg population with a shared capacity for circular migration across various healthy tissues. This thesis aims to explore the convergent gene expression pattern and TCR repertoire of NLT Treg cells from different healthy tissue in comparison to the TME and inflamed organs. By investigating tumors of different type and location, we try to identify a tumor tissue specific gene expression pattern as well as TCR similarities shared by all Treg cells. These investigations raise the following key questions:

- 1) How does the phenotype of NLT Treg cells change between healthy tissue compared to tumor and inflamed environment?
- 2) Are tumor-infiltrating Treg cells defined by tissue-specificity or tumor-specificity, or do these characteristics depend on different tumor types?
- 3) Does tumor type and location influence the phenotype of NLT Treg cells?

Introduction

- 4) Where do tumor-infiltrating Tregs originate or develop, and does this vary across different tumor types and locations?

To answer these questions, we first performed both flow-cytometry-based as well as single-cell gene expression-based characterization of Treg cells from different murine organs in healthy animals.

Single-cell gene expression analysis (scRNA-seq) has become a powerful tool for studying cellular transcriptional programs. Immune cells, such as T and B cells, exhibit extreme heterogeneity due to their diverse receptor repertoires, which enable the recognition of various foreign invaders [98, 99]. Recent advancements in single-cell methods allow for the simultaneous measurement of gene expression and T-cell receptor clonality, so called scRNA/TCR-seq. This technology helps identify and characterize distinct immune cell subsets in both health and disease, revealing novel pathogenic drivers and potential biomarkers [100, 101].

We performed a first characterization of Treg cells from secondary lymphoid environments (SLE), including the spleen, mesenteric lymph nodes (mLN), which drain the colon, and inguinal lymph nodes (iLN), the draining lymph nodes of the skin. Within these SLE, we identified three distinct populations: naïve/lymphoid, precursor non-lymphoid tissue (NLT)-like, and NLT-like Treg cells, providing insights into gene expression and TCR clonal expansion during tissue Treg development.

To investigate tissue-specific Treg markers, we selected the skin as an example of NLT. Given the established role of colon pTreg cells in tumor-mediated immune suppression, we also included colon-derived Treg cells in our study [102, 103]. Alongside gene expression analysis, we examined the clonality and clonal distribution of TCRs from Treg cells in different mouse organs. While gene expression comparisons could be performed across mice, TCR analysis required a mouse-specific approach due to the individuality of each TCR repertoire. Nevertheless, tissue-specific TCR clonality can be directly compared within the same individual across different tissues.

Introduction

Following our scRNA/TCR-seq analysis in healthy mice, we extended the study to investigate Treg cells under inflammatory and tumor conditions. We used the Azoxymethane (AOM)/Dextran Sodium Sulfate (DSS) model, which induces chemical DNA damage followed by repeated cycles of colitis. This two-step model mimics key features of inflammatory bowel disease (IBD) within 14 days, with tumor development typically occurring after 60 days. Due to its accuracy in replicating colitis-associated cancer (CAC), it serves as a valuable model for studying inflammation-driven tumors [104, 105].

To explore how tumor location impact the Treg cell phenotype and TCR sharing, we incorporated two additional tumor models. The first involved the subcutaneous implantation of MC38 colorectal carcinoma cells, providing a tumor model external to the colon. The second was a skin-specific model using B16-F10 melanoma cells implanted subcutaneously at their site of origin.

This comprehensive analysis across three distinct tumor models aimed to uncover how the tumor microenvironment and anatomical site influence the gene expression and TCR repertoire of tumor-infiltrating Treg cells. **Figure 5** illustrates the mouse models included in this study.

Introduction

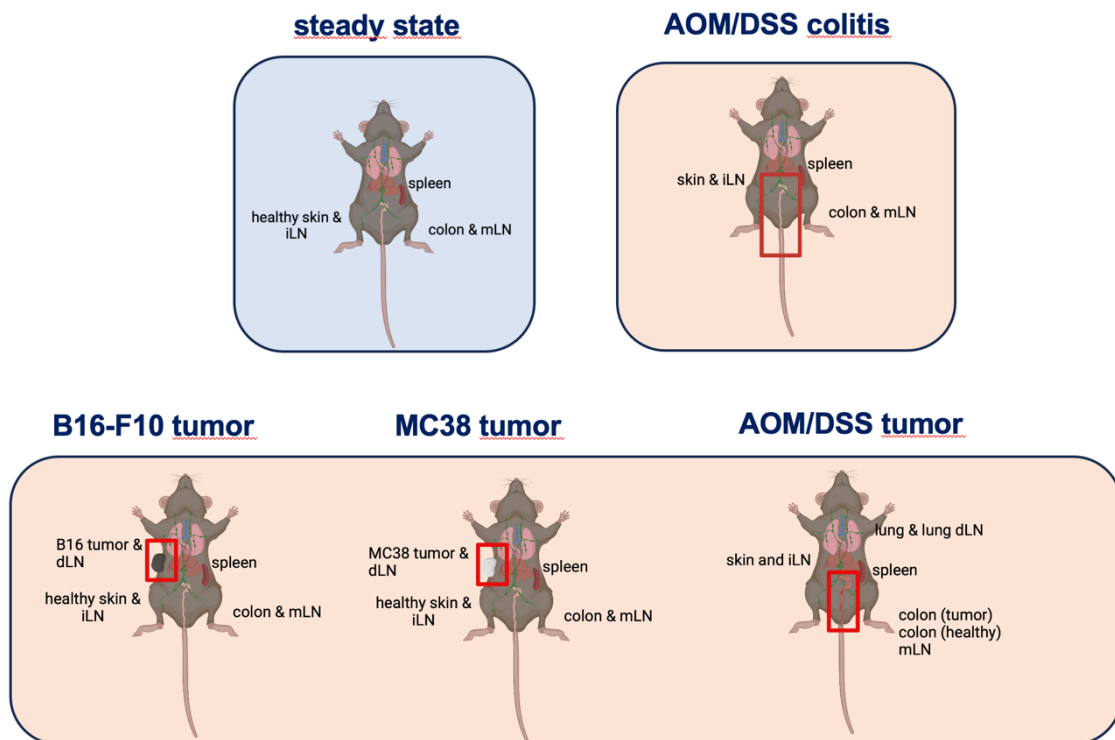


Figure 5: Overview of different mouse models investigated in this thesis. The steady state displays a wild-type mouse at the age of 10-12 weeks and is highlighted in blue. The disease types are colored in yellow, including a AOM/DSS-treated colitis, AOM/DSS-induced colorectal carcinoma, a adenocarcinoma model using MC38 cells and a melanoma model using B16-F10 cells which both induced subcutaneous tumor. Created with Biorender.

2. Material

Table 1: Consumables

Material	Company
100 µm strainer	Greiner, 542000
15 mL Falcon	Thermo Scientific Inc., 339650
45 µm filters	Labomedic
50 mL Falcon	Thermo Scientific Inc., 339652
70 µm strainer	Greiner, 542070
Eppendorf 1,5 mL tubes	Merck, Z606340
Eppendorf® DNA-LoBind-Röhrchen	Merck, EP0030108051
GentleMACS tube	Miltenyi Biotec, 130-096-334
Greiner round bottom tubes, polystyrene	Merck, Z617776-1500EA
PCR tubes and stripes	Thermo Scientific Inc., AB-0337

Table 2: Chemicals and Reagents

Chemicals	Company
Accutase® solution	Sigma Aldrich, SLCP8683
Anti-PE MicroBeads UltraPure	Miltenyi Biotec, 130-105-639
Ammonium-Chloride-Kalium (ACK) lysis buffer	Thermo Scientific Inc., A1049201
Bovine Serum Albumin (BSA)	Thermo Scientific Inc., 11924.04
CD4 (L3T4) MicroBeads	Miltenyi Biotec, 130-117-043
CD45 MicroBeads	Miltenyi Biotec, 130-052-301
Dextran-Sodium-Sulfat (DSS)	Sigma, 42867
DMEM	Gibco 10938-025
Fc blocking reagent	Miltenyi Biotec, 130-092-575
Fetal Calf Serum (FCS)	Gibco 26140079
HBSS (Ca ₂ ⁺ , Mg ₂ ⁺)	Thermo Scientific Inc., 14025092
HEPES	PAN-Biotech P05-01100
Percoll	Sigma Aldrich, 17-0891-01
RLT buffer	Qiagen, 79216

Material

RPMI	Gibco 11875093
β -Mercaptoethanol	Sigma, 60-24-2

Table 3: Enzymes

Enzymes	Company
Collagenase II	Sigma, C6885-1G
Collagenase IV	Sigma, C5138-1G
Collagenase V	Sigma, C9263-1G
Collagenase D	Roche 11088882001
DNase I	Roche, 11284932001
Azoxymethan (AOM)	Merck, 23843-45-2

Table 4: Antibodies

Antibodies	Company
Alexa Fluor® 488 anti-mouse FOXP3	BioLegend®, 320012
APC anti-mouse CD11b	BioLegend®, 101212
APC anti-mouse CD11c	BioLegend®, 117310
APC anti-mouse CD19	BioLegend®, 115512
APC anti-mouse CD206	BioLegend®, 141708
APC anti-mouse MHC class II	BioLegend®, 107614
APC anti-mouse NK1.1	BioLegend®, 108710
APC-Cy7 Zombie NIR Dye	BioLegend®, 423104
Batf (D7C5) Rabbit mAb	Cell Signaling Technology®, 8638S
BB700 anti-mouse KLRG1	BD Biosciences, 742199
Biotin anti-mouse CD198 (CCR8)	BioLegend®, 150316
BUV737 anti-mouse CD45	BD, 748371
BV 421 Streptavidin	BioLegend®, 405225
BV 510 anti-mouse CD62L	BioLegend®, 104441
BV 605 anti-mouse CD279 (PD-1-)	BioLegend®, 135220
BV 711 anti-mouse IL-33R (ST2)	BioLegend®, 745549
BV 785 anti-mouse CD3e	BioLegend®, 100355
PE anti-mouse CD25	BioLegend®, 102008

Material

PE-Cy7 anti-mouse CD8a	BioLegend®, 100722
R718 Rat anti-mouse CD4	BD Biosciences, 566939
TotalSeq C0301 anti-mouse Hashtag 1 Antibody	BioLegend®, 155861
TotalSeq C0000 anti-mouse Hashtag 10 Antibody	BioLegend®, 155879
TotalSeq C0000 anti-mouse Hashtag 2 Antibody	BioLegend®, 155863
TotalSeq C0000 anti-mouse Hashtag 3 Antibody	BioLegend®, 155865
TotalSeq C0000 anti-mouse Hashtag 4 Antibody	BioLegend®, 155867
TotalSeq C0000 anti-mouse Hashtag 5 Antibody	BioLegend®, 155869
TotalSeq C0000 anti-mouse Hashtag 6 Antibody	BioLegend®, 155871
TotalSeq C0000 anti-mouse Hashtag 7 Antibody	BioLegend®, 155873
TotalSeq C0000 anti-mouse Hashtag 8 Antibody	BioLegend®, 155875
TotalSeq C0000 anti-mouse Hashtag 9 Antibody	BioLegend®, 155877

Table 5: Biological Material

Biological Material	Supplier
B16-F10 cells (ATCC CRL-6475)	Institute of Immunology, UM Mainz, AG Schild
C57BL/6J0laHsd Mouse strain	Envigo
MC38 cells (Merck, SCC172)	Institute of Immunology, UM Mainz, AG Schild

Table 6: Kits

Kits	Company
5' Feature Barcode Kit	10X Genomics, PN-1000256
Chromium Next GEM Chip K	10X Genomics, PN-1000286
Chromium Next GEM Single Cell 5' Reagent Kit v2	10X Genomics, PN-1000263
Chromium Single Cell Mouse TCR Amplification Kit	10X Genomics, PN-1000254
Dual Index Kit TN Set A	10X Genomics, PN-1000250
Dual Index Kit TT Set A	10X Genomics, PN-1000215

Material

High Sensitivity DNA Kit	Agilent, 5067-4626
High Sensitivity RNA Kit	Agilent, 5067-5579
Library Construction Kit	10X Genomics, PN-1000190
NextSeq 500/550 High Output Kit v2.5 (75 Cycles)	Illumina, 20024906
NextSeq 500/550 High Output Kit v2.5 (150 Cycles)	Illumina, 20024907
RNeasy Kit	Qiagen, 74104
SMART-Seq v4 PLUS Kit	Takara, R400752 and R400753
Tumor Dissociation Kit, mouse	Miltenyi Biotec, 130-096-73B

Table 7: Laboratory software and Equipment

Laboratory software and Equipment	Supplier
2200 TapeStation Controller	Agilent
Agilent Software Packages (TapeStation Controller Software and Analysis Software)	Agilent
BD FACSDiva™ Software	© 2024 BD Bioscience
BD FACSymphony A5	BD
BioRender	© 2024 BioRender
Centrifuge 5418 R	Eppendorf SE
Chromium Controller	10X Genomics
FACS Aria II	BD
FlowJo™ v10 Software	© 2024 BD Bioscience
GentleMACS	Miltenyi Biotec, 130-096-427
gentleMACS OctoDissociator	Miltenyi Biotec
GraphPad Prism v10.4.0	© 2024 GraphPad Software
Multifuge 3 L-R	Heraeus group
NextSeq 500/550	Illumina

Material

Table 8: Buffer and Cell Culture Media

Buffer	Reagents
10x PBS Buffer (5 L)	NaCl (402 g) NaH ₂ PO ₄ x H ₂ Odest (78 g) + dest H ₂ O to 5 L pH = 6.6, sterile filtration
1x PBS Buffer (1 L)	10x PBS (100 mL) dest H ₂ O (900 mL)
1x Permeabilization Buffer	Permeabilization Buffer 10x (1 mL) Sterile dest H ₂ O (9 mL)
40 % Percoll	10x PBS (2 mL) Percoll (8 mL) dest H ₂ O (10 mL)
80 % Percoll	10x PBS (2 mL) Percoll (16 mL) dest H ₂ O (2 mL)
Colon Digestion Buffer	0.85mg/ml Collagenase V (450 uL) 1.25mg/ml Collagenase D (125 uL) 1mg/ml Dispase (1 uL) 30ug/ml DNase (30 uL) DMEM (8.4 uL)
Colon Pre-Digestion Buffer	1 x HBSS (10 mL) 2 mM EDTA (40 uL)
FACS Buffer	1x PBS (980 mL) 2 % FCS (20 mL)
Fixation Buffer	Fixation/Permeabilization Concentrate (250 µL) Fixation/Permeabilization Diluent (750 µL)
Gey's Lysis Buffer	150 mM ammonium chloride 1 mM Potassium hydrogen carbonate 1 mM EDTA In dest H ₂ O: pH 7.3, sterile filtrated 0.2 µm

Material

Lung Digestion Buffer	DMEM (8.5 mL) 5 mg/mL BSA (0.5 mL from 100 g/L stock) 1 mg/mL Collagenase Type IV (1 mL from 10 mg/mL stock) 20 µg/mL DNase I (20 µL from 10 mg/mL stock)
MACS Buffer	1x PBS (980 mL) 5 mM EDTA 0,5 % BSA
MC38/B16-F10 Cell Culture Media	DMEM (500 mL) 200 mg/mL Penicillin 200 U/mL Streptomycin 2 mM L-Glutamine 1 mM Natrium Pyruvate (5 mL) 10 % FCS
Skin Digestion Buffer	DMEM (5.5 mL) 5 mg/mL BSA (0.5 mL from 100 g/L stock) 1 mg/mL Collagenase Type IV (4 mL from 10 mg/mL stock) 20 µg/mL DNase I (20 µL from 10 mg/mL stock)
Tumor Digestion Enzyme Mix	Tumor Digestion Media, 2.5 mL Enzyme D, 100 µL Enzyme R, 50 µL Enzyme A, 12.5 µL
Tumor Digestion Media	RPMI 1650 Media (500 mL) 1 mM Natrium Pyruvate (5 mL) 10 FCS (50 mL)

Table 9: Software and Packages

Software	Version	References
AnnotationHub	3.10.0	DOI: 10.18129/B9.bioc.AnnotationHub
apeglm shrinkage estimator	1.22.1	[106]
bedtools	24.0	[107]

Material

BiocSingular	1.18.0	[108]
CellChat	2.1.2	[109]
Cellranger	7.1.0	[110]
circlize	0.4.15	[111]
ClusterProfiler	4.10.0	[112]
ComplexHeatmap	2.18.0	[113]
DESeq2	1.40.2	[114]
dittoSeq	1.14.2	[115]
dplyr	1.1.4	DOI: 10.32614/CRAN.package.dplyr
DropletUtils	1.22.0	[116]
DT	0.31	DOI: 10.32614/CRAN.package.DT
edgeR	4.0.9	[117]
EnhancedVolcano	1.20.0	DOI: 10.18129/B9.bioc.EnhancedVolcano
enrichplot	1.22.0	DOI: 10.18129/B9.bioc.enrichplot
EnsemblDb	2.26.0	[118]
ggplot2	3.4.4	DOI: 10.32614/CRAN.package.ggplot2
ggrepel	0.9.5	DOI: 10.32614/CRAN.package.ggrepel
ggvenn	0.1.10	[119]
harmony	1.2.0	[120]
ideal	1.24.1	[121]
igraph	2.0.1.1	[117]
limma	3.58.1	[122]
org.Mm.eg.db	3.18.0	DOI:10.18129/B9.bioc.org.Mm.eg.db
PcaExplorer	2.26.1	[123]
pheatmap	1.0.12	DOI: 10.32614/CRAN.package.pheatmap
plotly	4.10.1	DOI: 10.32614/CRAN.package.plotly
R	4.3.1	[124]
RColorBrewer	1.1.3	DOI: 10.32614/CRAN.package.RColorBrewer
readxl	1.4.3	DOI: 10.32614/CRAN.package.readxl
RStudio	4.3.1	[125]
Rsubread	2.14.2	[126]
sambamba	0.6.5	DOI: 10.1093/bioinformatics/btv098

Material

samtools	0.1.19/ 1.3.1	[127]
scater	1.30.1	[128]
scDblFinder	1.16.0	[129]
scraper	1.30.1	[117]
Seurat	4.4.0	[108]
SingleCellExperiment	1.24.0	[108]
SingleR	2.4.1	DOI: 10.18129/B9.bioc.SingleR
spiralize	1.0.6	[130]
STAR aligner	2.6.1a	[131]
stringr	1.5.1	DOI: 10.32614/CRAN.package.stringr
topGO	2.52.0	[132]
TSCAN	1.40.0	[133]
VennDiagram	1.7.3	DOI: 10.32614/CRAN.package.VennDiagram
viridis	0.6.5	DOI: 10.32614/CRAN.package.viridis

3. Methods

3.1. Mouse Models

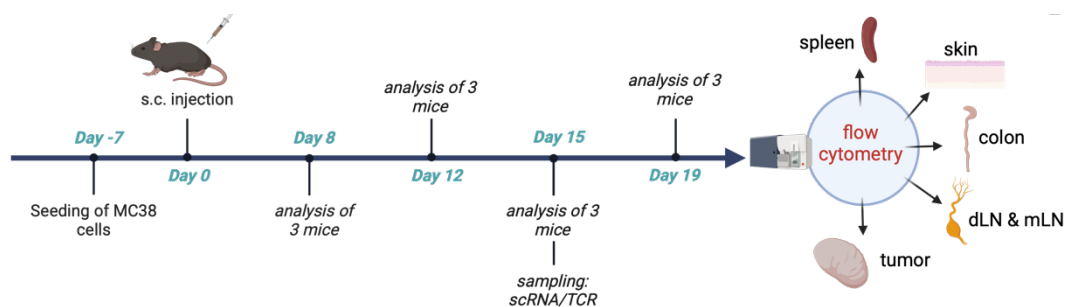
3.1.1. Healthy mice

C57BL/6J01aHsd wild-type (WT) female mice were purchased from Envigo. For the characterization of the T cell landscape and scRNA/TCR-seq, mice aged 10–12 weeks were sacrificed. The protocol for immune cell isolation remained consistent for all subsequent analysis.

3.1.2. MC38: subcutaneous colorectal carcinoma model

The MC38 murine colon adenocarcinoma cell line, commonly used as a model for colorectal carcinoma, was derived from a colon tumor in a female C57BL/6 mouse after prolonged exposure to 1,2-dimethylhydrazine dihydrochloride (DMH). Subcutaneous (s.c.) inoculated MC38 cells demonstrate rapid *in vivo* growth, with a doubling time of approximately 4 days [134, 135].

For the analysis, first a characterization of the T cell landscape over time was performed by flow cytometry. Therefore, mice were sacrificed on 4 different timepoints to track the immune cell infiltration of Treg cells into the tumor site. Mice were monitored for body weight, general condition, and clinical signs per ethical guidelines. Tumor volume was measured on days 8, 12, 15 and 19 using a digital caliper. Mice were anesthetized with isoflurane for each measurement. An overview of this first characterization kinetic experiment is provided in **Figure 6**.



Methods

Figure 6: Overview of the kinetic from the MC38 adenocarcinoma model. Seven days before the s.c. injection, MC38 cells were seeded. MC38 cells were s.c. injected and 3 animals were analyzed for T cell surface marker expression on day 8, day 12, day 15 and day 19 as well as scRNA/TCR-seq on day 15.

After this detailed characterization of Treg cells in the environment of the MC38 adenocarcinoma model via flow cytometry, we chose one timepoint (day 15) of high Treg infiltration for the following scRNA/TCR analysis. A detailed protocol for flow cytometry and scRNA/TCR workflow is described in 3.4.

3.1.3. Skin Cancer: subcutaneous B16-F10 melanoma model

The murine B16-F10 melanoma model is one of the most studied skin cancer models in mouse. It can be classified as a “cold tumor”, because of it is very low immune cell infiltration. B16-F10 is also known for their resistance to immunological treatments [136, 137]. In vitro, these cells grow as an adherent population taking on an epithelial morphology. In vivo, subcutaneous implant of B16-F10 cells results in an aggressively growing tumor [138].

To investigate Treg cell infiltration in this "cold tumor model", we initially selected four timepoints to determine when Treg cells are recruited into the tumor environment. Mice were monitored for body weight, general condition, and clinical signs per ethical guidelines, and flow cytometry of surface marker for T cells were performed on days 8, 11, 13 and 15. Based on these findings, we identified a timepoint with high Treg cell infiltration (day 13) to further characterize the Treg cells within the TME using scRNA/TCR-seq.

Methods

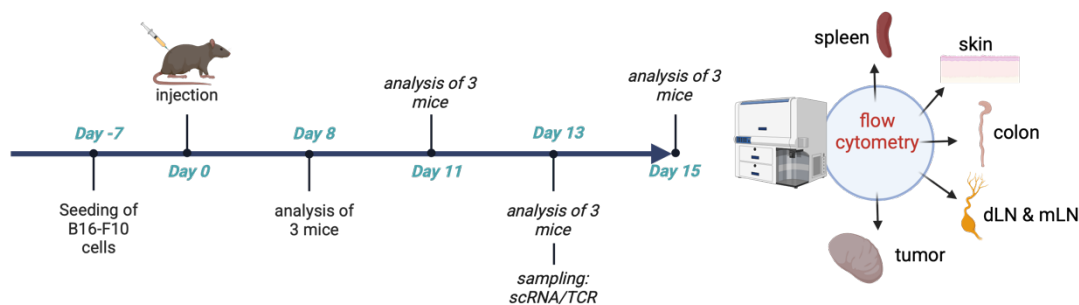


Figure 7: Overview of the kinetic of the B16-F10 melanoma model. Seven days before the s.c. injection, B16-F10 cells were seeded. Cells were s.c. injected and 3 animals were analyzed for T cell surface marker expression on day 8, day 11, day 13 and day 15 as well as scRNA/TCR-seq on day 13.

3.1.4. Tumor cell line cultivation (B16-F10 and MC38)

2×10^6 MC38 adenocarcinoma cells and B16-F10 melanoma cells were thawed from a liquid nitrogen tank and transferred into a 75 cm^2 cell flask with cell culture media. The cells were incubated at 37°C with 95% humidity and 5% CO_2 . On day 3, the media was refreshed to ensure sufficient nutrients, and the cells were split once they reached $\sim 70\%$ confluence, as confirmed under a microscope. The media was removed using an Integra Vacusave pump, and the cells were washed with 10 mL of 1x PBS. Then, 7 mL of Accutase[®] solution was added per flask, and the flask was incubated at 37°C for 5 minutes. Once the cells detached from the bottom, as observed under a microscope, 10 mL of cell culture media was added to stop the Accutase[®] reaction. The cell suspension was transferred to a 50 mL falcon tube and centrifuged at $500 \times g$ for 5 minutes at 4°C . After discarding the supernatant, the pellet was resuspended in 5 mL of cell culture media. 1×10^6 cells were distributed into two fresh 75 cm^2 flasks, each refilled with 15–20 mL of cell culture media based on the initial confluence. The cells were harvested again after 2 days.

3.1.5. Tumor cell injection (MC38 and B16-F10)

On day 7, the cells were harvested as previously described and measured after centrifugation. The cells were resuspended in 10 mL of sterile PBS, and $18 \mu\text{L}$ of the

Methods

suspension were transferred into a 0.5 mL Eppendorf tube. Then, 2 μ L of Acridine Orange/Propidium Iodide Stain were added and mixed. A 10 μ L sample was pipetted into one chamber of a Photon-Slide™ Ultra-low Fluorescence Counting Slide and analyzed using the LUNA-FL™ cell counter to determine the number of living cells. The cell suspension was adjusted to 1×10^6 cells/mL by adding sterile PBS. Once adjusted, the mice were anesthetized with isofluran. While under anesthesia, the lateral side of their bodies was shaved. A suspension of 1×10^6 cells in 100 μ L sterile PBS (MC38) and 5×10^5 cells in 100 μ L sterile PBS (B16-F10) was injected subcutaneously into the shaved area.

3.1.6. Colitis-Associated Cancer: AOM/DSS-induced colitis model

Colorectal cancer (CRC), the third most common cancer worldwide, is a highly heterogeneous disease arising from complex interactions between genetic and environmental factors. Chronic inflammation, such as colitis, predisposes individuals to CRC by creating a microenvironment rich in immune cells that produce proinflammatory cytokines, growth factors, and elevated levels of reactive oxygen species [139]. This two-step tumor model involves severe inflammation mimicking certain features of inflammatory bowel disease (IBD) within 14 days. Tumor development typically occurs after 60 days, making it a highly accurate model for studying colitis-associated cancer (CAC) [104, 105].

In highly inflammatory settings, Treg cells play a key role in preventing immune overactivation and minimizing tissue damage. While Treg cells are known to support tumor development in various tissues, their role in CAC progression remains unclear. To address this, we used scRNA/TCR-seq to characterize the gene expression and TCR repertoire of Treg cells in an inflammatory condition like colitis (day 14) and in the TME of CAC (day 60).

Methods

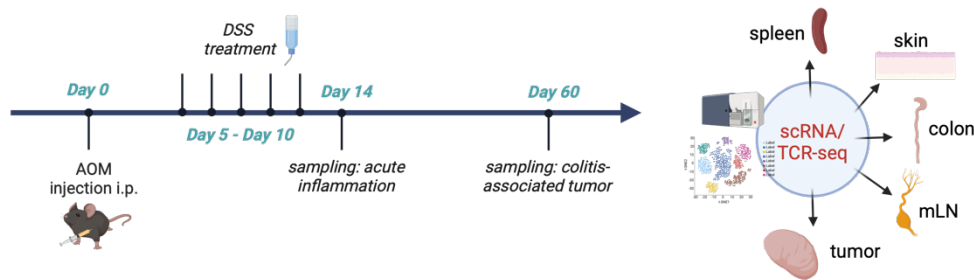


Figure 8: Schematic Overview of the AOM/DSS model for CAC induction. Mice were injected intraperitoneally with AOM (10 mg/kg body weight) on day 0. From day 5 to day 10, the mice received 2.5% weight per volume (wv) dextran sulfate sodium (DSS) dissolved in autoclaved drinking H₂O. Mice were sacrificed on day 14 for evaluation of colitis or on day 60 for analysis of CAC.

With support of AG Clausens group from the Institute of Molecular Medicine, CAC was induced in 10-12-week-old female WT mice by intraperitoneal injection of AOM (10 mg/kg body weight) on day 0. From days 5 to 10, mice received 2.5% DSS (36-50 kDa) in drinking water, followed by regular autoclaved water until the experiment's end, as shown in **Figure 8**. Mice were monitored for body weight, general condition, and clinical signs per ethical guidelines. Weight loss $\geq 20\%$ of initial body weight prompted euthanasia. Protocol was adapted from [104, 140]. Mini-endoscopy was performed one day before sacrifice to confirm tumor development and state of inflammation by AG Clausen.

3.2. Immune Cell Isolation for phenotype and transcriptome analysis

Single-cell RNA and TCR sequencing technologies offer an unparalleled resolution for understanding the complexity and heterogeneity of biological systems at the cellular level. This dual approach provides comprehensive insights into both transcriptomic profiles and TCR diversity, enabling detailed exploration of immune responses and cellular interactions across various tissues [141]. scRNA-seq facilitates the unbiased profiling of individual cells, revealing diverse cell-types and states within a complex tissue environment. Integrating TCR sequencing with scRNA-seq allows for the simultaneous characterization of T cell phenotypes and

Methods

their corresponding antigen specificity. The TCR acts as a "biological barcode" for each cell, aiding in the identification of clonal expansions and relationships among T cells within an individual [142].

Our workflow for generating high quality scRNA/TCR-seq data generally requires four main steps, including (1) tissue digestion and target cell enrichment, (2) barcoding, amplifying and preparing of GEX, VDJ and CSP libraries, (3) sequencing and data processing as well as (4) data analysis using R and Bioconductor. This streamlined process ensures reliable and reproducible data generation, enabling robust analyses of cellular and molecular mechanisms.

The following text passages have been adapted from our own publication, partially rewritten and marked as such (Nedwed and Helbich et al., 2023, [143]).

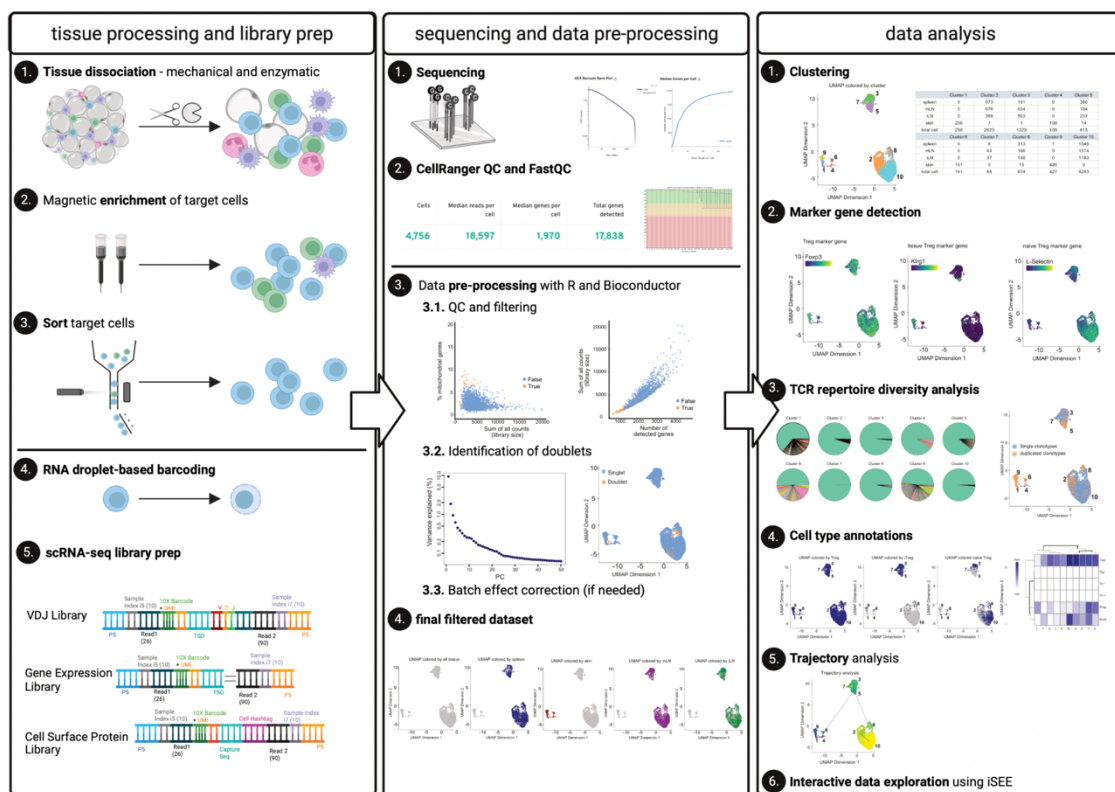


Figure 9: Overview of scRNA/TCR-seq workflow. The schematic provides an overview of the scRNA/TCR-seq process, divided into three main panels: tissue processing and library preparation, sequencing and quality control, and data analysis. Tissue Processing and Library Preparation (left panel): Tissues harvested from an individual mouse are subjected to enzymatic and mechanical digestion (1), followed by target cell enrichment (2) to optimize cell sorting efficiency (3). Subsequently, cells labeled with BioLegend® TotalSeqC anti-mouse Hashtagging antibodies and 10X beads are loaded onto the 10X Chromium

Methods

controller (4). This is followed by scRNA-seq library preparation (5). Sequencing and Quality Control (middle panel): Sequencing (1) generates raw data, which undergoes quality control (2). Pre-processing of the data is performed using R and Bioconductor to produce a final, filtered dataset ready for analysis (3). Data Analysis (right panel): The analysis includes clustering (1), marker gene detection (2), TCR repertoire diversity assessment (3), cell-type annotation (4), and trajectory analysis (5). For interactive exploration, the iSEE platform (6) can be utilized. Copied from Nedwed and Helbich et al. [143].

3.2.1. Isolation of immune cells from murine secondary lymphoid environment (SLE)

For isolation of Treg cells from murine secondary lymphoid tissues such as spleen or lymph nodes, a midline incision was performed to expose the peritoneal cavity. The spleen is harvested immediately and stored at 4°C. For mesenteric lymph nodes (mLN), the cecum is located, the small intestine is moved aside, and the mLN chain is exposed. The nodes are harvested with forceps, placed in FACS buffer and stored at 4°C. Inguinal lymph nodes are collected from both hemispheres beneath the skin and stored similarly. Furthermore, the tissue is mechanically dissociated on a 100 µm filter unit using a plunger or forceps. After centrifugation (2 min, 1000g, 4°C), red blood cells are lysed with Ammonium-Chloride-Kalium (ACK) lysis buffer. The cell suspension was filtered through a 70 µm strainer, resuspended in 500 µL FACS buffer, and counted.

3.2.2. Isolation of immune cells from murine tissue – skin

To isolate T cells from murine skin tissue, hair was removed from the animal's back using an electric shaver and depilatory cream. The cream was applied for 2 minutes, followed by thorough washing with tap water to remove all hair, ensuring smooth downstream filtration. The skin was then separated from the dorsal surface, cut into small pieces, and placed in a GentleMACS tube containing 10 mL of skin digestion buffer using 10 mL buffer per 0.5 g of tissue. The sample was digested with the GentleMACS Dissociator (program: 37_C_Multi_H). After completion of the tissue-specific program, the cell suspension was centrifuged (10 min, 400g, 4°C), resuspended in 500 µL FACS buffer, and filtered through a 100 µm filter.

Methods

3.2.3. Isolation of immune cells from murine tissue – colon

To isolate immune cells from murine colon tissue, the colon was removed and soaked in PBS + 3% fetal calf serum (FCS) to remove as much fat and feces as possible. The colon was then opened longitudinally and washed thoroughly to ensure all remaining fecal matter was removed. The tissue was then pre-digested two times, including an incubation in 10 mL of HBSS with 2 mM EDTA in a shaking water bath or orbital shaker at 225 rpm, with 37°C for 15 minutes, manually shaking the tubes 2–3 times during the incubation. After incubation, tubes were shaken vigorously, and the supernatant was filtered through a 50 µm mesh. The remaining tissue was washed in 10 mL of warmed HBSS, shaken vigorously, and filtered again through a 50 µm mesh. After ensuring no EDTA residues remained from the previous steps, the tissue pieces were placed in 10 mL of the enzyme digestion mix in 50 mL tubes. The samples were incubated in a shaker at 37°C, shaking manually every 5–7 minutes. After 15 minutes, the single-cell suspension was passed through a 50 µm mesh and the supernatant was collected. The suspension was then diluted to 40 mL with PBS containing 3% FCS and centrifuged at 1200 rpm for 10 minutes at 4°C. The resulting cell pellet was resuspended in 500 µL PBS with 3%.

3.2.4. Isolation of immune cells from murine tissue – subcutaneous tumor tissue

Immune cells (CD45⁺ TIL cells) were isolated out of MC38- and B16-F10-bearing mice. Any healthy surrounding tissue was removed to ensure sample purity. The tumor was then processed using the Tumor Dissociation Kit from Miltenyi, following the manufacturer's protocol.

3.2.5. Isolation of immune cells from murine tissue – lung

Lung tissue was isolated and immediately transferred into 10 mL of digestion buffer at room temperature. The lungs were then cut into small pieces and digested with

Methods

the GentleMACS Dissociator (program: 37_C_m_LDK). Following digestion, the tissue was filtered through a 100 μm filtration unit, and the remaining pieces were dissociated using a syringe plunger. The filter was thoroughly flushed with PBS or DMEM to maximize cell recovery. The cell suspension was centrifuged at 300xg for 5 minutes at room temperature, and the supernatant was discarded. The pellet was resuspended in 1 mL of ACK lysis buffer and transferred to an Eppendorf tube for incubation at room temperature for 1 minute to lyse red blood cells. The sample was centrifuged at 1000xg for 2 minutes at 4°C, and the resulting pellet was resuspended in FACS buffer. To ensure single-cell suspension, the sample was passed through a 70 μm filter into a new tube with 500 μL FACS buffer, after which it was ready for downstream staining procedures.

3.3. Characterization of Treg cells from different tissue by scRNA/TCR-seq analysis

3.3.1. Magnetic Activated Cell Sorting (MACS)

For scRNA/TCR sequencing, cells isolated from the different murine tissue were enriched via MACS to shorten the time of Fluorescence-activated cell sorting (FACS) afterwards. To prevent nonspecific antibody binding, Fc blocking reagent were added. Cells are labeled with PE-conjugated anti-mouse CD4 or CD25 antibodies and stained for 20 min at 4°C. After staining, cells were washed and resuspended in MACS buffer. Target cells were bound by anti-PE microbeads for 20 min at 4°C, followed by two washes and centrifugations (2 min, 1000g, 4°C). The sample was loaded onto an equilibrated MACS column with a 70 μm filter unit and washed twice with 5 mL MACS buffer. The final elution was performed in 500 μL FACS buffer.

Methods

3.3.2. FACS

To ensure high quality and cell viability, MACS-enriched cells were sorted. For generating the CD25⁺ T cell dataset, cells from the SLE were sorted based on CD25 expression, whereas cells from the skin, colon, lung, and liver were sorted based on CD4 expression. To create a CD45⁺ immune cell dataset, cells were sorted based on CD45 expression and viability.

Cells were stained for 30 minutes at 4°C using the fluorescent antibodies (**Table 4**). For cell labelling each tissue was stained with a different TotalSeqC anti-mouse Hashtaging antibody (**Table 4**). To enhance labelling, cells were washed 3–5 times with 500 µL FACS buffer after staining. To prevent aggregation during antibody staining, the antibody mix was centrifuged at 14,000g for 10 minutes at 4°C, and the supernatant was transferred to a new tube.

Cells were sorted using the gating strategy shown in **Figure 10**. After sorting, a small sample was analyzed to assess post-sort purity, viability, and efficiency.

Methods

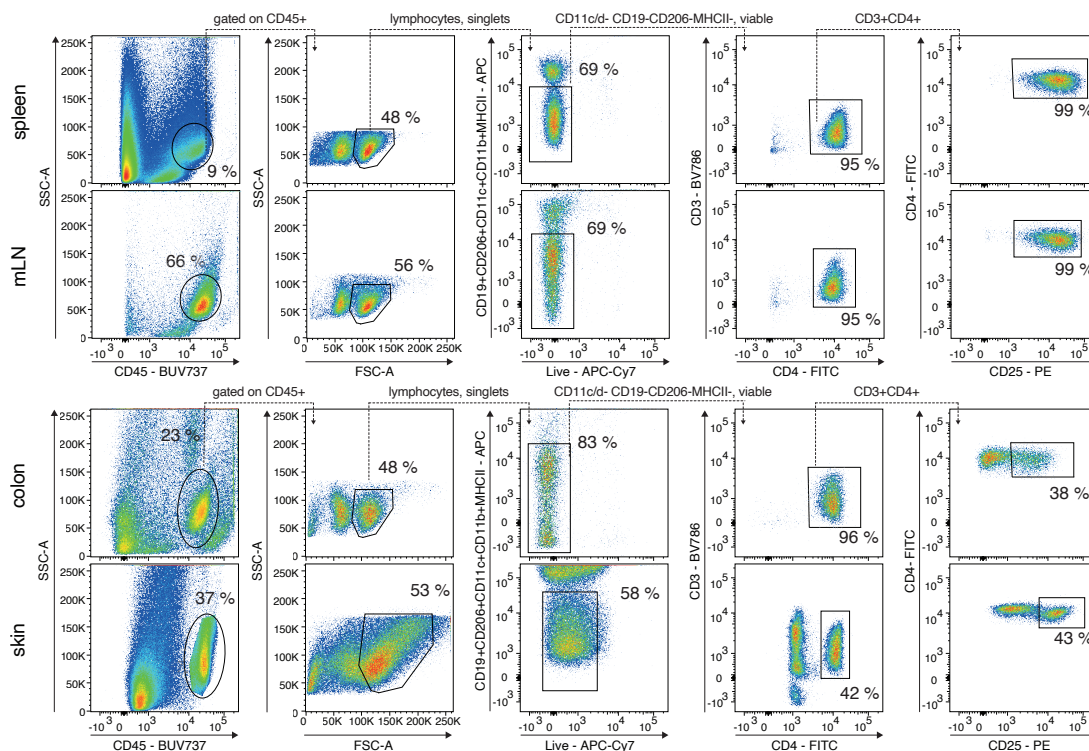


Figure 10: Overview of the gating scheme to sort CD25⁺ T cells of SLE (spleen, mLN, iLN), CD4⁺ T cells of colon and skin tissue. All sample sorted into the same collection tube. Immune cells were first identified by CD45⁺, afterwards doublets and dead cells were removed. By using a dump channel for CD19, CD11b, CD11c, MHCII, CD206 and CD3⁺ T cells were isolated and further gated on their CD4 or CD8 expression. Dotplots are created from one example of healthy animal used in this thesis and representative for all other analysis.

3.3.3. Single droplet barcoding of T cells, amplification and library preparation

Target cells from all murine organs were sorted into a single 1.5 mL Eppendorf tube containing 350 μ L PBS + 0.05% BSA. The sample was processed quickly after sorting to reduce the number of dying or dead cells in the collection tube. Shortly after sorting, the cells were pelleted by centrifugation (5 minutes, 300xg, 4°C). The supernatant was removed, and the sample was supplemented with master mix and beads to a final volume of 70 μ L, loaded onto a 10X Chromium Next GEM Chip K, and processed using the 10X Chromium Controller. Subsequently, cDNA amplification was performed using the Chromium Next GEM Single Cell 5' Reagent Kit v2 and the 5' Feature Barcode Kit. Following this, V(D)J amplification was carried

Methods

out using cDNA and the Chromium Single Cell Mouse TCR Amplification Kit. Libraries for GEX, CSP, and VDJ were prepared according to the Library Construction Protocol. The fragment length composition was evaluated via electrophoretic separation of the samples using Agilent High Sensitivity D1000 ScreenTape assay and reagents (**Figure 11**).

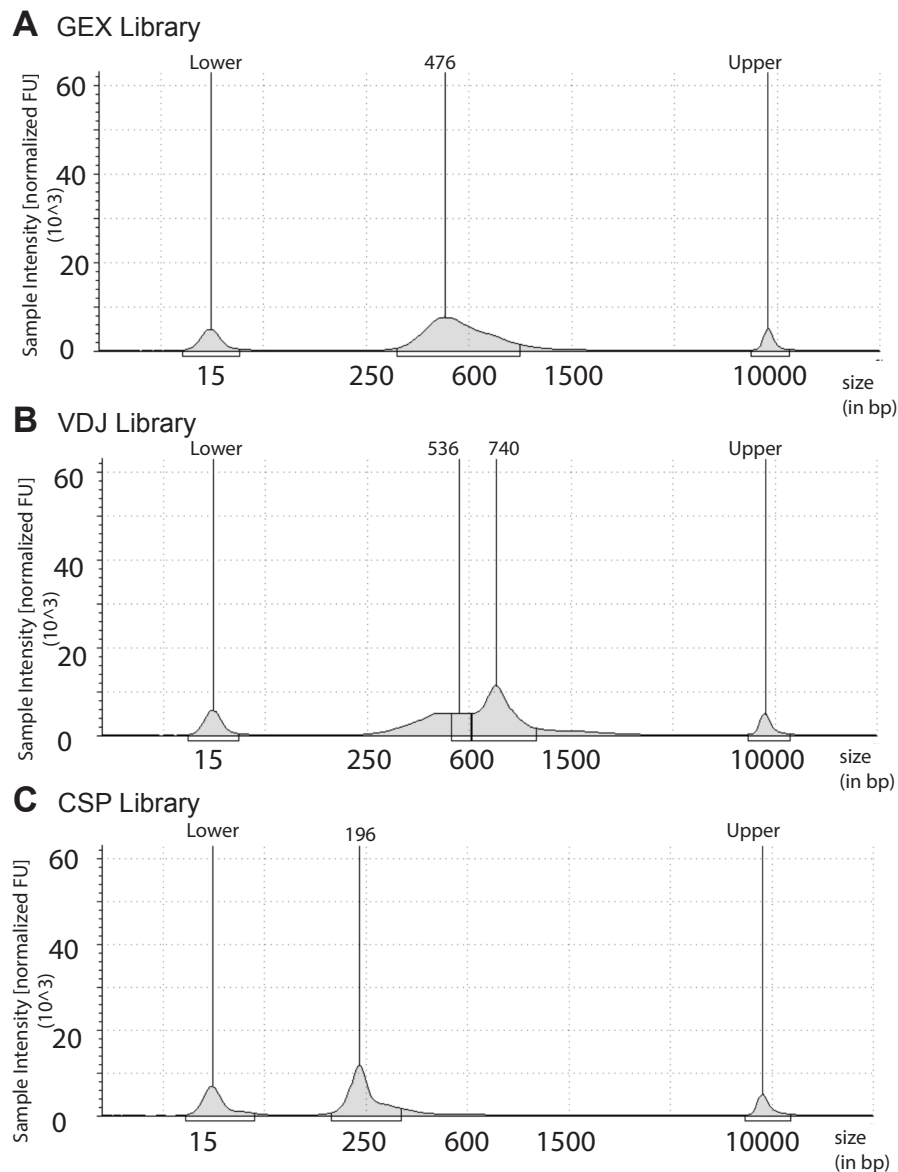


Figure 11: scRNA/TCR library profiles measured on a TapeStation. A-C: One representative image of the library fragment distribution of the GEX library (A), VDJ library (B) and CSP library (C) is shown.

Methods

3.3.4. Next Generation Sequencing (NGS) strategy

scRNA/TCR-libraries were sequenced on a NextSeq 500/550 with a 150-cycle high-output cartridge from Illumina. Sequencing was performed according to the manufactures protocol: paired-end, with 26 base pairs (bp) for Read1, 90 bp for Read2 and 10 bp for the Index i5 and Index i7 (PE 26-10-10-90) **Figure 12**.

GEX Library	read 1	index i5	index i7	read 2
purpose	10X Barcode, UMI	Sample Index	Sample Index	cDNA fragment
recommended length	26	10	10	90
VDJ Library	read 1	index i5	index i7	read 2
purpose	10X Barcode, UMI	Sample Index	Sample Index	VDJ info
recommended length	26	10	10	90
CSP Library	read 1	index i5	index i7	read 2
purpose	10X Barcode, UMI	Sample Index	N/A	Multiplex Barcode
recommended length	26	10	10	90

Figure 12: Overview of gene expression (GEX), VDJ and cell surface protein (CSP) library and recommended sequencing length. Copied from Nedwed and Helbich et al.[143].

3.3.5. Computation

scRNA/TCR data analysis was performed on the MOGON, which is a high-performing computing cluster at Johannes Gutenberg University Mainz.

3.3.6. Alignment of reads to the reference genome

After sequencing the GEX, VDJ, and CSP libraries, FASTQ files were aligned to the reference genome *refdata-gex-mm10-2020-A* using Cell Ranger, a software tool designed for single-cell sequencing datasets generated with 10X Genomics chemistry. Integration of GEX, VDJ, and Feature Barcode information was performed using Cell Ranger Multi, a method developed for processing scRNA samples with specific multiplexing antibodies. This approach supports the analysis of 3' multiplexed data. Since the 3' and 5' assays capture different transcript ends, and the 5' chemistry was employed to generate the GEX, CSP, and VDJ libraries,

Methods

modifications to the CellRanger Multi pipeline were made to ensure dataset compatibility.

The pipeline was executed twice: initially to assign cells to individual samples by combining the GEX and CSP libraries, and subsequently to integrate the T cell receptor library with the gene expression data from each tissue. Output files generated from each run were used for further analysis in R. A detailed protocol for this step was provided in our methods paper [143].

A table of sorted cells as well as aligned cells after sequencing for every mouse replicate used in this thesis can be found below:

Table 10: Sorted and aligned cells per organ for the individual mouse models.

Model	Organs	Sorted Cells	Aligned Cells	Genes per Cell	Reads per Cells
WT1	spleen	10000	3394	1491	20863
	mLN	10000	3375	1558	22307
	iLN	10000	3868	1680	26504
	colon	9800	3328	1490	20795
	skin	30000	7615	1306	22252
WT2	spleen	20000	6290	1819	22322
	mLN	15000	4666	1695	21387
	iLN	2200	674	1754	22120
	colon	3420	716	1449	16175
	skin	45000	15749	1435	21302
WT3	spleen	10000	907	1346	16992
	mLN	10000	862	1468	20491
	iLN	10000	896	1386	18254
	colon	3200	229	1364	19042
	skin	10000	580	1190	16622

Methods

Model	Organs	Sorted Cells	Aligned Cells	Genes per Cell	Reads per Cells
AOM/DSS_1 D14	spleen	6000	1805	1935	50118
	mLN	4000	862	2225	66677
	iLN	4000	1181	2008	54497
	colon	10000	4291	2057	69071
AOM/DSS_2 D14	spleen	6000	1999	2005	52195
	mLN	6000	2153	2154	60325
	iLN	6000	2858	476	8781
	colon	10000	4011	2751	94533
AOM/DSS_3 D14	spleen	6000	2700	1762	55102
	mLN	6000	2993	1999	70152
	dLN	6000	2858	1867	63873
	colon	10000	3203	1887	75077

Model	Organs	Sorted Cells	Aligned Cells	Genes per Cell	Reads per Cells
AOM/DSS_1 D60	spleen	10000	2027	1415	28978
	mLN	10000	2039	1426	29740
	iLN	10000	2037	1493	32177
	colon (NAT)	12000	2196	1875	42155
	colon (tumor)	12000	1982	1647	34640
	skin	4.000	767	1090	21068
AOM/DSS_2 D60	spleen	10000	3678	1431	49267
	mLN	10000	4991	1442	51204
	iLN	5000	2233	1425	50527
	colon (NAT)	2000	378	1420	53877
	colon (tumor)	4500	1303	1332	46749
	skin	10000	2666	1141	39316
AOM/DSS_3 D60	spleen	10000	3358	1406	58021
	mLN	10000	3306	1442	63876
	iLN	8000	2673	1525	68000
	colon (NAT)	1500	528	1370	57717
	colon (tumor)	6000	548	1353	56466
	skin	4000	532	1060	43353

Methods

Model	Organs	Sorted Cells	Aligned Cells	Genes per Cell	Reads per Cells
MC38_1	spleen	5000	785	558	39113
	mLN	5000	498	609	41989
	iLN	5000	615	1027	45694
	dLN	5000	669	635	48533
	tumor	10000	1839	772	53838
	colon	0	0	0	0
	skin	12000	926	967	37958
MC38_2	spleen	10000	1349	761	5541
	mLN	5000	1000	811	6189
	iLN	1000	134	872	7232
	dLN	3100	624	816	6397
	colon	5000	600	832	5975
	tumor	2500	252	920	11690
	skin	12500	1446	707	4645
MC38_3	spleen	6000	1887	1825	26332
	mLN	8000	3748	1932	33059
	iLN	4000	1609	1954	32406
	dLN	2000	783	1987	34460
	colon	10000	1697	1263	23510
	tumor	10000	3980	2239	38159
	skin	6000	1183	1323	21378

Model	Organs	Sorted Cells	Aligned Cells	Genes per Cell	Reads per Cells
B16-F10_1	spleen	15000	5206	1906	23261
	mLN	10000	3443	2026	24840
	dLN	10000	3449	1947	23743
	colon	1800	369	1527	17292
	tumor	1650	523	2049	28763
	skin	20000	4954	1486	25558
B16-F10_2	spleen	15000	4470	1320	29108
	mLN	10000	2883	1347	32588
	dLN	10000	2978	1303	25897
	colon	257	0	0	0
	tumor	4500	671	2093	66927
	skin	20000	4744	1095	26124
B16-F10_1	spleen	10.000	4368	1154	27015
	mLN	10.000	4525	1212	17014
	dLN	10.000	4420	1143	26954
	colon	6.300	2009	1100	25202
	tumor	2.000	622	1249	30095
	skin	5.000	1920	869	19030

Methods

Model	Organs	Sorted Cells	Aligned Cells	Genes per Cell	Reads per Cells
MC38_CD45_1	spleen	10.000	2719	2025	27216
	mLN	5.000	851	1905	25729
	iLN	2.500	391	1898	24398
	dLN	2.500	482	1788	23027
	tumor	15.000	1440	3553	71026
	colon	5.000	950	2407	49482
	lung	10.000	2533	1967	26852

3.3.7. Creating the count matrix from CellRanger Multi output

scRNA-seq data analysis begins with a count matrix containing the number of unique molecular identifier (UMIs) or reads per gene in each cell. CellRanger provides two matrices: an unfiltered feature-barcode matrix, including all barcodes with at least one count (containing both background and cell-associated barcodes), and a filtered matrix with only detected cell-associated barcodes. Unfiltered data often contain significant debris and noise, which is why we decided to use the filtered data in all analysis. The *Read10X()* function from the Seurat package was used to load the filtered matrix and the resulting count matrix processed with the *SingleCellExperiment()* constructor from the SingleCellExperiment package. Tissue origin was stored as metadata in the respective SingleCellExperiment object.

3.3.8. Gene level annotation and linking TCR information

The AnnotationHub package was used to map gene identifiers to their respective gene names by using the reference genome of *Mus musculus* from the Ensemble database *ens.mm.v102*. Additionally, genes mapping to the mitochondrial genome were identified for later use in filtering and quality control (QC). Before QC, the dataset was filtered to include only T cells with productive TCR information from the VDJ library, which were beforehand identified by CellRanger Multi. Cells without TCR data were excluded. TCR chain and clonotype information were added to the SingleCellExperiment objects. To work with shared clonotypes across tissues, identical TCR chains were assigned the same clonotype ID based on their amino

Methods

acid sequence and this harmonized TCR chain and clonotype data were saved as metadata in the SingleCellExperiment objects.

3.3.9. Per sample quality control and doublet detection

Quality control (QC) was conducted to filter out low-quality cells during pre-processing. Key parameters included library size, the number of detected genes (features), and the percentage of reads mapped to the mitochondrial genome. QC was performed on a sample-level basis, as individual samples often varied in quality due to differences in processing, sequencing batches, or tissue-specific properties. The *addPerCellQC()* function from the scater package, was used, using a data-driven approach to determine appropriate threshold values. Low-quality cells were removed, and doublet detection was applied using the *scDblFinder()* function from the scDblFinder package. This method simulates expression profiles of potential doublets by randomly combining two cells from the dataset, assigning each cell a doublet score based on its similarity to these artificial doublets. A small proportion of doublets, commonly resulting from cell sorting or capturing errors, was expected in droplet-based scRNA-seq protocols [144].

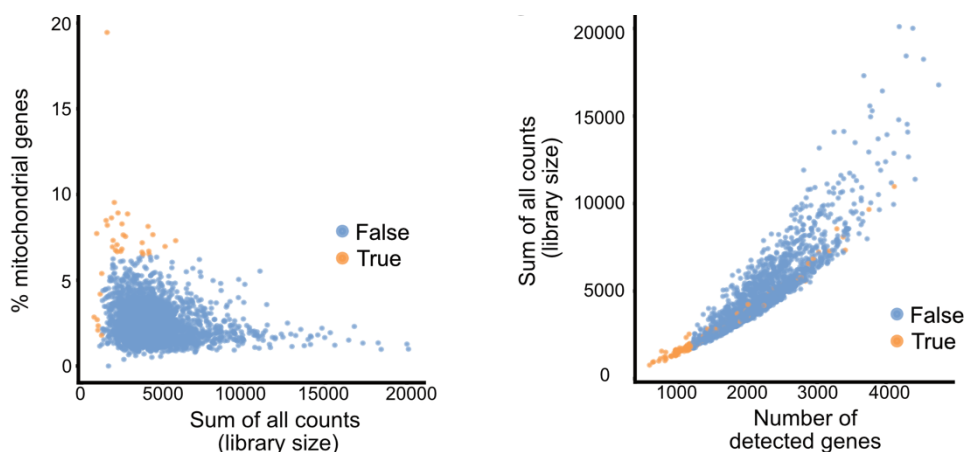


Figure 13: QC and doublet detection. Scatter plots of the library size and mitochondrial content and (left) library size and number of detected genes (right). Each dot in the plot represents a cell, blue cells are of high quality, orange cells are of low quality and were filtered out for downstream analysis. Copied from Nedwed and Helbich et al. [143].

Methods

3.3.10. Normalisation and feature selection

In order to quantify the differences in gene expression between cells, a subset of genes is selected such that this set contains useful information about the biological variation, while removing random noise and technical differences. Expression values were log-scaled using the scater package *logNormCounts()* function [117]. The *modelGeneVar()* function of the scran package was then used for calculating the variation in gene expression and the 10% of genes showing the highest variability were extracted using the *getTopHVGs()* function. These 10% of highly variable genes were used as features for downstream analysis.

3.3.11. Data integration and Batch Correction

After this quality control steps the individual SingleCellExperiment objects were now merged into one single object for downstream analysis. Usually, scRNAseq data sets do not only contain different samples and tissues but also different batches. For those samples from different batches, a batch correction was needed to avoid the influence of technical differences between samples of different batches. The *fastMNN()* function of the scater package was used to align shared cell populations across batches using mutual nearest neighbors. 50 principal components and 20 nearest neighbors were used for mutual nearest neighbor identification and the *BSPARAM=BiocSingular::RandomParam()* function.

3.3.12. Dimensionality reduction and clustering

Dimensionality reduction was conducted using principal component analysis (PCA) based on the top 10% of highly variable genes. The *runPCA()* function from the BiocSingular package was used to compute principal components. The number of PCs used for clustering was determined using scree plots. Graph-based clustering was then performed using the *buildSNNGraph()* function from the scran package and the *cluster_walktrap()* function from the igraph package. Clusters were

Methods

visualized using Uniform Manifold Approximation and Projection (UMAP) or t-Distributed Stochastic Neighbor Embedding (t-SNE).

3.3.13. Cell-type annotation and reassignment of clusters

Cell-type annotation was performed manually using predefined marker genes and tissue-specific differences. The following genes were visualized on a t-SNE plot to distinguish cell-types: for naive/lymphoid Treg cells: *Foxp3*, *Il2ra*, *Sell*, *Ccr7*, *Ly6v1*, *Klf2*, *Tmsb10*, *Bcl2*, *Arhgap15*, for NLT/effector Treg cells: *Foxp3*, *Il2ra*, *Klrg1*, *Mki67*, *Batf*, *Pdcd1*, *Areg*, *Ccr4*, *Il10*, *Tnfrsf4*, *Ccr8*, *4-1BB*, *Sytl3*, *Tnfrsf8*, *Cd44*, *Ctla4*, *Icos* and *Rorc* to distinguish pTreg cells from tTreg cells, which express *Ikzf2*, *Nrp1*, in the colon tissue.

3.3.14. Defining gene expression signatures

After identifying T cell populations and clusters, genes and expression patterns driving cluster separation were analyzed. The *scoreMarkers()* function from the *scran* package was used for pairwise cluster comparisons. This method provides detailed insights into marker genes and their role in cluster differentiation. Effect size summaries, such as log fold-change, quantified gene expression differences between clusters. Genes with the highest log fold-change served as marker genes for each cluster. With this function, signatures for Treg cells in each individual tissue were created, as the clustering was based on cell-type and tissue type. Individual genes included in the different tissue-specific Treg cell signatures are shown all three healthy mice in **Figure 14**.

Methods

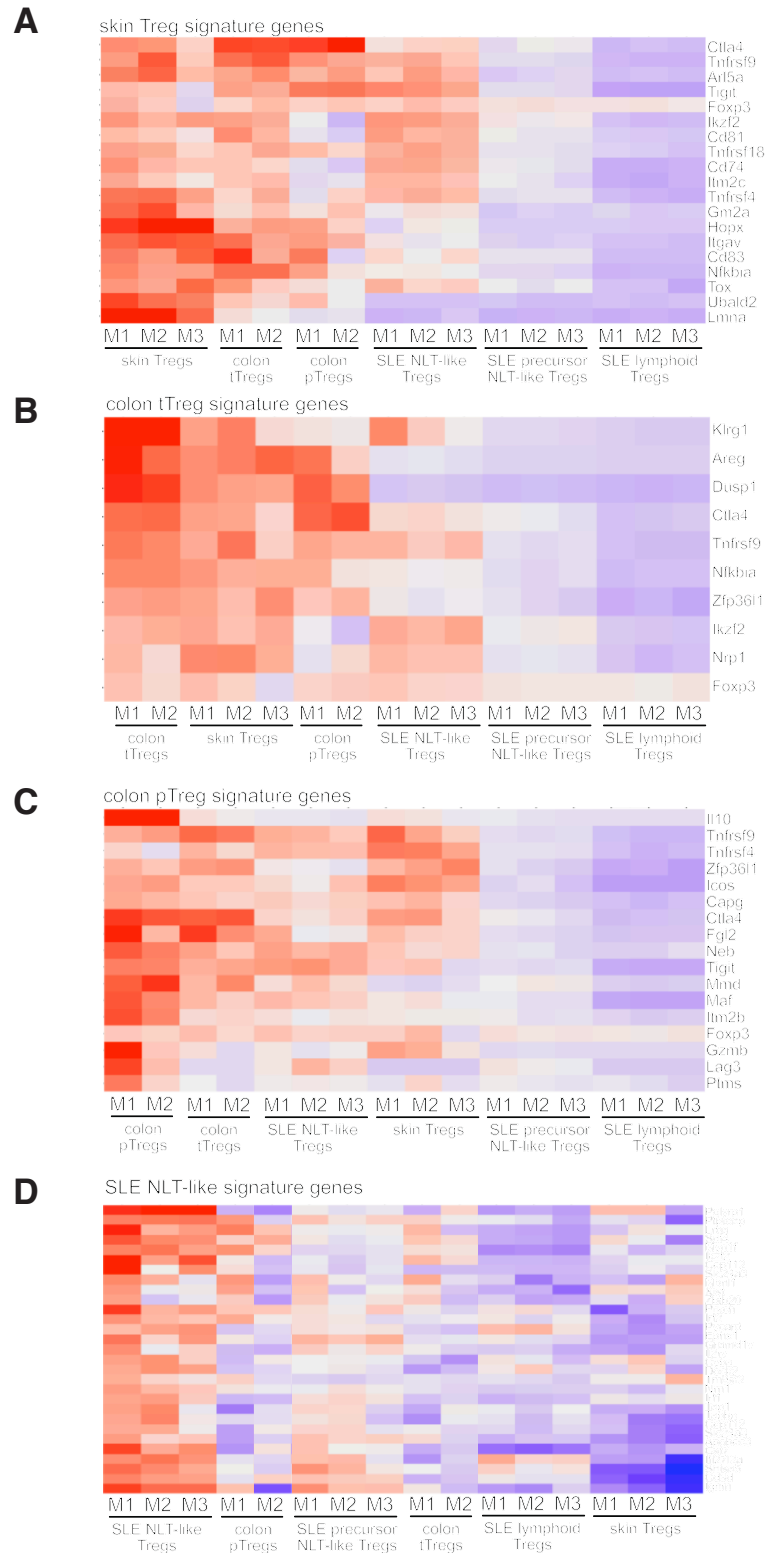


Figure 14: Tissue-specific Treg cell signature genes. A-C: Gene expression score of the individual genes of the skin Treg signature (A), colon tTreg signature (B), colon pTreg signature (C) and SLE NLT-like signature (D) are displayed for each mouse (M1, M2, M3) as well as each Treg cell cluster. Normalized for each individual gene.

Methods

Additionally, a core Treg signature was established using marker genes differentially expressed with a logFC > 0.25 and p-value < 0.05 in comparisons of all *Foxp3*⁺ Treg cells versus *Foxp3*⁻ T conventional (Tconv) cells within the dataset (**Figure 15A**).

A regenerative Treg signature was developed based on marker genes with a logFC > 1 and p-value < 0.05 in *Areg*⁺ Treg cells from spleen, colon, and skin NLT (**Figure 15B**), comprising 21 specific marker genes. Finally, a suppressive Treg signature was defined using marker genes differentially expressed with a logFC > 0.25 and p-value < 0.05 in *Foxp3*⁺ *Ctla4*⁺ Treg cells (**Figure 15C**). All individual genes included in the signatures are shown in **Figure 16**.

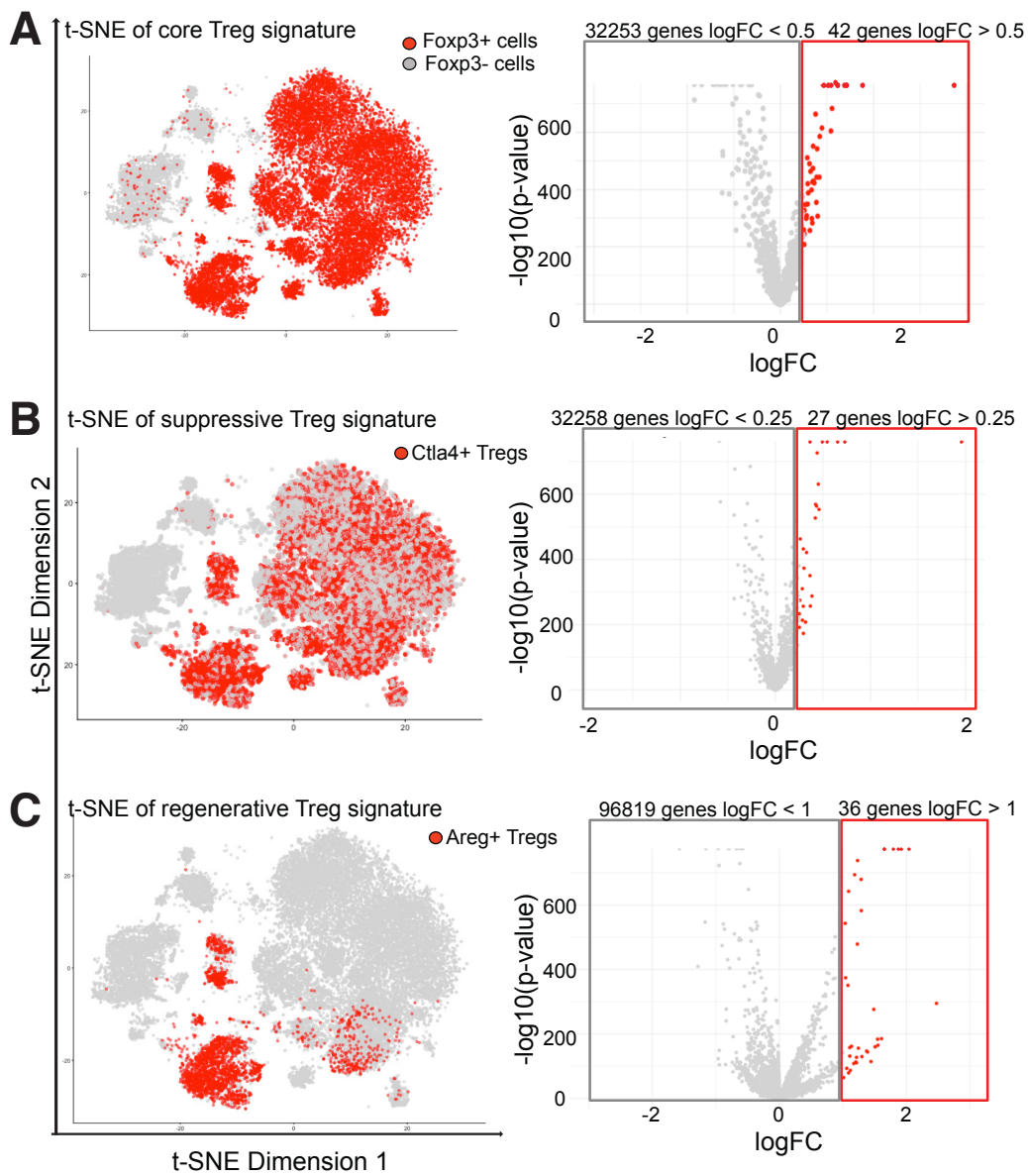


Figure 15: Calculation of specific Treg signatures. A-C: Core Treg signature (A, left panel), suppressive Treg signature (B, left panel) and regenerative signature (C, left panel) are shown in a t-SNE dimension plot. Cells used for the analysis for *scoreMarkers()* function are colored in red. Volcano plot (right panel) displaying the amount of used genes for the individual signatures.

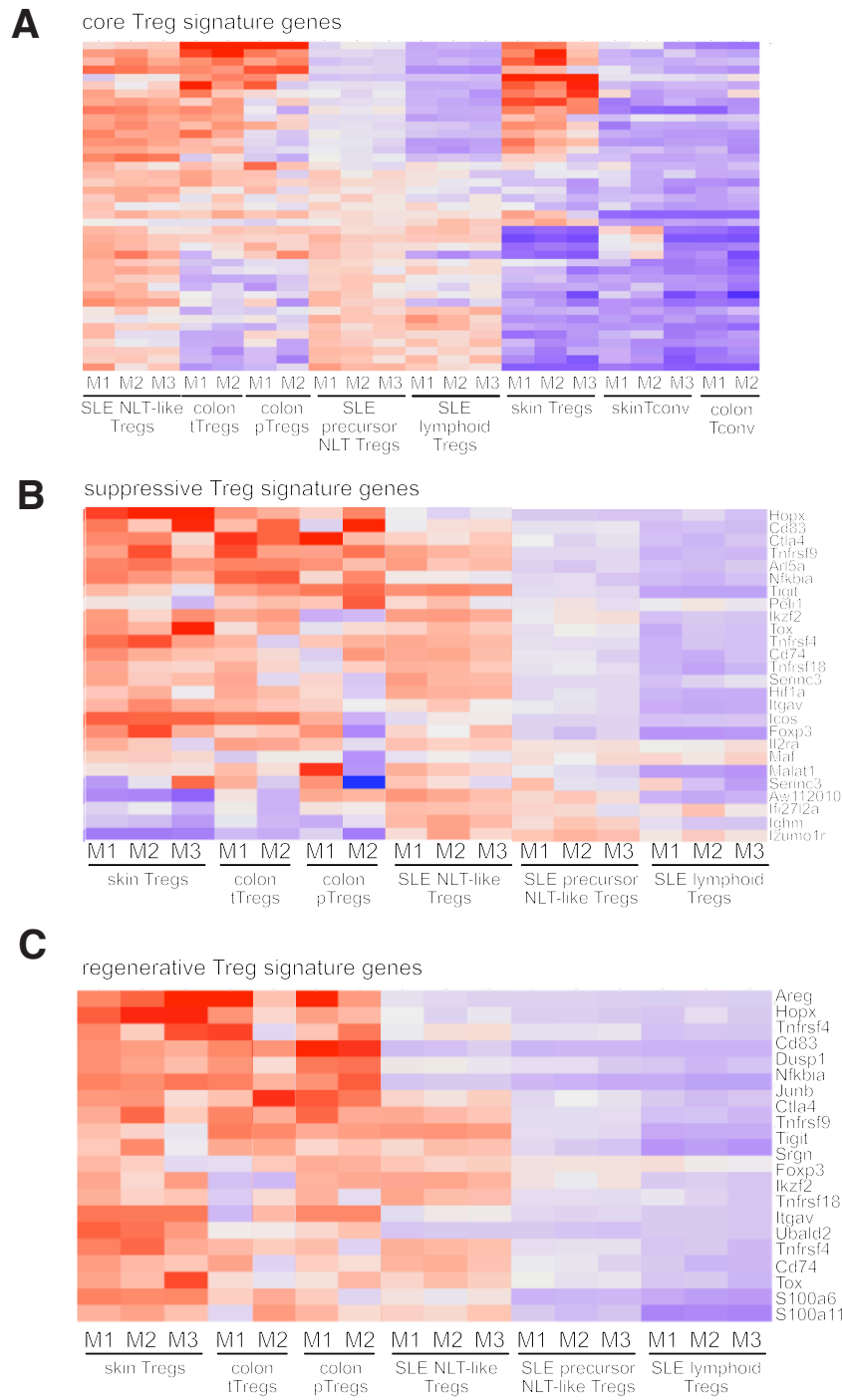


Figure 16: Individual Genes included for the Treg signatures. A-C: Gene expression score of the individual genes of the core signature (A), suppressive signature (B) and regenerative signature (C) are displayed for each mouse (M1, M2, M3) as well as each Treg cell cluster. Normalized for each individual gene. *Due to the large number of genes included in the core Treg signature, the gene list was extracted and attached in section 9.5.

To validate the overlapping genes from the regenerative Treg signature and the suppressive Treg signature a Venn Diagram illustrated in **Figure 17** was used.

Methods

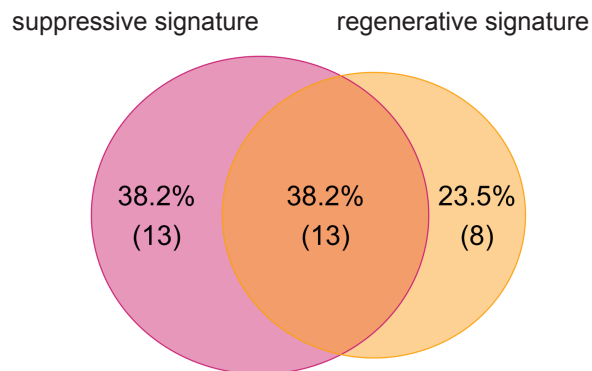


Figure 17: Venn-Diagram showing the overlap of marker genes for the regenerative Treg signature and suppressive Treg signature.

To validate and compare this dataset with the one from other labs, different Treg signatures from published data were created, including an activated Treg signature [145, 146], suppressive Treg signature [147], stress Treg signature [147], and effector Treg signature [145, 147]. These signatures include a larger set of marker genes.

3.3.15. Differential gene expression (DGE) analysis

Analysis of differentially expressed genes between cell-types and conditions was performed by using *pseudobulk()* and *edgeR()* from edgeR package. Pseudobulk data are generated by aggregating data from this scRNA-seq to analyze them as if they were bulk RNA sequencing data. This was achieved using the *aggregateAcrossCells()* function. The aggregated counts are used to construct a *DGEList* object and normalization factors were computed with the *calcNormFactors()* to account for library size differences. Contrasts were defined for pairwise comparisons, allowing for statistical testing of differential expression between conditions. Using a quasi-likelihood generalized linear model (GLM), differential expression analysis was performed.

Methods

3.3.16. Functional enrichment analysis

DGEs were filtered based on specific thresholds for log-fold change (logFC) and p-value. Genes with $\logFC > 2$ and $p\text{-value} < 0.05$ were retained for each comparison. The significant genes (identified by their gene symbols) were converted to Entrez IDs using the *bitr()* function from the ClusterProfiler package and the org.Mm.eg.db annotation database for mouse genes. The *enrichGO()* function was used to identify enriched GO terms in the Biological Processes (BP) category. The analysis used adjusted p-values (using the Benjamini-Hochberg method) with a cutoff of 0.05 to determine significant pathways. The *dotplot()* function was used to visualize the top enriched GO terms. It displays the most significant terms with their corresponding gene ratios. The *emapplot()* function from the enrichplot package was used to create an enrichment map.

3.3.17. Cell Interaction Analysis

The functional enrichment analysis of cell-cell communication was performed using the CellChat package. The normalized data matrix was extracted from a SingleCellExperiment object using the *logcounts()* function. Metadata containing cell labels and sample information was extracted and formatted for compatibility with CellChat. A CellChat object was created using the normalized data matrix and metadata. The grouping was based on cell labels. The *CellChatDB.mouse* database was used, containing signaling pathway information specific to mouse data. To reduce computational cost, signaling-related genes were subset using the *subsetData()* function. Overexpressed genes and signaling interactions were identified using the *identifyOverExpressedGenes()* function. Communication probabilities were computed using the *computeCommunProb()* function with the "triMean" method. Communications involving fewer than 10 cells were filtered out. Finally, the communication probabilities for signaling pathways were computed and aggregated. Total number of interactions and interaction weights/strengths were visualized as circle plots.

Methods

3.3.18. Pseudo-time analysis

The *aggregateAcrossCells()* function from the SingleCellExperiment package was used to aggregate the data by clustering cells based on their features. Afterwards the *reducedDim()* function was employed to perform dimensionality reduction on the aggregated data using PCA. The *createClusterMST()* function from the scater package was used to construct a Minimum Spanning Tree (MST) from the PCA-reduced data. MST represents the nearest neighboring relationships between clusters in a connected tree structure. The *reportEdges()* function was applied to extract edges from the MST, which represent the paths between clusters in the reduced dimensional space. This was used to visualize transitions between clusters in the end. Afterwards, the *mapCellsToEdges()* function was employed to map individual cells onto the edges of the MST, allowing us to determine the position of each cell along the trajectory. The *averagePseudotime()* function was applied to calculate the average pseudo-time for each cluster, providing a continuous measure of differentiation state.

3.3.19. TCR repertoire diversity analysis

TCR V(D)J sequencing combined with single-cell RNA sequencing enables the profiling of paired TCR α and TCR β chains at single-cell resolution, alongside global gene expression data from the same cell. In this dataset, all clonotypes were included in the analysis, regardless of whether they expressed only one TCR chain or both TCR chains. The analysis focused on the amino acid sequences of the TCRs. A duplicated clonotype was identified if it had the exact same chain combination and amino acid sequence.

Pie charts were used to visualize TCR repertoire diversity within each cluster. Additionally, gene expression analysis was conducted on Treg cells sharing the same clonotype, and duplicated clonotypes from each tissue were displayed on a t-SNE plot. Chord diagrams and heatmaps were utilized to illustrate the overlapping clonotypes among Treg cells from different tissues and cell-types.

Methods

Part of the code used in this thesis has been published in the accompanying methods paper (Nedwed and Helbich et al., 2023) and is included as an attachment [143].

3.4. Investigation the transcriptional profiles of tumor and healthy tissue using bulk RNA-seq

3.4.1. Sample preparation for RNA-seq of cells from tumor and healthy tissue

For bulk RNA analysis, cells were isolated from the tumor tissue, colon and skin tissue of two B16-F10 and two MC38 tumor-bearing mice at day 13 (B16-F10) and day 15 (MC38) after subcutaneous injection. Cells were pre-enriched with anti-CD45 Microbeads and the flowthrough was collected, including the CD45- fraction. RNA was isolated the same day using the RNeasy Micro Kit, quality and quantity assessed via Qubit dsDNA HS Assay and Agilent 2200 TapeStation system. Samples were sent to Novogene for library preparation and sequencing.

3.4.2. Analysis of bulk RNA-seq data

RNA sequencing reads were aligned to the reference genome of *Mus musculus* from the ENSEMBL database (version GRCm38) using the STAR aligner with annotation data retrieved from the ENSEMBL FTP website. Alignments were processed using the *featureCounts()* function of the Rsubread package, applying the same annotation file. Data exploration, modeling, and interpretation followed established protocols [148]. Exploratory data analysis utilized the *pcaExplorer* package, generating Principal Component Analysis plots based on the top 500 most variable genes. Differential expression analysis was performed with DESeq2 package, setting the false discovery rate (FDR) cutoff to 0.05. Accurate estimation of the effect sizes (described as log₂ fold change) was performed using the *apeglm* shrinkage estimator. Further analyses included Gene Ontology pathway enrichment by topGO, setting all expressed genes as background dataset, and were

Methods

performed using the ideal package. The enrichment results were further processed with the GeneTonic package for visualization and summarizing [149].

3.5. Flow cytometry analysis of immune cells in healthy and tumor-bearing mice

Two different antibody master mix were prepared, one including anti-mouse CD25 antibody and one including anti-mouse Areg antibody. Intracellular antibodies are marked in blue. Cells were stained in 100 μ L of surface staining mix and incubated for 30 minutes at 4°C. After staining, 500 μ L of FACS buffer was added to each sample, followed by centrifugation at 1000xg for 2 minutes. Fixation and permeabilization was performed by using 1x fix/perm buffer concentrate with 3x fix/perm diluent from the eBioscience Fix/Perm Kit. Cells were resuspended in 200 μ L of the fix/perm buffer and incubated for 45 minutes at room temperature (RT) or overnight at 4°C. Perm buffer was prepared by diluting 10x perm buffer in water to 1x perm buffer, and 1 mL of perm buffer was added to each sample, followed by centrifugation at 1000xg for 2 minutes. For intracellular staining, intracellular staining mix was added, and cells were incubated for 30 minutes at RT. Afterward, 1 mL of perm buffer was added, and samples were centrifuged (1000xg, 2 minutes). Secondary antibodies were added in 100 μ L perm buffer and incubated for 30 minutes at RT. Following another wash with 1 mL perm buffer and centrifugation, cells were resuspended in 150–200 μ L of FACS buffer and kept on ice until analysis.

Table 11: Antibody mix 1 for Immune Cell analysis via flow cytometry

Antigen	Label	Laser	BD Filter	Dilution
CD45 - BUV395	UV - 395	355 nm	779/28	200
Ccr8 - BV421	Vio - 431	405 nm	450/40	100
CD62L - BV510	Vio - 525	405 nm	525/50	100
PD-1- BV605	Vio - 605	405 nm	610/20	100
CD3 - BV785	Vio - 780	405 nm	780/60	100
Batf- AF488*	Blue - 530	488nm	530/30	400
Klrg1 - BB700	Blue - 670	488nm	780/60	100
CD25 - PE	YG - 586	561nm	586/15	100
CD8a - PE-Cy7	YG - 670	561nm	670/30	100
Foxp3 – APC*	Red - 670	633 nm	661/20	20
CD4 - R718	Red - 730	633 nm	710/40	100
Zombie - NIR	Red - 780	633 nm	780/60	500

*intracellular antibodies are marked in blue.

Table 12: Antibody mix 2 for Immune Cell analysis via flow cytometry

Antigen	Label	Laser	BD Filter	Dilution
CD45 - BUV395	UV - 395	355 nm	779/28	200
Ccr8 - BV421	Vio - 431	405 nm	450/40	100
CD62L - BV510	Vio - 525	405 nm	525/50	100
PD-1- BV605	Vio - 605	405 nm	610/20	100
CD3 - BV785	Vio - 780	405 nm	780/60	100
Batf- AF488*	Blue - 530	488nm	530/30	400
Klrg1 - BB700	Blue - 670	488nm	780/60	100
Foxp3 – PE*	YG - 586	561nm	586/15	20
CD8a - PE-Cy7	YG - 670	561nm	670/30	100
Areg - AF647*	Red - 670	633 nm	661/20	20
CD4 - R718	Red - 730	633 nm	710/40	100
Zombie - NIR	Red - 780	633 nm	780/60	500

*intracellular antibodies are marked in blue.

4. Results

In this thesis, we studied the gene expression profile as well as the TCR clonality and distribution of Treg cells within tissues from not only healthy animals, but also colitis and tumor-bearing mice. Our analysis aimed to identify the differences in the phenotype of NLT Treg cells between healthy and diseased animals. Using different tumor models, we sought to determine whether tumor-resident Treg cells are more tumor-specific or tissue-specific and whether this changes when the site of tumor induction is altered. By using combined scRNA/TCR-seq, we also aimed to investigate whether the tumor recruits and primes tumor-infiltrating Treg cells in the SLO. To this end, we began by characterizing NLT Treg cells in healthy animals and continued our analysis in inflamed and tumor environments.

4.1. Treg cells across lymphoid and non-lymphoid tissues show distinct marker gene expression

Much is already known about the gene expression profiles and TCR repertoires of Treg cells from lymphoid and NLT tissues. Therefore, our focus was not on analyzing the Treg cell populations from individual mouse organs separately. Instead, we aimed a comprehensive analysis to investigate the dynamics and TCR overlaps between different murine tissues, including the skin and colon, their respective draining lymph nodes (iLN and mLN), and the spleen, which can be considered a peripheral tissue of the circulatory system, within the same mouse.

In order to prepare the transcriptomic analysis of tissue Treg cells we first aimed to identify the frequency of Treg cells and NLT Treg cells in different murine organs in a healthy state.

Therefore, T cells from healthy 12-week-old female mice were collected from lymphoid organs, including spleen, mesenteric lymph nodes (mLN), and inguinal lymph nodes (iLN) as well as non-lymphoid organs, including skin, colon, lung, and liver (**Figure 18A-B**). Their expression of key markers, including Foxp3, Klrp1, PD-1,

Results

Ccr8, and Batf, was analyzed via flow cytometry. Treg cells were detected in all murine organs, with their frequency being notably higher in the murine colon and skin compared to the SLE, lung, and liver tissue (**Figure 18C**). Further phenotypic analysis of Treg cells revealed increased expression of Klrp1 and PD-1 in all non-lymphoid tissues compared to their lymphoid counterparts (**Figure 18D**). Treg cells from lymphoid organs were then classified into lymphoid Treg cells, precursor NLT-like Treg cells, and NLT-like Treg cells based on their Klrp1 and PD-1 expression as previously described section 1.2.3.

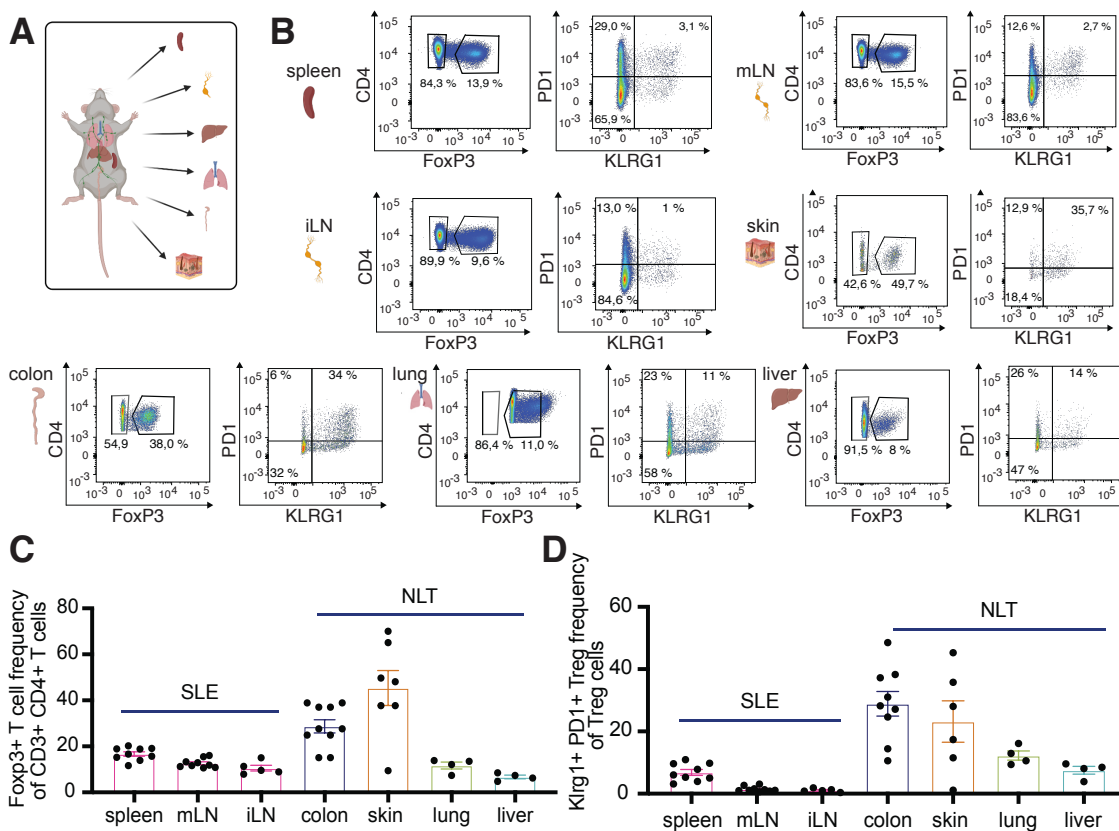


Figure 18: Treg cells from murine lymphoid and non-lymphoid tissue show distinct marker gene expression via flow analysis. A: Schematic overview of analyzed murine tissue. B: FACS plots of a representative sample for spleen, mesenteric lymph node (mLN), inguinal lymph node (iLN), skin, colon, lung and liver. Pregated on CD4⁺ T cells. C: Foxp3⁺ T cell frequency of CD3⁺ CD4⁺ T cells. D: Klrp1⁺ PD1⁺ Treg frequency of Treg cells. All analysis is based on flow cytometry based on T cells isolated from spleen (n=9), mLN (n=9), iLN (n=5), skin (n=6), colon(n=9), lung (n=4) and liver(n=4).

Results

After identifying the NLT Treg subset across different organs, we proceeded to characterize the Treg cell type by examining the expression of Batf and Ccr8. We classified Treg cells isolated from the SLE into three clusters: lymphoid Tregs, precursor NLT-like Tregs, and NLT-like Tregs based on their expression of Klrg1 and PD-1.

Figure 19A illustrates the mean fluorescence intensity (MFI) of the transcription factor Batf and the surface molecule Ccr8. The spleen (**Figure 19A** right) was selected as an example for the SLE. An increase in MFI was clearly observed for precursor NLT-like and even more for NLT-like Treg cells for both Batf and Ccr8. The skin and colon (**Figure 19A** middle) showed quite overlapping MFI values for both markers. In contrast, the lung and liver (**Figure 19A** left) demonstrated lower MFI levels for the lung compared to the liver for Batf expression, while both organs exhibited similarly low levels of Ccr8 expression.

Figure 19B displays the frequencies of Batf and Ccr8 expression in Treg cells from the SLE and NLT tissues, with NLT-like Treg cells from the SLE showing the highest frequency compared to those from skin, colon, lung, and liver.

Key phenotypic differences were found between Treg cells from lymphoid and non-lymphoid tissues, with higher Batf and Ccr8 expression in non-lymphoid tissue Tregs. Classifying Treg cells into lymphoid, precursor NLT-like, and NLT-like subsets based on these markers revealed the distinct characteristics of these populations. This also highlights the importance of classifying SLE Treg cells into three populations due to their heterogeneity in marker expression for scRNA analysis. Furthermore, these findings underscore the phenotypic diversity of Treg cells across different tissues and provide insights into their tissue-specific functions and adaptation.

Results

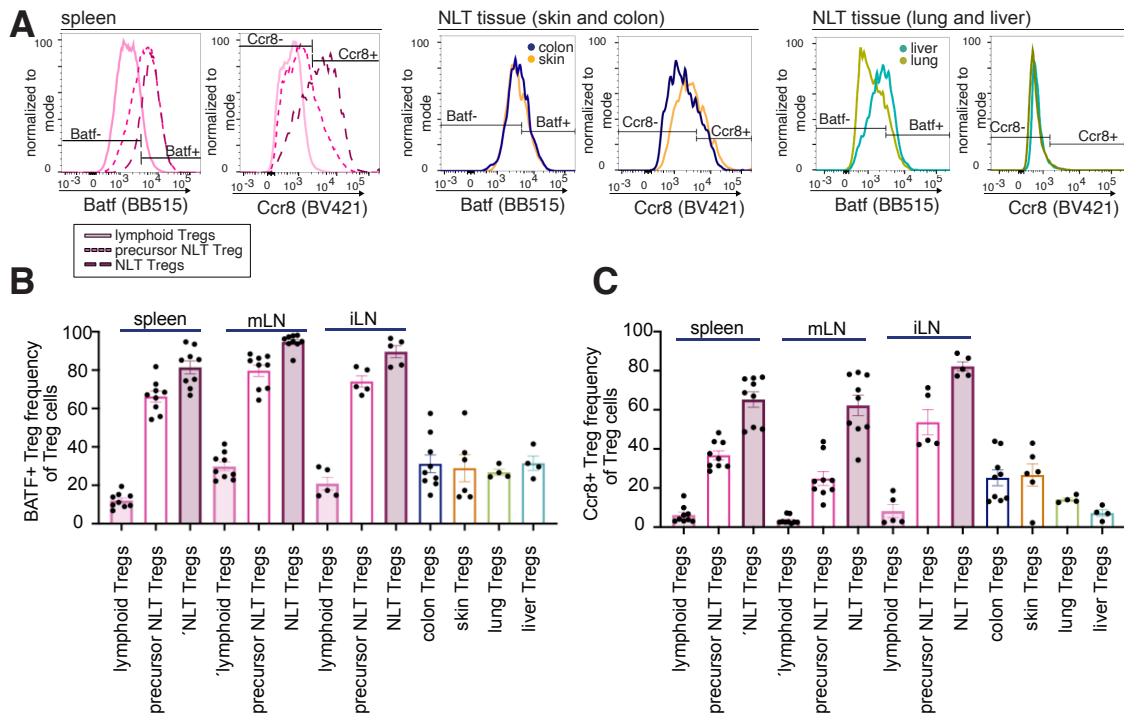


Figure 19: NLT-like Treg cells from the SLE show a high frequency of Batf and Ccr8. **A:** FACS plot showing the MFI of Batf and Ccr8 of a representative sample for lymphoid (Foxp3⁺ Klrp1⁻ PD-1⁻) precursor NLT-like (Foxp3⁺ Klrp1⁻ PD-1⁺) and NLT-like Tregs (Foxp3⁺ Klrp1⁺ PD-1⁺) isolated from the spleen, skin, colon, lung and liver. Pregated on viable CD4⁺ Foxp3⁺ T cells. **B:** Batf⁺ Treg frequency of Treg cells, SLE are again divided into lymphoid Treg cells (Klrp1⁻, PD-1⁻), precursor NLT-like Treg cells (Klrp1⁻, PD-1⁺) and NLT-like Treg cells (Klrp1⁺, PD-1⁺). **F:** Ccr8⁺ Treg frequency of Treg cells. All analysis is based on flow cytometry based on T cells isolated from spleen (n=9), mLN (n=9), iLN (n=5), skin (n=6), colon(n=9), lung (n=4) and liver(n=4).

4.2. Treg cells from non-lymphoid tissue show shared gene expression pattern but have a tissue-specific signature

Since we we're able to characterize Treg cells based on cell surface markers via flow cytometry we wanted to compare gene expression level of Treg cells from different murine organs (**Figure 20A**). We sorted on CD25⁺ cells for lymphoid organs (spleen, mLN and iLN) and on CD4⁺ cells for non-lymphoid organs (skin, colon). Bioinformatic analysis were performed as described in our method paper and code for the analysis can be found attached in this paper [143]. Our scRNA/TCR analysis involves three healthy wild-type mice. Samples were collected at three separate time points and combined after sequencing for downstream analysis.

Results

As illustrated in **Figure 20A**, T cells from three healthy wild-type mouse replicates clustered together in the t-SNE projection plot. A t-SNE plot enables the visualization of the dataset in two or three dimensions, effectively capturing its overall structure while maintaining key features, such as the presence of distinct clusters. We manually assigned the clusters for cells from different tissues and classified the dataset into eight distinct clusters: a cluster defining skin Tconv cells (cluster 1), SLE NLT-like Treg cells (cluster 2), skin Treg cells (cluster 3), SLE precursor NLT-like Treg cells (cluster 4), colon pTreg cells (cluster 5), colon Tconv cells (cluster 6), SLE lymphoid Treg cells (cluster 7) and colon tTreg cells (cluster 8). Cells from the different tissue were identified using distinct TotalSeqC Hashtagging antibodies. Lymphoid and non-lymphoid tissues separated clearly from each other, forming distinct clusters (**Figure 20B**). Further marker gene analysis and cell-type identification revealed three distinct populations within the SLE: a lymphoid Treg cell population (cluster 7), a precursor NLT-like Treg cell population (cluster 4), and an NLT-like Treg cell population (cluster 2). For T cells isolated from the skin, which were sorted based on CD4 expression, two major populations were identified: a Foxp3⁺ Treg cell population (cluster 3) and a Foxp3⁻ Tconv cell population (cluster 1). A similar classification was achieved for the colon, where Treg cells were further categorized into a tTreg population (Klrg1⁺, Ikzf2⁺, Nrpl1⁺) and a pTreg population (Klrg1⁻, Rorc⁺), corresponding to clusters 8 and 5 in **Figure 20A**.

Using the cluster information, we were able to create tissue-specific signatures based on gene expression differences from each tissue described in **3.3.14** and displayed on a t-SNE projection in **Figure 20C-F**. While these signatures include tissue-specific marker genes, they also share common genes across different tissues, which is shown in a Venn Diagram (**Figure 20G**). The density plot revealed that the highest gene expression score for each tissue-specific signature was predominantly observed in its corresponding tissue. However, NLT Treg cell populations from other tissues also showed elevated expression levels across all tissue-specific Treg signatures. This suggests a shared transcriptional program among NLT Treg cells, indicating potential functional similarities across different

Results

tissue environments. In contrast, the lymphoid SLE Treg cell population displayed the lowest gene expression scores across the tissue-specific NLT Treg signatures (Figure 20C-F).

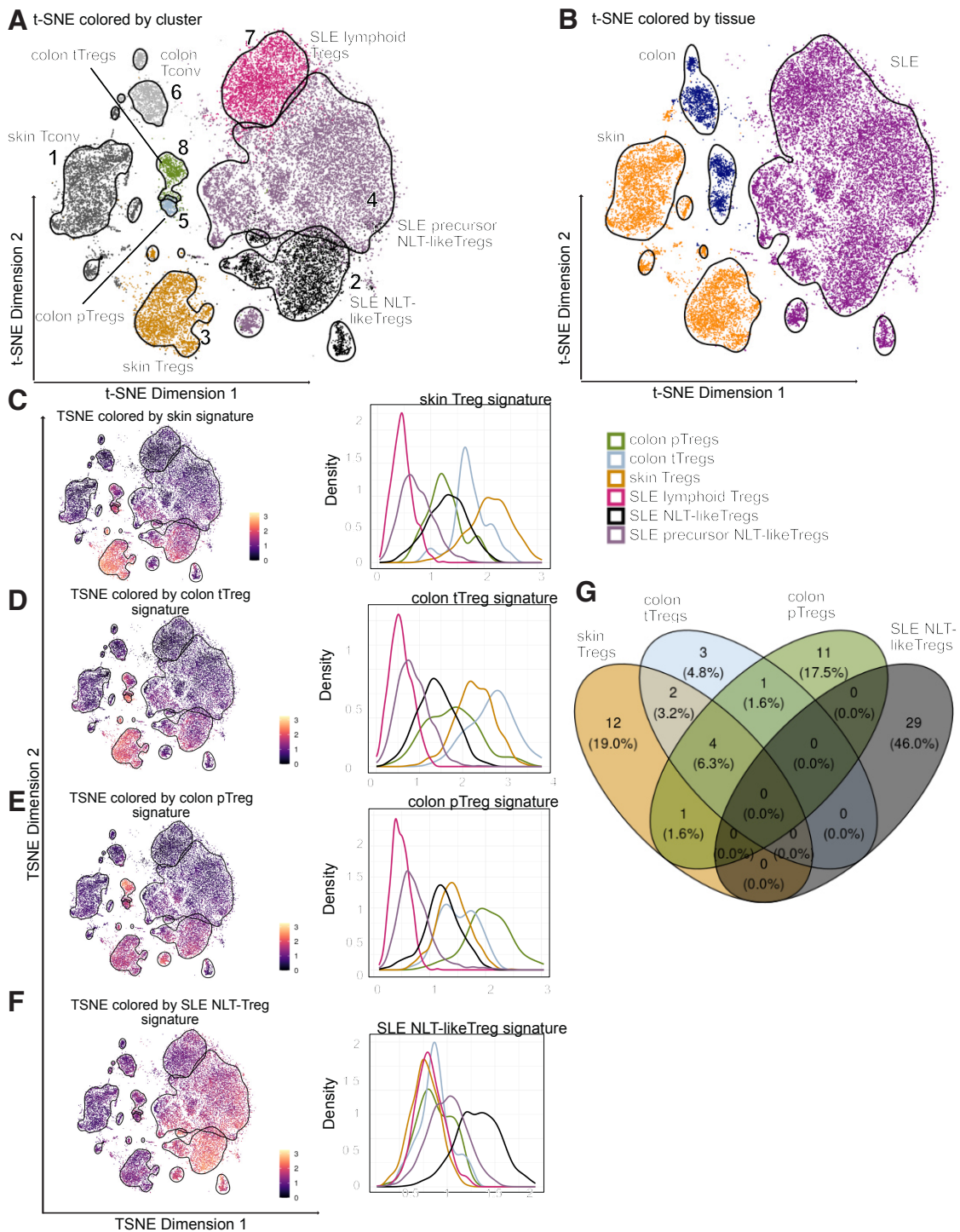


Figure 20: scRNA-seq analysis of Treg cells from non-lymphoid and lymphoid tissue of healthy mice revealed tissue-specific signatures. A-B: t-SNE plot colored by cluster (A) and

Results

tissue types (B). Confidence ellipses applied to the t-SNE plot displaying the 95% confidence level of the individual cluster (A) and tissue types (B). C-F: Signatures for skin Treg cells (C), colon tTreg cells (D), colon pTreg cells (E) and SLE NLT-like Treg cells (F) based on differential expressed genes are plotted on a t-SNE and density plot showing the signature score for the different Treg cluster. Cell-types are colored based on their cluster color showed in A. G: Venn-Diagram showing overlapping genes of the tissue-specific signatures. n = 3 individual mice.

4.3. Pseudo-time analysis reveals trajectory of Treg cells

A wide range of biological processes can be represented as a continuum of changes in cellular states. This is particularly evident in cell-type differentiation, which can be observed in various T cell subpopulations from different tissue. In our scRNA-seq data, we aim to characterize this differentiation process by identifying a trajectory. Along with this trajectory, pseudo-time serves as an important metric, representing the position of each cell along the trajectory. So, it can be treated as the relative position of a cell in the trajectory. Cells with larger values are considered to be “after” their counterparts with smaller values [150].

The t-SNE plot (**Figure 21A**) represents the color-coded pseudo-time and scatter plot (**Figure 21B**), which show the trajectory or pathway along which cells progress during a biological process, such as differentiation or developmental changes. It visually depicts the continuum of states cells pass through as they transition from one cellular state to another. It cannot be observed as a continuous development trajectory between cells from different tissues. The analysis revealed that skin and colon Tconv cells exhibit the lowest pseudo-time scores compared to cells from other clusters. The pseudo-time values for the SLE clusters revealed a trajectory from the lymphoid Treg cell cluster (cluster 7) towards the precursor NLT-like Treg cells (cluster 4) ending at the NLT-like Treg cell cluster (cluster 2). This had been already described in previous publication [45]. Additionally, colon tTreg cells show slightly lower pseudo-time scores than pTreg cells.

In the following we applied this pseudo-time analysis for detecting the cell state of duplicated T cells from the inflamed or tumor-bearing tissues within other murine organs.

Results

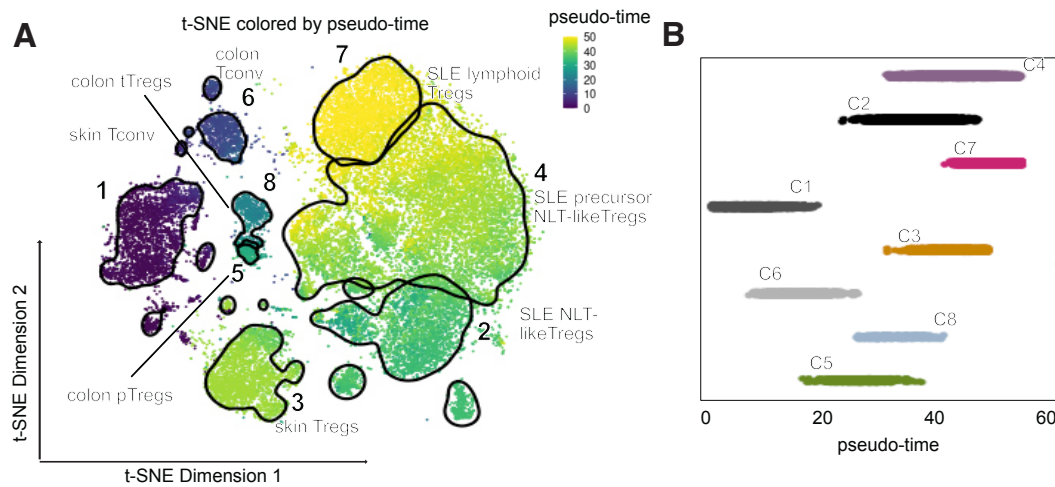


Figure 21: Pseudo-time analysis of scRNA data from different organs of healthy mice reveals Treg trajectories. A: pseudo-time is displayed in a color-coded t-SNE plot, with purple indicating a low and yellow indicating a high pseudo-time. Confidence ellipses applied to the t-SNE plot displaying the 95% confidence level of the individual cluster. B: Scatter plot showing the distribution of pseudo-time values across the different cluster applied from **Figure 20**. n = 3 individual mice.

4.4. Functional Treg signatures are shared across various tissues

To further characterize our Treg cells, we developed gene signatures associated with their two distinct functions: suppression and regeneration. These signatures were designed to identify differences between healthy colon, skin, and NLT Treg cells in comparison to tumor-infiltrating Treg cells or those from inflamed colon tissue. As a first step, we aimed to distinguish Treg cells from Tconv cells by generating a core Treg cell signature. This signature includes all upregulated genes in skin, colon, and SLE Treg cells compared to Tconv cells from the skin and colon. Ideally, the Tconv cell population from SLE should also be included in this comparison. However, we chose to exclude them from the dataset to avoid a substantial increase in dataset size. While this exclusion helped maintain dataset manageability, it represents a limitation of the core Treg cell signature, as it may affect the completeness of the comparison.

Results

The calculation of the signatures is described in section 3.3.14 and displayed in a t-SNE projection and density plot in **Figure 22A-C**. These signatures are not limited to specific tissues but are shared across various tissues. The core Treg signature was observed in all Treg cell clusters. However, naive Treg cells from the SLE showed lower expression of these signature genes. Additionally, SLE lymphoid Treg cells and SLE NLT-precursor Treg cells exhibited reduced expression of suppressive and regenerative Treg signatures compared to the other clusters. Marker genes for each signature are visualized on a t-SNE plot. The overlap between regenerative and suppressive signature genes is displayed in a Venn diagram, showing an 23.7% overlap (**Figure 22D**).

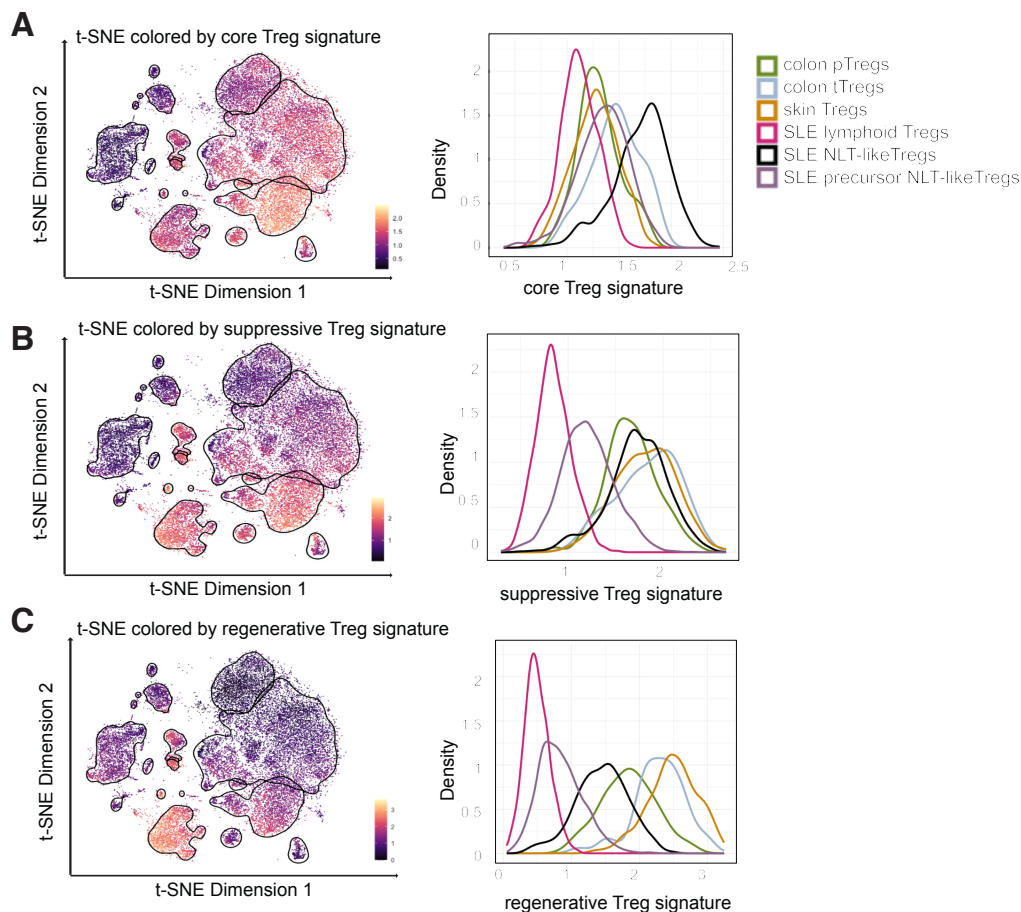


Figure 22: Gene expression signatures plotted on the t-SNE of healthy mice. A-C: The core Treg signature (A), suppressive Treg signature (B) and regenerative Treg signature (C) is plotted on a t-SNE plot (left) and density plot (right). Cell-types are colored based on their cluster color showed in **Figure 20A**. n = 3 individual mice.

Results

4.5. Treg cells from NLT are higher in clonal expansion

We further analyzed the TCR repertoire in this healthy mouse dataset to gain insights into the clonality and clonal relationships of Treg cells from different murine organs (**Figure 23A**). TCR clonal expansion among Treg cells in non-lymphoid tissues was generally high, with approximately 79% of skin Treg cells in cluster 3, around 45% of pTreg cells from the colon, and about 50% of tTreg cells from the colon showing clonal expansion. In contrast, Tconv cell populations in non-lymphoid tissues exhibited even higher TCR clonal expansion, with approximately 84% of skin Tconv cells in cluster 1 and around 76% of colon Tconv cells in cluster 6. Additionally, SLE NLT-like Treg cells from cluster 2 demonstrated considerably higher clonal expansion compared to their lymphoid/naïve counterparts in cluster 7, with about 52% versus 2% clonal expansion. In the precursor NLT-like Treg cell population from the SLE (cluster 4), approximately 21% of TCR clonotypes were duplicated. However, these clonotypes appeared to be less enriched compared to the TCRs of NLT(-like) Treg populations from other tissues. **Figure 23B** shows the t-SNE plot colored by duplicated TCR clonotypes.

These findings underscore the tissue-specific and environmental influences on TCR clonal expansion in Treg and Tconv cells.

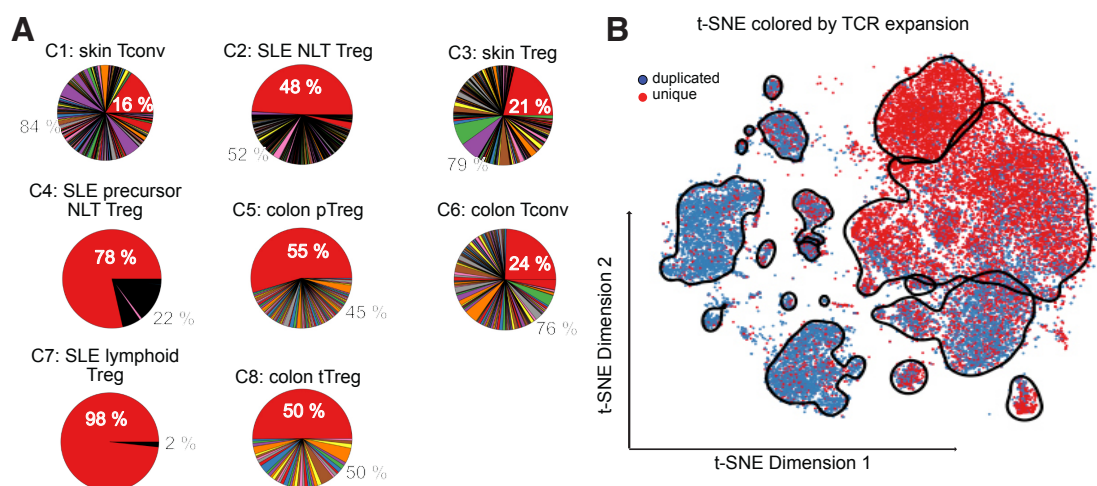


Figure 23: TCRs from NLT Treg cells are higher clonal expanded. **A:** Pie charts showing the TCR repertoire composition for each cluster, highlighting the percentage of singletons (grouped together in the red slice) and the distinct duplicated TCRs. **B:** t-SNE plot colored

Results

by all duplicated TCRs detected in this dataset. Red dots showing cells with duplicated TCRs. Confidence ellipses applied to the t-SNE plot displaying the 95% confidence level of the individual cluster. n = 3 individual mice.

4.6. Tissue-dependent TCR overlaps among Treg cell populations

To investigate the clonal relationships of TCRs in our dataset, we analyzed shared TCR clonotypes across clusters and tissues. **Figure 24A** illustrates chord diagrams representing the overlap of TCR clonotypes within all clusters. Notably, **Figure 24A** highlights a significant overlap of TCR clonotypes between skin Tconv cells (cluster 1) and skin Treg cells (cluster 3), as well as between SLE precursor NLT-like Treg cells (cluster 4) and SLE NLT-like Treg cells (cluster 2). Furthermore, we were able to detect a high overlap of SLE NLT-like Treg cells (cluster 2) and skin Treg cells (cluster 3).

For a more detailed analysis, we combined cluster and tissue information to assess overlapping TCRs. **Figure 24B** shows a heatmap of the percentage of overlapping duplicated TCR clonotypes for each individual population. Most cell populations exhibit a high overlap of duplicated TCRs within themselves.

In the lymphoid Treg cell population (cluster 7) of iLN, mLN, and spleen, the overlap of duplicated TCRs with other populations was minimal. These cells shared 96% (iLN), 97% (mLN), and 95% (spleen) of their TCRs within their respective populations. In contrast, the precursor NLT-like Treg cell population (cluster 4) exhibited a lower frequency of duplicated TCRs within themselves. This frequency further decreased in the NLT-like Treg cell population (cluster 2). NLT-like Treg cells from iLN shared 39% of their TCRs with skin Treg cells, while NLT-like Treg cells from mLN shared 24% of their TCRs with spleen NLT-like Treg cells. Among NLT-like Treg cells from the spleen, 15% of the TCRs overlapped with precursor NLT-like Treg cells from the spleen, and 12% were found in skin Treg cells.

Within the colon, the pTreg cell population shared 9% of its TCRs with the tTreg population, while tTreg cells conversely shared 10% with pTreg cells. The pTreg population also overlapped with colon Tconv cells by 8%, but notably, tTreg cells

Results

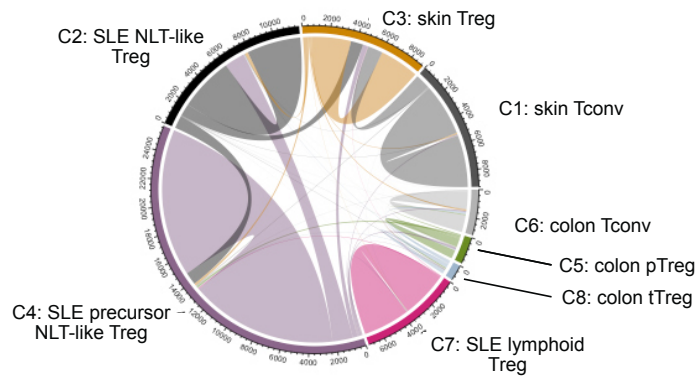
exhibited a higher overlap of 27%. Furthermore, pTreg cells had a higher frequency of shared TCRs within themselves (66%) compared to the tTreg population (48%). In contrast, duplicated TCRs from colon Tconv cells were detected at a frequency of approximately 4% in both Treg populations.

In the skin, Treg cells exhibited low overall TCR overlap. They shared approximately 3% of their TCRs with skin Tconv cells and colon Tconv cells, and around 4% with spleen NLT-like Treg cells.

In conclusion, Treg cell populations displayed distinct patterns of TCR sharing depending on their tissue origin. Lymphoid Treg cells from iLN, mLN, and spleen exhibited high TCR retention within their respective populations, indicating a strong tissue-specific identity. In contrast, NLT-like Treg populations, particularly those from iLN and spleen, showed increased TCR overlap with other tissue-resident populations, reflecting greater plasticity. Within the colon, pTreg cells demonstrated a higher frequency of internal TCR sharing compared to tTreg cells, while tTreg cells exhibited a stronger overlap with Tconv cells. Skin Treg cells displayed minimal TCR overlap with other populations, emphasizing their distinct tissue-specific signature. These findings highlight the variable degrees of TCR sharing among Treg cell populations based on their tissue residency and differentiation status.

Results

A chord diagram colored by cluster



B shared duplicated TCR clonotypes

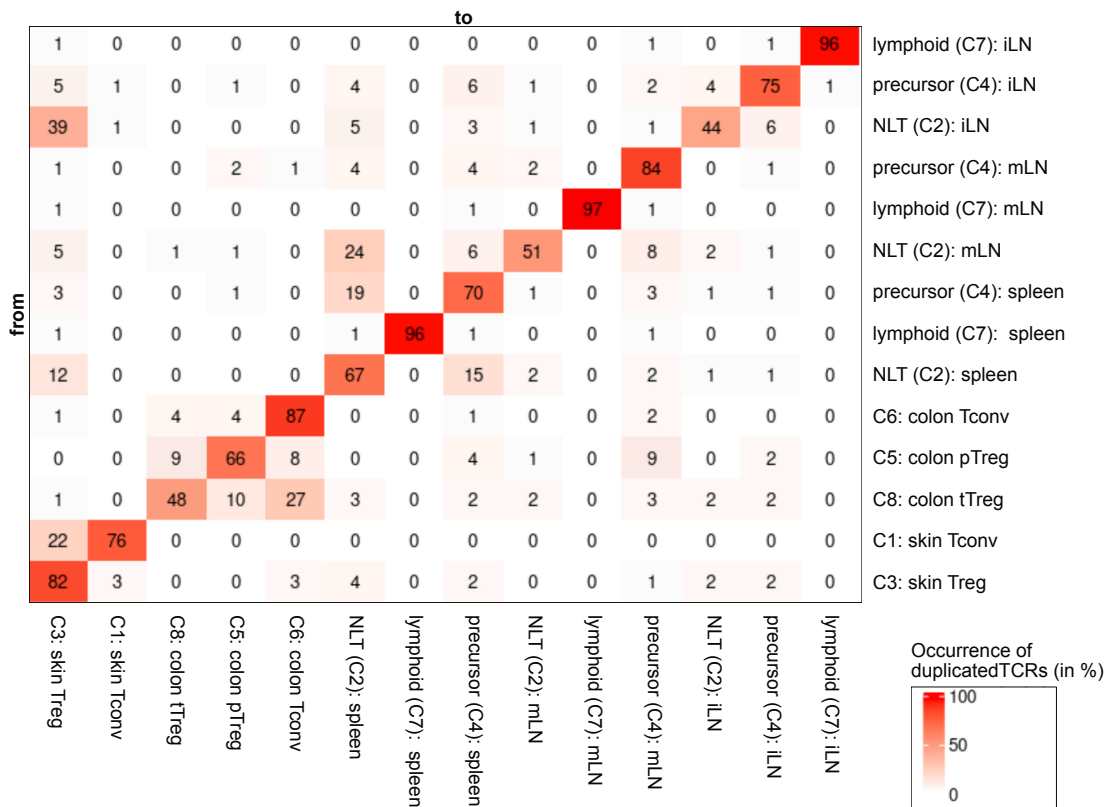


Figure 24: Tissue-dependent TCR overlaps among Treg cell populations. A: Chord diagram illustrates the shared TCR usage between different clusters, revealing inter-cluster relationships. Cell-types are colored based on their cluster color showed in **Figure 20A**. B: A heatmap visualizes the overlap of shared TCR clones among various tissue-specific cell populations, quantifying their extent.

Results

4.7. Shared TCR clonotypes across different tissues exhibit tissue-specific gene signatures

Finally, we compared the gene expression profiles of duplicated TCR clones across different tissues. **Figure 25A** presents a 2D-PCA of all duplicated TCRs from skin Treg cells, grouped by their gene expression profiles across tissues. This analysis clearly distinguished SLE Treg populations from skin and colon Treg cell populations, highlighting their unique tissue-specific transcriptional signatures.

To further explore this, we examined the expression of core Treg marker genes in duplicated TCR clones across different tissues. An example of this analysis is shown in a heatmap in **Figure 25B**. Interestingly, duplicated TCRs from Treg cells exhibited limited gene expression overlap, not only within the same tissue but also when found in different tissues.

This analysis revealed distinct transcriptional signatures across tissues, suggesting a high degree of tissue-specific adaptation in Treg functionality and demonstrating the complex interplay between clonality and tissue-specific adaptation in shaping Treg identity and function.

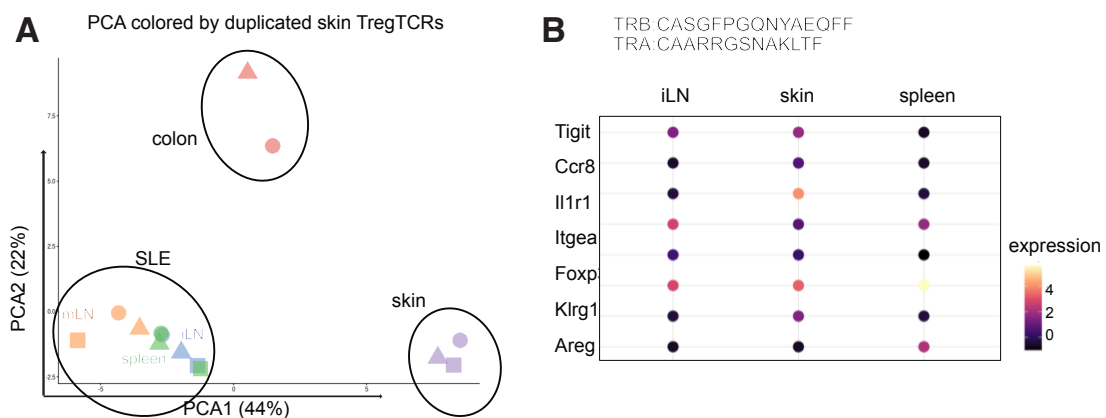


Figure 25: Shared TCR clonotypes across different tissues exhibit tissue-specific gene signatures. **A:** 2D-PCA plot colored by tissue cell-type, highlighting the distances between duplicated TCRs of skin Treg cells found in various tissues. Different shapes of the symbols highlight the mouse individual replicates. **B:** Dotplot illustrating the expression of Treg marker genes for a specific TCR based on their amino acid sequence (TRB: CASGFPQNYAEQFF; TRA: CAARRGSNAKLTF) shared among iLN, skin, and spleen, highlighting tissue-specific expression patterns. n = 3 individual mice.

Results

In conclusion, the scRNA/TCR dataset of healthy mice allowed us to establish tissue-specific Treg gene expression signatures along with a regenerative and suppressive signature. Additionally, we gained valuable insights into the TCR repertoire usage of T cells across different murine tissues. Building on these results, we extended our analysis to the disease models, including colitis (acute inflammation induced by AOM/DSS treatment), colitis-associated carcinoma, colorectal carcinoma (MC38) and a skin melanoma (B16-F10).

4.8. Acute colitis is induced by AOM/DSS

Inflammation has been shown to promote tumor development by creating an environment that favors the accumulation of mutations and interfering with crucial signaling pathways that control tumor initiation and progression [151]. Treg cells play a crucial part in inflammatory settings as they promote not just immune tolerance but also prevent the inflamed tissue from extended damage. Therefore, we are using the AOM/DSS model in which treatment causes colitis and, after approximately 60 days, promotes the formation of an intestinal tumor. A schematic overview of this workflow is shown in **Figure 8**. Ten to twelve-weeks old mice were injected intraperitoneal (i.p.) with AOM followed by one cycle of 2.5% DSS in the drinking water for five consecutive days. We generated scRNA/TCR-seq profiles on day 14 after AOM/DSS treatment to compare tissue-specific Treg signatures and the TCR usage in an inflamed colon.

As shown in **Figure 26A** mice lost body weight following AOM/DSS application suggesting DSS-induced intestinal inflammation. Moreover, a high infiltration of inflammatory cells in the lamina propria and submucosa could be shown in **Figure 26B**, where colon tissue was analyzed by histology on day 14. **Figure 26C** showing an endoscopy of inflamed colon on day 13 after treatment, suggesting that the AOM/DSS treatment induced colitis.

Results

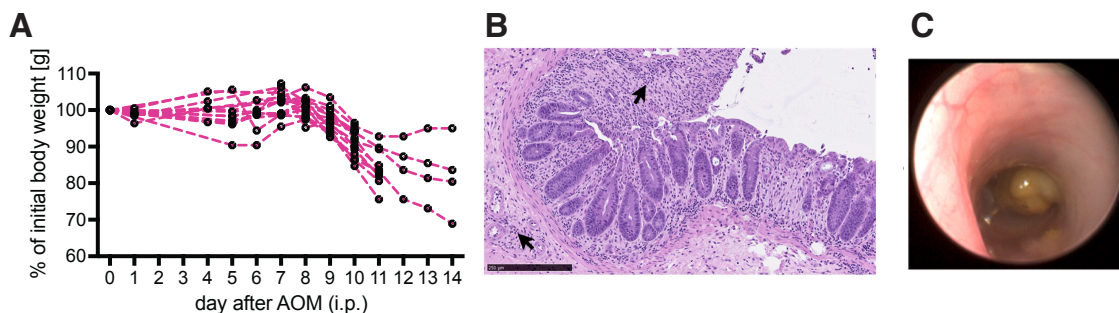


Figure 26: Colitis development assessed by body weight, endoscopy and hematoxylin (HE) staining. A: Weight curve showing the percentage of body weight relative to day 0 of wt mice ($n = 7$). B: H&E staining of inflamed colon swiss roll at day 14 after AOM/DSS treatment displaying on representative mouse. Black arrows illustrate infiltrating immune cells. C: Representative endoscopic image was taken on day 13. The scale bar is $250 \mu\text{m}$.

4.9. Colon pTreg and tTreg cells express cell-type specific signatures

We performed scRNA/TCR-seq on day 14 after AOM treatment in three wild-type mice. On this day the AOM/DSS treatment induced an acute inflammation as shown in **Figure 26**. Samples were collected from three independent experiments. After sequencing and batch correction, datasets from two mice were bioinformatically merged, since we couldn't integrate all three datasets into a single t-SNE. This limitation is likely due to three independent experiments resulting in strong batch effects, which would have masked the underlying biological signals, and additional batch correction proved too stringent, removing genuine tissue-specific biological effects. Hence, we decided for an individual analysis. However, the integration of only the inflamed and healthy colon from all three datasets was successful, preserving biological differences while removing technical noise caused by the different batches.

A t-SNE plot of the two merged mouse datasets illustrates cells colored by clusters (**Figure 27A**) and tissue types (**Figure 27B**). The same cell-types identified in the healthy animals were also observed in this dataset. Next, we plotted the pTreg and tTreg cell signatures (**Figure 27C-D**), defined in our analysis of healthy mice and allowing us to distinguish colonic Treg cells into two populations: pTreg (Klrg1^+

Results

Rorc⁺) and tTreg cells (Klrg1⁺, Ikzf2⁺, Np1⁺). A density plot comparing the expression levels to the healthy tTreg and pTreg cell signature (**Figure 20**) in this dataset.

We detected that inflamed colon tTreg cells express the same level of pTreg signature genes than the inflamed pTreg cells, as these two populations were quite overlapping in the density plot (**Figure 27C**, right panel). The tTreg signature was again more present in the inflamed tTreg cell population within the colon compared to the colon pTreg cells.

We observed that inflamed colon tTreg cells expressed pTreg signature genes at levels comparable to those of inflamed pTreg cells, as indicated by their overlapping distribution in the density plot (**Figure 27C**, right panel). However, the tTreg signature was more prominently expressed in the inflamed tTreg cell population within the colon compared to colon pTreg cells.

Overall, in this inflamed setting, colonic populations exhibited gene expression patterns similar to their healthy counterparts as shown in **Figure 27E**. Specifically, colonic tTreg cells expressed more marker genes associated with healthy colon tTreg cells, with 86% of the cells resembling the healthy tTreg signature and 14% resembling the healthy pTreg signature. Conversely, colonic pTreg cells expressed more marker genes associated with healthy pTreg cells, with 82% of the cells displaying the pTreg signature and 18% exhibiting the tTreg signature.

Results

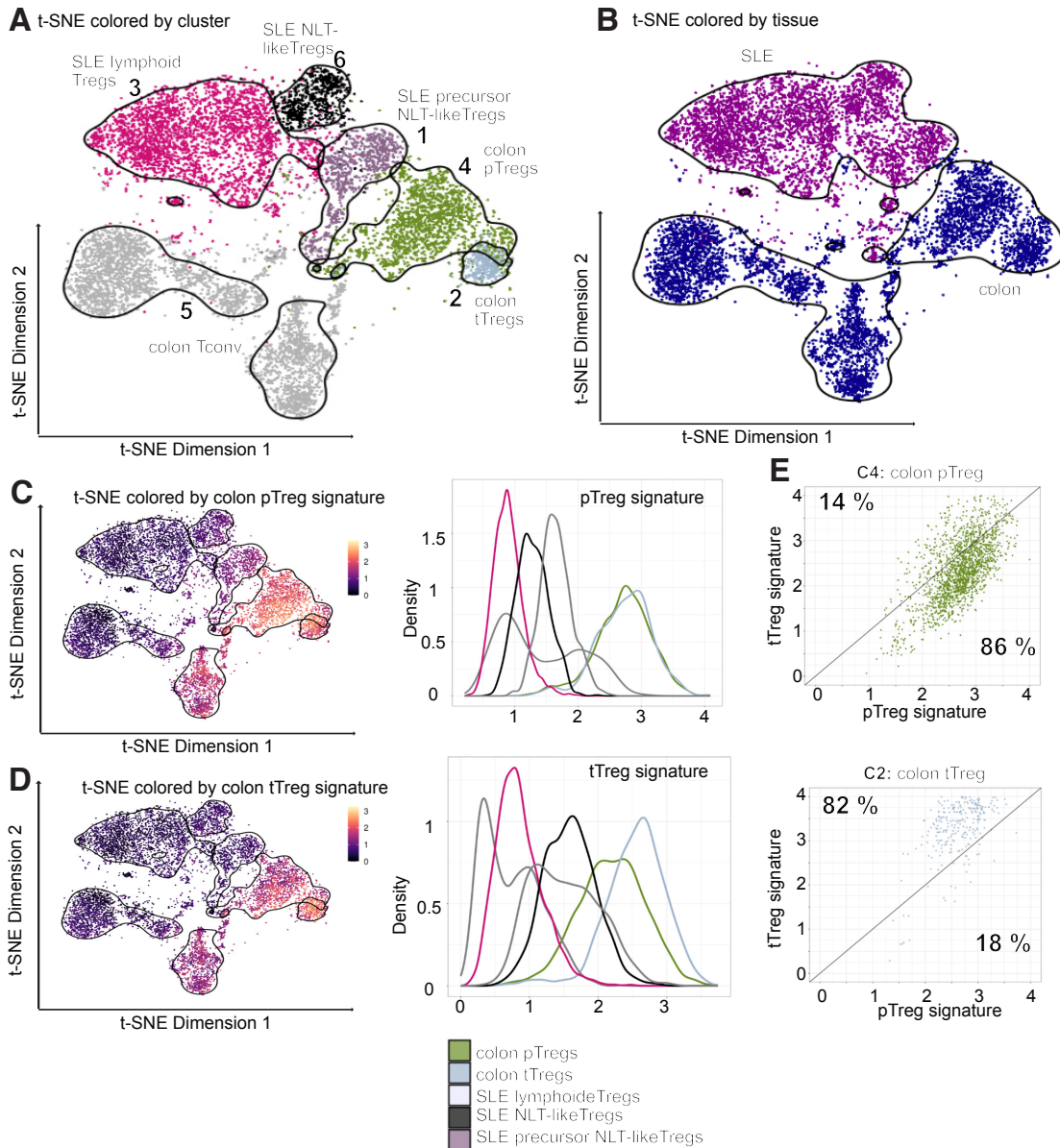


Figure 27: scRNA/TCR-seq at day 14 after AOM/DSS treatment. A-B: t-SNE plot colored by cluster (A) and tissue types (B). Confidence ellipses applied to the t-SNE plot displaying the 95% confidence level. C: pTreg signature from healthy mice (**Figure 20**) is applied to this dataset and visualized through a t-SNE plot (left) and density plot (right). D: tTreg signature from healthy mice (**Figure 20**) is applied to this dataset and visualized through a t-SNE plot (left) and density plot (right). E: Colon pTreg cells (cluster 4) and colon tTreg cells (cluster 2) are compared with the tTreg cell and pTreg cell healthy signature. Percentage showing the frequency of cells in the area. n=2 individual mice.

Results

4.10. Inflamed colon Treg cells express more suppressive and regenerative genes

We further aimed to apply the suppressive and regenerative Treg signatures previously defined in our studies of healthy mice.

We first performed batch correction of the datasets from healthy animals and AOM/DSS-treated mice. The integration of pTreg and tTreg cells from the colon and lymphoid spleen cells was successful, preserving biological differences while removing technical noise caused by the different batches. The t-SNE colored by integrated cell types and condition after batch correction is shown in **Figure 28A-B**. We chose the lymphoid Treg cell population in the spleen as a reference population because they were expected to remain unaffected by AOM/DSS treatment. These naive cells, which theoretically have not yet encountered any antigen, should remain uninfluenced by colitis and retain their naive state within the spleen.

By performing a DGE analysis between the lymphoid Treg cells of healthy and colitis-induced mice we found 75 upregulated and 635 downregulated genes within a total of 32285 genes (**Figure 28C**). We hypothesized that these gene expression differences occur not due to the condition but rather are batch/mouse-based. Therefore, we decided to next use this population as a reference for normalization of gene expression counts for colon Treg cells in each individual mouse. Following this normalization, we did a comparative analysis of the expression of regenerative and suppressive signature genes between colon pTreg and tTreg cells from both healthy and colitis-induced mice. The approach of normalization allowed us not just to assess the impact of colitis on the expression patterns of regenerative and suppressive signatures, but also in the detection of differentially expressed genes between the healthy and colitis-induced mice.

Results

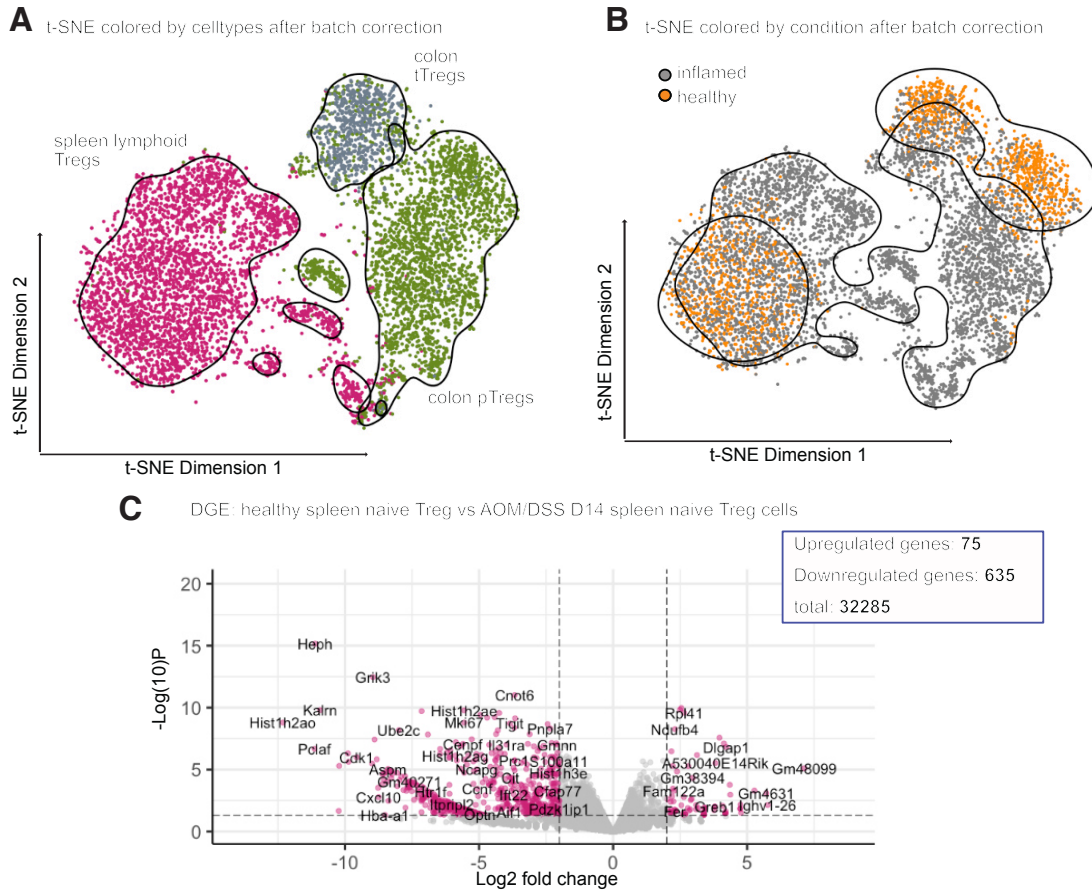


Figure 28: Datasets of healthy and colitis-induced mice were successfully integrated after batch correction. A-B: t-SNE colored by cell types (A) and condition (B). Confidence ellipses applied to the t-SNE plot displaying the 95% confidence level of cell types (A) and condition (B). C: DGE between naive Treg cells isolated from splenocyte of healthy and colitis-induced mice cells plotted on a volcano plot. Non-significant (ns) genes and genes which were either a $\log_2FC > 2$ or $p\text{-value} < 0.05$ are colored grey, while genes with $\log_2FC > 2$ and $p\text{-value} < 0.05$ are shown in pink. $n=3$ individual mice.

Figure 29A and **B** display t-SNE plots (left) illustrating both signatures at day 14 after AOM injection, along with density plots (right) comparing the colonic pTreg and tTreg populations between the healthy and inflamed datasets. The density plots reveal an overall higher density of pTreg cells from both healthy and inflamed colon tissues for the regenerative and suppressive signatures. Additionally, the expression levels of these signatures were notably elevated in the inflamed colon dataset.

DGE analysis between colonic healthy pTreg cells and colonic inflamed pTreg cells identified 423 upregulated and 353 downregulated features out of a total of 32285

Results

features (**Figure 29C**). For this DGE the three samples from healthy colon tissue and inflamed colon tissue were integrated successfully after batch correction, preserving biological differences while removing technical noise caused by the different batches. Functional enrichment analysis revealed several upregulated pathways, including those involved in metabolic processes, cell differentiation and migration as well as translation and T cell activation (**Figure 29E**). Similarly, the DGE analysis comparing colonic healthy tTreg cells with colonic inflamed tTreg cells showed 364 upregulated and 180 downregulated genes (**Figure 29D**), with an enrichment of upregulated pathways related to immune cell development, lymphocyte differentiation and cell proliferation (**Figure 29F**).

This analysis demonstrates that the regenerative and suppressive Treg signatures from studies of the healthy mice are robustly applicable to inflamed colon datasets, with elevated expression levels in the inflamed environment. Colonic pTreg cells exhibited higher signature densities compared to tTreg cells in both healthy and inflamed tissues. DGE and pathway enrichment analyses highlighted a few transcriptional changes in inflamed Treg cells, including upregulated pathways related to cell proliferation and metabolic processes, emphasizing the functional adaptation of Treg cells in the inflamed colon microenvironment.

Results

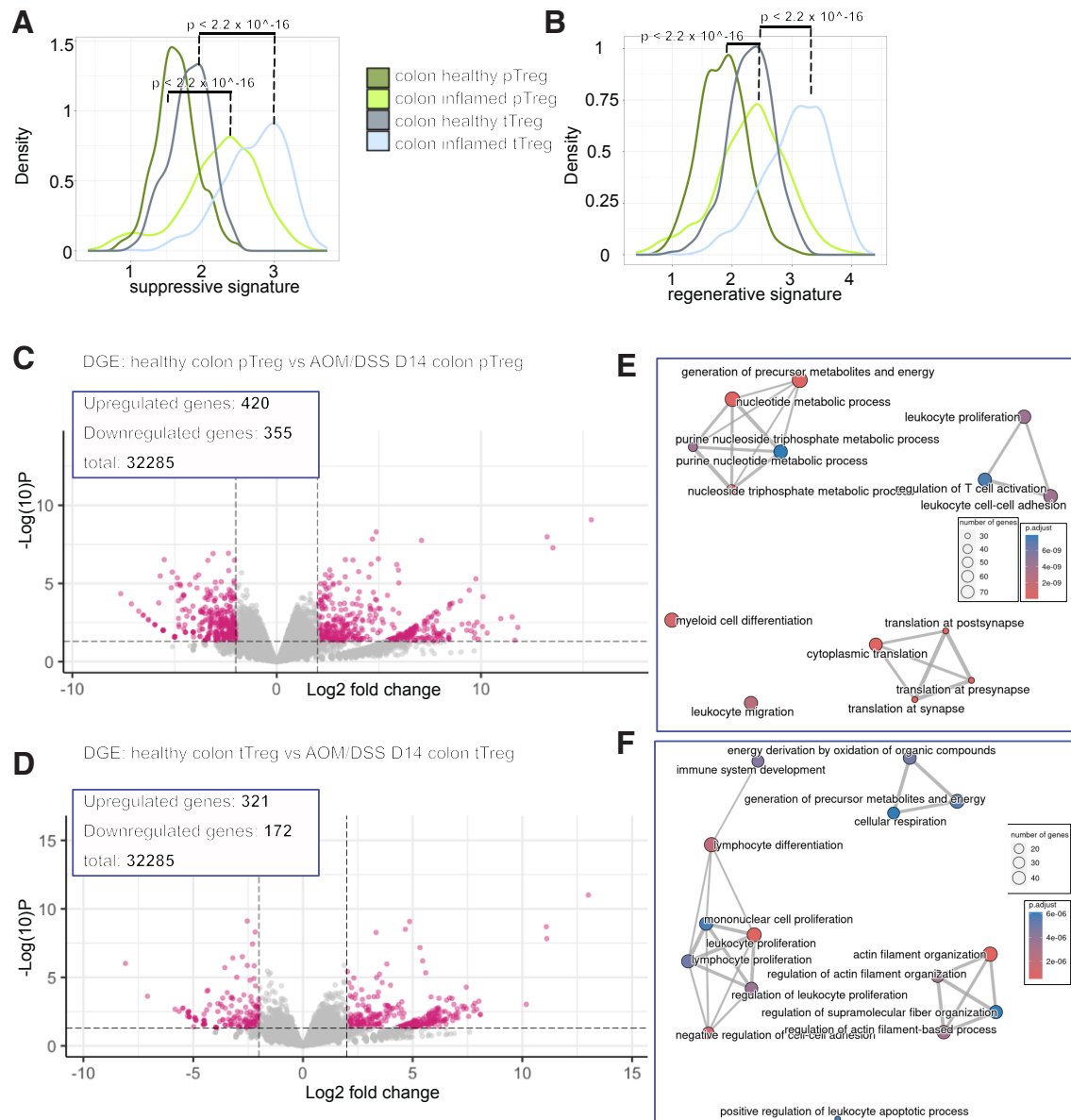


Figure 29: Colon Treg cells from AOM/DSS-induced colitis are high in expression of suppressive and regenerative signatures. A-B: A density plot displaying the differences for the suppressive Treg cell signature (A) and regenerative Treg cell signature (B) between colon pTreg and tTreg cells from AOM/DSS-induced colitis and healthy animals. p-value calculated by the Wilcoxon rank sum test. C: DGE of healthy and inflamed colon pTreg cells. D: DGE between healthy and inflamed colon tTreg cells plotted on a volcano plot. Non-significant (ns) genes and genes which were either a $\log_2FC > 2$ or $p\text{-value} < 0.05$ are colored grey, while genes with $\log_2FC > 2$ and $p\text{-value} < 0.05$ are shown in pink. E: Functional enrichment results of the analysis shown in C plotted on an enrichment map. F: Functional enrichment results of the analysis shown in D plotted on an enrichment map. n=3 individual mice.

4.11. Precursor NLT-like Treg cells share TCR with inflamed colon Treg cells

We further analyzed TCR usage by generating a t-SNE plot highlighting all duplicated TCRs within the dataset (**Figure 30A**). Pie charts revealed that colonic pTreg cells exhibited greater clonal diversity compared to tTreg cells, which showed a lower percentage of unique clonotypes (**Figure 30B**). The chord diagram and table in **Figure 30C** and **D** further illustrate the extensive TCR sharing. As already seen in the lymphoid cells from the healthy animals, we found a high degree of TCR shared with the tissue itself for the lymphoid cell cluster (cluster 3). Notably a high percent of TCRs from precursor NLT-like Treg cells in the spleen (31%), mLN (39%) and iLN (50%) shared TCRs with the pTreg cells (cluster 4) within the colon.

Among the TCRs detected in tTreg cells (cluster 2), 27% were shared with pTreg cells (cluster 2). Additionally, 7% overlapped with precursor NLT-like Treg cells from the mLN and another 7% with NLT-like Treg cells from the spleen. Interestingly, for the pTreg cells just 6% of the identified TCRs were found in colon Tconv cells and precursor NLT-like Treg cells from the mLN. The overall TCR expansion to other tissue was much higher in the tTreg cells compared to the pTreg cells.

When comparing the overlap between tTreg and pTreg TCR clonotypes, tTreg TCR clones displayed a considerably higher degree of sharing with other tissues. In contrast, pTreg cells exhibited greater self-sharing, with 74% of their TCR clonotypes remaining within the same population, compared to only 50% for tTreg cells.

Afterwards, we focused on the pseudo-time of duplicated Treg TCRs isolated from inflamed colon tissue. A trajectory analysis was performed, which is illustrated in **Figure 30E** and **F**. The highest pseudo-time was observed in the Tconv cells from colon tissue (cluster 5), with the red trajectory line displaying the “progression” of pseudo-time starting from this population, moving through SLE lymphoid Treg cells, precursor NLT-like Treg cells, and extending towards tTreg cells and pTreg cells. The lowest pseudo-time was found in the colonic tTreg and pTreg cell populations, with tTreg cells exhibiting the lowest pseudo-time overall, while the pseudo-time in pTreg cells appears to be slightly more variable.

Results

These findings underscore the interconnected nature of TCR repertoires across colonic T cell populations, suggesting a complex interplay between Treg cells in the inflamed colonic microenvironment and precursor NLT-like Treg cells from lymphoid tissue. Interestingly, it illustrated that colon tTreg cells seem to have a higher clonal expansion within other tissues than colon pTreg cells, which displayed a higher sharing of TCR clonotypes with itself. It also gives insight into the differentiation states of Treg TCRs isolated from inflamed colon tissue, revealing the distinct pseudo-time dynamics across different cell populations, from Tconv cells to Treg cells, highlighting the complex continuum of cellular progression during inflammation.

Results

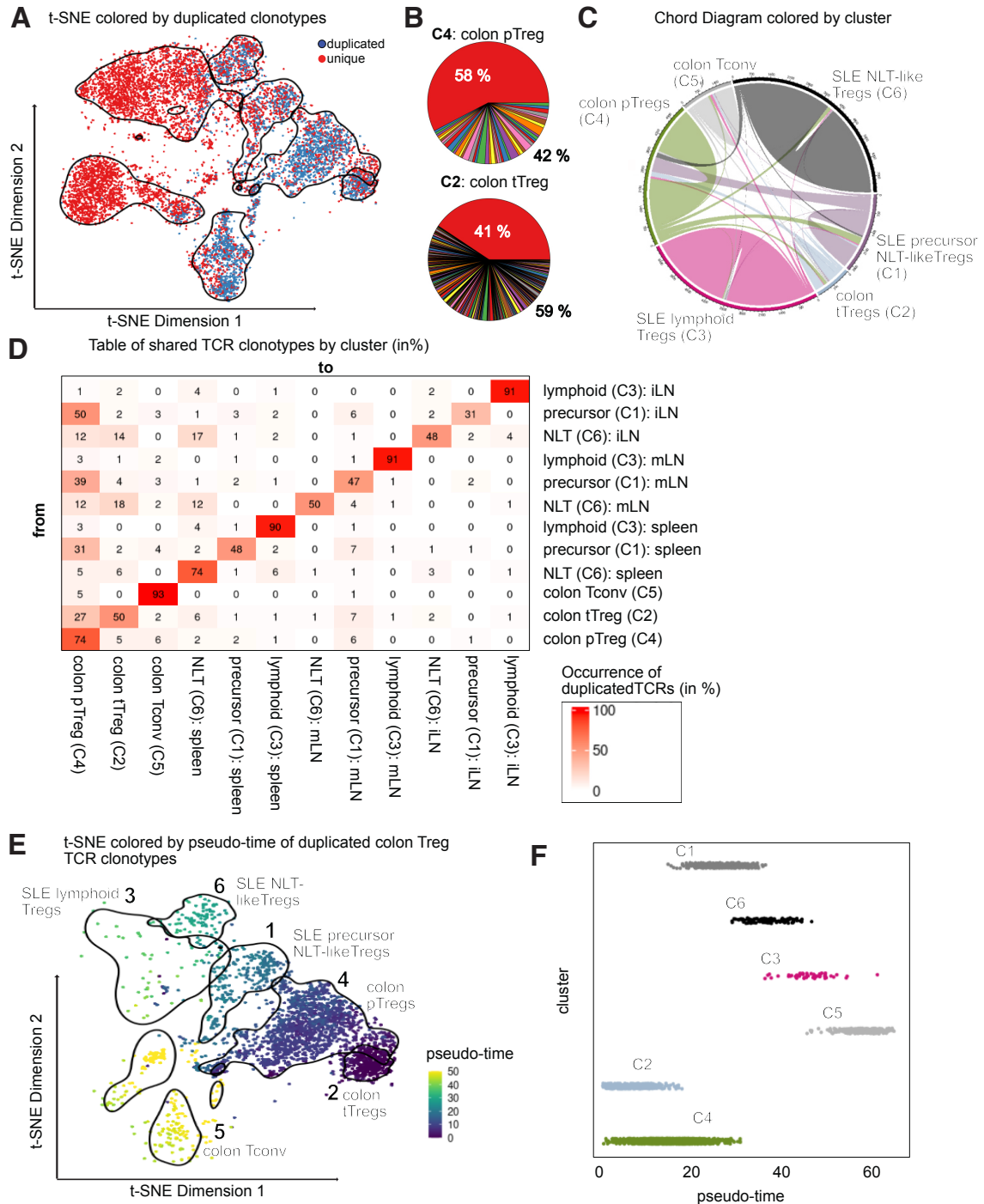


Figure 30: Precursor NLT-like Treg cells share TCR with inflamed colon Treg cells. TCR repertoire analysis of T cells from different murine organs were performed at day 14 after AOM/DSS-induced colitis. **A:** t-SNE plot colored by all duplicated TCRs detected in this dataset. Red dots showing cells with duplicated TCRs. Confidence ellipses applied to the t-SNE plot displaying the 95% confidence level. **B:** Pie charts showing the TCR repertoire composition for colon pTreg (cluster 4) and colon tTreg (cluster 2) cells, highlighting the percentage of singletons (grouped together in the red slice) and the distinct duplicated TCRs. **C:** Chord diagram illustrates the shared TCR usage between different clusters, revealing inter-cluster relationships. Clusters are colored based on their cluster color showed in **Figure 27A**. **D:** Shared TCRs among all other clusters illustrated in a table. **E:**

Results

Pseudo-time is displayed in a color-coded t-SNE plot, with purple indicating a low and yellow indicating a high pseudo-time. F: Scatter plot showing the distribution of pseudo-time values across the different cell-types.

4.12. CAC is induced by AOM/DSS treatment

CAC was induced to investigate inflammation-associated tumorigenesis. The histological analysis of tumor-bearing colon tissue on day 60 of AOM/DSS treatment revealed invasive dysplastic regions and loss of regular mucosal organization, indicated by irregularly shaped crypts. It also confirmed tumor development in the colon (**Figure 31A**) but not in the healthy tissue adjacent to the tumor (**Figure 31B**). Tumor formation was observed in the distal colon, as shown in the representative image of the tumor in **Figure 31C**. Tumor burden was monitored via mini-endoscopy on day 59, with arrows highlighting the distal tumors (**Figure 31D**).

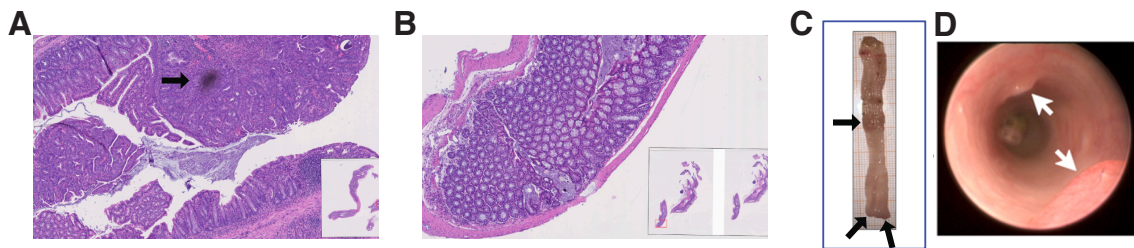


Figure 31: CAC induction after 60 days of AOM/DSS treatment. 12 weeks old WT mice were injected i.p. with AOM (10 $\mu\text{g/g}$ body weight) on day 0 and received one cycle of 2.5% DSS ad libitum from day 5 to day 10. Mini-endoscopy was performed one day before sacrifice to confirm tumor development and state of inflammation. Colons were collected on day 60 of AOM/DSS treatment, opened longitudinally, and rolled up from the distal part to generate ‘Swiss rolls’. Histopathological grading was performed by a trained pathologist (AG Matthias Gaida). A: H&E staining showing distal tumor and B: tumor-free tissue (NAT). C: Representative image of longitudinally opened colon showing tumor development in the distal colon of the mice. D: Representative endoscopic images of wild-type mice on day 59 of AOM/DSS-induced CAC. Arrows indicate tumors.

Results

4.13. Colon tumor and NAT pTreg cells express more tTreg signature genes

After confirming tumor development, we performed scRNA/TCR-seq at day 60 after treatment start on three individual wild-type mice, with samples collected from three independent experiments. Also, for this study, only one representative mouse is shown in **Figure 32A-E**, since we couldn't integrate all three datasets into a single t-SNE. However, the integration of cells from tumor colon tissue and NAT colon tissue from all three datasets was successful, preserving biological differences while removing technical noise caused by the different batches. A t-SNE projection, generated after successful batch correction, is presented in the **Supplementary Figures**.

Cells were collected by sorting CD25⁺ T cells from the spleen, iLN, and mLN, as well as CD4⁺ T cells from the skin, colon (normal adjacent tissue) NAT, and colon tumor tissues. **Figure 32** illustrates t-SNE plots colored by cluster (A) and by tissue-specific cell-types (B). Due to the high similar gene expression profiles of the colon tumor and colon NAT Treg cells, we were unable to distinguish the colonic tumor pTreg cells and tTreg cells from their healthy NAT counterparts for the cluster reassignment. Consequently, these cells were grouped into a single cluster: Cluster2 for colonic tumor/NAT tTreg cells and cluster7 for colonic tumor/NAT pTreg cells.

Additionally, we applied healthy tissue-specific signatures to this dataset (**Figure 32 C-E**), revealing that pTreg and tTreg cells from both tumor and NAT tissues exhibited behavior similar to their healthy colonic Treg counterparts. Following this, we differentiated between tumor and NAT colonic Treg cells and compared them to the healthy tTreg and pTreg signatures from colon tissue (**Figure 32 F-I**). This analysis was done for all three individual mice. It revealed that tumor and NAT tTreg cells retained a high proportion of tTreg signature genes (93% for tumor, 94% for NAT). In contrast, tumor pTreg cells expressed only 53% of the pTreg signature, while NAT pTreg cells expressed just 43%.

Our findings suggest that tumor and NAT tTreg cells maintain a strong resemblance to the healthy colon tTreg signature, indicating a conserved function in both tumor

Results

and healthy tissues. However, colon tumor and NAT pTreg cells display a reduced alignment with the healthy colon pTreg signature, suggesting a potential functional divergence influenced by the TME and highlighting the complexity of Treg cell behavior in the context of inflammation-associated tumorigenesis.

Results

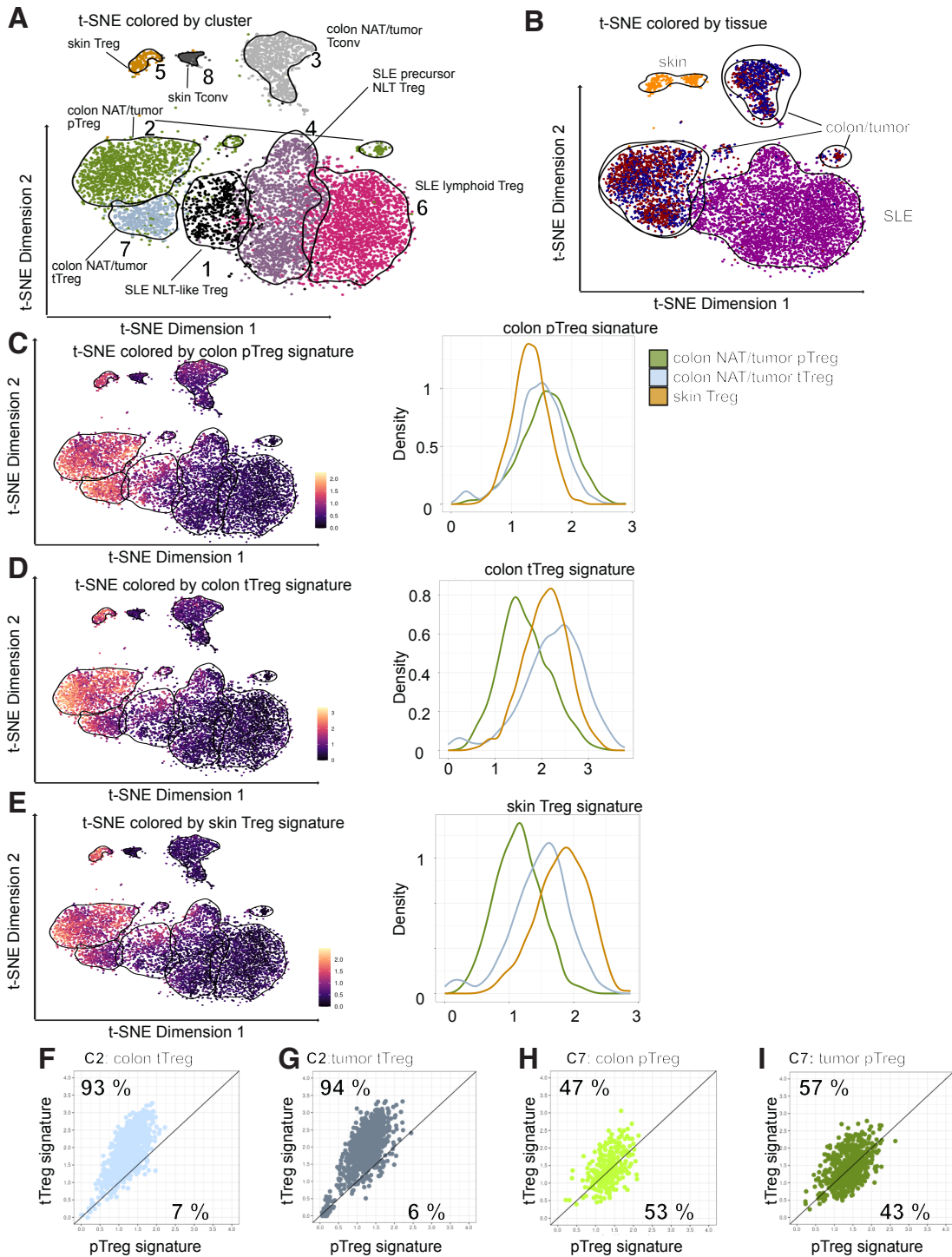


Figure 32: scRNA/TCR-seq at day 60 after AOM/DSS treatment. A-B: t-SNE plot colored by cluster (A) and tissue types (B). Confidence ellipses applied to the t-SNE plot displaying the 95% confidence level for cluster (A) and tissue (B). C: pTreg signature from healthy mice (**Figure 20**) is applied to this dataset and visualized by a t-SNE plot (left) and density plot (right). D: tTreg signature from healthy mice (**Figure 20**) is applied to this dataset and visualized by a t-SNE plot (left) and density plot (right). E: Skin Treg signature from healthy mice (**Figure 20**) is applied to this dataset and visualized by a t-SNE plot (left) and density plot (right). F: Tumor tTreg cells (cluster 2). Confidence ellipses applied to the t-SNE plot (right). F: Tumor tTreg cells (cluster 2). Confidence ellipses applied to the t-SNE plot (right).

Results

displaying the 95% confidence level for clusters displayed in (A) G: Colon tTreg cells (cluster 2), H: Tumor pTreg cells (cluster 7) and I: Colon pTreg cells (cluster 7) are compared with the tTreg cell and pTreg cell healthy signature. Percentage showing the frequency of cells in the area. A-E: n =1, F-I: n=3.

We further compared tumor and NAT pTreg and tTreg cells based on the expression of the regenerative and suppressive signatures identified in our scRNA/TCR-seq dataset of healthy mice. Colon tumor tTreg cells exhibited the highest expression levels for both signatures. Significant differences between tumor and NAT tissues were observed in both pTreg cells for the regenerative signature. In contrast, for the suppressive signatures, a significant change was detected only in the comparison of pTreg cells (**Figure 33A+B**).

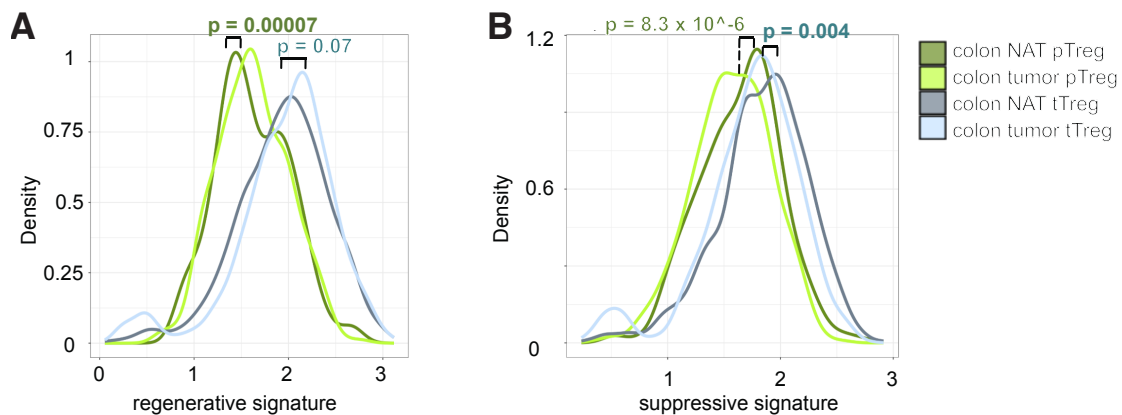


Figure 33: Tumor tTreg cells exhibited the highest expression of the regenerative and suppressive signature. A: Density plot showing density differences between NAT and tumor pTreg and tTreg cells of the regenerative Treg cell signature. B: Density plot showing density differences between NAT and tumor pTreg and tTreg cells of the suppressive Treg cell signature. n = 3 individual mice. p-value calculated by using the Wilcoxon rank sum test.

4.14. DGE revealed highly shared gene expression pattern of tumor and NAT Treg cells

Since we were unable to distinguish between tumor and NAT pTreg cells and tTreg cells during the clustering process, we performed a DGE analysis on these two populations (**Figure 34A and B**). For this DGE the three samples from tumor colon tissue and NAT colon tissue were integrated successfully after batch correction. We

Results

also split cluster 2 (colonic tumor and NAT tTreg cells) and cluster 7 (colonic tumor and NAT pTreg cells) into the tumor and NAT subsets. The DGE analysis for pTreg cells identified 68 upregulated and 47 downregulated genes ($\log_2\text{Fc} > 2$, $p\text{-value} < 0.05$) out of 32285 features, including genes like *Plek*, *Kif22*, *Rsad2* and *Ifit3b*. Similarly, the differences between NAT and tumor tTreg cells were relatively modest, with 78 upregulated and 67 downregulated genes. This DGE indicated that while there are transcriptional differences between tumor and NAT Treg cells, the overall magnitude of these differences remains relatively small, reflecting the high degree of similarity between these populations.

By further performing functional enrichment analysis, we identified a limited number of enriched pathways by comparing the colon tumor and NAT tTreg and pTreg cells. **Figure 34C** presents a dotplot and cluster network (CNET) plot for the gene expression differences involved in signaling pathways between tumor and NAT tTreg cells. Pathways related to regulation of lymphocyte mediated immunity and immune effector processes, involving genes such as *Klrb1b*, *Klrk1*, *Muc4*, *Klrg1*, *Clnm* and *Mill2* as well as cell killing processes were enriched.

For the comparison of tTreg cells between NAT and tumor tissue no significant enriched pathways could be found.

This analysis revealed a highly shared transcriptional program between tumor-infiltrating and NAT Treg cells. However, tTreg cells exhibited a slight enrichment in pathways related to immune response regulation, immunity, and the regulation of cell killing. Notably, Treg cells within colon tumors appeared to represent an activated state of colon NAT Treg cells. Based on this observation, one could hypothesize that their TCR repertoires also show a high degree of overlap. To investigate this, we next performed a TCR analysis of colon NAT and tumor Treg cells.

Results

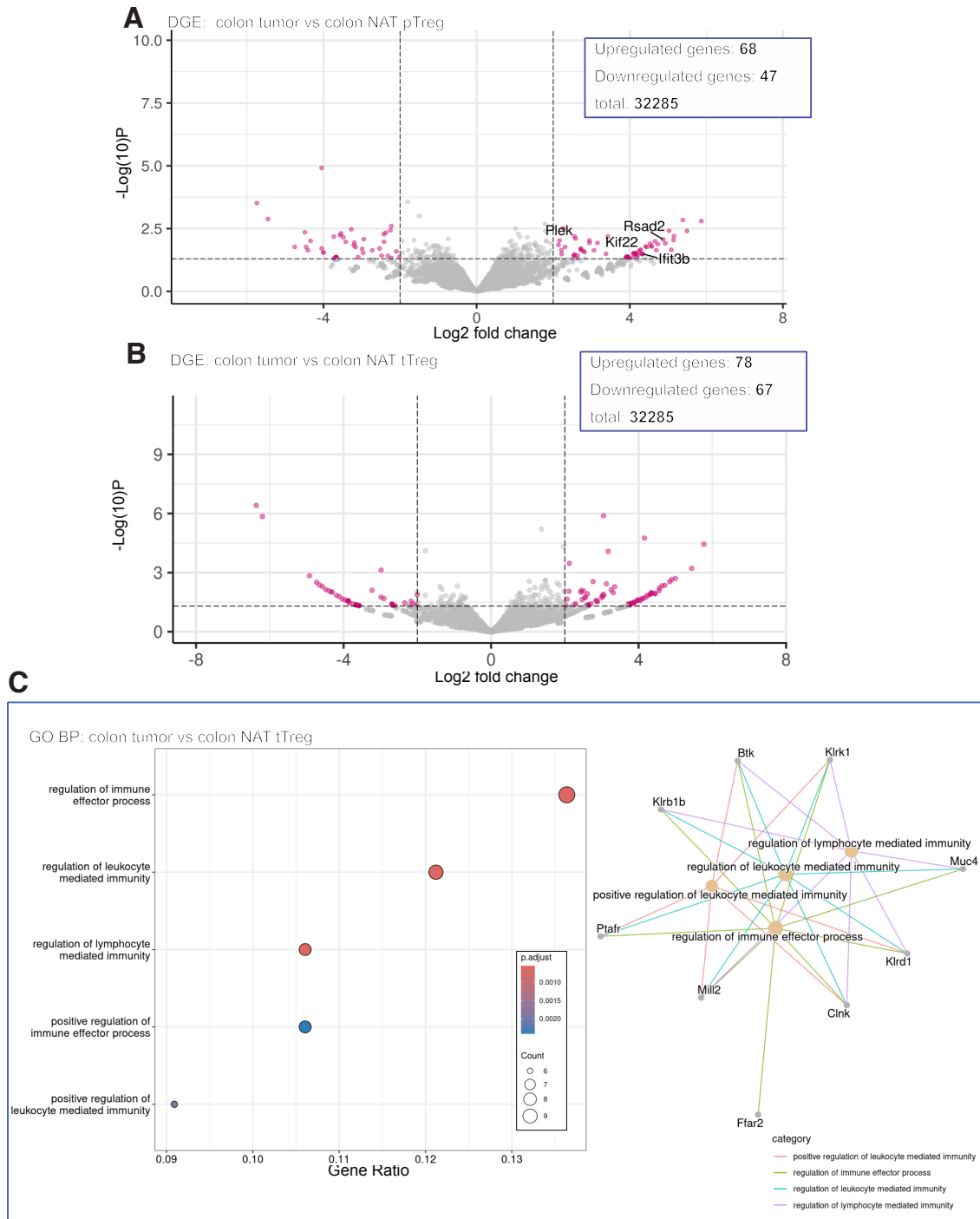


Figure 34: Colon Treg cells from AOM/DSS-induced CRC are highly similar in their gene expression profiles. A - B: Volcano plot illustrating the differential expressed genes between tumor Treg and colon pTreg cells (A) and Tumor Treg and tTreg cells (B). C: Enrichment Map and CNET-Plot showing enriched pathways of the Functional Enrichment analysis between colon tumor and colon NAT tTreg cells. Non-significant (ns) genes and genes which were either $\log_2FC > 2$ or $p\text{-value} < 0.05$ are colored grey, while genes with both, $\log_2FC > 2$ and $p\text{-value} < 0.05$ are shown in pink. $n = 3$ individual mice.

Results

4.15. TCR from NLT-like Treg cells in SLE are highly overlapping with tumor tTreg cells

Lastly, we aimed to identify clonal relationships between tumor and NAT tTreg and pTreg cells. **Figure 35** A and B display t-SNE plots colored by duplicated clonotypes across all four cell populations. Duplicated clonotypes from pTreg and tTreg cells from either colon tumor or colon NAT are illustrated in pie charts in **Figure 35C**.

The pie charts show a similar pattern for all of the four groups, with a duplicated clonotype fraction of 37% - 43%. A heatmap illustrates the percentage of shared TCR clonotypes between all the clusters (**Figure 35D**).

In the AOM/DSS-induced CAC model, the lymphoid Treg cell cluster (cluster 6) displayed the highest percentage of TCRs shared with the tissue itself. Specifically, 98% of lymphoid Treg TCRs from the iLN, 96% from the mLN, and 92% from the spleen were shared within this cluster. Additionally, many TCRs from NLT-like Treg cells in SLE overlapped with the colon/tumor tTreg cells (cluster 7). This included 18% of duplicated TCRs from the iLN, 20% from the mLN, and 8% from the spleen. Within the pTreg population (cluster 2), 7% of iLN NLT-like Treg TCRs, 6% of mLN NLT-like Treg TCRs, and only 1% of spleen NLT-like Treg TCRs were detected.

For colon/tumor tTreg cells, 75% of duplicated TCRs were confined to the cluster itself, while 10% were shared with Tconv cells (cluster 3) and 7% with pTreg cells.

In contrast, only 55% of duplicated pTreg TCRs were retained within the cluster itself. The remaining TCRs were evenly distributed between colon/tumor tTreg cells (20%) and colon/tumor Tconv cells (20%).

In **Figure 35E**, the gene expression profile of duplicated Treg TCRs from tumor tissue is visualized using a 2D-PCA plot. The plot clearly shows a distinct separation into four populations: one representing skin Treg and Tconv cells, another for SLE Treg cells, a third for tumor and NAT Tconv cells, and the last for tumor and NAT Treg cells. This separation highlights the gene expression differences between these Treg and Tconv populations in the different tissue types.

Results

The analysis demonstrates a consistent pattern of TCR clonotype duplication across the colon and tumor pTreg and tTreg compartment, with a clonotype fraction ranging from 37% to 43%. The lymphoid Treg cell cluster (cluster 6) showed the highest level of tissue-specific TCR sharing, highlighting also in the CAC model its strong association with the local tissue environment. Furthermore, our analysis revealed that tTreg cells in both tumors and NAT predominantly recruit tissue Treg cells from the NLT-like Treg population in SLE, whereas pTreg cells contribute to this process to a much lesser extent.

Results

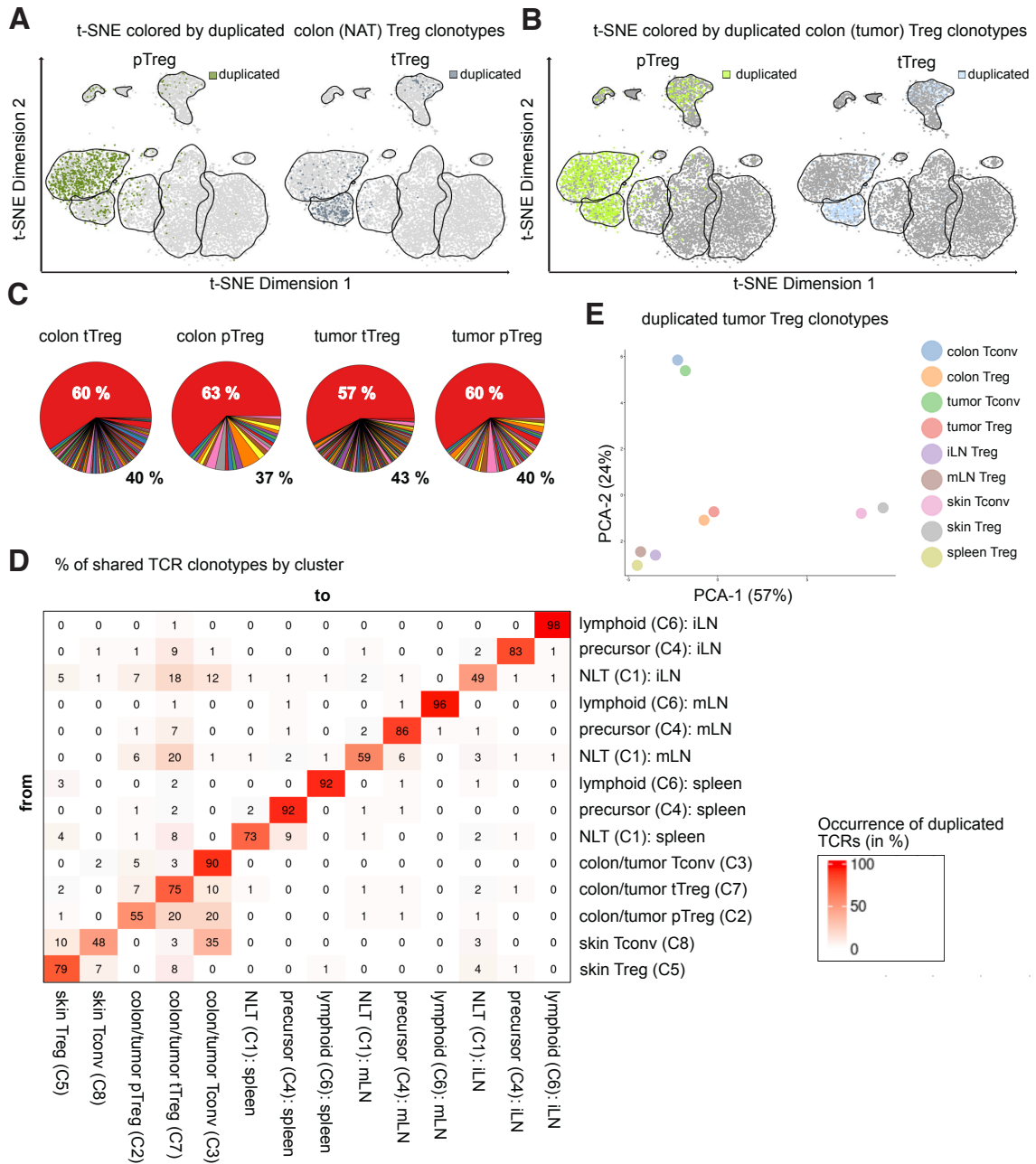


Figure 35: TCRs from NLT-like Treg cells in SLE are highly overlapping with tumor tTreg cells. A-B: t-SNE plot colored by duplicated pTreg and tTreg TCRs from either colon NAT (A) or colon tumor (B) tissue. Confidence ellipses applied to the t-SNE plot displaying the 95% confidence level for clusters. C: TCR clonality of tTreg and pTreg from the NAT colon and tumor tissue is plotted in a pie chart. D: Table illustrating the percent of duplicated TCRs shared with cells between clusters. E: 2D-PCA plot colored by tissue cell-type, highlighting the distances between duplicated TCRs of tumor Treg cells found in various tissues. n = 1.

We then focused on analyzing the pseudo-time of all cells isolated from the different tissues. A trajectory analysis was performed on the clustering, as

Results

illustrated in a t-SNE plot showed in **Figure 36A**. In this analysis, tumor and NAT from the colon tissue were not separated, as they were previously clustered together. The skin Tconv cells displayed the highest pseudo-time, whereas the Tconv cells from tumor/colon tissue (cluster 3) exhibited the lowest pseudo-time overall. A trajectory line originates from the SLE lymphoid Treg cells, passes through precursor cells and NLT-like Treg cells, and ultimately progresses toward tTreg cells in the tumor/colon tissue. When comparing tumor/colon tTreg to pTreg cells, the pTreg population demonstrated a slightly lower pseudo-time, indicating potential differences in differentiation or functionality.

Focusing on the pseudo-time of duplicated tumor Treg TCRs shared across other tissues (**Figure 36B**) the results were largely consistent with the pseudo-time values for all clonotypes. However, an exception was observed in the duplicated tumor Treg TCRs found within skin Treg cells, which exhibited the second-highest pseudo-time after skin Tconv cells. The findings suggest a possible migratory trajectory of skin Treg cells as well as SLE Treg cells to the disease site in colon tissue, where they may undergo differentiation or functional adaptation, leading to lower pseudo-time values. This raises important questions about the dynamic plasticity of NLT Treg cells derived from skin and SLE and their role in the tumor microenvironment.

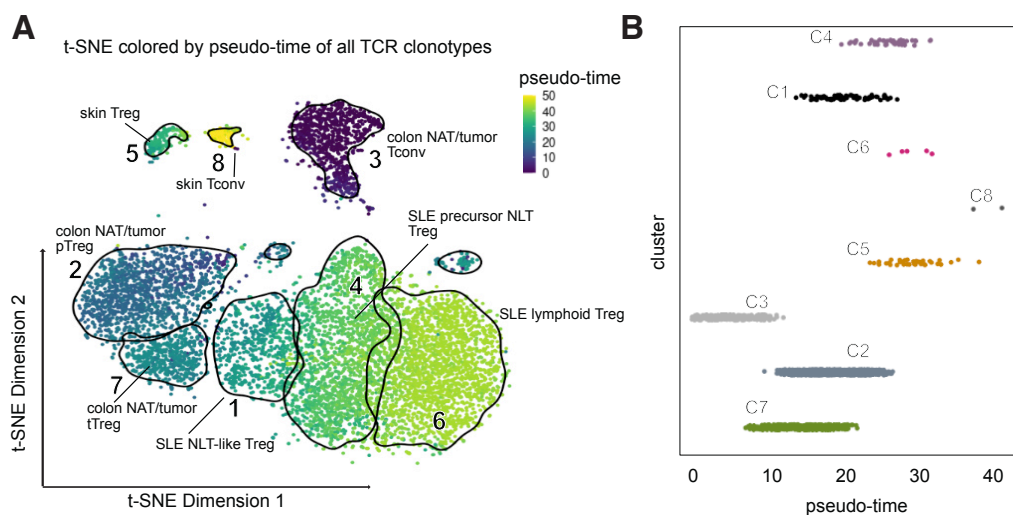


Figure 36: Migratory trajectory of skin and SLE Treg cells to colon disease sites in AOM/DSS-induced CAC mice. **A:** Pseudo-time of all duplicated TCR clonotypes is displayed in a color-coded t-SNE plot, with purple indicating a low and yellow indicating a high pseudo-time.

Results

Confidence ellipses applied to the t-SNE plot displaying the 95% confidence level for clusters. B: Scatter plot showing the distribution of pseudo-time values from duplicated and shared tumor/colon Treg TCRs (cluster2+7) across all other tissues. Cluster are colored based on their cluster color. n = 1.

4.16. Treg cells infiltrate the TME of MC38 tumors in high frequency

As we before analyzed a colitis-induced carcinoma, where a tumor is induced directly in the colon, we now aimed to study a tumor, where a colorectal carcinoma (MC38) is implanted underneath the skin. This analysis aimed to provide insights into how the tumor's location influences the gene expression profile and TCR sharing of tumor-infiltrating Treg cells.

For this, MC38 colon adenocarcinoma cells were subcutaneously transplanted into 10 mice after 7 days of cultivation. A schematic overview of this model can be found in **Figure 6**. Tumor growth was monitored by measuring tumor volume and is displayed for day 8, 12, 15 and 19 (**Figure 37A**). An increase in CD45⁺ immune cells in the TME was detected by flow cytometry analysis (**Figure 37B**). **Figure 37C** shows the Foxp3 expression on a representative MC38 tumor sample on day 15 after tumor cell injection, as well as the percentage of Foxp3⁺ cells within all CD3⁺ CD4⁺ cells over time. The frequency of Treg cells in the TME was overall higher compared to healthy tissue, with a slight decrease observed on day 15. The Treg population in healthy tissue remained relatively stable over time. **Figure 37D** presents the percentage of Klrp1⁺ PD-1⁺ cells within all Treg cells and a representative dotplot for an MC38 tumor sample on day 15. The frequency of Klrp1⁺ PD-1⁺ cells was highest in Treg cells isolated from the tumor, although the colon and skin tissues also showed high frequencies in comparison to the SLE. On day 12, a decrease in Klrp1⁺ PD-1⁺ cells isolated from skin was observed, which could be caused by a technical issue related to the extended digestion of skin tissue on this day.

Results

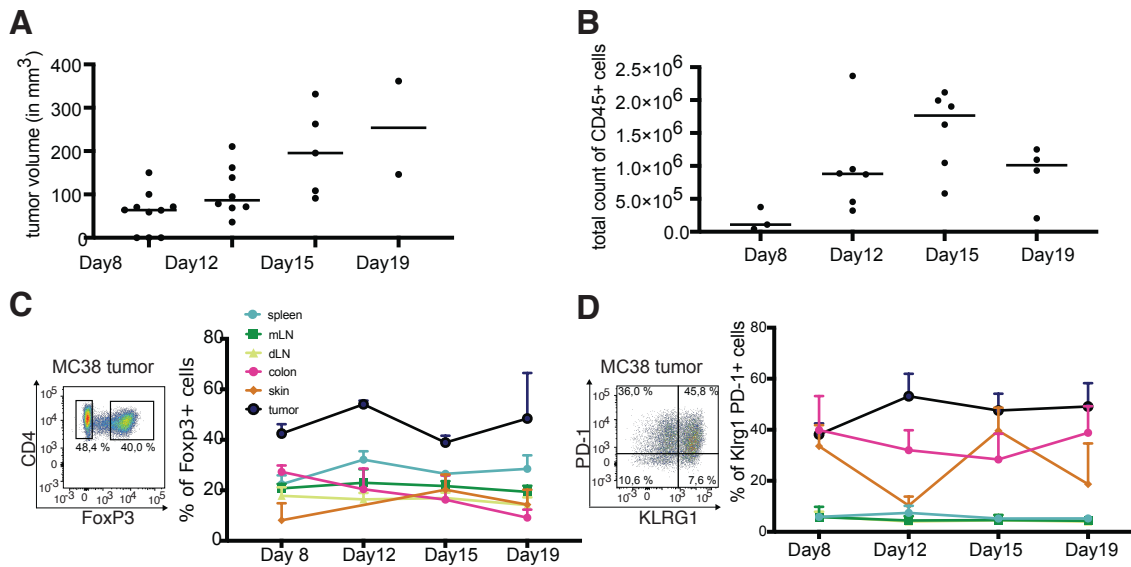


Figure 37: Flow analysis of different murine organs from MC38-bearing mice. A: tumor volume in mm³ on day 8, 12, 15 and 19. B: Total count of CD45⁺ and viable immune cells found in the TME on day 8, 12, 15 and 19. C: Dotplot (left) showing the expression of CD4 and Foxp3 in a representative tumor sample at day 15 and the frequency (right) of Foxp3⁺ cells on day 8, 12, 15 and 19 on the spleen, mLN, dLN, colon, skin and tumor tissue. D: Dotplot (left) showing the expression of PD-1 and Klrp1 in a representative tumor sample at day 15 and the frequency (right) of Klrp1⁺ PD-1⁺ cells on day 8, 12, 15 and 19 on the spleen, mLN, dLN, colon, skin and tumor tissue. A-B: n = 4-6 individual mice. Lines represent the median, and dots represent individual mice. C-D: n = 3 individual mice were analyzed on day 8, 12, 15 and 19 within the distinct organs.

4.17. Tumor-infiltrating Treg cells share more genes with colon Treg cells

We further investigated Treg cells isolated from the TME of MC38 tumor-bearing mice. Using flow cytometry data from different time-points (**Figure 37**) we identified a day with high infiltration of CD45⁺ immune cells in the TME. We selected day 15 after MC38 tumor cell injection and performed scRNA/TCR-seq on CD25⁺ cells from the spleen, mLN, iLN, and tumor-draining LN (dLN), as well as CD4⁺ cells from the colon, skin, and TME. As we are investigating tumor-infiltrated Treg cells from different tumor locations, including the skin and the distal colon, we were including the healthy colon and healthy skin in our tumor studies. This helps us to investigate transcriptomic and TCR similarities of tumor-infiltrating Treg cells to those found in healthy colon and skin.

Results

Figure 38 presents the t-SNE plot after clustering (A) and separate t-SNE plots for each tissue type (B). We performed three independent scRNA/TCR experiments on three individual wild-type mice, always at day 15 after the start of the experiment. Since we couldn't integrate all three datasets into a single t-SNE, only one representative mouse is shown in **Figure 38**. This limitation is likely due to strong batch effects, which would have masked the underlying biological signals. Additional batch correction proved too stringent, removing genuine tissue-specific biological effects. Hence, we decided for an individual analysis. However, the integration of only the NLT (skin, colon, tumor) from all three datasets was successful, preserving biological differences while removing technical noise caused by the different batches. A t-SNE projection, generated after successful batch correction, is presented in the **Supplementary Figures**

The MC38 tumor is a colon adenocarcinoma that was subcutaneously implanted and grows therefore subcutaneously. We aimed to investigate whether the Treg cells in the TME express more of the skin Treg, colon pTreg, or colon tTreg signature genes. The t-SNE and density plots for all three signatures from the steady state show a high expression of all three signatures in the tumor Treg cells (**Figure 38C-E**). Additionally, we plotted Treg cells from the TME to compare the merged colon signature with the skin signature. The colon pTreg and tTreg signatures were merged, as this model did not allow for clear differentiation between colon tTreg and pTreg cells due to lower number of cells isolated from the colon. This limitation is likely due to technical issues.

Figure 38F shows that, although the tumor is growing beneath the skin, the Treg cells in the TME predominantly exhibit a merged colon Treg signature, with 63% of all Treg cells in the TME behaving more like colon Treg cells. We further analyzed these cells to determine whether those with a stronger colon signature exhibit a phenotype more consistent with tTreg or pTreg cells (**Figure 38H**), showing 68% behaving more like colon tTreg cells.

Results

This analysis reveals that Treg cells in the TME of MC38 tumor-bearing mice predominantly exhibit a colon tTreg signature, despite the tumor's subcutaneous location.

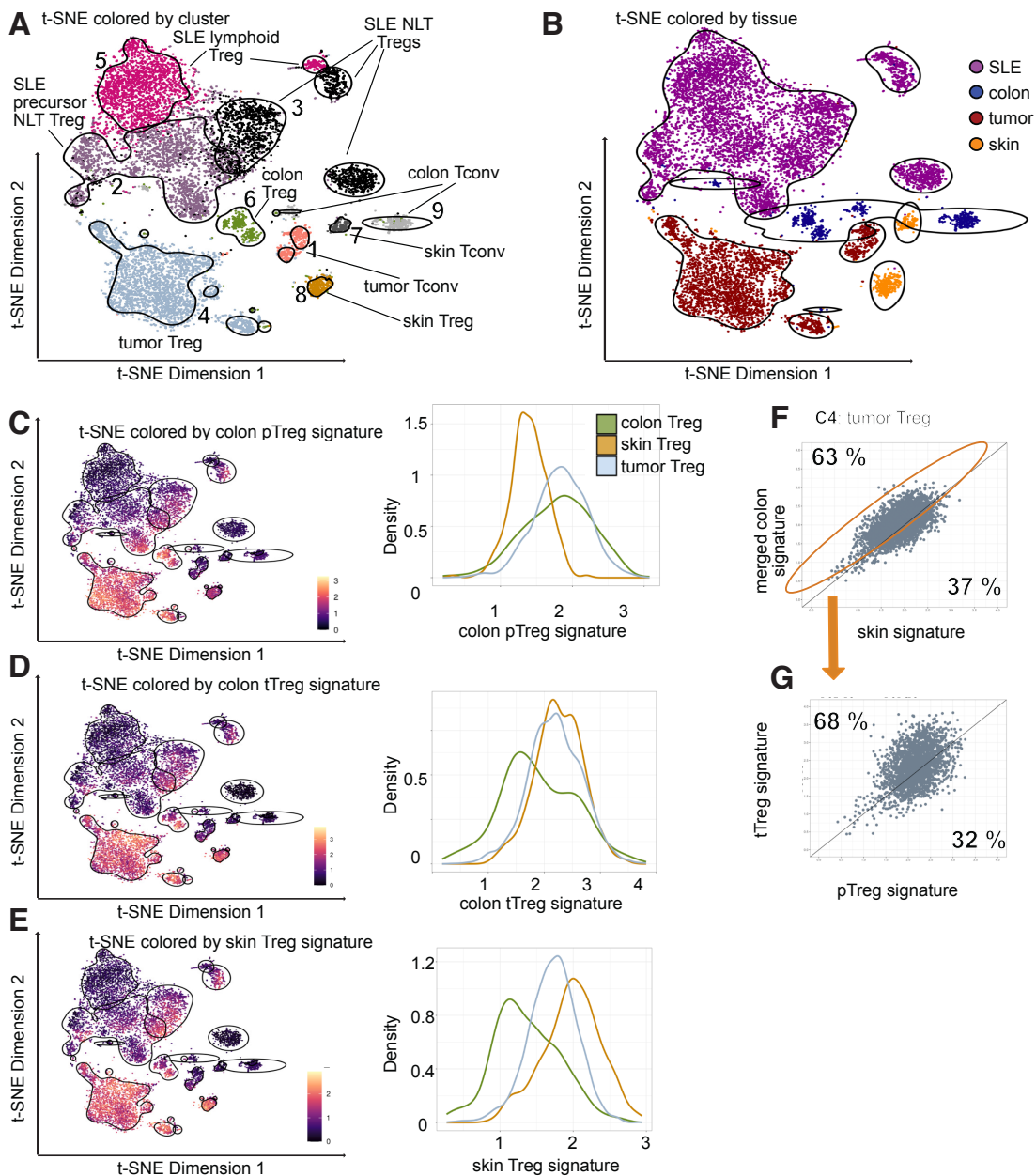


Figure 38: Tumor-infiltrating Treg cells share more genes with colon Treg cells. scRNA/TCR-seq was performed at day 15 after MC38 tumor cell injection. A-B: t-SNE plot colored by cluster (A) and tissue types (B). Confidence ellipses applied to the t-SNE plot displaying the 95% confidence level of the individual cluster (A) and tissue types (B). C: pTreg cell signature from healthy mice (**Figure 20**) is applied to this dataset and visualized by a t-SNE plot (left) and density plot (right). D: tTreg cell signature from healthy mice (**Figure 20**) is applied to this dataset and visualized by a t-SNE plot (left) and density plot (right). E: skin

Results

Treg cell signature from healthy mice (**Figure 20**) is applied to this dataset and visualized by a t-SNE plot (left) and density plot (right). Confidence ellipses applied to the t-SNE plot displaying the 95% confidence level of the individual cluster shown in (A). F- G: Tumor Treg cells (cluster 4) are compared with the merged colon and skin Treg cell signature (F), as well as colon tTreg cell and pTreg cell healthy signature (G). Percentage showing the frequency of cells in the area. n=1 individual mice.

Using the regenerative and suppressive signatures derived from healthy mice, we found that tumor Treg cells exhibit higher signature scores for both the regenerative and suppressive signatures compared to colon Treg cells (**Figure 39**). However, for the regenerative signature Treg cells isolated from the skin were the highest. Statistical analysis using the Wilcoxon test revealed a significantly higher expression of genes associated with these signatures in tumor Treg cells compared to colon Treg cells. This suggests that tumor Treg cells not only adopt suppressive functions but also acquire regenerative properties, potentially contributing to tumor progression and immune evasion.

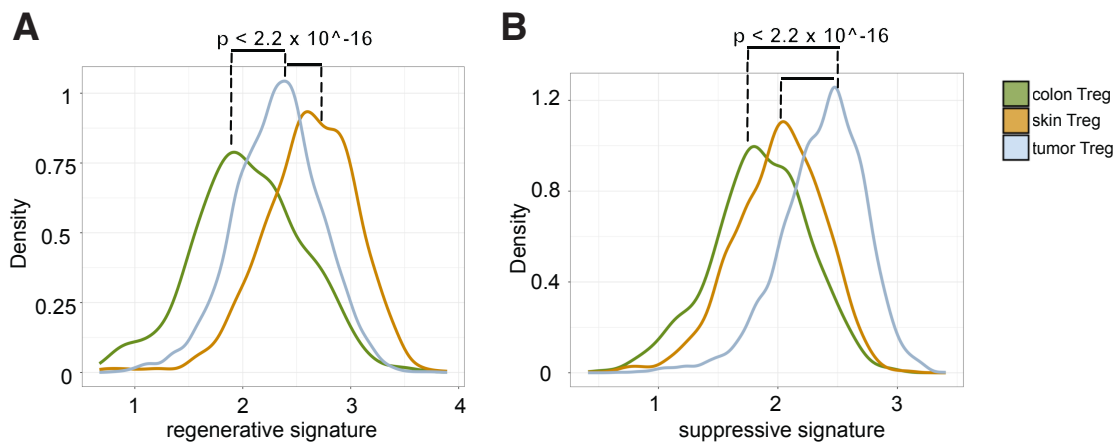


Figure 39: Tumor Treg cells not only adopt suppressive functions but also acquire regenerative properties. A+B: Regenerative (A) and suppressive (B) signature applied on tumor Treg cells from the MC38 tumor model and plotted by using density plots. n = 3 individual mice. p-value calculated using the Wilcoxon rank sum test.

Results

4.18. MC38 tumor Treg cells show enhanced roles in immune response and cytokine signaling

After determining that Treg cells from the TME exhibit a stronger colon Treg signature, we compared Treg cells from the TME, skin tissue and colon tissue based on their differentially expressed genes. In the comparison between tumor and colon Treg cells, we identified 352 upregulated and 2120 downregulated genes out of a total of 32285 genes (**Figure 40A**). The upregulated genes included for instance *Sell*, *Tbx21*, *Pparg*, *Klrc1*, *Tlr2*, *Cd14*, *Adora2b* and *Spp1*. When comparing skin and tumor Treg cells, the number of differentially expressed genes was even greater, with 741 upregulated and 715 downregulated genes (**Figure 40B**). The upregulated genes included, among others, *Lag3*, *Sell*, *Tbx21*, *Klrc1*, *Spp1*, *Pdcd1*, *Cxcr3*, *Pparg* and *Id1*.

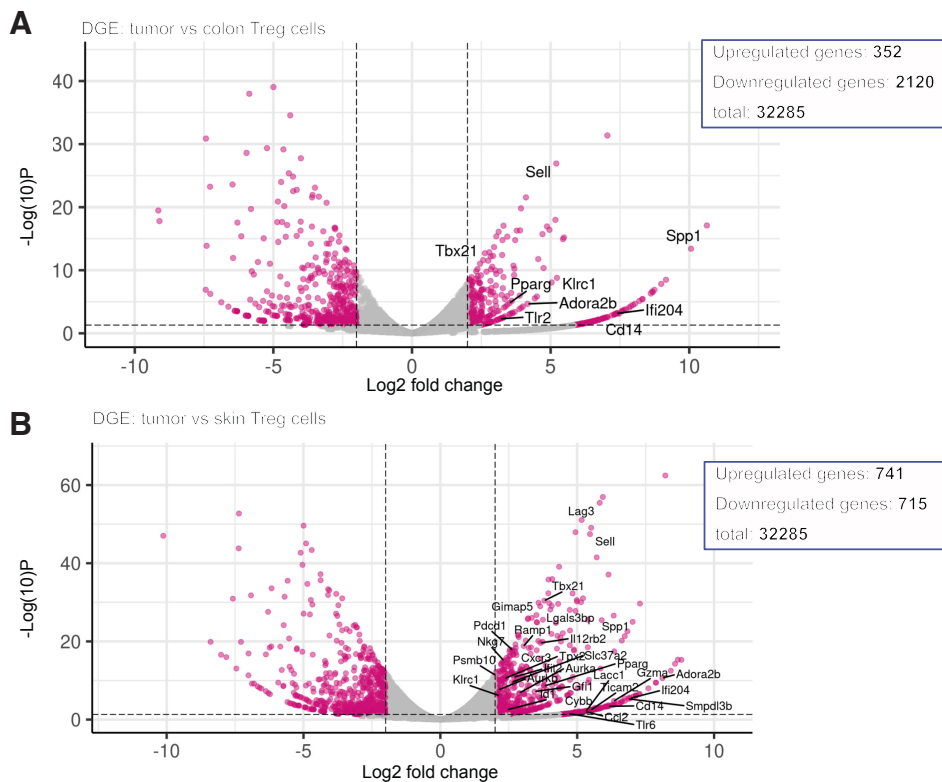


Figure 40: Tumor Treg cells from MC38 tumor model show gene expression differences to the healthy tissue. A- B: Volcano plot illustrating the differential expressed genes between tumor Treg and colon Treg cells (A) and tumor Treg and skin Treg cells (B). ns cells and cells with either a \log_2 FC > 2 or p-value < 0.05 are colored grey, while cells with \log_2 FC > 2 and p-value < 0.05 are shown in pink. n = 3 individual mice.

Results

We further investigated the pathways involved in these changes, focusing on those enriched in tumor Treg cells. To this end, we performed a functional enrichment analysis. Compared to colon Treg cells, the Treg cell population from the TME showed enrichment in pathways related to cytokine-mediated signaling, positive regulation and activation of innate immune response. Additionally, genes involved in the response to Interferon β (IFN- β) were enriched, including *Ifit1*, *Ifi204*, *Ifi213*, *Ifit3*, *Ifi211*, *Ifi214*, *Bast2* and *Igtb* (**Figure 41A**).

When comparing tumor Treg cells with skin Treg cells, pathways related to chromosome segregation, (defense) response to virus and symbiont, activation and regulation of innate immune response were enriched. Other enriched genes were included in pathways important for the cellular response to IFN- β (**Figure 41B**).

Results

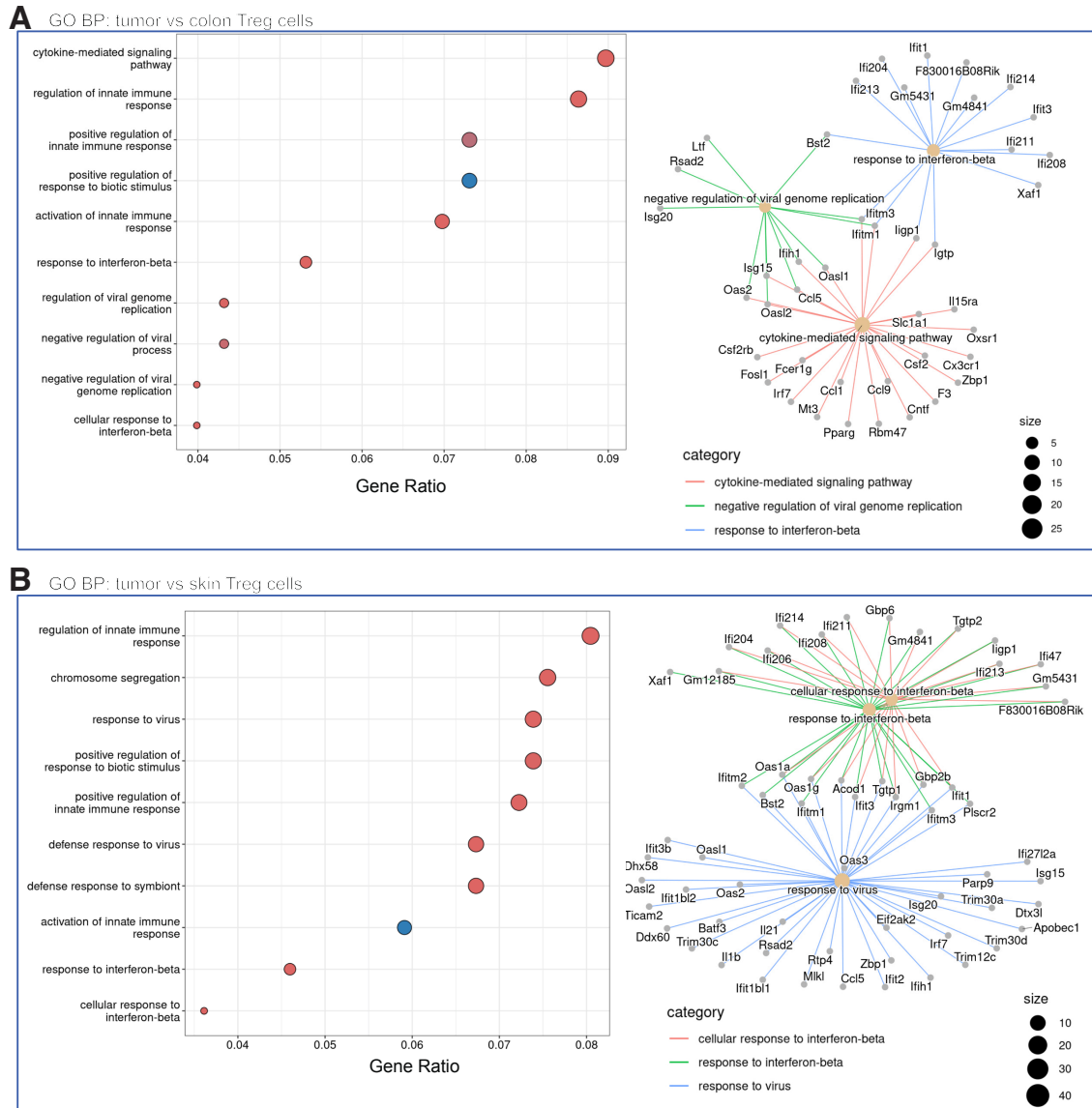


Figure 41: Tumor Treg cells in the TME undergo acquiring enhanced roles in immune response and cytokine signaling. A-B: Functional enrichment analysis showing the differences in the DGE of the comparison between MC38 tumor Treg and colon Treg cells (A) on a dotplot (right) and CNET plot (left) and MC38 tumor Treg and skin Treg cells (B). n = 3 individual mice.

Overall, less genes were upregulated, but the findings suggest that tumor-infiltrating Treg cells undergo functional reprogramming, acquiring enhanced roles in response to immune modulation, activation and differentiation and may contribute to the tumor's inflammatory environment, which either promotes or suppress tumor progression.

Results

4.19. MC38 tumor Treg cells show overlap in TCR usage with SLE and colon Treg cells

We further investigated the clonal expansion of tumor, colon, and skin Treg cells and found the highest clonal expansion in tumor Treg cells, with a frequency of 88%. The frequency of duplicated Treg TCR clonotypes in the skin and colon tissues was much lower, at 42% for colon Treg cells and 44% for skin Treg cells (**Figure 42A**).

We then examined the TCR usage of Treg cells from the TME. The duplicated clonotypes were observed, as plotted in **Figure 42B** on a t-SNE plot and displayed in a table shown in **Figure 42C**.

As observed in previous analyses of the healthy animals and animals analyzed after AOM/DSS treatment, the highest percentage of TCRs from lymphoid Treg cells (cluster 5) in the spleen (96%), iLN (97%), mLN (98%), and dLN (96%) was found within the respective tissues. TCRs from precursor NLT-like Treg cells (cluster 2) in the iLN and dLN showed a strong overlap with spleen-derived NLT-like Treg cells. Additionally, TCRs from NLT-like Treg cells (cluster 3) across all SLE samples were frequently found in tumor-associated Treg cells (cluster 4), with notable percentages: 31% for the iLN, 44% for the dLN, 43% for the mLN, and 39% for the spleen.

When looking at the colon tissue, 19% of duplicated TCRs from colon Treg cells (cluster 6) and 18% from colon Tconv cells (cluster 9) were also present in tumor-associated Treg cells. Furthermore, and 18% from tumor Tconv cells (cluster 1) were also present in Treg cells in the TME. Taking a closer look at the TCRs from Tumor-associated Treg cells, 84% shared their sequences within the same cluster, but only a small fraction was detected in other clusters. The highest overlap was with NLT-like Treg cells from the spleen (5%) and tumor Tconv cells (3%).

Interestingly, despite the tumor being located beneath the skin, only 2% of duplicated TCRs from skin Treg cells were detected in tumor-associated Treg cells. We then explored whether the duplicated TCRs from tumor Treg cells show a trend toward one of the other tissues in a 2D-PCA plot (**Figure 42D**).

Results

The PCA plot, colored by tissue types, shows duplicated tumor Treg TCRs shared with SLE Treg cells in purple, forming one "cluster". The skin (orange), colon (blue), and tumor (dark red) tissues are also distinct from each other. There was no clear trend for the duplicated tumor Treg TCRs toward any of the other tissues, although they appeared a bit closer to the TCRs shared with skin Treg cells.

This finding illustrates the limited overlap between shared TCR skin Treg cells between the tumor and skin Treg populations while highlighting the significant overlap between TCRs from SLE precursor and NLT-like Treg cells, as well as colon Treg and Tconv cells, with tumor-associated Treg cells. Interestingly, the PCA plot of duplicated TCRs from tumor-associated Treg cells reveals a small trend toward skin cell similarity.

Results

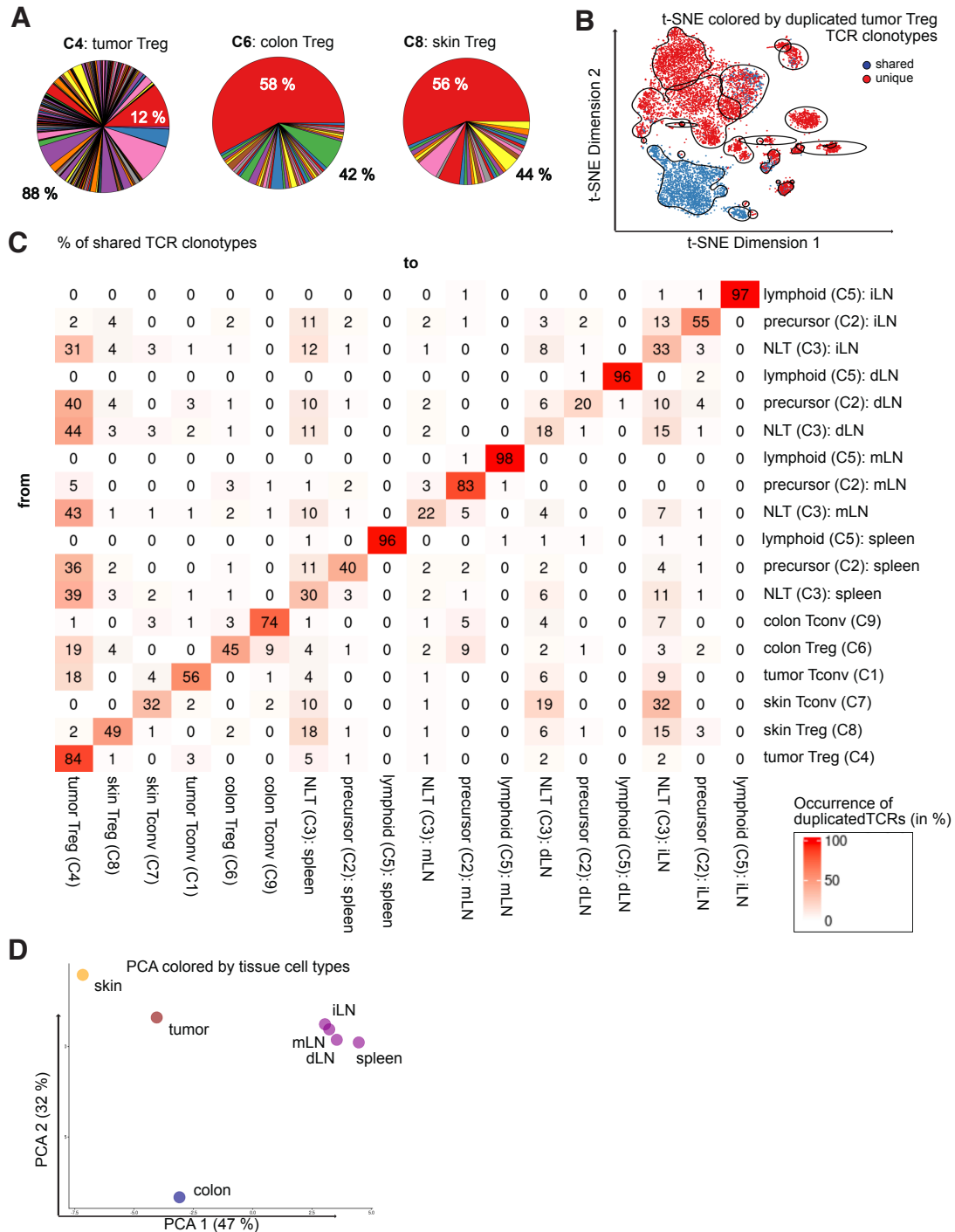


Figure 42: Tumor-infiltrating Treg cells show overlap in TCR usage with SLE and colon Treg cells. A-B: pie charts (A) showing the diversity of duplicated tumor Treg TCRs across different tissues and t-SNE plot (B) showing duplicated tumor Treg cell TCR clonotypes. Confidence ellipses applied to the t-SNE plot displaying the 95% confidence level of the individual cluster. C: shared TCRs among all other clusters illustrated in a table. D: 2D-PCA plot colored by tissue cell-type, highlighting the distances between duplicated TCRs of tumor Treg cells found in other tissues. n = 1.

Results

We afterwards focused on the pseudo-time of all cells detected in this dataset (**Figure 44A**). For the tumor Tconv cells, the pseudo-time was overall the lowest. In contrast, the other tissues showed higher pseudo-times, with the highest observed in shared TCRs found in the SLE lymphoid Treg cell cluster (cluster 5) and the SLE precursor NLT-like Treg cell cluster (cluster 2). When examining the pseudo-time of duplicated TCRs from tumor-associated Treg cells that are shared with cells from other tissues (**Figure 44B**), the pseudo-time for tumor Tconv cells remained the lowest. Tumor TCRs themselves exhibited a broader pseudo-time distribution, falling between the pseudo-times observed in duplicated TCRs within tumor Tconv cells (which had the lowest pseudo-time values) and SLE cells (which had the highest pseudo-time values).

This analysis revealed that duplicated tumor Treg TCRs are primarily confined to the tumor microenvironment but also demonstrate notable overlap with Treg cells and Tconv cells in other tissues, especially SLE-related lymphoid tissues. These findings suggest an intricate network of TCR sharing between tumor-associated and peripheral Treg populations, hinting at shared antigenic experiences or common differentiation pathways. The high degree of TCR clonotype sharing between tumor Treg cells and SLE, especially with the precursor NLT-like and NLT-like Treg populations, suggests a potential overlap in TCR usage that could provide insights into the similarities between these Treg cell subsets in different tissues.

Results

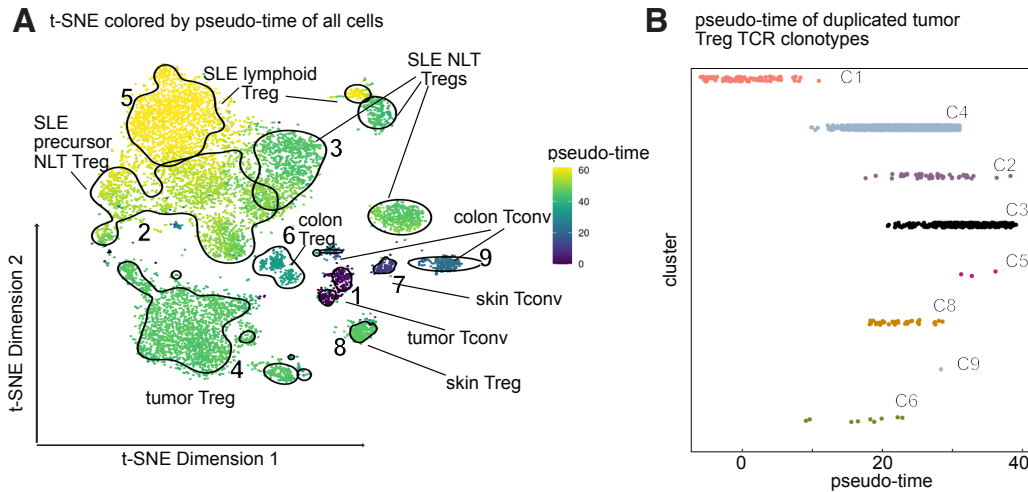


Figure 43: Tumor Tconv exhibit lowest pseudo-time values. A: pseudo-time of all cells in this dataset is displayed in a color-coded t-SNE plot, with purple indicating a low and yellow indicating a high pseudo-time. Confidence ellipses applied to the t-SNE plot displaying the 95% confidence level of the individual cluster B: Scatter plot showing the distribution of pseudo-time values from only tumor Treg TCRs which are duplicated and shared across different cell-types. n = 1.

4.20. scRNA analysis of CD45⁺ immune cells revealed strong immune cell interaction within the TME

To explore immune cell interactions in our MC38 tumor-bearing mice, we performed a scRNA/TCR-seq experiment on CD45⁺ immune cells from the TME, colon tissue, lung tissue, and secondary lymphoid organs (SLEs), including the spleen, mLN, iLN, and tumor-draining LN. CD45⁺ cells were isolated and enriched using CD45⁺ Microbeads from Miltenyi Biotec, followed by sorting based on viable CD45⁺ cells.

For the analysis we used the CellChat package to identify and visualize cell-cell communication pathways among CD45 positive immune cells. The CellChat package is designed to visualize and analyze intercellular communication from scRNA-seq data and therefore helps to identify cell-state-specific signaling dynamics. It helps to enable a deeper understanding of intercellular communication within complex tissues [152]. With this we were able to quantitatively analyze intracellular communication networks. The approach

Results

highlighted major signaling inputs and outputs for cells and how those cells and signals coordinate for functions. By displaying the strength of communications between different cell groups we aimed to provide insights into the functional roles of immune cells in the tumor as well as healthy non-lymphoid and lymphoid tissue. **Figure 44A** presents a t-SNE plot colored by the cell-types identified in this dataset, while **Figure 44B** shows these cell-types separated by tissue origin: SLEs (purple), healthy tissue (lung and colon, blue) and tumor tissue (dark red). We performed a cell interaction analysis to assess the interaction strength between cell-types across tissue types. In healthy (**Figure 44C**), tumor (**Figure 44D**), and SLE tissues (**Figure 44E**), Treg cells (cluster 7) exhibited significant interactions with other immune cell-types, but these interactions varied between the tissue types. In healthy tissue, the strongest interaction was observed between NK cells (cluster 5) and B cells (cluster 4). In contrast, tumor tissue showed a high level of receptor-ligand-interaction between Treg cells and myeloid cells (cluster 1), with no interaction observed between Treg cells and plasma cells (cluster 6). For SLE tissue, Treg cells displayed the strongest interactions with CD8⁺ T cells (cluster 3) and B cells.

We further analyzed three key signaling networks in each tissue type, as illustrated in **Figure 44C-E** (upper plots). In healthy tissue and tumor tissue the TGF β , IL-10, and CCL signaling networks were evaluated. In SLE tissue no IL-10 signaling was detected, but a dominant Inducible T Cell Co-stimulator (ICOS) signaling network was observed.

Quantifying interactions in the TGF- β signaling network revealed consistent connections between Treg cells (cluster 7) and myeloid cells (cluster 1) across all three tissue types. In tumor tissue, additional interactions were observed between Treg cells and B cells (cluster 4) as well as Tconv cells (cluster 2). In SLE tissue, interactions were prominent between Treg cells and Tconv cells (cluster 2). Both tumor and SLE tissues exhibited a higher quantity of interactions in the TGF β signaling network compared to healthy tissue.

Results

The IL-10 signaling network in healthy tissue was limited to interactions between Treg cells and myeloid cells, B cells, and NK cells. No other cell-types were involved in this pathway. Conversely, tumor tissue showed IL-10 signaling among almost all cell-types except plasma cells, with Treg cells interacting broadly.

The CCL signaling network was strongest in tumor tissue, where Treg cells interacted with all cell-types except plasma cells. In healthy tissue, this network was limited to interactions between myeloid cells and NK cells. Similarly, in SLE tissue, the CCL signaling network predominantly involved myeloid cells and NK cells, with minor interactions observed between CD8⁺ T cells and Treg cells. For the SLE tissue, the ICOS signaling network is also visualized, revealing strong interactions between Treg cells and B cells. Additionally, B cells showed interactions with all other clusters except myeloid cells and NK cells.

This analysis highlights tissue-specific variations in immune cell interactions and signaling networks. Tumor tissue exhibited broader and more robust interactions, particularly involving Treg cells, compared to healthy and SLE tissues. Notably, the absence of IL-10 signaling in SLE tissue and the dominance of ICOS signaling underscore unique immunological features in this context. These findings provide valuable insights into how Treg cells engage with the immune environment across different tissue types.

Results

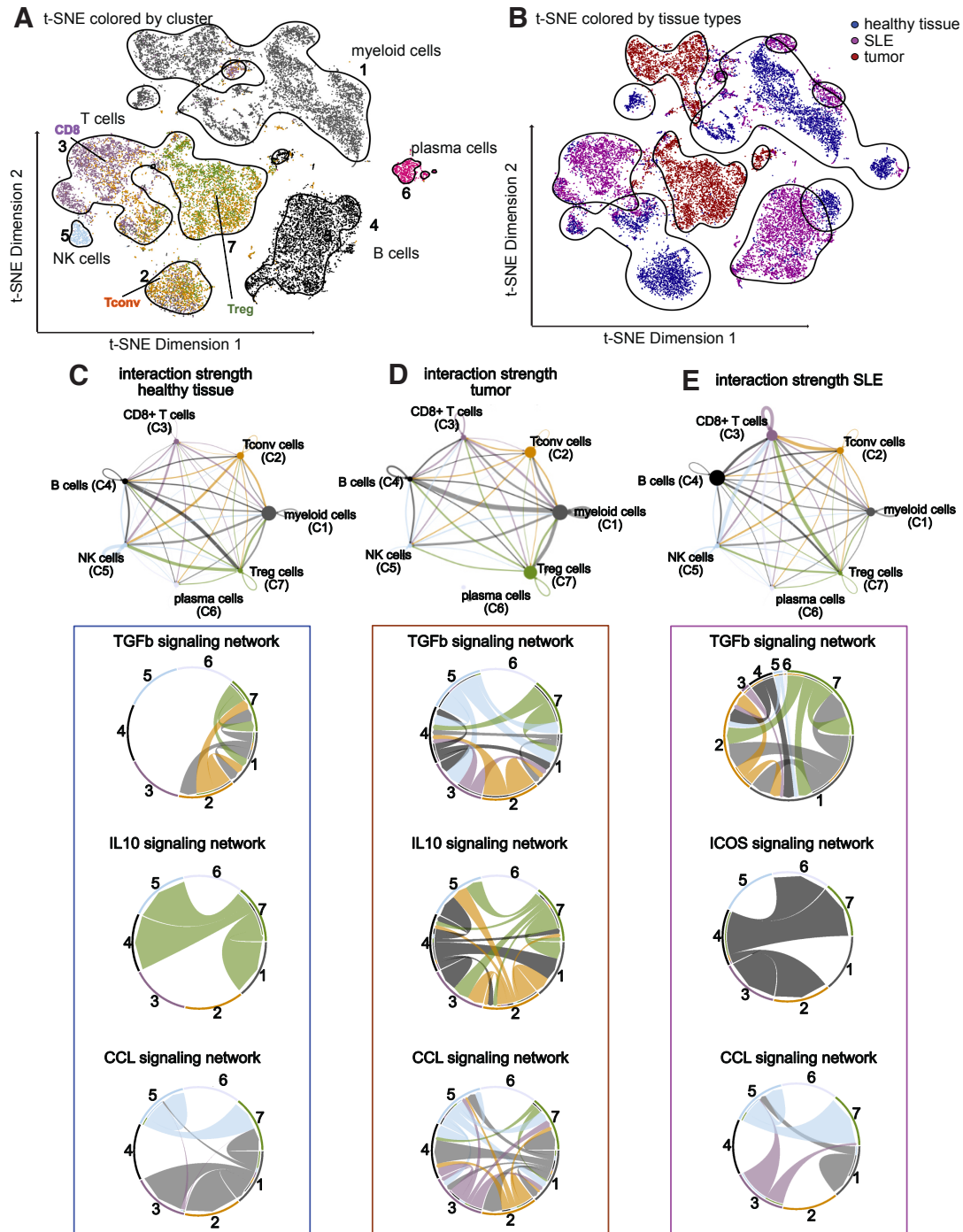


Figure 44: scRNA-seq of CD45⁺ immune cells revealed strong immune cell interaction within the TME. Analysis of CD45⁺ immune cells was performed at day 15 after tumor induction from a MC38 tumor-bearing mouse. A-B: t-SNE plot colored by cluster (A) and tissue types (B). Confidence ellipses applied to the t-SNE plot displaying the 95% confidence level of the individual cell types (A) and tissue types (B). C-E: Circle plot illustrating the interaction strength of the different cluster in healthy tissue (C), tumor tissue (D) and SLE (E) and showing the interaction of different signaling networks in the representative tissue. n = 2 individual mice.

4.21. Treg cell infiltration in a B16-F10 melanoma skin model

Having previously studied Treg cells in the TME of AOM/DSS-induced CRC and in the TME of MC38 adenocarcinoma growing beneath the skin, we now aimed to focus on a skin-specific tumor model. For this purpose, we selected the B16-F10 skin melanoma model, in which B16-F10 cells are subcutaneously implanted. Our aim was to identify the gene expression signature and TCR clonal expansion of Treg cells within the TME when a skin cancer cell line is implanted at its site of origin. Additionally, we aimed to highlight changes in gene expression and TCR clonal sharing by comparing this model to MC38-implanted tumor cells.

To achieve this, we first needed to determine the optimal time point for scRNA/TCR-seq analysis, as this tumor model is characterized by low immune cell infiltration and is therefore referred to as a "cold" tumor model [153].

Figure 45A illustrates the tumor volume recorded on the analysis days during the flow kinetics study. On these days, we also analyzed the total count of CD45⁺ immune cells within the TME (**Figure 45B**). Over the time, we observed an increase in both tumor volume and immune cell infiltration. Although tumor-bearing mice appeared to have lower tumor volumes on day 15, this was primarily due to a significant tumor volume increase that reached the pre-defined ethical endpoints. **Figure 45C** shows a representative flow cytometry plot of Foxp3 expression in CD4⁺ T cells from the TME, along with the kinetics of this expression across the four analysis days. We observed consistently stable Foxp3 expression within CD4⁺ T cells, with a slight decrease on day 13. Additionally, we examined Klrp1⁺ PD-1⁺ cells among all Treg cells and noted a gradual increase in this population in cells isolated from the colon, TME, and skin tissue over time (**Figure 45D**).

Results

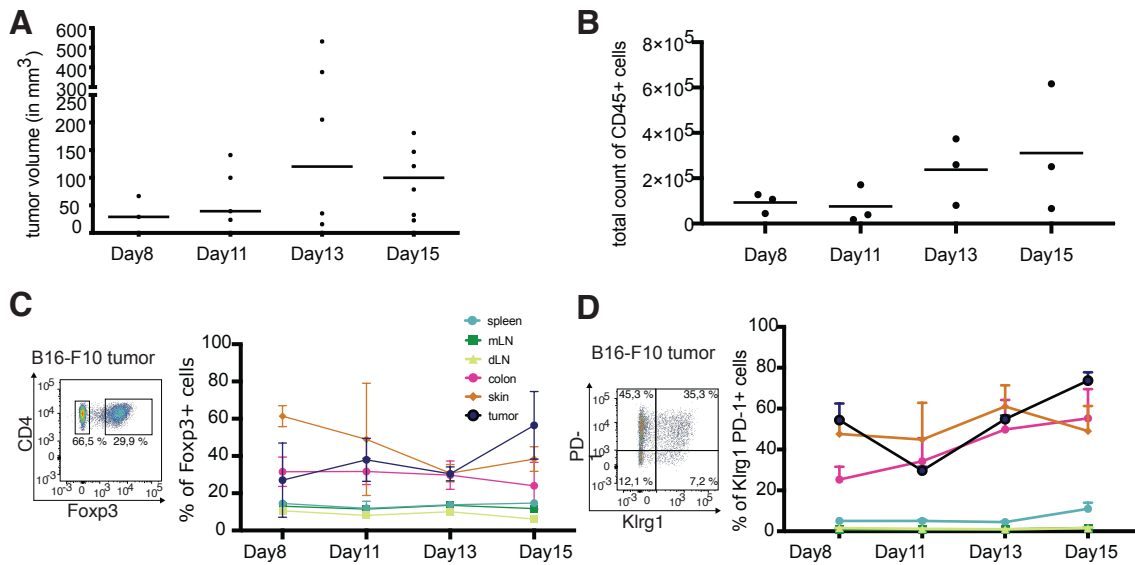


Figure 45: FACS analysis B16-F10 tumor-bearing mice over the time. A: tumor volume in mm³ on day 8, 11, 13 and 15. B: Total count of CD45⁺ and viable immune cells found in the TME on day 8, 11, 13 and 15. C: Dotplot (left) showing the expression of CD4 and Foxp3 in a representative tumor sample at day 15 and the frequency (right) of Foxp3⁺ cells on day 8, 12, 15 and 19 on the spleen, mLN, dLN, colon, skin and tumor tissue. D: Dotplot (left) showing the expression of PD-1 and Klrp1 in a representative tumor sample at day 15 and the frequency (right) of Klrp1⁺ PD-1⁺ cells on day 8, 12, 15 and 19 on the spleen, mLN, dLN, colon, skin and tumor tissue. A-B: n = 4-6 individual mice. Lines represent the median, and dots represent individual mice. C-D: n = 3 individual mice were analyzed on day 8, 11, 13 and 15 within the distinct organs.

4.22. B16-F10 tumor Treg cells show co-expression of skin- and colon-specific genes

After performing the FACS analysis on 4 different days, we identified day 13 as an optimal time point due to the observed increase in tumor volume and immune cell infiltration. On this day, the percentage of Foxp3⁺ cells within CD4⁺ T cells and Klrp1⁺ PD-1⁺ Treg cells increased in the TME, skin, and colon. As the B16-F10 model has low immunogenicity, it is particularly important to select a time point with high immune infiltration. Additionally, we aimed to investigate the origin of the increase in the NLT Treg population in the tumor, considering potential recruitment or local induction of conversion from Tconv.

We performed three independent scRNA/TCR experiments on three individual wild-type mice, always at day 13 after the start of the experiment. Since we couldn't

Results

integrate all three datasets into a single t-SNE, only one representative mouse is shown in **Figure 46**. However, the integration of only the NLT (skin, colon, tumor) from all three datasets was successful, preserving biological differences while removing technical noise caused by the different batches.

For scRNA/TCR-seq, immune cells were isolated from the spleen, mLN, iLN (SLE), skin, colon, and TME. Cells from the SLE were enriched for CD25⁺ cells, while non-lymphoid tissues were enriched for CD4⁺ cells. Sorting was performed to ensure purity and viability. Consistent with the low immune infiltration characteristic of the B16-F10 skin melanoma model, we obtained fewer immune cells from the TME compared to other tumor models. However, we successfully isolated and characterized a Treg cell population from the TME. A t-SNE projection, generated after successful batch correction, is presented in the **Supplementary Figures**. **Figure 46A** presents a t-SNE plot colored by clusters, where manual cell-type annotation was performed. **Figure 46B** is showing a t-SNE plot colored by tissue types, highlighting distinct separation of T cells isolated from the SLE, colon, skin, and TME cells. Tissue-specific signatures from our scRNA-seq analysis of healthy mice were visualized using t-SNE and density plots, including data from three individually analyzed mice (**Figure 46C-E**).

In this melanoma model, skin Treg cells displayed the highest expression of colon pTreg, colon tTreg, and skin-specific signature genes. Treg cells from the TME exhibited two distinct populations in the density plots for tissue-specific signatures, suggesting heterogeneity among tumor Treg cells, although marker gene analysis during clustering did not distinguish these populations. Further analysis of tumor Treg cells revealed that their gene expression aligned with both skin and colon signatures: 51% resembled the skin signature, and 49% aligned with the colon signature (**Figure 46F**). Among the 49% of cells expressing more colon Treg genes, 66% displayed a tTreg phenotype (**Figure 46G**).

The gene expression analysis of tissue-specific signatures of the B16-F10 melanoma model demonstrated unique immune characteristics, with Treg cells in the TME exhibiting mixed tissue-specific signatures. This duality, particularly the co-

Results

expression of skin- and colon-specific genes, highlights the complex nature of Treg cell populations in TME.

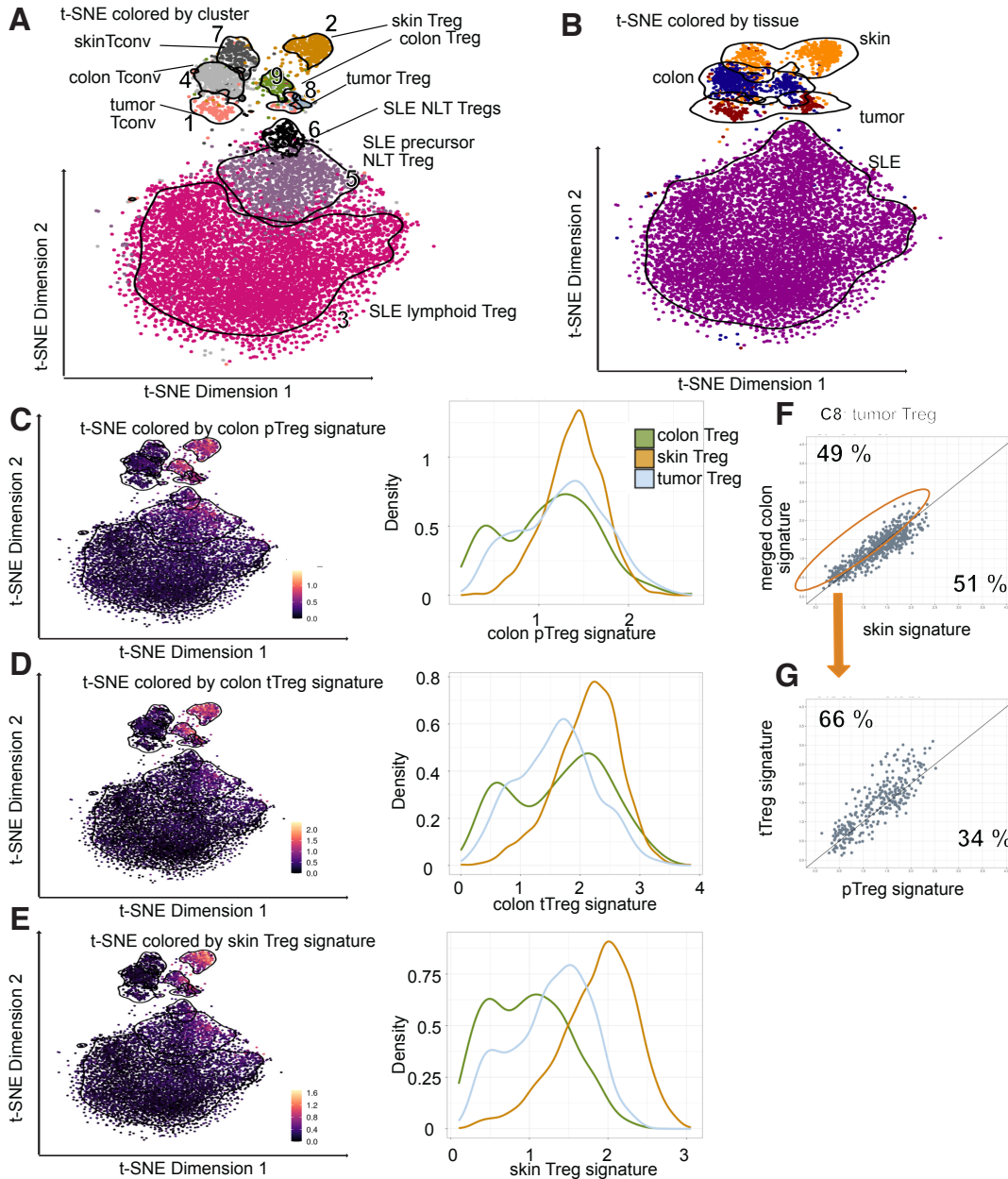


Figure 46: B16-F10 tumor-infiltrating Treg cells show co-expression of skin- and colon-specific genes. scRNA/TCR-seq were performed at day 15 after B16-F10 tumor cell injection. A-B: t-SNE of T cells from different murine tissue colored by cluster (A) and tissue (B). Confidence ellipses applied to the t-SNE plot displaying the 95% confidence level of the individual cluster (A) and tissue ty (B). C: pTreg cell signature from healthy mice (**Figure 20**) is applied to this dataset and visualized by a t-SNE plot (left) and density plot (right). D: tTreg cell signature from healthy mice (**Figure 20**) is applied to this dataset and visualized by a t-SNE plot (left) and density plot (right). E: skin Treg cell signature from healthy mice (**Figure 20**) is applied to this dataset and visualized by a t-SNE plot (left) and density plot (right).

Results

Confidence ellipses applied to the t-SNE plot displaying the 95% confidence level of the individual cluster displayed in (A). F-G: Tumor Treg cells (cluster 4) are compared with the merged colon and skin Treg cell signature (F), as well as colon tTreg cell and pTreg cell healthy signature (G). Percentage showing the frequency of cells in the area. n=1.

Using the regenerative and suppressive signatures derived from healthy mice, we found that Treg cells from the healthy skin exhibit higher signature scores for both the regenerative and suppressive signatures compared to colon and tumor Treg cells (**Figure 47**). However, the Treg cells isolated from the colon seemed to express both signatures in a very low level. For the tumor Treg cells we again detected two populations, where one showed stronger expression of these signatures. Statistical analysis using the Wilcoxon test revealed a significantly higher expression of genes associated with these signatures in skin Treg cells compared to tumor Treg cells.

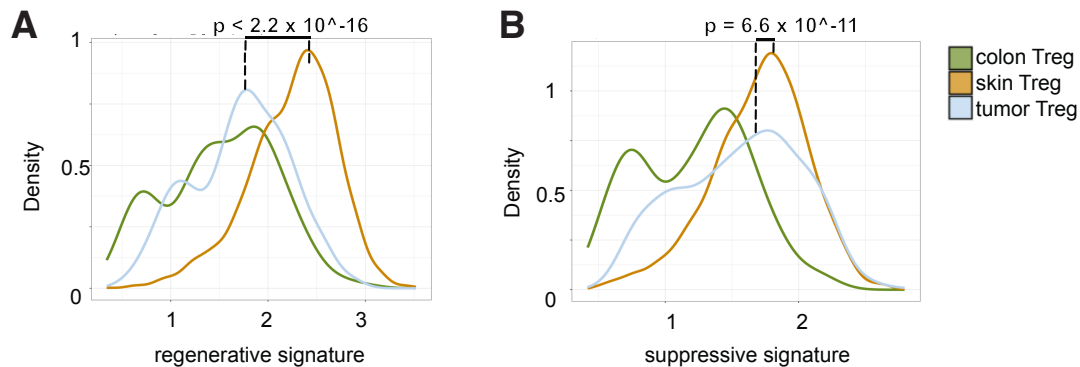


Figure 47: B16-F10 tumor-infiltrating Treg cells show lower expression of the regenerative and suppressive signature compared to skin Treg cells. Signatures are applied on tumor Treg cells from the B16-F10 tumor model and plotted by using density plots. n = 3 individual mice. p-value calculated by using the Wilcoxon rank sum test.

4.23. B16-F10 tumor Treg cells express genes involved in response to biotic stimuli and innate immune response

As previously described, Treg cells isolated from the B16-F10 tumors express more skin signature genes. We then performed a DGE analysis between B16-F10 tumor and colon Treg cells (**Figure 48A**), as well as skin and tumor Treg cells (**Figure 48B**). The analysis of differentially expressed genes between colon Treg cells and tumor

Results

Treg cells revealed 375 upregulated genes and 355 downregulated genes out of a total of 32285 genes. The upregulated genes included, among others, *Lag3*, *Id1*, *Spp1*, *Tlr2*, *Tpx2*, *Pparg*, *Ifi204*, *Aurka*, *Aurkb* and *Smpdl3b*. The comparison between skin Treg cells and tumor Treg cells showed slightly more upregulated and downregulated genes, with 699 upregulated and 535 downregulated genes. The upregulated features included genes such as *Pdcd1*, *Lag3*, *Sell*, *Tbx21*, *Cxcr3*, *Spp1*, *Gzma*, *Ccl2*, *Tlr6* and *Il12rb2*.

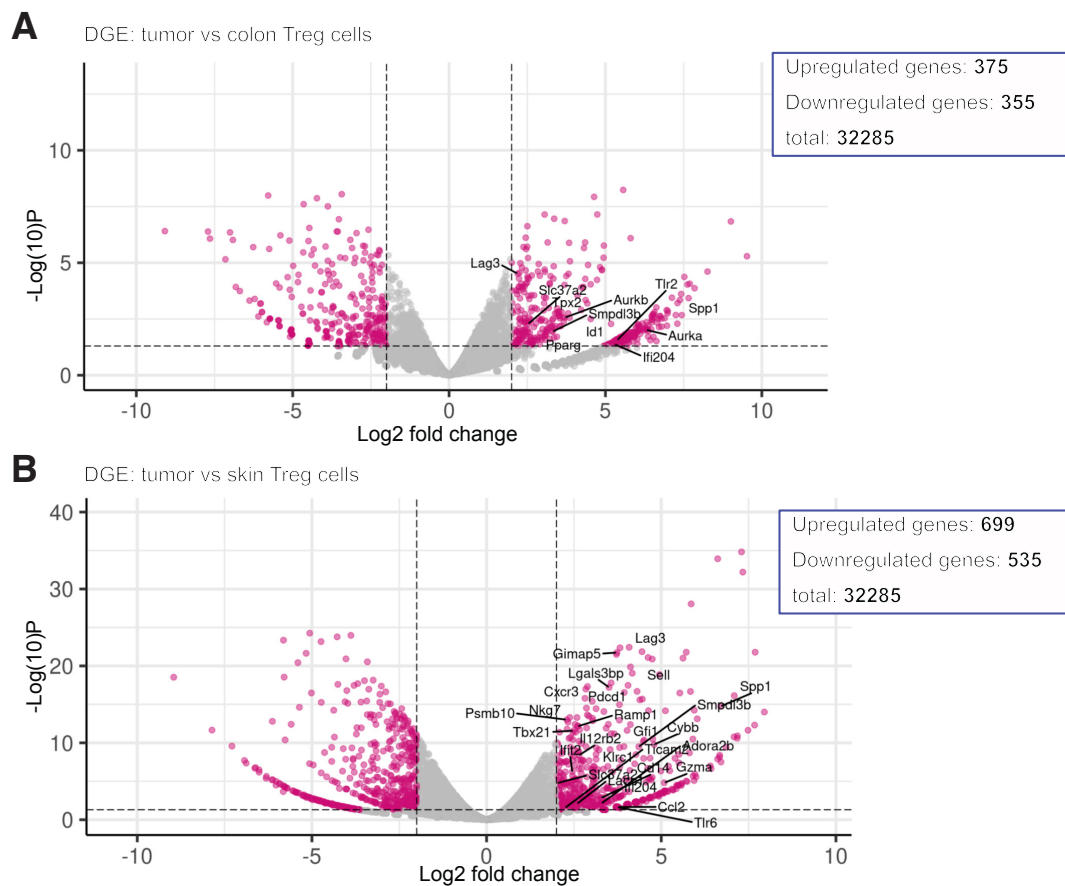


Figure 48: Tumor Treg cells from B16-F10 tumor model show gene expression differences to the healthy tissue. A-B: Volcano plot illustrating the differential expressed genes between tumor Treg and colon Treg cells (A) and tumor Treg and skin Treg cells (B). Non-significant (ns) genes and genes which were either $\log_2FC > 2$ or $p\text{-value} < 0.05$ are colored grey, while genes with both, $\log_2FC > 2$ and $p\text{-value} < 0.05$ are shown in pink. $n = 3$ individual mice.

We further analyzed the pathways associated with these upregulated genes. In the comparison between colon and tumor Treg cells, pathways related to nuclear

Results

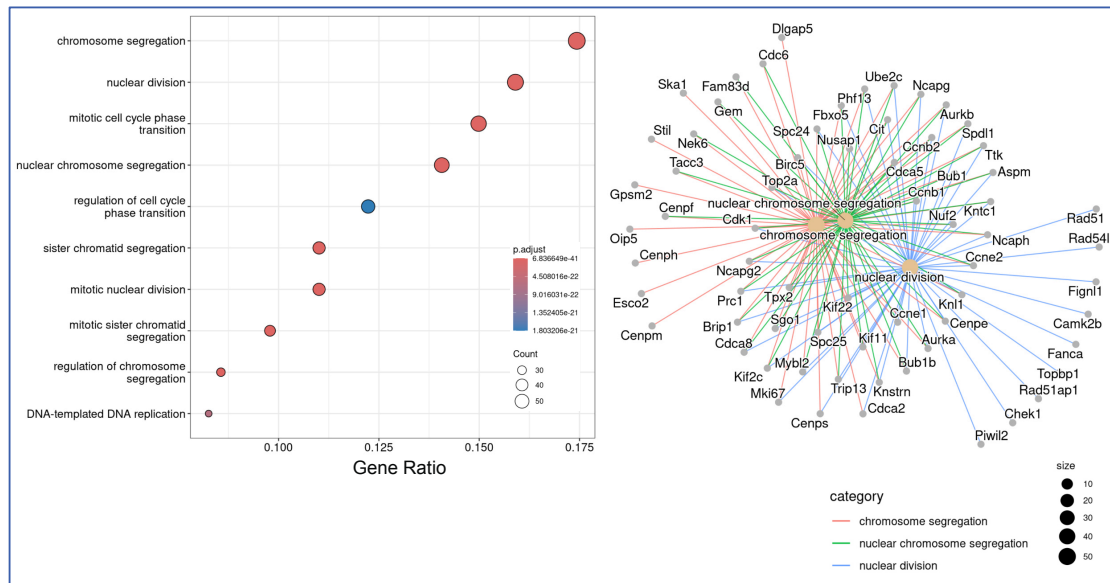
division and mitotic processes as well as regulation of cell cycle phase transition. Additionally, the regulation of nuclear chromosome segregation emerged as one of the top regulated pathways. The CNET plot (**Figure 49A**, right panel) highlights the genes involved in the top three upregulated pathways.

The functional enrichment results of skin vs tumor Treg cells revealed upregulation of pathways including regulation of innate immune response, response to biotic stimuli and the response to Type II interferon as well as IFN- β , including genes illustrated in the CNET plot (**Figure 49B**, right panel).

In summary, the differential gene expression analysis between Treg cells from colon and tumor tissue, as well as between skin and tumor tissue, highlights the critical involvement of pathways regulating innate immune response, cell cycle phases and IFN- β response, which is known to directly promote Treg cell induction [154].

Results

A GO BP: tumor vs colon Treg cells



B GO BP: tumor vs skin Treg cells

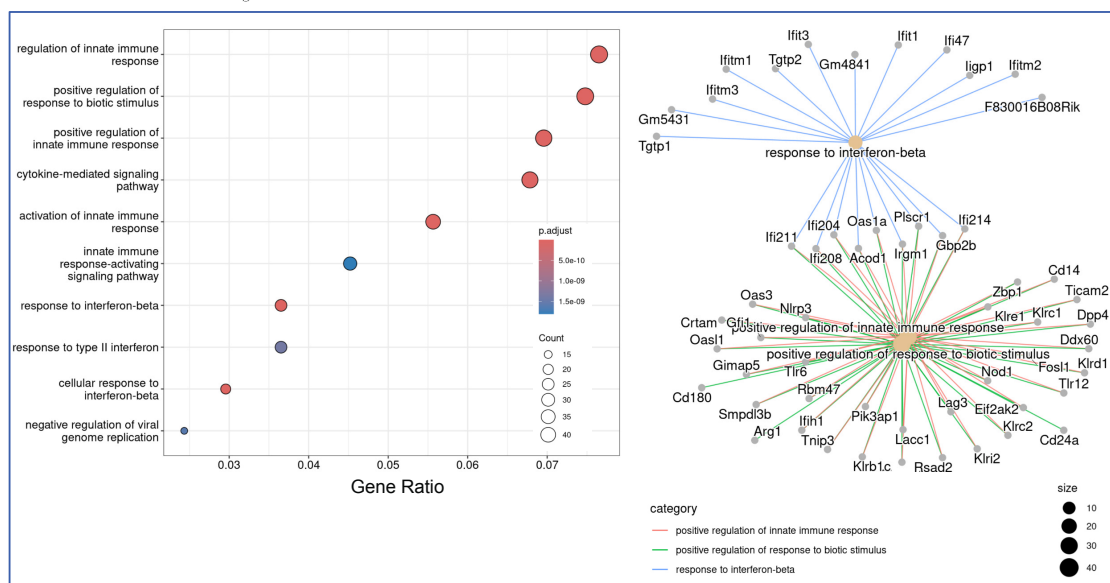


Figure 49: Tumor Treg cells in the TME undergo acquiring enhanced roles in response to biotic stimuli and innate immune response. A-B: Functional enrichment analysis showing the differences in the DGE of the comparison between B16-F10 tumor Treg and colon Treg cells (A) on an enrichment map (left) and CNET plot (right) and B16-F10 tumor Treg and skin Treg cells (B). $n = 3$ individual mice.

4.24. TCR repertoire in tumor-associated Treg cells show limited tissue overlaps

After analyzing the gene expression characteristics of skin melanoma Treg cells, we proceeded to examine the TCR repertoire. We found that the majority of TCRs are

Results

duplicated in Treg cells isolated from the TME, with a frequency of 61% (**Figure 50A**). While specific clones are enriched, it is important to note that fewer immune cells are detected in the TME overall. Shared clonotypes were plotted using t-SNE (**Figure 50B**). **Figure 50C** reveals the overlap of duplicated TCR clonotypes from tumor-associated Treg cells (cluster 8) with skin Treg cells (cluster 2) at a frequency of 19% of all detected duplicated tumor Treg TCRs and with tumor-associated Tconv cells (cluster 1) at a frequency of 6%. Conversely, only 1% of duplicated TCRs from skin Treg cells were detected within the tumor Treg cell compartment. Additionally, 4% of tumor Treg TCRs were found in iLN NLT-like Treg cells (cluster 6). Notably, 64% of duplicated TCRs from the tumor tissue were detected within the tumor tissue itself. A small percentage of precursor and NLT-like Treg cells from SLE (iLN, mLN, and spleen) were found to share clonotypes with tumor-associated Treg cells. The highest overlap was observed with TCRs from NLT-like Treg cells in the iLN, where 8% were detected in tumor-associated Treg cells.

When comparing the distances between the gene expression of duplicated tumor Treg TCRs across different tissues and plotted in the PCA (**Figure 50D**), a clear separation between spleen, iLN, mLN, and non-lymphoid tissues (skin, colon) was detected. Tumor cells appear to cluster closer to colon and skin cells, though no tissue shows a clear preferential association.

The data presented in **Figure 50C** highlights a distinct sharing pattern of TCR clonotypes between tumor-associated Treg cells and other tissue-derived Treg populations. A significant proportion (64%) of duplicated tumor TCRs were restricted to the tumor tissue itself, emphasizing a compartmentalized TCR distribution. The highest overlap was observed with skin Treg cells. These findings suggest a primarily tumor-specific TCR repertoire, with limited but noteworthy connections to Treg populations from surrounding tissues and the iLN. Moreover, duplicated TCRs from tumor-associated Treg cells showing closer proximity to the NLT Treg cells.

Results

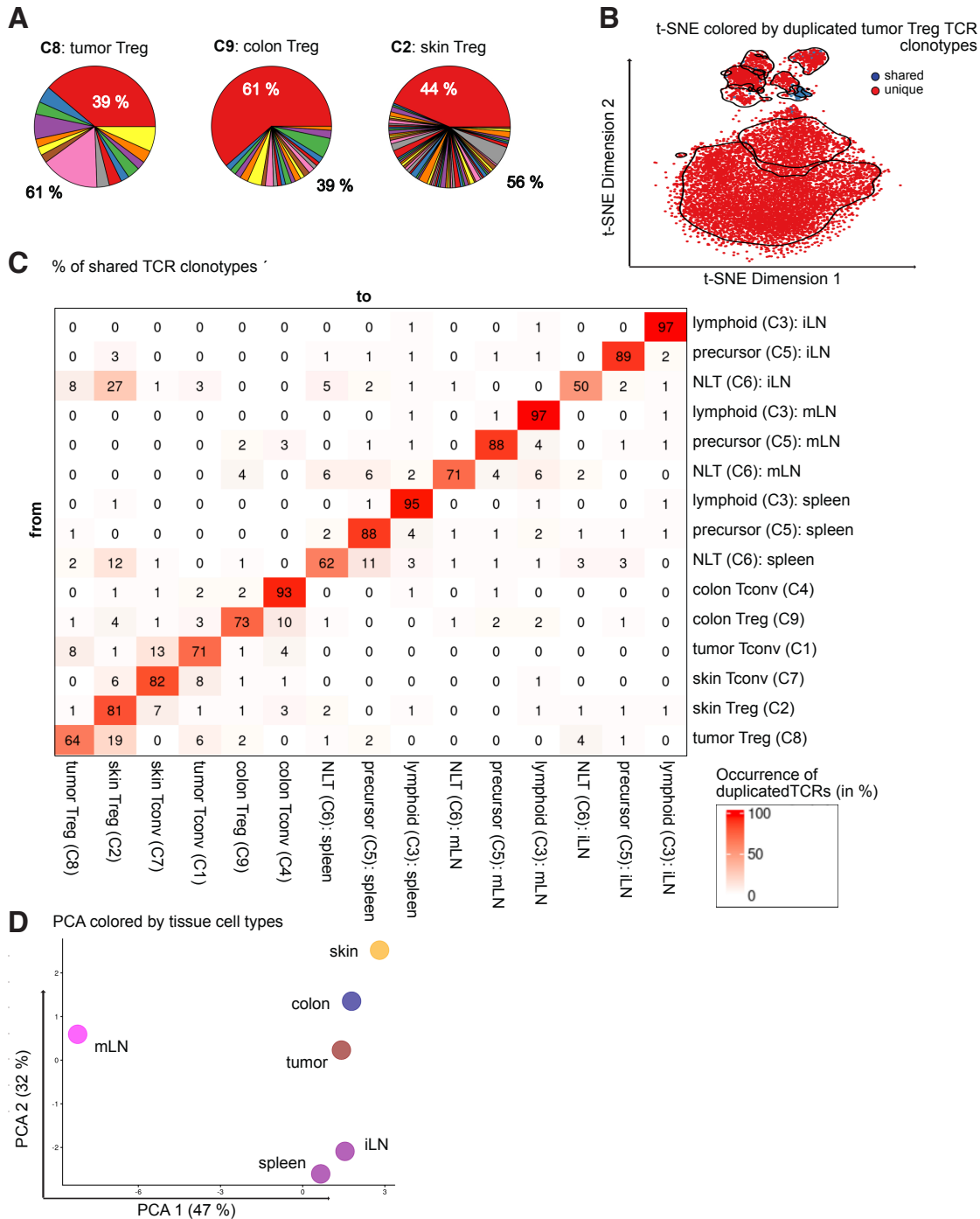


Figure 50: TCRs from tumor-associated Treg cells show limited overlaps with healthy tissue. The TCR repertoire of B16-F10 tumor, colon, and skin Treg cells. A: pie charts showing the diversity of duplicated tumor, colon and skin Treg TCRs. B: t-SNE plot showing duplicated tumor Treg cell TCR clonotypes. C: shared TCRs among all other clusters illustrated in a table. D: 2D-PCA plot colored by tissue cell-type, highlighting the distances between duplicated TCRs of tumor Treg cells found in other tissues. n = 1.

Results

Due to the low number of Treg cells from the B16-F10 tumor tissue, we could not perform pseudo-time analysis exclusively on duplicated TCRs from tumor Treg cells. Instead, the analysis was conducted on the entire dataset. The highest pseudo-time was observed within the SLE population (**Figure 51A - B**), as indicated by the trajectory line originating from the lymphoid population and extending through precursor and NLT-like Treg cells.

The trajectory line continues through the tumor Treg cells, which exhibited relatively high pseudo-time compared to all other cells derived from non-lymphoid tissues. From there, it proceeds to the tumor Tconv cells, moves to colon Tconv cells via colon Treg cells, and terminates at skin Treg cells, which had the lowest pseudo-time overall. Additionally, a separate trajectory is observed from tumor Tconv cells to colon Tconv cells.

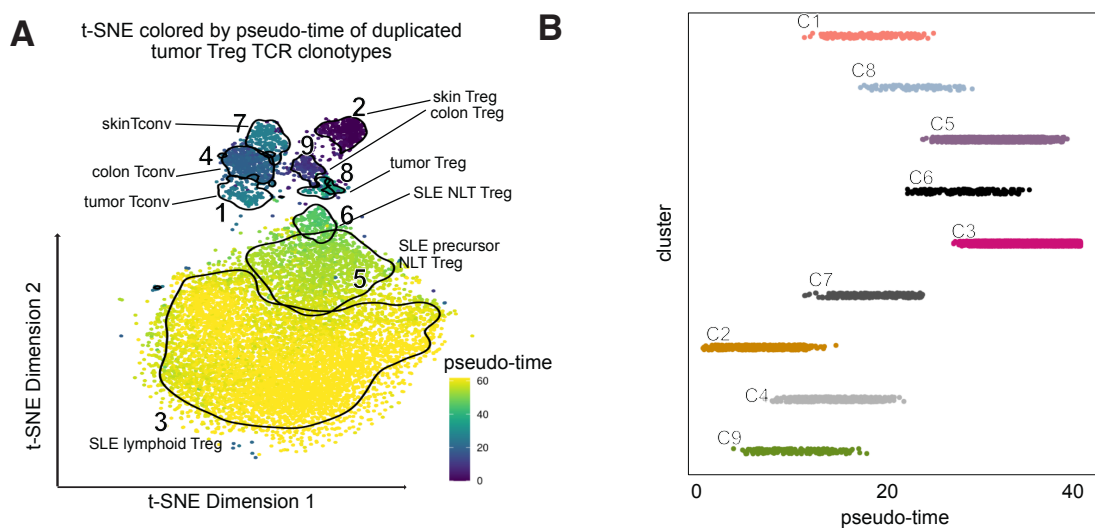


Figure 51: Pseudo-time analysis of scRNA data from different organs of healthy mice. A: pseudo-time is displayed in a color-coded t-SNE plot, with purple indicating a low and yellow indicating a high pseudo-time. B: Scatter plot showing the distribution of pseudo-time values across the different cluster. n = 1.

4.25. Tumor-specific Treg marker genes as potential targets for immunotherapy

Finally, we aimed to compare the differential gene expression (DGE) analysis across different tumor models: AOM/DSS, MC38, and B16-F10. To do this, we selected

Results

DEGs with a logFC > 2 and a p-value < 0.05 from each dataset and examined the intersecting genes. The overlap between the upregulated tumor Treg genes in AOM/DSS was relatively small, with only 5 genes (**Figure 52A**), including *Rsad2*, *Ifit3b*, *Kif22*, *Gzmk* and *Plek*. This was due to the low number of DEGs in the AOM/DSS colon tumor Treg cells compared to the AOM/DSS colon NAT Treg cells (**Figure 34**). The intersection analysis between MC38 and B16-F10 tumor Treg cells showed a greater overlap of upregulated genes, with a total of 427 genes (**Figure 52B**).

We then performed functional enrichment analysis on these genes (**Figure 52C**), which revealed enrichment in pathways such as Interferon beta and Type II Interferon response, cytokine-mediated signaling pathways, and regulation of innate immune response to biotic stimuli.

Using the open-source database BioMart, we examined tumor-related genes and compared these to the upregulated genes in the B16-F10 and MC38 tumor Treg cells. We identified 32 matching genes in our dataset, including *Adora2b*, *Ifi204*, *Smpdl3b*, *Gzma*, *Cd14*, *Spp1*, *Lag3*, *Ticam2*, *Sell*, *Lacc1*, *Ccl2*, *Cybb*, *Tlr6*, *Lgals3bp*, *Tbx21*, *Pparg*, *Il12rb2*, *Gimap5*, *Gfi1*, *Ramp1*, *Aurka*, *Ifit2*, *Pdcd1*, *Slc37a2*, *Cxcr3*, *Id1*, *Tpx2*, *Nkg7*, *Klrc1*, *Aurkb*, *Psmb10* and *Tlr2*. These genes were highlighted in the DGE analysis comparing tumor and healthy tissue Tregs from AOM/DSS-induced CAC (**Figure 34**), the MC38 colorectal carcinoma model (**Figure 40**), and the B16-F10 melanoma model (**Figure 48**).

The comparative DGE analysis across the AOM/DSS, MC38, and B16-F10 tumor models identified distinct and overlapping gene expression patterns in tumor-associated Treg cells. Further analysis using BioMart identified 32 tumor-related genes upregulated in Tregs across the models, including key markers such as *Adora2b*, *Lag3*, *Gzma* and *Pdcd1*. These findings highlight both tumor model-specific and shared Treg transcriptional signatures, offering insights into the regulatory roles of Tregs in different tumor microenvironments. Furthermore, they suggest potential prognostic markers and therapeutic targets for Treg-directed immunotherapies.

Results

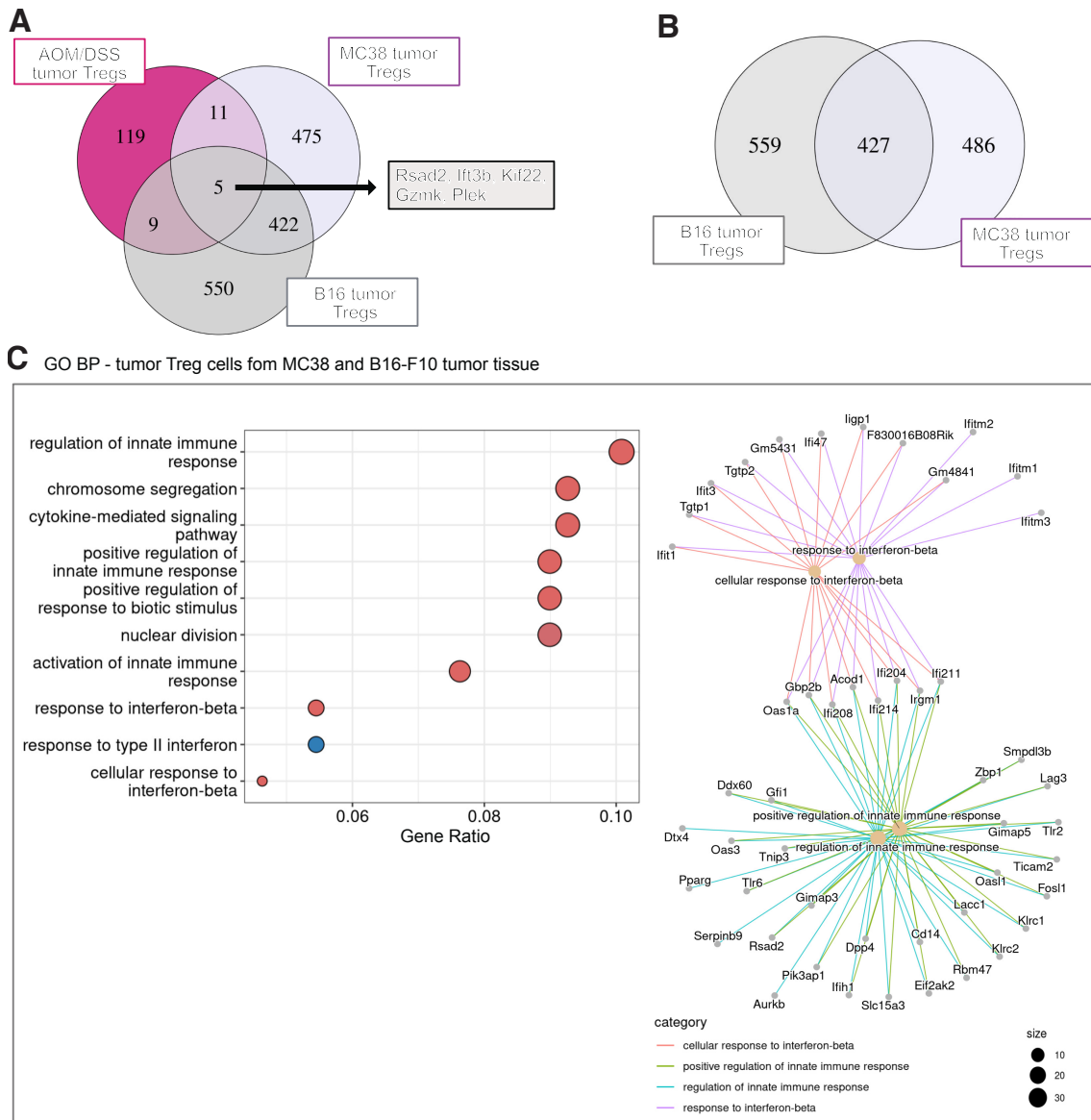


Figure 52: Tumor-specific Treg marker genes as potential targets for immunotherapies. A-B: Venn-Diagram showing the intersection of upregulated genes of the DGE analysis between tumor and healthy tissue of the AOM/DSS model (**Figure 34**), MC39 model and B16-F10 model (**Figure 40**) (A) and MC39 model and B16-F10 model (**Figure 48**) (B). C: Functional enrichment results of upregulated pathways associated to the 427 intersected genes from B. n = 3 individual mice.

4.26. bulkRNA-seq reveals strong tissue specificity in healthy and tumor tissues

In our previous investigations, we concentrated on the CD45⁺ immune cell population from various tumor models. Our goal was to determine the tissue-specificity of Treg cells isolated from different tissues in healthy animals and under conditions of inflammation and cancer. Given that the tissue specificity of cells is influenced by tissue-specific homing factors and distinct cell-cell interactions within different tissues [155, 156], we also aimed to conduct bulk RNA-seq on healthy colon and skin CD45⁻ tissue, as well as B16-F10 and MC38 CD45⁻ tumor tissue. This analysis is expected to provide insights to phenotypic changes and distinct molecular characteristics between tumor and healthy tissue in the CD45⁻ compartment that may influence Treg cell characteristics.

Therefore, we isolated the CD45⁻ fraction of healthy and tumor tissue after CD45 MACS enrichment and purified RNA from two MC38- and B16-F10-bearing mice. For comparison, we also enriched CD45⁻ cells from healthy skin and colon tissue, using the negative fraction as a healthy control tissue. **Figure 53A** shows the PCA plot which is used to reduce the dimensionality of this dataset based on the top 5,000 genes. We observe a clear separation between healthy skin cells and healthy colon cells. Furthermore, CD45⁻ cells isolated from tumor tissue show closer relationships, clustering together between healthy skin and healthy colon tissues, particularly in PC2, which accounts for 34% of the variance. The PCA analysis reveals distinct gene expression profiles between healthy skin and colon tissues, with tumor cells from MC38 and B16-F10 models clustering closely together, suggesting shared molecular features in these tumor environments.

We further compared CD45⁻ cells from MC38 tumor tissue to B16-F10 tumor tissue (**Figure 53B**), revealing a total of 3927 upregulated genes (11% of all) and 4147 downregulated genes (11% of all) within 36954 total expressed genes. In MC38 tumor tissues, pathways involved in neurogenesis, stem cell differentiation, tissue remodeling, migration, and Ras protein-mediated signal transduction were upregulated, with myeloid cell differentiation also appeared to be enhanced.

Results

Comparing CD45⁻ cells from healthy skin tissue to CD45⁻ cells from B16-F1 tumor tissue (C), a total of 6751 genes were upregulated (18% of all) and 4283 genes were downregulated (12% of all). The most significant pathways included mononuclear cell differentiation, neurogenesis, ameboid-type cell migration, and chemotaxis. Additionally, pathways involved in cell-cell adhesion, T cell activation, and skin development were enriched.

For the comparison between CD45⁻ MC38 tumor cells and CD45⁻ colon cells (D), we found 6648 upregulated genes (18% of all) and 3959 downregulated genes (11% of all). CD45⁻ MC38 tumor cells showed enriched pathways related to energy metabolite generation, cellular respiration, various biosynthetic processes, and aerobic respiration.

These analyses highlight distinct molecular processes in tumor versus healthy tissue environments, with CD45⁻ tumor cells displaying unique metabolic and migration pathways, while shared pathways such as mononuclear cell differentiation and cell adhesion play key roles across different tissues.

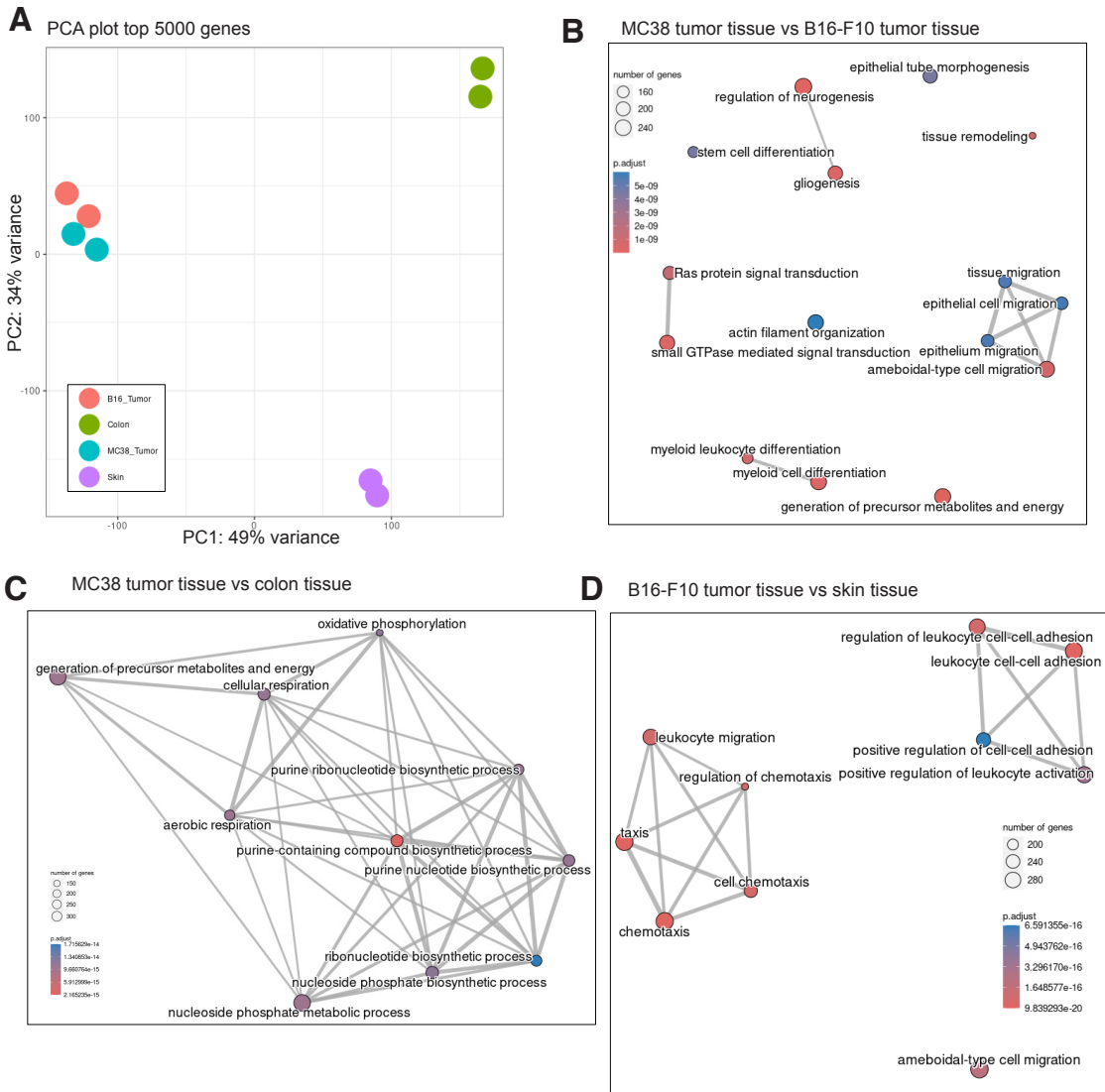


Figure 53: bulkRNA-seq of CD45 negative cells from healthy skin, healthy colon as well as tissue from B16-F10 and MC38 tumor-bearing mice reveals strong tissue specificity. A: 2D-PCA plot showing clustering pattern of CD45 negative cells from healthy skin, healthy colon and B16-F10 and MC38 tumor tissue. DGE and functional enrichment analysis were performed and Enrichment Map showing the results of the comparison between MC38 and B16-F10 tumor tissue (B), MC38 tumor tissue and healthy colon tissue (C) and B16-F10 tumor tissue vs healthy skin tissue (D). n = 2 individual mice.

5. Discussion

Treg cells play a crucial role in immune tolerance, regeneration, and prevention of autoimmunity. Besides their classical function in immune regulation, a highly-activated subset of Treg cells can also migrate into tissues and promote homeostasis as well as regeneration. The role of tissue-resident Treg cells is well studied in both steady state and in inflamed or infectious diseases. However, in the context of cancer, the role of Treg cells remains poorly understood.

Therefore, we investigated the impact of tissue-specificity and TCR clonality of Treg cells found in different murine organs in healthy animals as well as upon inflammation and tumor progression. Within these studies we aimed to specific target four main questions, which will be answered in the following paragraphs:

- 1) How does the phenotype of NLT Treg cells change between healthy tissue compared to tumor and inflamed environment?
- 2) Are tumor-infiltrating Treg cells defined by tissue-specificity or tumor-specificity, or do these characteristics depend on different tumor types?
- 3) Does tumor type and location influence the phenotype of NLT Treg cells?
- 4) Where do tumor-infiltrating Tregs originate or develop, and does this vary across different tumor types and locations?

5.1. NLT-Treg cells show tumor-type-dependent alteration in the Treg cell phenotype

To address the question of whether the phenotype of Treg cells differs in inflamed or tumor tissues compared to healthy tissues, we first needed to define what tissue specificity means in this context. We observed that the NLT Treg cell subset exhibited significantly elevated expression of Foxp3, indicating a highly suppressive phenotype, along with increased expression of the surface marker genes Klr1, PD-1 and Ccr8 as well as the major TF of NLT Treg cells Batf. This suggests active tissue

Discussion

regeneration properties across all tissues. But can we also identify specific gene markers to distinguish cells isolated from different tissues?

It has been suggested that Treg cells are not inherently tissue-specific but can undergo a dynamic pan-tissue-like adaptation. This adaptability is supported by a recent study on Treg cells from various lymphoid and non-lymphoid tissues in healthy mice [47]. However, it is also known that cell types exhibit different phenotypes due to distinct tissue-specific homing factors contribute to attracting Treg cells to particular environments [155, 156]. Consequently, the same NLT-like Treg population in the SLE should show a different gene expression pattern compared to NLT Treg cells from the skin or colon. Some studies have already demonstrated that NLT Treg cell populations share common genes across different tissues, such as *Ccr4*, *Ccr8*, and *Cxcr4*, while also expressing unique genes specific to each tissue type. Previous research has identified key marker genes for Treg cells in various tissues, including *Ccr1* and *Ccr6* for colon Treg cells and *Ccr1* for skin Treg cells [46].

Therefore, we first identified tissue-specific Treg signatures for skin Treg cells, pTreg and tTreg cells from the colon, and NLT-like Treg cells isolated from the SLE (spleen, draining LN, mLN). We observed that these tissue-specific signatures were most highly expressed in their tissue of origin. However, all NLT Treg cells from other tissues also showed moderate expression of these signatures.

Notably, we also subdivided the Treg cells from the SLE into three distinct clusters based on their expression of *Klrg1* and *PD-1*, which have previously been described as markers for the development of tissue-resident Treg cell populations [45].

After defining these signatures in a healthy animal, we wanted to investigate whether we could also identify tissue-specific Treg signatures during inflammation and cancer. We first examined Treg cells from colon tissue in AOM/DSS-treated colitis mice. Colonic Treg cells during colitis largely maintain gene expression patterns similar to their healthy counterparts. However, during colitis-induced CAC progression, pTreg cells from tumor and NAT colon tissue adopt a more tTreg-like

Discussion

signature, which is particularly pronounced in Treg cells from NAT tissue. Tumor and NAT tTreg cells retain a strong resemblance to the healthy tTreg signature, indicating a conserved function in both tumor and healthy tissues. In contrast, tumor and NAT pTreg cells show a reduced alignment with the healthy pTreg signature, suggesting functional divergence potentially driven by the TME.

During tumor development of the colorectal tumor cell line MC38, which is implanted beneath the skin, Treg cells in the TME acquired more colon-specific genes than skin-specific genes, despite the tumor's subcutaneous location. Similarly, in the B16-F10 tumor model, Treg cells from the TME displayed a mix of both, healthy colon and skin gene signatures. This co-expression of skin- and colon-specific genes highlights the complex adaptability of Treg cells in the TME. These findings suggest that Treg cells do not undergo strict tissue-specific adaptation during tumor progression but instead exhibit a dynamic and context-dependent gene expression profile influenced by the TME and inflammatory signals.

This hypothesis of pan-tissue adaptability was further supported by our scTCR-seq analyses. By combining gene expression analysis with TCR analysis, we were able to gain a unique perspective on TCR clonotypes of Treg cells shared across different tissues. This gene expression analysis of shared TCR clones revealed distinct transcriptional signatures across tissues under steady-state conditions and during inflammation, indicating a high degree of tissue-specific adaptation and highlighting the complex interplay between clonality and tissue-specific functionality in shaping Treg identity. These findings were further validated during tumor development, where tumor Treg cells exhibited significant clonal expansion, possibly driven by the proliferation of specific TCRs after recognizing distinct antigens in the TME.

As previously mentioned, tissue specificity is determined by tissue-specific homing factors and distinct cell-cell interactions within different tissues [155, 156]. For this reason, we also performed bulkRNA-seq on healthy colon and skin CD45⁺ tissue, as well as B16-F10 and MC38 CD45⁺ tumor tissue. With this analysis we aimed to assess phenotypic changes in the CD45⁺ compartment that may influence Treg cell

Discussion

characteristics. Our findings could highlight distinct molecular characteristics between tumor and healthy tissue. Subcutaneous CD45⁺ tumor tissue displays a markedly different gene expression pattern compared to adjacent healthy skin or colon tissue. Sophisticated cell-cell interactions between stromal and immune cells play a crucial role in various biological processes, including immune responses to pathogens and tissue maintenance and repair [157]. In tumor tissues, CD45⁺ tumor cells exhibited unique metabolic and migratory pathways, while shared pathways such as mononuclear cell differentiation and cell adhesion remained critical across tissues. These findings indicate that tumor-associated signals may direct Treg cells to migrate into tumor sites and engage with the surrounding environment. For instance, the crosstalk between Treg cells and tumor cells via surface lymphotoxin (LT) α 1 β 2 has recently been demonstrated to play a crucial role in Treg-mediated tumor growth [157-159].

Taken together, our study demonstrates that Treg cells exhibit a complex and dynamic gene expression profile influenced by tissue context, inflammation and the TME. While maintaining some tissue-specific gene signatures, Treg cells display significant adaptability, adopting mixed tissue gene expression patterns when exposed to tumor environments. This highlights a pan-tissue adaptability rather than strict tissue-specific programming during tumor progression.

5.2. Treg cells modulate immune responses within both the SLE and TME

Our analysis underscores the remarkable adaptability of Treg cells, which integrate signals from both their tissue of origin and the tumor microenvironment. This adaptability raises important questions about how cellular interactions within the TME compare to those in healthy tissues and autoimmune conditions like the SLE. Phenotypic changes in cells often arise due to varying tissue-specific environmental signals as well as differences in cellular interactions [160]. Curious whether the interactions within the tumor microenvironment differ from those in

Discussion

healthy tissue and the SLE, we performed scRNA-seq on CD45⁺ immune cells in the context of an MC38 tumor.

As already described, Treg cells interact with various immune cell-types, which are essential for their priming in SLO. Within the T cell zone in the SLO, recirculating T cells enter lymph nodes and remain in this area for several hours [161]. Dendritic cells (DCs) that have captured antigens also migrate into the T zone from the periphery via lymphatics or the bloodstream. Consequently, the T zone is populated by numerous migratory immune cells and includes lymphatic endothelial cells (LECs) and blood endothelial cells (BECs), making it a highly dynamic region for diverse immune cell interactions [162]. Therefore, we investigated the cell-cell interaction occurring in the SLE, healthy tissue and tumor tissue by performed scRNA/TCR-seq on CD45⁺ cells from a MC38 tumor-bearing animal

Focusing first on the SLE we investigated an interaction between Treg cells and myeloid cells, where the TGF- β signaling network played a particularly significant role. TGF- β is important in regulating the generation and effector functions of various immune cell-types [163]. It modulates adaptive immunity by directly promoting the expansion of Treg cells while inhibiting the development and activity of effector T cells and antigen-presenting DCs [164]. Similarly, TGF- β influences the innate immune system by suppressing NK cells and regulating the behavior of macrophages and neutrophils, thereby creating a network of negative regulatory immune signals [165]. Additionally, TGF- β is a key factor in promoting Treg cell development [166].

We further analyzed interactions of the whole CD45⁺ immune cell populations in the SLE, in healthy tissue and tumor tissue. Within the SLE we were able to detect a strong interaction of Treg and B cells, with networks including the inducible T-cell co-stimulator (ICOS) and the chemokine (C-C motif) ligand (CCL) signaling network. The latter was revealed a strong interaction between Treg cells and NK cells. This network is known to play a role in guiding the Treg cells towards the T-cell zone within lymphoid organs, as it was reported that T cells migrated in accordance with CCL19, a chemokine expressed in the T-cell zone [167]. ICOS, a member of the

Discussion

CD28 superfamily, shares structural and functional similarities with CD28 but differs in its expression, as it is not constitutively expressed on resting T cells. Its unique ligand, ICOSL, is found on various APCs, including B cells, DCs, macrophages, and non-lymphoid tissue cells such as fibroblasts, endothelial cells, and epithelial cells [168]. Under homeostatic conditions, ICOS expression is predominantly found in FOXP3⁺ Tregs, comprising approximately 20% of the Treg population. Most ICOS⁺ Tregs are either CXCR3⁺ (Th1-like) or CXCR3⁻ CCR6⁺ CCR10⁻ (Th17-like) Tregs [169]. Studies in mouse revealed that ICOS is highly expressed in murine splenic CD44⁺ CD62L⁻ activated Tregs, which also express Helios, indicating they are mostly derived from the thymus [170]. Furthermore, Tregs with ICOS expression also co-express many immunosuppressive receptors, such as Ctlα-4, PD-1, Tigit, and Lag3, and exhibit a higher secretion of IL-10, providing them with superior suppressive potential [171, 172]. One could conclude that the Treg cells within the SLE represent a recirculating population and already display a more suppressive phenotype, likely induced by the highly inflammatory TME, as we could detect an increase expression of the immunosuppressive marker genes in cells from the tumor tissue compared to those of healthy tissue.

In the TME, we observed the most robust signaling network, particularly involving the TGFβ, IL-10, and CCL signaling pathways. This included interactions between Treg cells and B cells, NK cells, and myeloid cells. These findings highlight the highly immunosuppressive nature of the TME, which facilitates the infiltration of various immune cells that are subsequently suppressed in their functions by Treg cells. IL-10 is another suppressive key cytokine, known not only as the most potent anti-inflammatory cytokine but also for its role in facilitating cancer immune surveillance [173]. The CCL signaling is an important driver contributing to Treg cell recruitment at a tumor site, where specifically Ccr4 and Ccr8 are involved, as it has been shown in various reports of human tumors, including breast cancer, colon, gastric and lung carcinoma and melanoma [174-178].

Discussion

In conclusion our findings show the critical role of Treg cells in modulating immune responses within the SLE, healthy tissue and TME. In the SLE, Treg cells demonstrate extensive interactions with myeloid cells, B cells, and NK cells, primarily mediated by TGF- β , IL-10, ICOS, and CCL signaling pathways.

These interactions underline their highly suppressive phenotype, likely influenced by the inflammatory environment. The robust signaling networks observed in the TME further support the dynamic recruitment and functional adaptation of Treg cells, driven by factors such as CCL signaling and key cytokines like IL-10. This highlights the central role of Treg cells in maintaining immune regulation and their potential contribution to tumor progression through immune suppression.

5.3. Treg cell show tissue-plasticity and adaptation in the TME

Our next objective was to determine whether tumor-infiltrating Treg cells exhibit a general phenotype or if their characteristics are uniquely shaped by specific tumor models, influenced by different tumor types and locations. Additionally, we sought to determine whether these cells exhibit distinct functions depending on their tissue context. In recent studies, it has been extensively documented that Treg cells not only regulate immune responses but also play a role in tissue repair and regenerative processes in various murine and human tissues [49-52, 59, 179]. Therefore, we generated gene signatures based on the regenerative and suppressive properties of this cell type. From our healthy animal models, we used Areg⁺ cells from the skin, colon, and NLT-like Treg cells from the SLE to calculate a regenerative gene signature. Additionally, we used Ctla4⁺ cells from all Treg populations (including lymphoid and precursor NLT-like Treg cells within the SLE) to calculate a suppressive gene signature.

By applying our regenerative and suppressive gene signature we observed that Treg cells in the TME exhibit both regenerative and suppressive functions during inflammation and tumor development, playing a role in tumor progression and immune evasion. Treg cells from the TME express a more pronounced suppressive signature compared to those from healthy tissues.

Discussion

Differential expression analysis supports the hypothesis of both, a highly immunosuppressive and regenerative environment within the TME. Comparisons of gene expression between Treg cells from the TME and those from healthy tissues revealed only minor differences in their gene expression profiles. Notably, there was an upregulation of genes involved in lymphocyte regulation, T cell activation, and pathways related to IFN- β and Type II Interferon responses. The response to IFN- β pathways was consistently upregulated across almost all tumor types. As part of the Type I Interferons, IFN- β is well-known for its immunosuppressive properties. IFN- β was found to directly promote Treg cell induction through STAT1- and P300-dependent Foxp3 acetylation, highlighting its potential as an intriguing target for therapeutic applications [154]. Another study also highlighted the role of IFN- β in the survival of induced Treg cells in inflammatory processes and tumor progression [180].

By analyzing the upregulated genes in Treg cells from the TME compared to healthy adjacent tissue across various tumor types and locations, we identified five significantly upregulated genes. These include *Rasd2*, an interferon-inducible antiviral protein in the SAM enzyme superfamily [181], which plays a key role in the antiviral response and has been linked to prognosis and immunotherapy response in CRC [182]. Additionally Pleckstrin (*Plek*), involved in G protein-coupled receptor signaling and metabolic regulation, showed cancer specificity in recent studies and is negatively correlated with tumor purity [183]. Furthermore, Granzyme K (*Gzmk*), a serine protease in cytotoxic lymphocytes, is associated with poor clinical outcomes when highly expressed in CD8+ T cells [184]. *Kif22*, a kinase family member, promotes multiple myeloma progression [185]. Lastly, *Ifit3b*, an interferon-induced protein, which is predicted to be involved in cellular biology changes, including cell proliferation, apoptosis, differentiation, and cancer development [186].

By the overall analysis of significant upregulated genes and the comparison with open-source databases we found a few potential surface molecules, that might be an important target on Treg cells in the TME. We identified *Adora2b*, a cAMP-

Discussion

producing adenosine receptor, as upregulated in our analysis. CD39 and CD73 work together to modulate immune responses: CD39 neutralizes ATP's inflammatory effects via P2 purinergic receptors, while CD73 suppresses immune cells through cAMP-producing adenosine receptors, *Adora2a* (A2aR) and *Adora2b* (A2bR) [187, 188]. Tregs lacking *Adora2b* exhibited dysfunction and enhanced anti-tumor immune responses in mice [189, 190]. Another notable molecule among the 32 other genes is Secreted Phosphoprotein 1 (*Spp1*), which promotes T cell survival. The *Spp1* gene encodes the protein osteopontin and a osteopontin-induced survival of autoreactive T cells may contribute to the progression of autoimmune diseases. [191]. High expression of *Spp1* was observed with a significant increase in the abundance of Tregs in metastatic renal cell carcinoma (RCC). It was also found to be associated with therapeutic resistance and might serve as a potential of metastatic RCC [192].

These findings underscore a tumor-type-dependent alteration in the Treg cell phenotype. Treg cells within the TME appear to be influenced by their tissue of origin, indicating not only disease-specific but also tissue-specific gene expression patterns and behavior. Nevertheless, our results suggest that certain changes may be consistent among tumor-infiltrating Treg cells across different tumor types.

5.4. Recruitment of Treg cells into the TME is highly dependent on the tumor type

Building on these findings, we next sought to explore the origins and recruitment mechanisms of tumor-infiltrating Treg cells and whether these processes differ across various tumor types and locations.

Beyond the characterization of transcriptomic profiles analyzed by scRNA-seq, we were also able to determine the $\alpha\beta$ TCR sequences. This TCR analysis of Treg cells demonstrates substantial clonal expansion among Treg and Tconv cells in non-lymphoid tissues, with significant tissue-specific differences in TCR sharing and

Discussion

gene expression profiles. Under steady-state, Treg cells from the colon and skin showed a higher clonal expansion than Treg cells from the lymphoid tissue.

In the healthy animals, we already found a notable overlap of TCRs from NLT-like Treg cells of the SLE, particularly those from iLN and spleen, with skin-resident Treg cells. This reflects greater plasticity of these tissue Treg cells compared to lymphoid Treg cells. Anyhow, in the healthy animals, skin Treg cells displayed minimal TCR overlap with other populations, emphasizing their distinct tissue-specific signature. The extent of TCR overlap varied significantly across the different models we investigated. In the AOM/DSS colitis mouse model, the precursor NLT-like Treg population showed the highest TCR overlap with colitis-inflamed pTreg cells, with a notable 50% overlap between TCRs from iLN precursor Treg cells and pTreg cells. By day 50 after AOM/DSS treatment, which induced CAC, the highest overlap was observed between TCRs from NLT-like Treg cells in the SLE and tTreg cells from the colon NAT/tumor tissue.

In the MC38 tumor model, the greatest TCR overlap was found between precursor and NLT-like Treg cells from the SLE and tumor-infiltrating Tregs. A substantial frequency of Treg cells was observed in the colon tissue, while TCRs from skin Treg cells showed minimal overlap with tumor Tregs.

Conversely, in the B16-F10 melanoma tumor model, there was minimal overlap between skin or colon Treg cells and those from the tumor tissue. However, the reverse was observed, with TCRs from tumor tissue being detected at the highest frequency in skin Treg cells.

These findings highlight a tumor-type-dependent TCR repertoire overlap, suggesting that the extent of shared TCRs between tissue-specific and tumor-infiltrating Treg cells is influenced by both the tissue context and the nature of the tumor.

By examining the gene expression pattern of T cells with shared TCRs with tumor Treg cells, we identified a high tissue-specific expression, supporting again the pan-tissue hypothesis and highlighting the high circulating nature of Treg cells.

Discussion

Using pseudo-time analysis on cells from different tissues of a single animal that share TCRs with Tregs found in the TME, we observed that tumor Tregs display lower pseudo-time compared to skin Tregs and Tregs from SLE clusters. This suggests a temporal dependency, indicating that tumor Tregs may be primed in the SLE and migrate to tumors through altered microenvironments and migration signals. This hypothesis is further supported by the shared clonotypes found in both MC38 and colitis-induced CAC tumors and the SLE. The high degree of clonal sharing between SLE NLT-like Treg cells and tumor Treg cells highlights the migratory properties of this cell-type. A plausible hypothesis is that tumors actively recruit Treg cells from the SLE environment and that the SLE might play a role in priming tumor-associated Treg cells.

In contrast, for the B16-F10 melanoma tumor, skin Tregs exhibited the lowest pseudo-time overall. The TCR analysis in this model revealed a different pattern, with fewer Treg TCRs from the tumor sharing with the SLE and more with skin. This suggests that in the melanoma model, Treg induction may occur directly in the skin and the TME. Furthermore, the pseudo-time analysis illustrated the trajectory of naïve, precursor and NLT-like Treg cells within the SLE.

It might be also interesting to closer investigate the antigen specificity of these Treg cells. Research indicates that neoantigens, which are novel antigens arising from DNA mutations during malignant transformation, are characteristic of tumor cells and can be presented on the cell surface. These epitopes can induce the activation of CD4⁺ and CD8⁺ T cells and cellular immunity [193]. Our analysis suggests that melanoma-derived antigens could potentially be presented by Langerhans cells, which are the only DC subset in healthy skin tissue [194], possibly leading to the presence of melanoma-specific T cell precursors in the skin. In contrast, for tumors like MC38, which are associated with the colon, tumor-specific T cell precursors would likely originate in the colon and would need to migrate to other sites, such as the skin, to exert their effects.

Discussion

Our findings reveal distinct patterns of TCR clonal sharing, expansion and recruitment of Treg cells across different tissues and tumor models, supporting the pan-tissue adaptability of Treg cells. Tumor-associated Treg cells exhibit tissue- and tumor-type-specific characteristics, with evidence suggesting that tumors may recruit and prime Treg cells from SLE environments. The pseudo-time analysis further indicates temporal dependencies, highlighting different Treg migration and induction patterns between melanoma and colorectal tumor models. Previous research describes a migration scenario for Treg cells in a disease-free mouse model, with a residence time of 3–10 weeks in tissues [47]. Treg cells capable of recognizing antigens across multiple tissues reinforce the idea that Treg cells are not strictly tissue-specific but can persist in specific tissues when antigen presentation occurs. These results underscore the dynamic and migratory nature of Treg cells and suggest potential roles for the SLE in Treg priming and tumor adaptation.

5.5. Outlook

Our studies did not identify a uniform tumor-specific phenotype across all investigated tumor models. Instead, our findings emphasize the dynamic and adaptable nature of Treg cells, revealing tissue- and tumor-type-specific variations in their clonal sharing, expansion, cell interaction and recruitment patterns. Notably, these results suggest a potential role for the SLE as a priming environment for tumor-associated Tregs, with temporal dependencies in their migration and induction patterns differing between melanoma and colorectal tumor models. These insights provide a foundation for further research into antigen specificity, migration signals, and potential therapeutic targets.

Currently, it is not possible to determine the epitopes detected by a single TCR, making it unclear whether tumor Tregs migrate to tumor or infectious sites through TCR activation or other migration signals. Identifying what the TCR recognizes in tumor tissue could help identify potential targets for Treg-mediated tumor therapy. Therefore, it might be interesting to study TCR specificity by using ovalbumin (OVA)-

Discussion

specific CD4⁺ T cells (OT-II cells). OT-II mice, bred on a C57BL/6 background, carry a transgenic TCR specific for chicken ovalbumin (OVA) [195, 196]. These mice express an MHC-II-restricted TCR specific for the OVA-derived peptide 323-339, which leads to preferential selection of CD4⁺ T helper cells [197]. By using OVA-specific tumor cells, we could investigate whether specific antigen recognition plays a role in the migration and accumulation of Treg cells within the TME.

Our studies have revealed that Tregs from various tumor models share the upregulation of genes associated with immune suppression, tissue regeneration, and hematopoiesis. Furthermore, we identified a few universal marker genes present across all models. However, the tumor microenvironment (TME) exhibited significant variability depending on the tumor type and location. While surface molecule targets on Tregs, such as Ccr8 [198, 199], are being investigated, it is important to note that these markers are not tumor-specific, as Tregs from non-lymphoid tissues (NLT) also express them. Despite this, the surface molecules we identified on Tregs in the TME across different tumor models could serve as important targets or prognostic factors, warranting further investigation. Additionally, exploring TCR specificity in Treg cells is a crucial next step for understanding their role in the TME.

To understand the differences in Tregs involved in tumor progression and tissue regeneration, such as wound healing after injury, a mouse model combining tumor induction and wounding could be useful. This would allow for the examination of gene expression, TCR clonality and sharing across tissues, as well as potential differences in chromatin accessibility. Identifying a potential marker or antigen specificity that is exclusive to the TME, distinct from its role in wound healing and tissue regeneration, could provide valuable insights.

6. Abstract

Regulatory T cells (Treg) are an anti-inflammatory, immune-regulatory T cell type. Besides their classical function in immune regulation, a highly-activated subset of Treg cells can also migrate into tissues and promote homeostasis as well as regeneration. This non lymphoid tissue subset is characterized by the expression of tissue-specific marker genes and their highly regenerative and suppressive function. Previous research had highlighted the importance of tissue-specific Treg cells in regeneration upon organ damage and inflammation, but less is known in the context of tumor progression. In this study we therefore aimed to characterize murine Treg cells from three different tumor types (colorectal carcinoma, B16-F10 melanoma, MC38 adenocarcinoma) by their gene expression pattern and assess their clonal expansion via single cell RNA/TCR-sequencing.

Under steady-state conditions, Treg cells across different tissues exhibit a shared molecular program with only a few tissue-specific genes. Our studies did not identify a uniform tumor-specific phenotype across all investigated tumor models. Instead, our findings emphasize the dynamic and adaptable nature of Treg cells, revealing tissue- and tumor-type-specific variations in their clonal sharing, expansion, cell interaction and recruitment patterns. Notably, these results suggest a potential role for the SLE as a priming environment for tumor-associated Tregs, with temporal dependencies in their migration and induction patterns differing between melanoma and colorectal tumor models. These insights provide a foundation for further research into antigen specificity, migration signals, and potential therapeutic targets.

Finally, we identified genes that are specifically upregulated in the tumor context and thus indicate specific programs active in tumor-associated Treg cells, but absent in healthy non-lymphoid tissue Treg cells. These findings suggest potential targets or prognostic markers for Treg cell-specific immunotherapies and give valuable insights in the migration capacity of Treg cells in the context of cancer.

7. Zusammenfassung

Regulatorische T-Zellen (Treg) stellen eine antiinflammatorische, immunregulatorische Subpopulation von T-Zellen dar. Neben ihrer klassischen Funktion bei der Immunregulation kann eine hochaktivierte Subgruppe von Treg-Zellen auch in Gewebe migrieren und dort zur Homöostase sowie zur Regeneration beitragen. Diese Untergruppe von Treg-Zellen aus nicht-lymphoiden Gewebe zeichnet sich durch die Expression gewebespezifischer Markergene und eine ausgeprägte regenerative und suppressive Funktion charakterisiert.

Frühere Studien haben die Bedeutung gewebespezifischer Treg-Zellen für die Regeneration bei Organschäden und Entzündungen hervorgehoben. Im Kontext der Tumorprogression sind jedoch noch viele Aspekte ungeklärt. In dieser Studie zielten wir daher darauf ab, murine Treg-Zellen aus drei verschiedenen Tumortypen anhand ihres Genexpressionsprofils zu charakterisieren und ihre klonale Expansion mittels Einzelzell-RNA/TCR-Sequenzierung zu analysieren.

Unter homöostatischen Bedingungen zeigen Treg-Zellen verschiedener Gewebe ein übergreifendes molekulares Programm, während sie gleichzeitig gewebespezifische Gene exprimieren. Daher untersuchten wir gezielt die gewebespezifischen Merkmale tumorinfiltrierender Treg-Zellen sowie den Einfluss der Gewebespezifität über verschiedene Tumorarten (kolorektales Karzinom, B16-F10-Melanom, MC38-Adenokarzinom) und Lokalisationen hinweg. Unsere Analysen ergaben kein einheitliches tumorspezifisches Phänotypmuster über alle untersuchten Tumormodelle, stattdessen unterstreichen unsere Ergebnisse die dynamische und anpassungsfähige Natur von Treg-Zellen und offenbaren tumortyp- und gewebespezifische Unterschiede hinsichtlich klonaler Überlappung, Expansion, Zellinteraktionen und Rekrutierungsmustern. Unsere Ergebnisse zeigen zudem, dass sekundäre lymphatische Organe eine wichtige Rolle bei der Beeinflussung von tumorassoziierten Treg-Zellen spielen, wobei zeitabhängige Unterschiede in Migrations- und Induktionsmechanismen zwischen Melanom- und

kolorektalen Tumormodellen beobachtet wurden. Diese Erkenntnisse bilden eine Grundlage für weiterführende Untersuchungen zur Antigen-spezifität, zu Migrationssignalen sowie zu potenziellen therapeutischen Zielstrukturen.

Abschließend identifizierten wir Gene, die spezifisch im Tumorkontext hochreguliert sind und somit auf tumorspezifische Programme in Treg-Zellen hinweisen, die in gesunden nicht-lymphoiden Geweben nicht aktiv sind. Diese Erkenntnisse könnten zur Identifikation potenzieller Zielstrukturen oder prognostischer Marker für Treg-spezifische Immuntherapien beitragen und liefern wertvolle Einsichten in die Migrationsfähigkeit von Treg-Zellen im Kontext der Tumorbiologie.

8. Appendix

8.1. Supplementary Figures

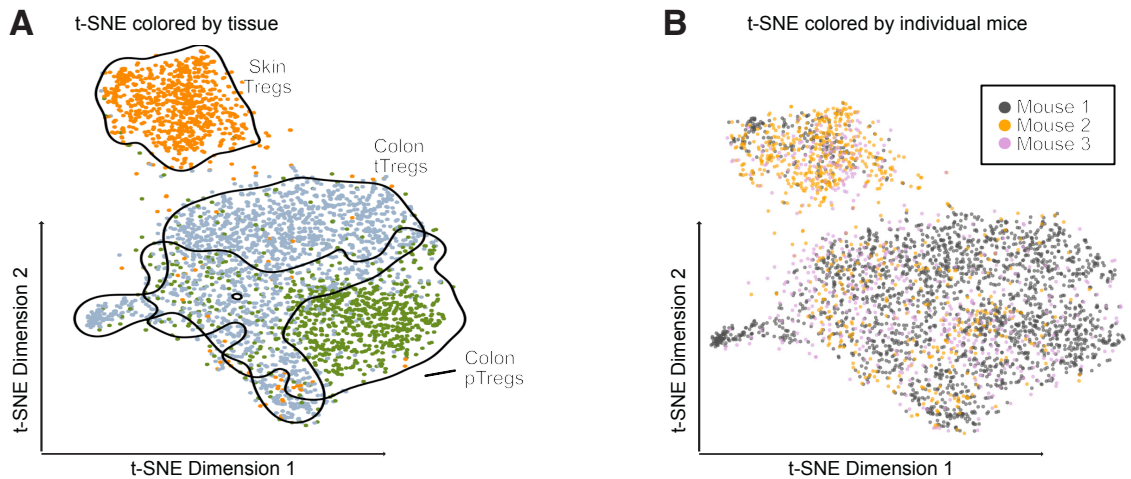


Figure 54: Batch correction was successfully applied to skin Treg cells, colon Treg cells, and tumor-infiltrating Treg cells from all three individual AOM/DSS-treated mouse replicates. scRNA/TCR-seq analysis was performed 60 days start of AOM/DSS-treatment. A: t-SNE projection colored by tissue, with skin Treg cells in orange, colon tTreg cells in blue and colon pTreg cells in green. Confidence ellipses indicate the 95% confidence level for each tissue. B: t-SNE projection colored by individual mouse replicates.

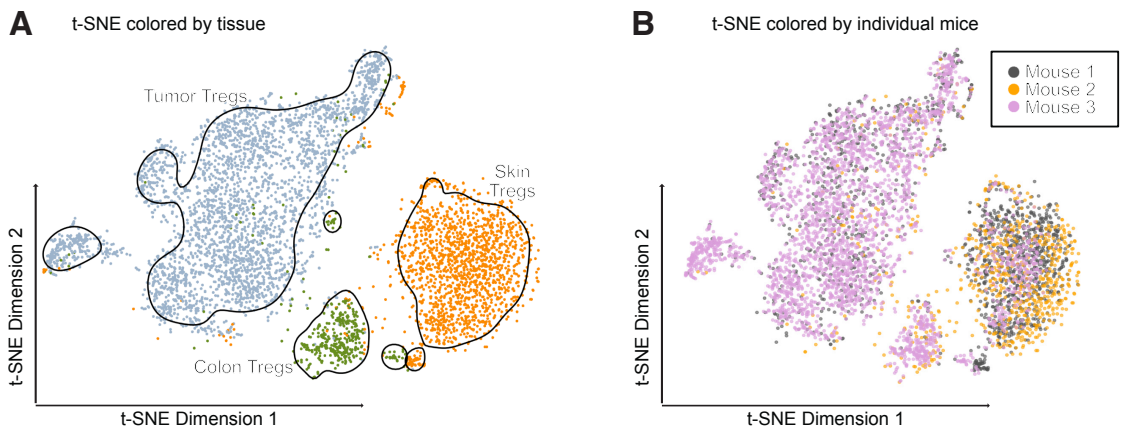


Figure 55: Batch correction was successfully applied to skin Treg cells, colon Treg cells, and tumor-infiltrating Treg cells from all three individual MC38-injected mouse replicates. scRNA/TCR-seq analysis was performed 15 days after the subcutaneous injection MC38 colorectal carcinoma cells. A: t-SNE projection colored by tissue, with tumor Treg cells in blue, skin Treg cells in orange, and colon Treg cells in green. Confidence ellipses indicate

Appendix

the 85% confidence level for each tissue. B: t-SNE projection colored by individual mouse replicates.

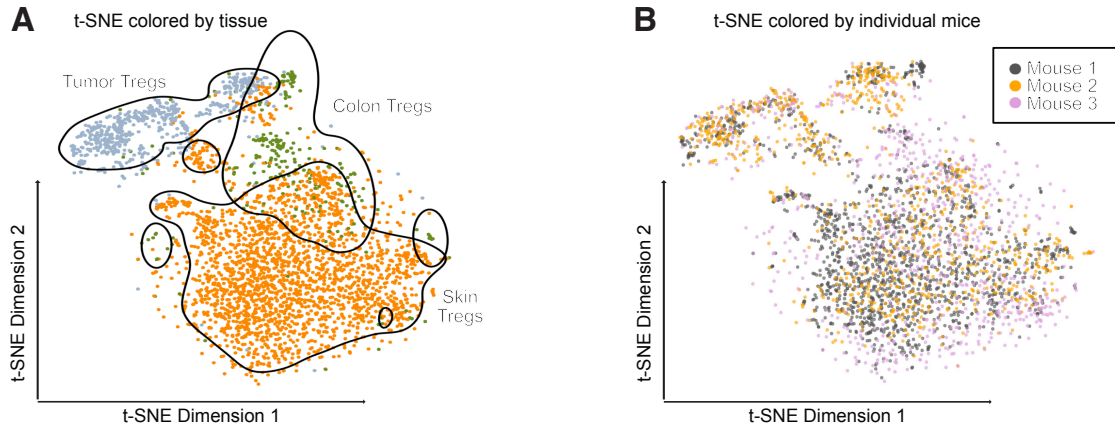


Figure 56: Batch correction was successfully applied to skin Treg cells, colon Treg cells, and tumor-infiltrating Treg cells from all three individual B16-F10-injected mouse replicates. scRNA/TCR-seq analysis was performed 15 days after the subcutaneous injection of B16-F10 melanoma cells. A: t-SNE projection colored by tissue, with tumor Treg cells in blue, skin Treg cells in orange, and colon Treg cells in green. Confidence ellipses indicate the 90% confidence level for each tissue. B: t-SNE projection colored by individual mouse replicates.

8.2. List of Abbreviations

ACK	Ammonium-Chloride-Kalium
AML1	Acute myeloid leukemia-1
AOM	Azoxymethane
APC	Antigen-presenting cell
Areg	Amphiregulin
ATP	adenosine triphosphate
Batf	basic leucine zipper transcription factor
Bcl2	B-cell lymphoma 2
BCR	B cell receptor
bp	Basepairs
BP	Biological Processes
CAC	colitis-associated cancer
cAMP	cyclic adenosine monophosphate
CAR	Chimeric Antigen Receptor
CNS	central nervous system
CRC	Colorectal cancer
CSP	cell surface protein
Ctla4	cytotoxic T cell-associated antigen-4
DC	Dendritic cell
DGE	Differential gene expression
DMH	1,2-dimethylhydrazine dihydrochloride
DNA	desoxyrinonucleic acid
DSS	Dextran Sodium Sulfate
EAE	experimental autoimmune encephalomyelitis
ECM	extracellular matrix
EGFR	epidermal growth factor receptor
FACS	Fluorescent-activated cell sorting
FASL	Fas ligand
FCS	Fetal calf serum
FDR	false discovery rate

Appendix

Foxp3	forkhead box protein 3
GEX	Gene expression
GFP	Green fluorescent protein
GLM	generalized linear model
HAT	histone acetyl transferase
HDAC	histone deacetyl transferase
HE	Hematoxylin
HSV-1	Herpes simplex virus 1
i.p.	Intraperitoneal
IBD	inflammatory bowel disease
ICI	Immune Checkpoint Inhibitors
ICOS	Inducible T Cell Costimulator
Id3	inhibitor of desoxyrinonucleic acid binding 3
IL-2	Interleukin 2
ILC	Innate lymphoid cell
iLN	inguinal lymph node
IPEX	immunodysregulation polyendocrinopathy enteropathy X-linked
iTreg	inducible Treg cell
Klrg1	Killer cell lectin-like receptor G1
logFc	log-fold change
mAb	monoclonal antibodies
MACS	Magnetic activated cell sorting
MHC	Major histocompatibility complex
mLN	mesenteric lymph nodes
mTEC	medullary thymic epithelial cells
NAT	normal adjacent tissue
NFAT	Nuclear factor of activated T cells
Nfil-3	nuclear factor interleukin-3
NK cell	Natural killer cell
NKG2D	natural killer group 2 member D
NKT cell	Natural killer T cell
NLT	Non-lymphoid tissue

Appendix

NSCLC	non-small cell lung cancer
PAMP	Pathogen-associated molecular pattern
PCA	Principial component analysis
PD-1	programmed cell death protein 1
PRR	Pattern recognition receptor
pTreg	peripheral-induced Treg cell
QC	Quality control
RFS	recurrence-free survival
Runx1	runt-related transcription factor 1
s.c.	Subcutaneous
Satb1	SATB homeobox 1
scRNA-seq	single cell ribonucleic acid sequencing
Sell	L-selectin
SLE	Secondary lymphoid environment
SLO	Secondary lymphoid organs
STING	stimulators of interferon genes
t-SNE	t-distributed stochastic neighbor embedding
TAA	tumor-associated antigens
Tconv cell	T conventional cell
TCR	T cell receptor
Teff	Effector T cell
TF	transcription factor
TGF- β	Transforming Growth Factor Beta
Th	T helper cell
TIL	Tumor-Infiltrating Lymphocytes
TLR	Toll-like receptor
TME	tumor microenvironment
Tnfsf4	TNF superfamily member 4
TRAIL	Tumor Necrosis Factor Related Apoptosis Inducing Ligand
Treg cell	Regulatory T cell
tTreg	Thymus-derived Treg cell
UMI	unique molecular identifier

Appendix

wt	wild-type
----	-----------

8.3. List of Figures

Figure 1: Treg cells regulate the immune system and repair tissue damage. Left: Immune suppression - Treg cells suppress effector T cells (Teff) by secretion of immunosuppressive and anti-inflammatory cytokines, induction of apoptosis via granzyme secretion, via Ctl4 or metabolic disruption via CD39. Right: Tissue regeneration – Treg cells mediate tissue repair program and upregulate surface molecules like Killer cell lectin-like receptor G1 (Klrg1). Effector programs are activated via IL-10 and murine Amphiregulin (Areg) and support wound healing and epithelial regeneration in the murine lung. Created with Biorender. 8

Figure 2: Development of NLT Treg cells and their expression of Foxp3, Nfil3, Batf and their surface receptors programmed cell death protein 1 (PD-1), Killer Cell Lectin Like Receptor G1 (Klrg1) and ST2 (IL-33 receptor); created with Biorender, adapted from Delacher et al., 2020 [45]. 9

Figure 3: Overview of NLT Treg-mediated regeneration in murine tissues. NLT Treg cells are characterized by the expression of the transcription factors Foxp3, Batf and Nfil3. They exhibit surface markers such as Klrg1, St2 (IL-33R), PD-1, CD39, CD25 and Ctl4-4, along with a T cell receptor (TCR). Across various tissues - including visceral adipose tissue (VAT), skin, lung, liver, heart, muscle, and the central nervous system (CNS) - NLT Tregs facilitate tissue regeneration through effector molecules such as amphiregulin (Areg), proenkephalin (Penk), IL-10, IL-33, IL-13, and CD103. In the tumor microenvironment (TME), these cells not only produce regenerative factors but also contribute to immunosuppression, notably through TGF- β . Created with Biorender..... 12

Figure 4: Hallmarks of Cancer – Six classical hallmarks of cancer defined by Hanahan and Weinberg in 2000 marked in grey, two enabling factors colored in pink and two emerging hallmarks colored in yellow. Created with Biorender, adapted from Hanahan and Weinberg, 2010 [69]. 15

Figure 5: Overview of different mouse models investigated in this thesis. The steady state displays a wild-type mouse at the age of 10-12 weeks and is highlighted in blue. The disease types are colored in yellow, including a AOM/DSS-treated colitis,

AOM/DSS-induced colorectal carcinoma, a adenocarcinoma model using MC38 cells and a melanoma model using B16-F10 cells which both induced subcutaneous tumor. Created with Biorender. 22

Figure 6: Overview of the kinetic from the MC38 adenocarcinoma model. Seven days before the s.c. injection, MC38 cells were seeded. MC38 cells were s.c. injected and 3 animals were analyzed for T cell surface marker expression on day 8, day 12, day 15 and day 19 as well as scRNA/TCR-seq on day 15..... 32

Figure 7: Overview of the kinetic of the B16-F10 melanoma model. Seven days before the s.c. injection, B16-F10 cells were seeded. Cells were s.c. injected and 3 animals were analyzed for T cell surface marker expression on day 8, day 11, day 13 and day 15 as well as scRNA/TCR-seq on day 13..... 33

Figure 8: Schematic Overview of the AOM/DSS model for CAC induction. Mice were injected intraperitoneally with AOM (10 mg/kg body weight) on day 0. From day 5 to day 10, the mice received 2.5% weight per volume (wv) dextran sulfate sodium (DSS) dissolved in autoclaved drinking H₂O. Mice were sacrificed on day 14 for evaluation of colitis or on day 60 for analysis of CAC. 35

Figure 9: Overview of scRNA/TCR-seq workflow. The schematic provides an overview of the scRNA/TCR-seq process, divided into three main panels: tissue processing and library preparation, sequencing and quality control, and data analysis. Tissue Processing and Library Preparation (left panel): Tissues harvested from an individual mouse are subjected to enzymatic and mechanical digestion (1), followed by target cell enrichment (2) to optimize cell sorting efficiency (3). Subsequently, cells labeled with BioLegend® TotalSeqC anti-mouse Hashtagging antibodies and 10X beads are loaded onto the 10X Chromium controller (4). This is followed by scRNA-seq library preparation (5). Sequencing and Quality Control (middle panel): Sequencing (1) generates raw data, which undergoes quality control (2). Pre-processing of the data is performed using R and Bioconductor to produce a final, filtered dataset ready for analysis (3). Data Analysis (right panel): The analysis includes clustering (1), marker gene detection (2), TCR repertoire diversity assessment (3), cell-type annotation (4), and trajectory analysis (5). For interactive

exploration, the iSEE platform (6) can be utilized. Copied from Nedwed and Helbich et al. [143]. 36

Figure 10: Overview of the gating scheme to sort CD25⁺ T cells of SLE (spleen, mLN, iLN), CD4⁺ T cells of colon and skin tissue. All sample sorted into the same collection tube. Immune cells were first identified by CD45⁺, afterwards doublets and dead cells were removed. By using a dump channel for CD19, CD11b, CD11c, MHCII, CD206 and CD3⁺ T cells were isolated and further gated on their CD4 or CD8 expression. Dotplots are created from one example of healthy animal used in this thesis and representative for all other analysis. 41

Figure 11: scRNA/TCR library profiles measured on a TapeStation. A-C: One representative image of the library fragment distribution of the GEX library (A), VDJ library (B) and CSP library (C) is shown. 42

Figure 12: Overview of gene expression (GEX), VDJ and cell surface protein (CSP) library and recommended sequencing length. Copied from Nedwed and Helbich et al.[143]. 43

Figure 13: QC and doublet detection. Scatter plots of the library size and mitochondrial content and (left) library size and number of detected genes (right). Each dot in the plot represents a cell, blue cells are of high quality, orange cells are of low quality and were filtered out for downstream analysis. Copied from Nedwed and Helbich et al. [143]. 48

Figure 14: Tissue-specific Treg cell signature genes. A-C: Gene expression score of the individual genes of the skin Treg signature (A), colon tTreg signature (B), colon pTreg signature (C) and SLE NLT-like signature (D) are displayed for each mouse (M1, M2, M3) as well as each Treg cell cluster. Normalized for each individual gene. 51

Figure 15: Calculation of specific Treg signatures. A-C: Core Treg signature (A, left panel), suppressive Treg signature (B, left panel) and regenerative signature (C, left panel) are shown in a t-SNE dimension plot. Cells used for the analysis for *scoreMarkers()* function are colored in red. Volcano plot (right panel) displaying the amount of used genes for the individual signatures. 53

Figure 16: Individual Genes included for the Treg signatures. A-C: Gene expression score of the individual genes of the core signature (A), suppressive signature (B) and regenerative signature (C) are displayed for each mouse (M1, M2, M3) as well as each Treg cell cluster. Normalized for each individual gene. *Due to the large number of genes included in the core Treg signature, the gene list was extracted and attached in section 9.5. 54

Figure 17: Venn-Diagram showing the overlap of marker genes for the regenerative Treg signature and suppressive Treg signature. 55

Figure 18: Treg cells from murine lymphoid and non-lymphoid tissue show distinct marker gene expression via flow analysis. A: Schematic overview of analyzed murine tissue. B: FACS plots of a representative sample for spleen, mesenteric lymph node (mLN), inguinal lymph node (iLN), skin, colon, lung and liver. Pregated on CD4⁺ T cells. C: Foxp3⁺ T cell frequency of CD3⁺ CD4⁺ T cells. D: Klrp1⁺ PD-1⁺ Treg frequency of Treg cells. All analysis is based on flow cytometry based on T cells isolated from spleen (n=9), mLN (n=9), iLN (n=5), skin (n=6), colon(n=9), lung (n=4) and liver(n=4). 62

Figure 19: NLT-like Treg cells from the SLE show a high frequency of Batf and Ccr8. A: FACS plot showing the MFI of Batf and Ccr8 of a representative sample for lymphoid (Foxp3⁺ Klrp1⁻ PD-1⁻) precursor NLT-like (Foxp3⁺ Klrp1⁻ PD-1⁺) and NLT-like Tregs (Foxp3⁺ Klrp1⁺ PD-1⁺) isolated from the spleen, skin, colon, lung and liver. Pregated on viable CD4⁺ Foxp3⁺ T cells. B: Batf⁺ Treg frequency of Treg cells, SLE are again divided into lymphoid Treg cells (Klrp1⁻, PD-1⁻), precursor NLT-like Treg cells (Klrp1⁻, PD-1⁺) and NLT-like Treg cells (Klrp1⁺, PD-1⁺). F: Ccr8⁺ Treg frequency of Treg cells. All analysis is based on flow cytometry based on T cells isolated from spleen (n=9), mLN (n=9), iLN (n=5), skin (n=6), colon(n=9), lung (n=4) and liver(n=4). 64

Figure 20: scRNA-seq analysis of Treg cells from non-lymphoid and lymphoid tissue of healthy mice revealed tissue-specific signatures. A-B: t-SNE plot colored by cluster (A) and tissue types (B). Confidence ellipses applied to the t-SNE plot displaying the 95% confidence level of the individual cluster (A) and tissue types (B). C-F: Signatures for skin Treg cells (C), colon tTreg cells (D), colon pTreg cells (E) and

SLE NLT-like Treg cells (F) based on differential expressed genes are plotted on a t-SNE and density plot showing the signature score for the different Treg cluster. Cell-types are colored based on their cluster color showed in A. G: Venn-Diagram showing overlapping genes of the tissue-specific signatures. n = 3 individual mice. 66

Figure 21: Pseudo-time analysis of scRNA data from different organs of healthy mice reveals Treg trajectories. A: pseudo-time is displayed in a color-coded t-SNE plot, with purple indicating a low and yellow indicating a high pseudo-time. Confidence ellipses applied to the t-SNE plot displaying the 95% confidence level of the individual cluster. B: Scatter plot showing the distribution of pseudo-time values across the different cluster applied from **Figure 20**. n = 3 individual mice. 68

Figure 22: Gene expression signatures plotted on the t-SNE of healthy mice. A-C: The core Treg signature (A), suppressive Treg signature (B) and regenerative Treg signature (C) is plotted on a t-SNE plot (left) and density plot (right). Cell-types are colored based on their cluster color showed in **Figure 20A**. n = 3 individual mice. 69

Figure 23: TCRs from NLT Treg cells are higher clonal expanded. A: Pie charts showing the TCR repertoire composition for each cluster, highlighting the percentage of singletons (grouped together in the red slice) and the distinct duplicated TCRs. B: t-SNE plot colored by all duplicated TCRs detected in this dataset. Red dots showing cells with duplicated TCRs. Confidence ellipses applied to the t-SNE plot displaying the 95% confidence level of the individual cluster. n = 3 individual mice. 70

Figure 24: Tissue-dependent TCR overlaps among Treg cell populations. A: Chord diagram illustrates the shared TCR usage between different clusters, revealing inter-cluster relationships. Cell-types are colored based on their cluster color showed in **Figure 20A**. B: A heatmap visualizes the overlap of shared TCR clones among various tissue-specific cell populations, quantifying their extent. 73

Figure 25: Shared TCR clonotypes across different tissues exhibit tissue-specific gene signatures. A: 2D-PCA plot colored by tissue cell-type, highlighting the distances between duplicated TCRs of skin Treg cells found in various tissues.

Different shapes of the symbols highlight the mouse individual replicates. B: Dotplot illustrating the expression of Treg marker genes for a specific TCR based on their amino acid sequence (TRB:CASGFPGQNYAEQFF; TRA:CAARRGSNAKLTF) shared among iLN, skin, and spleen, highlighting tissue-specific expression patterns. n = 3 individual mice..... 74

Figure 26: Colitis development assed by body weight, endoscopy and hematoxylin (HE) staining. A: Weight curve showing the percentage of body weight relative to day 0 of wt mice (n = 7). B: H&E staining of inflamed colon swiss roll at day 14 after AOM/DSS treatment displaying on representative mouse. Black arrows illustrate infiltrating immune cells. C: Representative endoscopic image was taken on day 13. The scale bar is 250 μ m. 76

Figure 27: scRNA/TCR-seq at day 14 after AOM/DSS treatment. A-B: t-SNE plot colored by cluster (A) and tissue types (B). Confidence ellipses applied to the t-SNE plot displaying the 95% confidence level. C: pTreg signature from healthy mice (**Figure 20**) is applied to this dataset and visualized through a t-SNE plot (left) and density plot (right). D: tTreg signature from healthy mice (**Figure 20**) is applied to this dataset and visualized through a t-SNE plot (left) and density plot (right). E: Colon pTreg cells (cluster 4) and colon tTreg cells (cluster 2) are compared with the tTreg cell and pTreg cell healthy signature. Percentage showing the frequency of cells in the area. n=2 individual mice..... 78

Figure 28: Datasets of healthy and colitis-induced mice were successfully integrated after batch correction. A-B: t-SNE colored by cell types (A) and condition (B). Confidence ellipses applied to the t-SNE plot displaying the 95% confidence level of cell types (A) and condition (B). C: DGE between naive Treg cells isolated from splenocyte of healthy and colitis-induced mice cells plotted on a volcano plot. Non-significant (ns) genes and genes which were either a $\log_2FC > 2$ or $p\text{-value} < 0.05$ are colored grey, while genes with $\log_2FC > 2$ and $p\text{-value} < 0.05$ are shown in pink. n=3 individual mice. 80

Figure 29: Colon Treg cells from AOM/DSS-induced colitis are high in expression of suppressive and regenerative signatures. A-B: A density plot displaying the

differences for the suppressive Treg cell signature (A) and regenerative Treg cell signature (B) between colon pTreg and tTreg cells from AOM/DSS-induced colitis and healthy animals. p-value calculated by the Wilcoxon rank sum test. C: DGE of healthy and inflamed colon pTreg cells. D: DGE between healthy and inflamed colon tTreg cells plotted on a volcano plot. Non-significant (ns) genes and genes which were either a $\log_2FC > 2$ or $p\text{-value} < 0.05$ are colored grey, while genes with $\log_2FC > 2$ and $p\text{-value} < 0.05$ are shown in pink. E: Functional enrichment results of the analysis shown in C plotted on an enrichment map. F: Functional enrichment results of the analysis shown in D plotted on an enrichment map. n=3 individual mice. 82

Figure 30: Precursor NLT-like Treg cells share TCR with inflamed colon Treg cells. TCR repertoire analysis of T cells from different murine organs were performed at day 14 after AOM/DSS-induced colitis. A: t-SNE plot colored by all duplicated TCRs detected in this dataset. Red dots showing cells with duplicated TCRs. Confidence ellipses applied to the t-SNE plot displaying the 95% confidence level. B: Pie charts showing the TCR repertoire composition for colon pTreg (cluster 4) and colon tTreg (cluster 2) cells, highlighting the percentage of singletons (grouped together in the red slice) and the distinct duplicated TCRs. C: Chord diagram illustrates the shared TCR usage between different clusters, revealing inter-cluster relationships. Clusters are colored based on their cluster color showed in **Figure 27A**. D: Shared TCRs among all other clusters illustrated in a table. E: Pseudo-time is displayed in a color-coded t-SNE plot, with purple indicating a low and yellow indicating a high pseudo-time. F: Scatter plot showing the distribution of pseudo-time values across the different cell-types..... 85

Figure 31: CAC induction after 60 days of AOM/DSS treatment. 12 weeks old WT mice were injected i.p. with AOM (10 $\mu\text{g/g}$ body weight) on day 0 and received one cycle of 2.5% DSS ad libitum from day 5 to day 10. Mini-endoscopy was performed one day before sacrifice to confirm tumor development and state of inflammation. Colons were collected on day 60 of AOM/DSS treatment, opened longitudinally, and rolled up from the distal part to generate ‘Swiss rolls’. Histopathological grading

was performed by a trained pathologist (AG Matthias Gaida). A: H&E staining showing distal tumor and B: tumor-free tissue (NAT). C: Representative image of longitudinally opened colon showing tumor development in the distal colon of the mice. D: Representative endoscopic images of wild-type mice on day 59 of AOM/DSS-induced CAC. Arrows indicate tumors..... 86

Figure 32: scRNA/TCR-seq at day 60 after AOM/DSS treatment. A-B: t-SNE plot colored by cluster (A) and tissue types (B). Confidence ellipses applied to the t-SNE plot displaying the 95% confidence level for cluster (A) and tissue (B). C: pTreg signature from healthy mice (**Figure 20**) is applied to this dataset and visualized by a t-SNE plot (left) and density plot (right). D: tTreg signature from healthy mice (**Figure 20**) is applied to this dataset and visualized by a t-SNE plot (left) and density plot (right). E: Skin Treg signature from healthy mice (**Figure 20**) is applied to this dataset and visualized by a t-SNE plot (left) and density plot (right). F: Tumor tTreg cells (cluster 2). Confidence ellipses applied to the t-SNE plot displaying the 95% confidence level for clusters displayed in (A) G: Colon tTreg cells (cluster 2), H: Tumor pTreg cells (cluster 7) and I: Colon pTreg cells (cluster 7) are compared with the tTreg cell and pTreg cell healthy signature. Percentage showing the frequency of cells in the area. A-E: n =1, F-I: n=3. 89

Figure 33: Tumor tTreg cells exhibited the highest expression of the regenerative and suppressive signature. A: Density plot showing density differences between NAT and tumor pTreg and tTreg cells of the regenerative Treg cell signature. B: Density plot showing density differences between NAT and tumor pTreg and tTreg cells of the suppressive Treg cell signature. n = 3 individual mice. p-value calculated by using the Wilcoxon rank sum test..... 90

Figure 34: Colon Treg cells from AOM/DSS-induced CRC are highly similar in their gene expression profiles. A - B: Volcano plot illustrating the differential expressed genes between tumor Treg and colon pTreg cells (A) and Tumor Treg and tTreg cells (B). C: Enrichment Map and CNET-Plot showing enriched pathways of the Functional Enrichment analysis between colon tumor and colon NAT tTreg cells. Non-significant (ns) genes and genes which were either $\log_2FC > 2$ or $p\text{-value} < 0.05$

are colored grey, while genes with both, $\log_2FC > 2$ and $p\text{-value} < 0.05$ are shown in pink. $n = 3$ individual mice. 92

Figure 35: TCRs from NLT-like Treg cells in SLE are highly overlapping with tumor tTreg cells. A-B: t-SNE plot colored by duplicated pTreg and tTreg TCRs from either colon NAT (A) or colon tumor (B) tissue. Confidence ellipses applied to the t-SNE plot displaying the 95% confidence level for clusters. C: TCR clonality of tTreg and pTreg from the NAT colon and tumor tissue is plotted in a pie chart. D: Table illustrating the percent of duplicated TCRs shared with cells between clusters. E: 2D-PCA plot colored by tissue cell-type, highlighting the distances between duplicated TCRs of tumor Treg cells found in various tissues. $n = 1$ 95

Figure 36: Migratory trajectory of skin and SLE Treg cells to colon disease sites in AOM/DSS-induced CAC mice. A: Pseudo-time of all duplicated TCR clonotypes is displayed in a color-coded t-SNE plot, with purple indicating a low and yellow indicating a high pseudo-time. Confidence ellipses applied to the t-SNE plot displaying the 95% confidence level for clusters. B: Scatter plot showing the distribution of pseudo-time values from duplicated and shared tumor/colon Treg TCRs (cluster2+7) across all other tissues. Cluster are colored based on their cluster color. $n = 1$ 96

Figure 37: Flow analysis of different murine organs from MC38-bearing mice. A: tumor volume in mm^3 on day 8, 12, 15 and 19. B: Total count of CD45^+ and viable immune cells found in the TME on day 8, 12, 15 and 19. C: Dotplot (left) showing the expression of CD4 and Foxp3 in a representative tumor sample at day 15 and the frequency (right) of Foxp3^+ cells on day 8, 12, 15 and 19 on the spleen, mLN, dLN, colon, skin and tumor tissue. D: Dotplot (left) showing the expression of PD-1 and Klrp1 in a representative tumor sample at day 15 and the frequency (right) of Klrp1^+ PD-1⁺ cells on day 8, 12, 15 and 19 on the spleen, mLN, dLN, colon, skin and tumor tissue. A-B: $n = 4-6$ individual mice. Lines represent the median, and dots represent individual mice. C-D: $n = 3$ individual mice were analyzed on day 8, 12, 15 and 19 within the distinct organs. 98

Figure 38: Tumor-infiltrating Treg cells share more genes with colon Treg cells. scRNA/TCR-seq was performed at day 15 after MC38 tumor cell injection. A-B: t-SNE plot colored by cluster (A) and tissue types (B). Confidence ellipses applied to the t-SNE plot displaying the 95% confidence level of the individual cluster (A) and tissue types (B). C: pTreg cell signature from healthy mice (**Figure 20**) is applied to this dataset and visualized by a t-SNE plot (left) and density plot (right). D: tTreg cell signature from healthy mice (**Figure 20**) is applied to this dataset and visualized by a t-SNE plot (left) and density plot (right). E: skin Treg cell signature from healthy mice (**Figure 20**) is applied to this dataset and visualized by a t-SNE plot (left) and density plot (right). Confidence ellipses applied to the t-SNE plot displaying the 95% confidence level of the individual cluster shown in (A). F- G: Tumor Treg cells (cluster 4) are compared with the merged colon and skin Treg cell signature (F), as well as colon tTreg cell and pTreg cell healthy signature (G). Percentage showing the frequency of cells in the area. n=1 individual mice.100

Figure 39: Tumor Treg cells not only adopt suppressive functions but also acquire regenerative properties. A+B: Regenerative (A) and suppressive (B) signature applied on tumor Treg cells from the MC38 tumor model and plotted by using density plots. n = 3 individual mice. p-value calculated using the Wilcoxon rank sum test.101

Figure 40: Tumor Treg cells from MC38 tumor model show gene expression differences to the healthy tissue. A- B: Volcano plot illustrating the differential expressed genes between tumor Treg and colon Treg cells (A) and tumor Treg and skin Treg cells (B). ns cells and cells with either a $\log_2FC > 2$ or $p\text{-value} < 0.05$ are colored grey, while cells with $\log_2FC > 2$ and $p\text{-value} < 0.05$ are shown in pink. n = 3 individual mice.102

Figure 41: Tumor Treg cells in the TME undergo acquiring enhanced roles in immune response and cytokine signaling. A-B: Functional enrichment analysis showing the differences in the DGE of the comparison between MC38 tumor Treg and colon Treg cells (A) on a dotplot (right) and CNET plot (left) and MC38 tumor Treg and skin Treg cells (B). n = 3 individual mice.104

Figure 42: Tumor-infiltrating Treg cells show overlap in TCR usage with SLE and colon Treg cells. A-B: pie charts (A) showing the diversity of duplicated tumor Treg TCRs across different tissues and t-SNE plot (B) showing duplicated tumor Treg cell TCR clonotypes. Confidence ellipses applied to the t-SNE plot displaying the 95% confidence level of the individual cluster. C: shared TCRs among all other clusters illustrated in a table. D: 2D-PCA plot colored by tissue cell-type, highlighting the distances between duplicated TCRs of tumor Treg cells found in other tissues. n = 1.....107

Figure 43: Tumor Tconv exhibit lowest pseudo-time values. A: pseudo-time of all cells in this dataset is displayed in a color-coded t-SNE plot, with purple indicating a low and yellow indicating a high pseudo-time. Confidence ellipses applied to the t-SNE plot displaying the 95% confidence level of the individual cluster B: Scatter plot showing the distribution of pseudo-time values from only tumor Treg TCRs which are duplicated and shared across different cell-types. n = 1.....109

Figure 44: scRNA-seq of CD45⁺ immune cells revealed strong immune cell interaction within the TME. Analysis of CD45⁺ immune cells was performed at day 15 after tumor induction from a MC38 tumor-bearing mouse. A-B: t-SNE plot colored by cluster (A) and tissue types (B). Confidence ellipses applied to the t-SNE plot displaying the 95% confidence level of the individual cell types (A) and tissue types (B). C-E: Circle plot illustrating the interaction strength of the different cluster in healthy tissue (C), tumor tissue (D) and SLE (E) and showing the interaction of different signaling networks in the representative tissue. n = 2 individual mice. .112

Figure 45: FACS analysis B16-F10 tumor-bearing mice over the time. A: tumor volume in mm³ on day 8, 11, 13 and 15. B: Total count of CD45⁺ and viable immune cells found in the TME on day 8, 11, 13 and 15. C: Dotplot (left) showing the expression of CD4 and Foxp3 in a representative tumor sample at day 15 and the frequency (right) of Foxp3⁺ cells on day 8, 12, 15 and 19 on the spleen, mLN, dLN, colon, skin and tumor tissue. D: Dotplot (left) showing the expression of PD-1 and Klrp1 in a representative tumor sample at day 15 and the frequency (right) of Klrp1⁺ PD-1⁺ cells on day 8, 12, 15 and 19 on the spleen, mLN, dLN, colon, skin and tumor

tissue. A-B: n = 4-6 individual mice. Lines represent the median, and dots represent individual mice. C-D: n = 3 individual mice were analyzed on day 8, 11, 13 and 15 within the distinct organs.....114

Figure 46: B16-F10 tumor-infiltrating Treg cells show co-expression of skin- and colon-specific genes. scRNA/TCR-seq were performed at day 15 after B16-F10 tumor cell injection. A -B: t-SNE of T cells from different murine tissue colored by cluster (A) and tissue (B). Confidence ellipses applied to the t-SNE plot displaying the 95% confidence level of the individual cluster (A) and tissue ty (B). C: pTreg cell signature from healthy mice (**Figure 20**) is applied to this dataset and visualized by a t-SNE plot (left) and density plot (right). D: tTreg cell signature from healthy mice (**Figure 20**) is applied to this dataset and visualized by a t-SNE plot (left) and density plot (right). E: skin Treg cell signature from healthy mice (**Figure 20**) is applied to this dataset and visualized by a t-SNE plot (left) and density plot (right). Confidence ellipses applied to the t-SNE plot displaying the 95% confidence level of the individual cluster displayed in (A). F-G: Tumor Treg cells (cluster 4) are compared with the merged colon and skin Treg cell signature (F), as well as colon tTreg cell and pTreg cell healthy signature (G). Percentage showing the frequency of cells in the area. n=1.....116

Figure 47: B16-F10 tumor-infiltrating Treg cells show lower expression of the regenerative and suppressive signature compared to skin Treg cells. Signatures are applied on tumor Treg cells from the B16-F10 tumor model and plotted by using density plots. n = 3 individual mice. p-value calculated by using the Wilcoxon rank sum test.....117

Figure 48: Tumor Treg cells from B16-F10 tumor model show gene expression differences to the healthy tissue. A-B: Volcano plot illustrating the differential expressed genes between tumor Treg and colon Treg cells (A) and tumor Treg and skin Treg cells (B). Non-significant (ns) genes and genes which were either $\log_2FC > 2$ or $p\text{-value} < 0.05$ are colored grey, while genes with both, $\log_2FC > 2$ and $p\text{-value} < 0.05$ are shown in pink. n = 3 individual mice.118

Figure 49: Tumor Treg cells in the TME undergo acquiring enhanced roles in response to biotic stimuli and innate immune response. A-B: Functional enrichment analysis showing the differences in the DGE of the comparison between B16-F10 tumor Treg and colon Treg cells (A) on an enrichment map (left) and CNET plot (right) and B16-F10 tumor Treg and skin Treg cells (B). n = 3 individual mice.

.....120

Figure 50: TCRs from tumor-associated Treg cells show limited overlaps with healthy tissue. The TCR repertoire of B16-F10 tumor, colon, and skin Treg cells. A: pie charts showing the diversity of duplicated tumor, colon and skin Treg TCRs. B: t-SNE plot showing duplicated tumor Treg cell TCR clonotypes. C: shared TCRs among all other clusters illustrated in a table. D: 2D-PCA plot colored by tissue cell-type, highlighting the distances between duplicated TCRs of tumor Treg cells found in other tissues. n = 1.....122

Figure 51: Pseudo-time analysis of scRNA data from different organs of healthy mice. A: pseudo-time is displayed in a color-coded t-SNE plot, with purple indicating a low and yellow indicating a high pseudo-time. B: Scatter plot showing the distribution of pseudo-time values across the different cluster. n = 1.123

Figure 52: Tumor-specific Treg marker genes as potential targets for immunotherapies. A-B: Venn-Diagram showing the intersection of upregulated genes of the DGE analysis between tumor and healthy tissue of the AOM/DSS model (**Figure 34**), MC39 model and B16-F10 model (**Figure 40**) (A) and MC39 model and B16-F10 model (**Figure 48**) (B). C: Functional enrichment results of upregulated pathways associated to the 427 intersected genes from B. n = 3 individual mice.

.....125

Figure 53: bulkRNA-seq of CD45 negative cells from healthy skin, healthy colon as well as tissue from B16-F10 and MC38 tumor-bearing mice reveals strong tissue specificity. A: 2D-PCA plot showing clustering pattern of CD45 negative cells from healthy skin, healthy colon and B16-F10 and MC38 tumor tissue. DGE and functional enrichment analysis were performed and Enrichment Map showing the results of the comparison between MC38 and B16-F10 tumor tissue (B), MC38

tumor tissue and healthy colon tissue (C) and B16-F10 tumor tissue vs healthy skin tissue (D). n = 2 individual mice.128

Figure 54: Batch correction was successfully applied to skin Treg cells, colon Treg cells, and tumor-infiltrating Treg cells from all three individual AOM/DSS-treated mouse replicates. scRNA/TCR-seq analysis was performed 60 days start of AOM/DSS-treatment. A: t-SNE projection colored by tissue, with skin Treg cells in orange, colon tTreg cells in blue and colon pTreg cells in green. Confidence ellipses indicate the 95% confidence level for each tissue. B: t-SNE projection colored by individual mouse replicates.145

Figure 55: Batch correction was successfully applied to skin Treg cells, colon Treg cells, and tumor-infiltrating Treg cells from all three individual MC38-injected mouse replicates. scRNA/TCR-seq analysis was performed 15 days after the subcutaneous injection MC38 colorectal carcinoma cells. A: t-SNE projection colored by tissue, with tumor Treg cells in blue, skin Treg cells in orange, and colon Treg cells in green. Confidence ellipses indicate the 85% confidence level for each tissue. B: t-SNE projection colored by individual mouse replicates.145

Figure 56: Batch correction was successfully applied to skin Treg cells, colon Treg cells, and tumor-infiltrating Treg cells from all three individual B16-F10-injected mouse replicates. scRNA/TCR-seq analysis was performed 15 days after the subcutaneous injection of B16-F10 melanoma cells. A: t-SNE projection colored by tissue, with tumor Treg cells in blue, skin Treg cells in orange, and colon Treg cells in green. Confidence ellipses indicate the 90% confidence level for each tissue. B: t-SNE projection colored by individual mouse replicates.146

8.4. List of Tables

Table 1: Consumables	23
Table 2: Chemicals and Reagents.....	23
Table 3: Enzymes.....	24
Table 4: Antibodies	24
Table 5: Biological Material	25
Table 6: Kits.....	25
Table 7: Laboratory software and Equipment	26
Table 8: Buffer and Cell Culture Media.....	27
Table 9: Software and Packages	28
Table 10: Sorted and aligned cells per organ for the individual mouse models. ...	44
Table 11: Antibody mix 1 for Immune Cell analysis via flow cytometry	60
Table 12: Antibody mix 2 for Immune Cell analysis via flow cytometry	60

8.5. List of References

- [1] D.D. Chaplin, Overview of the immune response, *J Allergy Clin Immunol* 125(2 Suppl 2) (2010) S3-23.
- [2] T. Hato, P.C. Dagher, How the Innate Immune System Senses Trouble and Causes Trouble, *Clin J Am Soc Nephrol* 10(8) (2015) 1459-69.
- [3] S. Thoma-Uszynski, S. Stenger, O. Takeuchi, M.T. Ochoa, M. Engele, P.A. Sieling, P.F. Barnes, M. Rollinghoff, P.L. Bolcskei, M. Wagner, S. Akira, M.V. Norgard, J.T. Belisle, P.J. Godowski, B.R. Bloom, R.L. Modlin, Induction of direct antimicrobial activity through mammalian toll-like receptors, *Science* 291(5508) (2001) 1544-7.
- [4] T. Kawai, S. Akira, The role of pattern-recognition receptors in innate immunity: update on Toll-like receptors, *Nat Immunol* 11(5) (2010) 373-84.
- [5] R. Medzhitov, C.A. Janeway, Jr., Innate immunity: impact on the adaptive immune response, *Curr Opin Immunol* 9(1) (1997) 4-9.
- [6] J.S. Marshall, R. Warrington, W. Watson, H.L. Kim, An introduction to immunology and immunopathology, *Allergy Asthma Clin Immunol* 14(Suppl 2) (2018) 49.
- [7] J. Liu, X. Zhang, Y. Cheng, X. Cao, Dendritic cell migration in inflammation and immunity, *Cell Mol Immunol* 18(11) (2021) 2461-2471.
- [8] D.L. Farber, N.A. Yudanin, N.P. Restifo, Human memory T cells: generation, compartmentalization and homeostasis, *Nat Rev Immunol* 14(1) (2014) 24-35.
- [9] J. Parkin, B. Cohen, An overview of the immune system, *Lancet* 357(9270) (2001) 1777-89.
- [10] H. Spits, Development of alphabeta T cells in the human thymus, *Nat Rev Immunol* 2(10) (2002) 760-72.
- [11] R. Rezzani, L. Nardo, G. Favero, M. Peroni, L.F. Rodella, Thymus and aging: morphological, radiological, and functional overview, *Age (Dordr)* 36(1) (2014) 313-51.
- [12] N.R. Gascoigne, V. Rybakin, O. Acuto, J. Brzostek, TCR Signal Strength and T Cell Development, *Annu Rev Cell Dev Biol* 32 (2016) 327-348.

Appendix

- [13] L. Klein, B. Kyewski, P.M. Allen, K.A. Hogquist, Positive and negative selection of the T cell repertoire: what thymocytes see (and don't see), *Nat Rev Immunol* 14(6) (2014) 377-91.
- [14] G. Lythe, C. Molina-Paris, Some deterministic and stochastic mathematical models of naive T-cell homeostasis, *Immunol Rev* 285(1) (2018) 206-217.
- [15] R.V. Luckheeram, R. Zhou, A.D. Verma, B. Xia, CD4(+)T cells: differentiation and functions, *Clin Dev Immunol* 2012 (2012) 925135.
- [16] B. Weigelin, A.T. den Boer, E. Wagena, K. Broen, H. Dolstra, R.J. de Boer, C.G. Figdor, J. Textor, P. Friedl, Cytotoxic T cells are able to efficiently eliminate cancer cells by additive cytotoxicity, *Nat Commun* 12(1) (2021) 5217.
- [17] S. Sakaguchi, Regulatory T cells: key controllers of immunologic self-tolerance, *Cell* 101(5) (2000) 455-8.
- [18] K. Adu-Berchie, F.O. Obuseh, D.J. Mooney, T Cell Development and Function, *Rejuvenation Res* 26(4) (2023) 126-138.
- [19] S. Hori, T. Nomura, S. Sakaguchi, Control of regulatory T cell development by the transcription factor Foxp3, *Science* 299(5609) (2003) 1057-61.
- [20] S. Sakaguchi, M. Miyara, C.M. Costantino, D.A. Hafler, FOXP3+ regulatory T cells in the human immune system, *Nat Rev Immunol* 10(7) (2010) 490-500.
- [21] H. Morikawa, S. Sakaguchi, Genetic and epigenetic basis of Treg cell development and function: from a FoxP3-centered view to an epigenome-defined view of natural Treg cells, *Immunol Rev* 259(1) (2014) 192-205.
- [22] M.E. Brunkow, E.W. Jeffery, K.A. Hjerrild, B. Paeper, L.B. Clark, S.A. Yasayko, J.E. Wilkinson, D. Galas, S.F. Ziegler, F. Ramsdell, Disruption of a new forkhead/winged-helix protein, scurf, results in the fatal lymphoproliferative disorder of the scurfy mouse, *Nat Genet* 27(1) (2001) 68-73.
- [23] F. Consonni, S. Ciullini Mannurita, E. Gambineri, Atypical Presentations of IPEX: Expect the Unexpected, *Front Pediatr* 9 (2021) 643094.
- [24] M. Voarino, F. Consonni, E. Gambineri, Expanding the spectrum of IPEX: from new clinical findings to novel treatments, *Curr Opin Allergy Clin Immunol* 24(6) (2024) 457-463.

- [25] M. Ono, H. Yaguchi, N. Ohkura, I. Kitabayashi, Y. Nagamura, T. Nomura, Y. Miyachi, T. Tsukada, S. Sakaguchi, Foxp3 controls regulatory T-cell function by interacting with AML1/Runx1, *Nature* 446(7136) (2007) 685-9.
- [26] G. Lal, N. Zhang, W. van der Touw, Y. Ding, W. Ju, E.P. Bottinger, S.P. Reid, D.E. Levy, J.S. Bromberg, Epigenetic regulation of Foxp3 expression in regulatory T cells by DNA methylation, *J Immunol* 182(1) (2009) 259-73.
- [27] D.L. Owen, R.S. La Rue, S.A. Munro, M.A. Farrar, Tracking Regulatory T Cell Development in the Thymus Using Single-Cell RNA Sequencing/TCR Sequencing, *J Immunol* 209(7) (2022) 1300-1313.
- [28] C.W. Lio, C.S. Hsieh, A two-step process for thymic regulatory T cell development, *Immunity* 28(1) (2008) 100-11.
- [29] Q. Tang, K.J. Henriksen, E.K. Boden, A.J. Tooley, J. Ye, S.K. Subudhi, X.X. Zheng, T.B. Strom, J.A. Bluestone, Cutting edge: CD28 controls peripheral homeostasis of CD4⁺CD25⁺ regulatory T cells, *J Immunol* 171(7) (2003) 3348-52.
- [30] J.M. Coquet, J.C. Ribot, N. Babala, S. Middendorp, G. van der Horst, Y. Xiao, J.F. Neves, D. Fonseca-Pereira, H. Jacobs, D.J. Pennington, B. Silva-Santos, J. Borst, Epithelial and dendritic cells in the thymic medulla promote CD4⁺Foxp3⁺ regulatory T cell development via the CD27-CD70 pathway, *J Exp Med* 210(4) (2013) 715-28.
- [31] C. Apert, A.O. Galindo-Albarran, S. Castan, C. Detraves, H. Michaud, N. McJannett, B. Haegeman, S. Fillatreau, B. Malissen, G. Hollander, S. Zuklys, J.C. Santamaria, O.P. Joffre, P. Romagnoli, J.P.M. van Meerwijk, IL-2 and IL-15 drive intrathymic development of distinct periphery-seeding CD4⁽⁺⁾Foxp3⁽⁺⁾ regulatory T lymphocytes, *Front Immunol* 13 (2022) 965303.
- [32] J.D. Fontenot, J.P. Rasmussen, M.A. Gavin, A.Y. Rudensky, A function for interleukin 2 in Foxp3-expressing regulatory T cells, *Nat Immunol* 6(11) (2005) 1142-51.
- [33] K. Kretschmer, I. Apostolou, D. Hawiger, K. Khazaie, M.C. Nussenzweig, H. von Boehmer, Inducing and expanding regulatory T cell populations by foreign antigen, *Nat Immunol* 6(12) (2005) 1219-27.

Appendix

- [34] W. Chen, W. Jin, N. Hardegen, K.J. Lei, L. Li, N. Marinos, G. McGrady, S.M. Wahl, Conversion of peripheral CD4⁺CD25⁻ naive T cells to CD4⁺CD25⁺ regulatory T cells by TGF-beta induction of transcription factor Foxp3, *J Exp Med* 198(12) (2003) 1875-86.
- [35] J.R. Ghali, M.A. Alikhan, S.R. Holdsworth, A.R. Kitching, Induced regulatory T cells are phenotypically unstable and do not protect mice from rapidly progressive glomerulonephritis, *Immunology* 150(1) (2017) 100-114.
- [36] K. Someya, H. Nakatsukasa, M. Ito, T. Kondo, K.I. Tateda, T. Akanuma, I. Koya, T. Sanosaka, J. Kohyama, Y.I. Tsukada, T. Takamura-Enya, A. Yoshimura, Improvement of Foxp3 stability through CNS2 demethylation by TET enzyme induction and activation, *Int Immunol* 29(8) (2017) 365-375.
- [37] M.A. Gavin, J.P. Rasmussen, J.D. Fontenot, V. Vasta, V.C. Manganiello, J.A. Beavo, A.Y. Rudensky, Foxp3-dependent programme of regulatory T-cell differentiation, *Nature* 445(7129) (2007) 771-5.
- [38] D.K. Sojka, Y.H. Huang, D.J. Fowell, Mechanisms of regulatory T-cell suppression - a diverse arsenal for a moving target, *Immunology* 124(1) (2008) 13-22.
- [39] A. Schmidt, N. Oberle, P.H. Krammer, Molecular mechanisms of treg-mediated T cell suppression, *Front Immunol* 3 (2012) 51.
- [40] Y. Zong, K. Deng, W.P. Chong, Regulation of Treg cells by cytokine signaling and co-stimulatory molecules, *Front Immunol* 15 (2024) 1387975.
- [41] Y. Ju, X. Shang, Z. Liu, J. Zhang, Y. Li, Y. Shen, Y. Liu, C. Liu, B. Liu, L. Xu, Y. Wang, B. Zhang, J. Zou, The Tim-3/galectin-9 pathway involves in the homeostasis of hepatic Tregs in a mouse model of concanavalin A-induced hepatitis, *Mol Immunol* 58(1) (2014) 85-91.
- [42] T. Bopp, C. Becker, M. Klein, S. Klein-Hessling, A. Palmetshofer, E. Serfling, V. Heib, M. Becker, J. Kubach, S. Schmitt, S. Stoll, H. Schild, M.S. Staeger, M. Stassen, H. Jonuleit, E. Schmitt, Cyclic adenosine monophosphate is a key component of regulatory T cell-mediated suppression, *J Exp Med* 204(6) (2007) 1303-10.

Appendix

- [43] A.R. Munoz-Rojas, G. Wang, C. Benoist, D. Mathis, Adipose-tissue regulatory T cells are a consortium of subtypes that evolves with age and diet, *Proc Natl Acad Sci U S A* 121(4) (2024) e2320602121.
- [44] J. Huehn, A. Hamann, Homing to suppress: address codes for Treg migration, *Trends Immunol* 26(12) (2005) 632-6.
- [45] M. Delacher, C.D. Imbusch, A. Hotz-Wagenblatt, J.P. Mallm, K. Bauer, M. Simon, D. Riegel, A.F. Rendeiro, S. Bittner, L. Sanderink, A. Pant, L. Schmidleithner, K.L. Braband, B. Echtenachter, A. Fischer, V. Giunchiglia, P. Hoffmann, M. Edinger, C. Bock, M. Rehli, B. Brors, C. Schmidl, M. Feuerer, Precursors for Nonlymphoid-Tissue Treg Cells Reside in Secondary Lymphoid Organs and Are Programmed by the Transcription Factor BATF, *Immunity* 52(2) (2020) 295-312 e11.
- [46] R.J. Miragaia, T. Gomes, A. Chomka, L. Jardine, A. Riedel, A.N. Hegazy, N. Whibley, A. Tucci, X. Chen, I. Lindeman, G. Emerton, T. Krausgruber, J. Shields, M. Haniffa, F. Powrie, S.A. Teichmann, Single-Cell Transcriptomics of Regulatory T Cells Reveals Trajectories of Tissue Adaptation, *Immunity* 50(2) (2019) 493-504.e7.
- [47] O.T. Burton, O. Bricard, S. Tareen, V. Gergelits, S. Andrews, L. Biggins, C.P. Roca, C. Whyte, S. Junius, A. Brajic, E. Pasciuto, M. Ali, P. Lemaitre, S.M. Schlenner, H. Ishigame, B.D. Brown, J. Dooley, A. Liston, The tissue-resident regulatory T cell pool is shaped by transient multi-tissue migration and a conserved residency program, *Immunity* 57(7) (2024) 1586-1602 e10.
- [48] M. Feuerer, L. Herrero, D. Cipolletta, A. Naaz, J. Wong, A. Nayer, J. Lee, A.B. Goldfine, C. Benoist, S. Shoelson, D. Mathis, Lean, but not obese, fat is enriched for a unique population of regulatory T cells that affect metabolic parameters, *Nat Med* 15(8) (2009) 930-9.
- [49] S. Knoedler, L. Knoedler, M. Kauke-Navarro, Y. Rinkevich, G. Hundeshagen, L. Harhaus, U. Kneser, B. Pomahac, D.P. Orgill, A.C. Panayi, Regulatory T cells in skin regeneration and wound healing, *Mil Med Res* 10(1) (2023) 49.
- [50] A. Nosbaum, N. Prevel, H.A. Truong, P. Mehta, M. Ettinger, T.C. Scharschmidt, N.H. Ali, M.L. Pauli, A.K. Abbas, M.D. Rosenblum, Cutting Edge: Regulatory T Cells Facilitate Cutaneous Wound Healing, *J Immunol* 196(5) (2016) 2010-4.

Appendix

- [51] N. Arpaia, J.A. Green, B. Molledo, A. Arvey, S. Hemmers, S. Yuan, P.M. Treuting, A.Y. Rudensky, A Distinct Function of Regulatory T Cells in Tissue Protection, *Cell* 162(5) (2015) 1078-89.
- [52] A. Sharma, D. Rudra, Emerging Functions of Regulatory T Cells in Tissue Homeostasis, *Front Immunol* 9 (2018) 883.
- [53] M. Ito, K. Komai, S. Mise-Omata, M. Iizuka-Koga, Y. Noguchi, T. Kondo, R. Sakai, K. Matsuo, T. Nakayama, O. Yoshie, H. Nakatsukasa, S. Chikuma, T. Shichita, A. Yoshimura, Brain regulatory T cells suppress astrogliosis and potentiate neurological recovery, *Nature* 565(7738) (2019) 246-250.
- [54] A. Liesz, E. Suri-Payer, C. Veltkamp, H. Doerr, C. Sommer, S. Rivest, T. Giese, R. Veltkamp, Regulatory T cells are key cerebroprotective immunomodulators in acute experimental stroke, *Nat Med* 15(2) (2009) 192-9.
- [55] Y. Dombrowski, T. O'Hagan, M. Dittmer, R. Penalva, S.R. Mayoral, P. Bankhead, S. Fleville, G. Eleftheriadis, C. Zhao, M. Naughton, R. Hassan, J. Moffat, J. Falconer, A. Boyd, P. Hamilton, I.V. Allen, A. Kissenpfennig, P.N. Moynagh, E. Evergren, B. Perbal, A.C. Williams, R.J. Ingram, J.R. Chan, R.J.M. Franklin, D.C. Fitzgerald, Regulatory T cells promote myelin regeneration in the central nervous system, *Nat Neurosci* 20(5) (2017) 674-680.
- [56] J. Wu, B. Ren, D. Wang, H. Lin, Regulatory T cells in skeletal muscle repair and regeneration: recent insights, *Cell Death Dis* 13(8) (2022) 680.
- [57] D. Burzyn, C. Benoist, D. Mathis, Regulatory T cells in nonlymphoid tissues, *Nat Immunol* 14(10) (2013) 1007-13.
- [58] J. Weirather, U.D. Hofmann, N. Beyersdorf, G.C. Ramos, B. Vogel, A. Frey, G. Ertl, T. Kerkau, S. Frantz, Foxp3⁺ CD4⁺ T cells improve healing after myocardial infarction by modulating monocyte/macrophage differentiation, *Circ Res* 115(1) (2014) 55-67.
- [59] L.D. Faustino, J.W. Griffith, R.A. Rahimi, K. Nepal, D.L. Hamilos, J.L. Cho, B.D. Medoff, J.J. Moon, D.A.A. Vignali, A.D. Luster, Interleukin-33 activates regulatory T cells to suppress innate gammadelta T cell responses in the lung, *Nat Immunol* 21(11) (2020) 1371-1383.

Appendix

- [60] T.K. Goswami, M. Singh, M. Dhawan, S. Mitra, T.B. Emran, A.A. Rabaan, A.A. Mutair, Z.A. Alawi, S. Alhumaid, K. Dhama, Regulatory T cells (Tregs) and their therapeutic potential against autoimmune disorders - Advances and challenges, *Hum Vaccin Immunother* 18(1) (2022) 2035-117.
- [61] T.M. Savage, K.T. Fortson, K. de Los Santos-Alexis, A. Oliveras-Alsina, M. Rouanne, S.S. Rae, J.R. Gamarra, H. Shayya, A. Kornberg, R. Cavero, F. Li, A. Han, R.A. Haeusler, J. Adam, R.F. Schwabe, N. Arpaia, Amphiregulin from regulatory T cells promotes liver fibrosis and insulin resistance in non-alcoholic steatohepatitis, *Immunity* 57(2) (2024) 303-318 e6.
- [62] R.R. Malla, P. Vasudevaraju, R.K. Vempati, M. Rakshmitha, N. Merchant, G.P. Nagaraju, Regulatory T cells: Their role in triple-negative breast cancer progression and metastasis, *Cancer* 128(6) (2022) 1171-1183.
- [63] N.M. Anderson, M.C. Simon, The tumor microenvironment, *Curr Biol* 30(16) (2020) R921-R925.
- [64] E.J. Sayour, P. McLendon, R. McLendon, G. De Leon, R. Reynolds, J. Kresak, J.H. Sampson, D.A. Mitchell, Increased proportion of FoxP3⁺ regulatory T cells in tumor infiltrating lymphocytes is associated with tumor recurrence and reduced survival in patients with glioblastoma, *Cancer Immunol Immunother* 64(4) (2015) 419-27.
- [65] K. Kos, K.E. de Visser, The Multifaceted Role of Regulatory T Cells in Breast Cancer, *Annu Rev Cancer Biol* 5 (2021) 291-310.
- [66] K. Shimizu, M. Nakata, Y. Hirami, T. Yukawa, A. Maeda, K. Tanemoto, Tumor-infiltrating Foxp3⁺ regulatory T cells are correlated with cyclooxygenase-2 expression and are associated with recurrence in resected non-small cell lung cancer, *J Thorac Oncol* 5(5) (2010) 585-90.
- [67] W. Asghar, R. El Assal, H. Shafiee, S. Pitteri, R. Paulmurugan, U. Demirci, Engineering cancer microenvironments for in vitro 3-D tumor models, *Mater Today (Kidlington)* 18(10) (2015) 539-553.
- [68] U.E. Hopken, A. Rehm, Targeting the Tumor Microenvironment of Leukemia and Lymphoma, *Trends Cancer* 5(6) (2019) 351-364.
- [69] D. Hanahan, R.A. Weinberg, The hallmarks of cancer, *Cell* 100(1) (2000) 57-70.

Appendix

- [70] D. Hanahan, R.A. Weinberg, Hallmarks of cancer: the next generation, *Cell* 144(5) (2011) 646-74.
- [71] O. Warburg, On the origin of cancer cells, *Science* 123(3191) (1956) 309-14.
- [72] G.P. Dunn, L.J. Old, R.D. Schreiber, The immunobiology of cancer immunosurveillance and immunoediting, *Immunity* 21(2) (2004) 137-48.
- [73] D. Hanahan, Hallmarks of Cancer: New Dimensions, *Cancer Discov* 12(1) (2022) 31-46.
- [74] P. Baldominos, A. Barbera-Mourelle, O. Barreiro, Y. Huang, A. Wight, J.W. Cho, X. Zhao, G. Estivill, I. Adam, X. Sanchez, S. McCarthy, J. Schaller, Z. Khan, A. Ruzo, R. Pastorello, E.T. Richardson, D. Dillon, P. Montero-Llopis, R. Barroso-Sousa, J. Forman, S.A. Shukla, S.M. Tolaney, E.A. Mittendorf, U.H. von Andrian, K.W. Wucherpfennig, M. Hemberg, J. Agudo, Quiescent cancer cells resist T cell attack by forming an immunosuppressive niche, *Cell* 185(10) (2022) 1694-1708 e19.
- [75] C.H. Chang, J. Qiu, D. O'Sullivan, M.D. Buck, T. Noguchi, J.D. Curtis, Q. Chen, M. Gindin, M.M. Gubin, G.J. van der Windt, E. Tonc, R.D. Schreiber, E.J. Pearce, E.L. Pearce, Metabolic Competition in the Tumor Microenvironment Is a Driver of Cancer Progression, *Cell* 162(6) (2015) 1229-41.
- [76] A.C. Tan, S.J. Bagley, P.Y. Wen, M. Lim, M. Platten, H. Colman, D.M. Ashley, W. Wick, S.M. Chang, E. Galanis, A. Mansouri, S. Khagi, M.P. Mehta, A.B. Heimberger, V.K. Puduvalli, D.A. Reardon, S. Sahebjam, J. Simes, S.J. Antonia, D. Berry, M. Khasraw, Systematic review of combinations of targeted or immunotherapy in advanced solid tumors, *J Immunother Cancer* 9(7) (2021).
- [77] M.F. Sanmamed, L. Chen, A Paradigm Shift in Cancer Immunotherapy: From Enhancement to Normalization, *Cell* 175(2) (2018) 313-326.
- [78] S. Tan, D. Li, X. Zhu, Cancer immunotherapy: Pros, cons and beyond, *Biomed Pharmacother* 124 (2020) 109821.
- [79] C.L. Ventola, Cancer Immunotherapy, Part 3: Challenges and Future Trends, *P T* 42(8) (2017) 514-521.
- [80] Q. Gao, H. Zhu, L. Dong, W. Shi, R. Chen, Z. Song, C. Huang, J. Li, X. Dong, Y. Zhou, Q. Liu, L. Ma, X. Wang, J. Zhou, Y. Liu, E. Boja, A.I. Robles, W. Ma, P. Wang, Y.

Appendix

Li, L. Ding, B. Wen, B. Zhang, H. Rodriguez, D. Gao, H. Zhou, J. Fan, Integrated Proteogenomic Characterization of HBV-Related Hepatocellular Carcinoma, *Cell* 179(5) (2019) 1240.

[81] J. Fu, D.B. Kanne, M. Leong, L.H. Glickman, S.M. McWhirter, E. Lemmens, K. Mechette, J.J. Leong, P. Lauer, W. Liu, K.E. Sivick, Q. Zeng, K.C. Soares, L. Zheng, D.A. Portnoy, J.J. Woodward, D.M. Pardoll, T.W. Dubensky, Jr., Y. Kim, STING agonist formulated cancer vaccines can cure established tumors resistant to PD-1 blockade, *Sci Transl Med* 7(283) (2015) 283ra52.

[82] X. Lin, X. Lu, G. Luo, H. Xiang, Progress in PD-1/PD-L1 pathway inhibitors: From biomacromolecules to small molecules, *Eur J Med Chem* 186 (2020) 111876.

[83] P. Sharma, S. Goswami, D. Raychaudhuri, B.A. Siddiqui, P. Singh, A. Nagarajan, J. Liu, S.K. Subudhi, C. Poon, K.L. Gant, S.M. Herbrich, S. Anandhan, S. Islam, M. Amit, G. Anandappa, J.P. Allison, Immune checkpoint therapy-current perspectives and future directions, *Cell* 186(8) (2023) 1652-1669.

[84] Y. Iwai, M. Ishida, Y. Tanaka, T. Okazaki, T. Honjo, N. Minato, Involvement of PD-L1 on tumor cells in the escape from host immune system and tumor immunotherapy by PD-L1 blockade, *Proc Natl Acad Sci U S A* 99(19) (2002) 12293-7.

[85] P.W. Huang, J.W. Chang, Immune checkpoint inhibitors win the 2018 Nobel Prize, *Biomed J* 42(5) (2019) 299-306.

[86] S.L. Maude, D.T. Teachey, D.L. Porter, S.A. Grupp, CD19-targeted chimeric antigen receptor T-cell therapy for acute lymphoblastic leukemia, *Blood* 125(26) (2015) 4017-23.

[87] S. Kaczanowska, T. Murty, A. Alimadadi, C.F. Contreras, C. Duault, P.B. Subrahmanyam, W. Reynolds, N.A. Gutierrez, R. Baskar, C.J. Wu, F. Michor, J. Altreuter, Y. Liu, A. Jhaveri, V. Duong, H. Anbunathan, C. Ong, H. Zhang, R. Moravec, J. Yu, R. Biswas, S. Van Nostrand, J. Lindsay, M. Pichavant, E. Sotillo, D. Bernstein, A. Carbonell, J. Derdak, J. Klicka-Skeels, J.E. Segal, E. Dombi, S.A. Harmon, B. Turkbey, B. Sahaf, S. Bendall, H. Maecker, S.L. Highfill, D. Stroncek, J. Glod, M. Merchant, C.C. Hedrick, C.L. Mackall, S. Ramakrishna, R.N. Kaplan, Immune

determinants of CAR-T cell expansion in solid tumor patients receiving GD2 CAR-T cell therapy, *Cancer Cell* 42(1) (2024) 35-51 e8.

[88] S.A. Rosenberg, N.P. Restifo, Adoptive cell transfer as personalized immunotherapy for human cancer, *Science* 348(6230) (2015) 62-8.

[89] S.L. Goff, F.O. Smith, J.A. Klapper, R. Sherry, J.R. Wunderlich, S.M. Steinberg, D. White, S.A. Rosenberg, M.E. Dudley, J.C. Yang, Tumor infiltrating lymphocyte therapy for metastatic melanoma: analysis of tumors resected for TIL, *J Immunother* 33(8) (2010) 840-7.

[90] S. Sakaguchi, R. Kawakami, N. Mikami, Treg-based immunotherapy for antigen-specific immune suppression and stable tolerance induction: a perspective, *Immunother Adv* 3(1) (2023) ltad007.

[91] K. Shitara, H. Nishikawa, Regulatory T cells: a potential target in cancer immunotherapy, *Ann N Y Acad Sci* 1417(1) (2018) 104-115.

[92] P. Spiliopoulou, P. Kaur, T. Hammett, G. Di Conza, M. Lahn, Targeting T regulatory (T(reg)) cells in immunotherapy-resistant cancers, *Cancer Drug Resist* 7 (2024) 2.

[93] in: K.K. Holmes, S. Bertozzi, B.R. Bloom, P. Jha (Eds.), *Major Infectious Diseases*, Washington (DC), 2017.

[94] K.R. Rai, P. Shrestha, B. Yang, Y. Chen, S. Liu, M. Maarouf, J.L. Chen, Acute Infection of Viral Pathogens and Their Innate Immune Escape, *Front Microbiol* 12 (2021) 672026.

[95] C. Yang, Z. Liu, Y. Yang, L.J. Cocka, Y. Li, W. Zeng, H. Shen, Chronic viral infection impairs immune memory to a different pathogen, *PLoS Pathog* 20(3) (2024) e1012113.

[96] S. Walton, S. Mandaric, A. Oxenius, CD4 T cell responses in latent and chronic viral infections, *Front Immunol* 4 (2013) 105.

[97] R. Baugh, H. Khaliq, L.W. Seymour, Convergent Evolution by Cancer and Viruses in Evading the NKG2D Immune Response, *Cancers (Basel)* 12(12) (2020).

Appendix

- [98] M. Efremova, R. Vento-Tormo, J.E. Park, S.A. Teichmann, K.R. James, *Immunology in the Era of Single-Cell Technologies*, *Annu Rev Immunol* 38 (2020) 727-757.
- [99] R. Satija, A.K. Shalek, *Heterogeneity in immune responses: from populations to single cells*, *Trends Immunol* 35(5) (2014) 219-29.
- [100] L. Mazzotti, A. Gaimari, S. Bravaccini, R. Maltoni, C. Cerchione, M. Juan, E.A. Navarro, A. Pasetto, D. Nascimento Silva, V. Ancarani, V. Sambri, L. Calabro, G. Martinelli, M. Mazza, *T-Cell Receptor Repertoire Sequencing and Its Applications: Focus on Infectious Diseases and Cancer*, *Int J Mol Sci* 23(15) (2022).
- [101] E. Papalexi, R. Satija, *Single-cell RNA sequencing to explore immune cell heterogeneity*, *Nat Rev Immunol* 18(1) (2018) 35-45.
- [102] M.M. Hossain, P. King, J. Hackett, H.C. Gerard, R. Niwinski, L. Wu, L. Van Kaer, G. Dyson, H. Gibson, A.D. Borowsky, E. Sebzda, *Peripheral-derived regulatory T cells contribute to tumor-mediated immune suppression in a nonredundant manner*, *Proc Natl Acad Sci U S A* 121(36) (2024) e2404916121.
- [103] A. Burocchi, M.P. Colombo, S. Piconese, *Convergences and divergences of thymus- and peripherally derived regulatory T cells in cancer*, *Front Immunol* 4 (2013) 247.
- [104] B. Parang, C.W. Barrett, C.S. Williams, *AOM/DSS Model of Colitis-Associated Cancer*, *Methods Mol Biol* 1422 (2016) 297-307.
- [105] D. Dzhaliilova, N. Zolotova, N. Fokichev, O. Makarova, *Murine models of colorectal cancer: the azoxymethane (AOM)/dextran sulfate sodium (DSS) model of colitis-associated cancer*, *PeerJ* 11 (2023) e16159.
- [106] A. Zhu, J.G. Ibrahim, M.I. Love, *Heavy-tailed prior distributions for sequence count data: removing the noise and preserving large differences*, *Bioinformatics* 35(12) (2019) 2084-2092.
- [107] A.R. Quinlan, I.M. Hall, *BEDTools: a flexible suite of utilities for comparing genomic features*, *Bioinformatics* 26(6) (2010) 841-2.
- [108] R.A. Amezcua, A.T.L. Lun, E. Becht, V.J. Carey, L.N. Carpp, L. Geistlinger, F. Marini, K. Rue-Albrecht, D. Risso, C. Sonesson, L. Waldron, H. Pages, M.L. Smith, W.

Appendix

Huber, M. Morgan, R. Gottardo, S.C. Hicks, Orchestrating single-cell analysis with Bioconductor, *Nat Methods* 17(2) (2020) 137-145.

[109] S. Jin, M.V. Plikus, Q. Nie, CellChat for systematic analysis of cell-cell communication from single-cell transcriptomics, *Nat Protoc* 20(1) (2025) 180-219.

[110] G.X. Zheng, J.M. Terry, P. Belgrader, P. Ryvkin, Z.W. Bent, R. Wilson, S.B. Ziraldo, T.D. Wheeler, G.P. McDermott, J. Zhu, M.T. Gregory, J. Shuga, L. Montesclaros, J.G. Underwood, D.A. Masquelier, S.Y. Nishimura, M. Schnall-Levin, P.W. Wyatt, C.M. Hindson, R. Bharadwaj, A. Wong, K.D. Ness, L.W. Beppu, H.J. Deeg, C. McFarland, K.R. Loeb, W.J. Valente, N.G. Ericson, E.A. Stevens, J.P. Radich, T.S. Mikkelsen, B.J. Hindson, J.H. Bielas, Massively parallel digital transcriptional profiling of single cells, *Nat Commun* 8 (2017) 14049.

[111] Z. Gu, L. Gu, R. Eils, M. Schlesner, B. Brors, circlize Implements and enhances circular visualization in R, *Bioinformatics* 30(19) (2014) 2811-2.

[112] G. Yu, L.G. Wang, Y. Han, Q.Y. He, clusterProfiler: an R package for comparing biological themes among gene clusters, *OMICS* 16(5) (2012) 284-7.

[113] Z. Gu, R. Eils, M. Schlesner, Complex heatmaps reveal patterns and correlations in multidimensional genomic data, *Bioinformatics* 32(18) (2016) 2847-9.

[114] M.I. Love, W. Huber, S. Anders, Moderated estimation of fold change and dispersion for RNA-seq data with DESeq2, *Genome Biol* 15(12) (2014) 550.

[115] D.G. Bunis, J. Andrews, G.K. Fragiadakis, T.D. Burt, M. Sirota, dittoSeq: universal user-friendly single-cell and bulk RNA sequencing visualization toolkit, *Bioinformatics* 36(22-23) (2021) 5535-5536.

[116] A.T.L. Lun, S. Riesenfeld, T. Andrews, T.P. Dao, T. Gomes, J. participants in the 1st Human Cell Atlas, J.C. Marioni, EmptyDrops: distinguishing cells from empty droplets in droplet-based single-cell RNA sequencing data, *Genome Biol* 20(1) (2019) 63.

[117] A.T. Lun, D.J. McCarthy, J.C. Marioni, A step-by-step workflow for low-level analysis of single-cell RNA-seq data with Bioconductor, *F1000Res* 5 (2016) 2122.

Appendix

- [118] J. Rainer, L. Gatto, C.X. Weichenberger, *ensemldb: an R package to create and use Ensembl-based annotation resources*, *Bioinformatics* 35(17) (2019) 3151-3153.
- [119] C.H. Gao, G. Yu, P. Cai, *ggVennDiagram: An Intuitive, Easy-to-Use, and Highly Customizable R Package to Generate Venn Diagram*, *Front Genet* 12 (2021) 706907.
- [120] I. Korsunsky, N. Millard, J. Fan, K. Slowikowski, F. Zhang, K. Wei, Y. Baglaenko, M. Brenner, P.R. Loh, S. Raychaudhuri, *Fast, sensitive and accurate integration of single-cell data with Harmony*, *Nat Methods* 16(12) (2019) 1289-1296.
- [121] F. Marini, J. Linke, H. Binder, *ideal: an R/Bioconductor package for interactive differential expression analysis*, *BMC Bioinformatics* 21(1) (2020) 565.
- [122] M.E. Ritchie, B. Phipson, D. Wu, Y. Hu, C.W. Law, W. Shi, G.K. Smyth, *limma powers differential expression analyses for RNA-sequencing and microarray studies*, *Nucleic Acids Res* 43(7) (2015) e47.
- [123] F. Marini, H. Binder, *pcaExplorer: an R/Bioconductor package for interacting with RNA-seq principal components*, *BMC Bioinformatics* 20(1) (2019) 331.
- [124] R.C. Team, *R: A Language and Environment for Statistical Computing*, R Foundation for Statistical Computing, Vienna, Austria, 2024.
- [125] R. Team, *RStudio: Integrated Development for R*, RStudio, PBC, Boston, MA, 2020.
- [126] Y. Liao, G.K. Smyth, W. Shi, *featureCounts: an efficient general purpose program for assigning sequence reads to genomic features*, *Bioinformatics* 30(7) (2014) 923-30.
- [127] H. Li, B. Handsaker, A. Wysoker, T. Fennell, J. Ruan, N. Homer, G. Marth, G. Abecasis, R. Durbin, S. Genome Project Data Processing, *The Sequence Alignment/Map format and SAMtools*, *Bioinformatics* 25(16) (2009) 2078-9.
- [128] D.J. McCarthy, K.R. Campbell, A.T. Lun, Q.F. Wills, *Scater: pre-processing, quality control, normalization and visualization of single-cell RNA-seq data in R*, *Bioinformatics* 33(8) (2017) 1179-1186.

- [129] P.L. Germain, A. Lun, C. Garcia Meixide, W. Macnair, M.D. Robinson, Doublet identification in single-cell sequencing data using scDblFinder, *F1000Res* 10 (2021) 979.
- [130] Z. Gu, D. Hubschmann, spiralize: an R package for visualizing data on spirals, *Bioinformatics* 38(5) (2022) 1434-1436.
- [131] A. Dobin, C.A. Davis, F. Schlesinger, J. Drenkow, C. Zaleski, S. Jha, P. Batut, M. Chaisson, T.R. Gingeras, STAR: ultrafast universal RNA-seq aligner, *Bioinformatics* 29(1) (2013) 15-21.
- [132] A. Alexa, J. Rahnenfuhrer, T. Lengauer, Improved scoring of functional groups from gene expression data by decorrelating GO graph structure, *Bioinformatics* 22(13) (2006) 1600-7.
- [133] Z. Ji, H. Ji, TSCAN: Pseudo-time reconstruction and evaluation in single-cell RNA-seq analysis, *Nucleic Acids Res* 44(13) (2016) e117.
- [134] B. Schrors, B.J. Hos, I.G. Yildiz, M. Lower, F. Lang, C. Holtstrater, J. Becker, M. Vormehr, U. Sahin, F. Ossendorp, M. Diken, MC38 colorectal tumor cell lines from two different sources display substantial differences in transcriptome, mutanome and neoantigen expression, *Front Immunol* 14 (2023) 1102282.
- [135] T.H. Corbett, D.P. Griswold, Jr., B.J. Roberts, J.C. Peckham, F.M. Schabel, Jr., Tumor induction relationships in development of transplantable cancers of the colon in mice for chemotherapy assays, with a note on carcinogen structure, *Cancer Res* 35(9) (1975) 2434-9.
- [136] J.C. Kim, X. Liu, K. Fitzgerald, J.S. Eng, J. Orf, S.A. O'Brien, B. Belmontes, A.J. Casbon, S.V. Novitskiy, K.V. Tarbell, J. DeVoss, J.G. Egen, Brief report: STING expressed in tumor and non-tumor compartments has distinct roles in regulating anti-tumor immunity, *Cancer Immunol Immunother* 72(5) (2023) 1327-1335.
- [137] B. Homet Moreno, J.M. Zaretsky, A. Garcia-Diaz, J. Tsoi, G. Parisi, L. Robert, K. Meeth, A. Ndoye, M. Bosenberg, A.T. Weeraratna, T.G. Graeber, B. Comin-Anduix, S. Hu-Lieskovan, A. Ribas, Response to Programmed Cell Death-1 Blockade in a Murine Melanoma Syngeneic Model Requires Costimulation, CD4, and CD8 T Cells, *Cancer Immunol Res* 4(10) (2016) 845-857.

- [138] I.J. Fidler, G.L. Nicolson, Organ selectivity for implantation survival and growth of B16 melanoma variant tumor lines, *J Natl Cancer Inst* 57(5) (1976) 1199-202.
- [139] M.S. Hossain, H. Karuniawati, A.A. Jairoun, Z. Urbi, J. Ooi, A. John, Y.C. Lim, K.M.K. Kibria, A.K.M. Mohiuddin, L.C. Ming, K.W. Goh, M.A. Hadi, Colorectal Cancer: A Review of Carcinogenesis, Global Epidemiology, Current Challenges, Risk Factors, Preventive and Treatment Strategies, *Cancers (Basel)* 14(7) (2022).
- [140] C.G. Whitem, A.D. Williams, C.S. Williams, Murine Colitis modeling using Dextran Sulfate Sodium (DSS), *J Vis Exp* (35) (2010).
- [141] M.J.T. Stubbington, T. Lonnerberg, V. Proserpio, S. Clare, A.O. Speak, G. Dougan, S.A. Teichmann, T cell fate and clonality inference from single-cell transcriptomes, *Nat Methods* 13(4) (2016) 329-332.
- [142] L. Zhang, X. Yu, L. Zheng, Y. Zhang, Y. Li, Q. Fang, R. Gao, B. Kang, Q. Zhang, J.Y. Huang, H. Konno, X. Guo, Y. Ye, S. Gao, S. Wang, X. Hu, X. Ren, Z. Shen, W. Ouyang, Z. Zhang, Lineage tracking reveals dynamic relationships of T cells in colorectal cancer, *Nature* 564(7735) (2018) 268-272.
- [143] A.S. Nedwed, S.S. Helbich, K.L. Braband, M. Volkmar, M. Delacher, F. Marini, Using combined single-cell gene expression, TCR sequencing and cell surface protein barcoding to characterize and track CD4⁺ T cell clones from murine tissues, *Front Immunol* 14 (2023) 1241283.
- [144] N.M. Xi, J.J. Li, Benchmarking Computational Doublet-Detection Methods for Single-Cell RNA Sequencing Data, *Cell Syst* 12(2) (2021) 176-194 e6.
- [145] M. Permanyer, B. Bosnjak, S. Glage, M. Friedrichsen, S. Floess, J. Huehn, G.E. Patzer, I. Odak, N. Eckert, R. Zargari, L. Ospina-Quintero, H. Georgiev, R. Forster, Efficient IL-2R signaling differentially affects the stability, function, and composition of the regulatory T-cell pool, *Cell Mol Immunol* 18(2) (2021) 398-414.
- [146] S. Dias, A. D'Amico, E. Cretney, Y. Liao, J. Tellier, C. Bruggeman, F.F. Almeida, J. Leahy, G.T. Belz, G.K. Smyth, W. Shi, S.L. Nutt, Effector Regulatory T Cell Differentiation and Immune Homeostasis Depend on the Transcription Factor Myb, *Immunity* 46(1) (2017) 78-91.

Appendix

- [147] R.J. Miragaia, T. Gomes, A. Chomka, L. Jardine, A. Riedel, A.N. Hegazy, N. Whibley, A. Tucci, X. Chen, I. Lindeman, G. Emerton, T. Krausgruber, J. Shields, M. Haniffa, F. Powrie, S.A. Teichmann, Single-Cell Transcriptomics of Regulatory T Cells Reveals Trajectories of Tissue Adaptation, *Immunity* 50(2) (2019) 493-504 e7.
- [148] A. Ludt, A. Ustjanzew, H. Binder, K. Strauch, F. Marini, Interactive and Reproducible Workflows for Exploring and Modeling RNA-seq Data with pcaExplorer, Ideal, and GeneTonic, *Curr Protoc* 2(4) (2022) e411.
- [149] F. Marini, A. Ludt, J. Linke, K. Strauch, GeneTonic: an R/Bioconductor package for streamlining the interpretation of RNA-seq data, *BMC Bioinformatics* 22(1) (2021) 610.
- [150] C. Trapnell, D. Cacchiarelli, J. Grimsby, P. Pokharel, S. Li, M. Morse, N.J. Lennon, K.J. Livak, T.S. Mikkelsen, J.L. Rinn, The dynamics and regulators of cell fate decisions are revealed by pseudotemporal ordering of single cells, *Nat Biotechnol* 32(4) (2014) 381-386.
- [151] M. Schmitt, F.R. Greten, The inflammatory pathogenesis of colorectal cancer, *Nat Rev Immunol* 21(10) (2021) 653-667.
- [152] S. Jin, C.F. Guerrero-Juarez, L. Zhang, I. Chang, R. Ramos, C.H. Kuan, P. Myung, M.V. Plikus, Q. Nie, Inference and analysis of cell-cell communication using CellChat, *Nat Commun* 12(1) (2021) 1088.
- [153] W.W. Overwijk, N.P. Restifo, B16 as a mouse model for human melanoma, *Curr Protoc Immunol Chapter 20* (2001) Unit 20 1.
- [154] F. Fueyo-Gonzalez, M. McGinty, M. Ningoo, L. Anderson, C. Cantarelli, A. Andrea, M. Demir, I. Llaudo, C. Purroy, N. Marjanovic, D. Heja, S.C. Sealfon, P.S. Heeger, P. Cravedi, M. Fribourg, Interferon-beta acts directly on T cells to prolong allograft survival by enhancing regulatory T cell induction through Foxp3 acetylation, *Immunity* 55(3) (2022) 459-474 e7.
- [155] M. Becker, S.M. Dirschl, M.G. Scherm, I. Serr, C. Daniel, Niche-specific control of tissue function by regulatory T cells-Current challenges and perspectives for targeting metabolic disease, *Cell Metab* 36(2) (2024) 229-239.

Appendix

- [156] Y. Ding, J. Xu, J.S. Bromberg, Regulatory T cell migration during an immune response, *Trends Immunol* 33(4) (2012) 174-80.
- [157] R. Roozendaal, R.E. Mebius, Stromal cell-immune cell interactions, *Annu Rev Immunol* 29 (2011) 23-43.
- [158] W. Piao, L. Wu, Y. Xiong, G.C. Zapas, C.M. Paluskievicz, R.S. Oakes, S.M. Pettit, M.L. Sleeth, K.L. Hippen, J. Schmitz, P. Ivanyi, A.C. Shetty, Y. Song, D. Kong, Y. Lee, L. Li, M.W. Shirkey, A. Kensiski, A. Alvi, K. Ho, V. Saxena, J.H. Brasen, C.M. Jewell, B.R. Blazar, R. Abdi, J.S. Bromberg, Regulatory T cells crosstalk with tumor cells and endothelium through lymphotoxin signaling, *Nat Commun* 15(1) (2024) 10468.
- [159] W. Piao, V. Kasinath, V. Saxena, R. Lakhan, J. Iyyathurai, J.S. Bromberg, LTbetaR Signaling Controls Lymphatic Migration of Immune Cells, *Cells* 10(4) (2021).
- [160] E. Armingol, H.M. Baghdassarian, C. Martino, A. Perez-Lopez, C. Aamodt, R. Knight, N.E. Lewis, Context-aware deconvolution of cell-cell communication with Tensor-cell2cell, *Nat Commun* 13(1) (2022) 3665.
- [161] S.A. Luther, T.K. Vogt, S. Siegert, Guiding blind T cells and dendritic cells: A closer look at fibroblastic reticular cells found within lymph node T zones, *Immunol Lett* 138(1) (2011) 9-11.
- [162] D. Banczyk, K. Kalies, L. Nachbar, L. Bergmann, P. Schmidt, U. Bode, B. Teegen, P. Steven, T. Lange, J. Textor, R.J. Ludwig, W. Stocker, P. Konig, E. Bell, J. Westermann, Activated CD4⁺ T cells enter the splenic T-cell zone and induce autoantibody-producing germinal centers through bystander activation, *Eur J Immunol* 44(1) (2014) 93-102.
- [163] S. Sanjabi, S.A. Oh, M.O. Li, Regulation of the Immune Response by TGF-beta: From Conception to Autoimmunity and Infection, *Cold Spring Harb Perspect Biol* 9(6) (2017).
- [164] R.A. Flavell, S. Sanjabi, S.H. Wrzesinski, P. Licona-Limon, The polarization of immune cells in the tumour environment by TGFbeta, *Nat Rev Immunol* 10(8) (2010) 554-67.

Appendix

- [165] E. Battle, J. Massague, Transforming Growth Factor-beta Signaling in Immunity and Cancer, *Immunity* 50(4) (2019) 924-940.
- [166] S.A. Oh, M. Liu, B.G. Nixon, D. Kang, A. Toure, M. Bivona, M.O. Li, Foxp3-independent mechanism by which TGF-beta controls peripheral T cell tolerance, *Proc Natl Acad Sci U S A* 114(36) (2017) E7536-E7544.
- [167] H.W. Lim, P. Hillsamer, C.H. Kim, Regulatory T cells can migrate to follicles upon T cell activation and suppress GC-Th cells and GC-Th cell-driven B cell responses, *J Clin Invest* 114(11) (2004) 1640-9.
- [168] R.J. Greenwald, G.J. Freeman, A.H. Sharpe, The B7 family revisited, *Annu Rev Immunol* 23 (2005) 515-48.
- [169] T. Duhon, R. Duhon, A. Lanzavecchia, F. Sallusto, D.J. Campbell, Functionally distinct subsets of human FOXP3+ Treg cells that phenotypically mirror effector Th cells, *Blood* 119(19) (2012) 4430-40.
- [170] K.S. Smigiel, E. Richards, S. Srivastava, K.R. Thomas, J.C. Dudda, K.D. Klonowski, D.J. Campbell, CCR7 provides localized access to IL-2 and defines homeostatically distinct regulatory T cell subsets, *J Exp Med* 211(1) (2014) 121-36.
- [171] M. Vocanson, A. Rozieres, A. Hennino, G. Poyet, V. Gaillard, S. Renaudineau, A. Achachi, J. Benetiere, D. Kaiserlian, B. Dubois, J.F. Nicolas, Inducible costimulator (ICOS) is a marker for highly suppressive antigen-specific T cells sharing features of TH17/TH1 and regulatory T cells, *J Allergy Clin Immunol* 126(2) (2010) 280-9, 289 e1-7.
- [172] N. Joller, E. Lozano, P.R. Burkett, B. Patel, S. Xiao, C. Zhu, J. Xia, T.G. Tan, E. Sefik, V. Yajnik, A.H. Sharpe, F.J. Quintana, D. Mathis, C. Benoist, D.A. Hafler, V.K. Kuchroo, Treg cells expressing the coinhibitory molecule TIGIT selectively inhibit proinflammatory Th1 and Th17 cell responses, *Immunity* 40(4) (2014) 569-81.
- [173] K.L. Dennis, N.R. Blatner, F. Gounari, K. Khazaie, Current status of interleukin-10 and regulatory T-cells in cancer, *Curr Opin Oncol* 25(6) (2013) 637-45.
- [174] M. Gobert, I. Treilleux, N. Bendriss-Vermare, T. Bachelot, S. Goddard-Leon, V. Arfi, C. Biota, A.C. Doffin, I. Durand, D. Olive, S. Perez, N. Pasqual, C. Faure, I. Ray-Coquard, A. Puisieux, C. Caux, J.Y. Blay, C. Menetrier-Caux, Regulatory T cells

Appendix

recruited through CCL22/CCR4 are selectively activated in lymphoid infiltrates surrounding primary breast tumors and lead to an adverse clinical outcome, *Cancer Res* 69(5) (2009) 2000-9.

[175] J. Faget, C. Biota, T. Bachelot, M. Gobert, I. Treilleux, N. Goutagny, I. Durand, S. Leon-Goddard, J.Y. Blay, C. Caux, C. Menetrier-Caux, Early detection of tumor cells by innate immune cells leads to T(reg) recruitment through CCL22 production by tumor cells, *Cancer Res* 71(19) (2011) 6143-52.

[176] W. Liu, X. Wei, L. Li, X. Wu, J. Yan, H. Yang, F. Song, CCR4 mediated chemotaxis of regulatory T cells suppress the activation of T cells and NK cells via TGF-beta pathway in human non-small cell lung cancer, *Biochem Biophys Res Commun* 488(1) (2017) 196-203.

[177] N.N. Zhang, J.N. Chen, L. Xiao, F. Tang, Z.G. Zhang, Y.W. Zhang, Z.Y. Feng, Y. Jiang, C.K. Shao, Accumulation Mechanisms of CD4(+)CD25(+)FOXP3(+) Regulatory T Cells in EBV-associated Gastric Carcinoma, *Sci Rep* 5 (2015) 18057.

[178] H. Svensson, V. Olofsson, S. Lundin, C. Yakkala, S. Bjorck, L. Borjesson, B. Gustavsson, M. Quiding-Jarbrink, Accumulation of CCR4(+)CTLA-4 FOXP3(+)CD25(hi) regulatory T cells in colon adenocarcinomas correlate to reduced activation of conventional T cells, *PLoS One* 7(2) (2012) e30695.

[179] L.F. Loffredo, T.M. Savage, O.R. Ringham, N. Arpaia, Treg-tissue cell interactions in repair and regeneration, *J Exp Med* 221(6) (2024).

[180] N. Nishiyama, C. Nakahashi-Oda, A. Shibuya, Interferon-beta promotes the survival and function of induced regulatory T cells, *Cytokine* 158 (2022) 156009.

[181]

[182] Y. Li, Q. Cui, B. Zhou, J. Zhang, R. Guo, Y. Wang, X. Xu, RSAD2, a pyroptosis-related gene, predicts the prognosis and immunotherapy response for colorectal cancer, *Am J Cancer Res* 14(5) (2024) 2507-2522.

[183] M. Bai, Q. Pan, C. Sun, Tumor Purity Coexpressed Genes Related to Immune Microenvironment and Clinical Outcomes of Lung Adenocarcinoma, *J Oncol* 2021 (2021) 9548648.

Appendix

- [184] S. Tiberti, C. Catozzi, O. Croci, M. Ballerini, D. Cagnina, C. Soriani, C. Scirgolea, Z. Gong, J. He, A.D. Macandog, A. Nabinejad, C.B. Nava Lauson, A. Quinte, G. Bertalot, W.L. Petz, S.P. Ravenda, V. Licursi, P. Paci, M. Rasponi, L. Rotta, N. Fazio, G. Ren, U. Fumagalli-Romario, M.H. Schaefer, S. Campaner, E. Lugli, L. Nezi, T. Manzo, GZMK(high) CD8(+) T effector memory cells are associated with CD15(high) neutrophil abundance in non-metastatic colorectal tumors and predict poor clinical outcome, *Nat Commun* 13(1) (2022) 6752.
- [185] M. Zhai, J. Miao, R. Zhang, R. Liu, F. Li, Y. Shen, T. Wang, X. Xu, G. Gao, J. Hu, A. He, J. Bai, KIF22 promotes multiple myeloma progression by regulating the CDC25C/CDK1/cyclinB1 pathway, *J Cancer Res Clin Oncol* 150(5) (2024) 239.
- [186] W. Zhang, Y. Li, S. Xin, L. Yang, M. Jiang, Y. Xin, Y. Wang, P. Cao, S. Zhang, Y. Yang, J. Lu, The emerging roles of IFIT3 in antiviral innate immunity and cellular biology, *J Med Virol* 95(1) (2023) e28259.
- [187] C.M. Rueda, C.M. Jackson, C.A. Chougnet, Regulatory T-Cell-Mediated Suppression of Conventional T-Cells and Dendritic Cells by Different cAMP Intracellular Pathways, *Front Immunol* 7 (2016) 216.
- [188] H. Ehrentraut, J.A. Westrich, H.K. Eltzschig, E.T. Clambey, Adora2b adenosine receptor engagement enhances regulatory T cell abundance during endotoxin-induced pulmonary inflammation, *PLoS One* 7(2) (2012) e32416.
- [189] J. Stagg, U. Divisekera, H. Duret, T. Sparwasser, M.W. Teng, P.K. Darcy, M.J. Smyth, CD73-deficient mice have increased antitumor immunity and are resistant to experimental metastasis, *Cancer Res* 71(8) (2011) 2892-900.
- [190] X. Sun, Y. Wu, W. Gao, K. Enjyoji, E. Csizmadia, C.E. Muller, T. Murakami, S.C. Robson, CD39/ENTPD1 expression by CD4+Foxp3+ regulatory T cells promotes hepatic metastatic tumor growth in mice, *Gastroenterology* 139(3) (2010) 1030-40.
- [191] I.M. Stromnes, J.M. Goverman, Osteopontin-induced survival of T cells, *Nat Immunol* 8(1) (2007) 19-20.
- [192] X. Xu, J. Lin, J. Wang, Y. Wang, Y. Zhu, J. Wang, J. Guo, SPP1 expression indicates outcome of immunotherapy plus tyrosine kinase inhibition in advanced renal cell carcinoma, *Hum Vaccin Immunother* 20(1) (2024) 2350101.

- [193] R.G. Gupta, F. Li, J. Roszik, G. Lizee, Exploiting Tumor Neoantigens to Target Cancer Evolution: Current Challenges and Promising Therapeutic Approaches, *Cancer Discov* 11(5) (2021) 1024-1039.
- [194] H. Strandt, D.F. Pinheiro, D.H. Kaplan, D. Wirth, I.K. Gratz, P. Hammerl, J. Thalhamer, A. Stoecklinger, Neoantigen Expression in Steady-State Langerhans Cells Induces CTL Tolerance, *J Immunol* 199(5) (2017) 1626-1634.
- [195] M.J. Barnden, J. Allison, W.R. Heath, F.R. Carbone, Defective TCR expression in transgenic mice constructed using cDNA-based alpha- and beta-chain genes under the control of heterologous regulatory elements, *Immunol Cell Biol* 76(1) (1998) 34-40.
- [196] S.R. Clarke, M. Barnden, C. Kurts, F.R. Carbone, J.F. Miller, W.R. Heath, Characterization of the ovalbumin-specific TCR transgenic line OT-I: MHC elements for positive and negative selection, *Immunol Cell Biol* 78(2) (2000) 110-7.
- [197] J.M. Robertson, P.E. Jensen, B.D. Evavold, DO11.10 and OT-II T cells recognize a C-terminal ovalbumin 323-339 epitope, *J Immunol* 164(9) (2000) 4706-12.
- [198] H.G. Roeder, S. Hoff, S.Y. Tseng, S. Berndt, M. Trautwein, K. Filarsky, U. Gritzan, J. Camps, W.M. Nadler, J. Grudzinska-Goebel, P. Ellinger, T. Pesch, C.F. Soon, M. Geyer, K. Gluske, B. Stelte-Ludwig, M. Gorjanacz, Selective depletion of tumor-infiltrating regulatory T cells with BAY 3375968, a novel Fc-optimized anti-CCR8 antibody, *Clin Exp Med* 24(1) (2024) 122.
- [199] Y. Kidani, W. Nogami, Y. Yasumizu, A. Kawashima, A. Tanaka, Y. Sonoda, Y. Tona, K. Nashiki, R. Matsumoto, M. Hagiwara, M. Osaki, K. Dohi, T. Kanazawa, A. Ueyama, M. Yoshikawa, T. Yoshida, M. Matsumoto, K. Hojo, S. Shinonome, H. Yoshida, M. Hirata, M. Haruna, Y. Nakamura, D. Motooka, D. Okuzaki, Y. Sugiyama, M. Kinoshita, T. Okuno, T. Kato, K. Hatano, M. Uemura, R. Imamura, K. Yokoi, A. Tanemura, Y. Shintani, T. Kimura, N. Nonomura, H. Wada, M. Mori, Y. Doki, N. Ohkura, S. Sakaguchi, CCR8-targeted specific depletion of clonally expanded Treg cells in tumor tissues evokes potent tumor immunity with long-lasting memory, *Proc Natl Acad Sci U S A* 119(7) (2022).

9. Marker genes for gene expression signatures

9.1. Skin Treg signature

gene	p-value	logFC
<i>Tnfrsf4</i>	0	2,5
<i>Ikzf2</i>	0	2,5
<i>Hopx</i>	0	2,5
<i>Ctla4</i>	0	2,2
<i>Cd74</i>	0	1,6
<i>Foxp3</i>	0	1,7
<i>Tox</i>	0	1,7
<i>Tnfrsf9</i>	0	1,5
<i>Nfkbia</i>	0	2,1
<i>Tnfrsf18</i>	0	1,4
<i>Cd83</i>	0	1,4
<i>Ubald2</i>	0	2,3
<i>Lmna</i>	0	3,2
<i>Arl5a</i>	0	1,2
<i>Itgav</i>	0	1,4
<i>Gm2a</i>	0	1,3
<i>Tigit</i>	0	1,2
<i>Itm2c</i>	0	1,2
<i>Cd81</i>	0	1,0

9.2. Colon tTreg signature

gene name	p-value	logFC
<i>Tnfrsf9</i>	6,86E-93	2,2
<i>Ikzf2</i>	1,1E-111	2,1
<i>Zfp36l1</i>	7,3E-106	2,4
<i>Ctla4</i>	7,3E-141	3,1

Marker genes for gene expression signatures

<i>Klrg1</i>	3,42E-86	2,0
<i>Dusp1</i>	1,2E-175	4,3
<i>Nfkbia</i>	4,85E-93	2,4
<i>Areg</i>	2,43E-50	1,9
<i>Tnfrsf4</i>	4,46E-95	2,3
<i>Foxp3</i>	5,4E-71	1,6

9.3. Colon pTreg signature

gene name	p-value	logFC
<i>Ctla4</i>	0E+00	3,4
<i>Zfp36l1</i>	8E-161	1,7
<i>Tigit</i>	1E-200	2,0
<i>Capg</i>	3E-301	2,4
<i>Foxp3</i>	6E-160	1,5
<i>Il10</i>	2E-102	1,5
<i>Tnfrsf9</i>	8E-107	1,4
<i>Gzmb</i>	4E-69	1,4
<i>Lag3</i>	1E-120	1,5
<i>Tnfrsf4</i>	2E-149	1,8
<i>Itm2b</i>	4E-253	1,9
<i>Maf</i>	5E-246	2,3
<i>Icos</i>	2E-206	1,9
<i>Neb</i>	3E-120	1,2
<i>Fgl2</i>	3E-158	1,6
<i>Mmd</i>	2E-108	1,1
<i>Ptms</i>	2E-137	1,4

Marker genes for gene expression signatures

9.4. SLE NLT-like Treg signature

gene name	p-value	logFC
<i>Ighm</i>	4,73E-41	0,9
<i>Ifi272a</i>	2,51E-27	0,8
<i>Pglyrp1</i>	7,79E-32	0,7
<i>Shisa5</i>	2,19E-28	0,6
<i>Cyba</i>	1,08E-18	0,5
<i>Ptprcap</i>	1,11E-14	0,5
<i>Cst7</i>	2,06E-33	0,4
<i>Prkch</i>	9,92E-24	0,4
<i>Mbnl1</i>	1,83E-10	0,4
<i>Xist</i>	8,06E-11	0,4
<i>Dock2</i>	1,85E-09	0,4
<i>Ephx1</i>	9,19E-15	0,3
<i>Tap1</i>	2,17E-11	0,3
<i>Irf1</i>	1,42E-09	0,3
<i>Lrba</i>	2,87E-20	0,3
<i>Il2rb</i>	1,35E-15	0,3
<i>Pycard</i>	1,05E-14	0,3
<i>Zbtb20</i>	1,13E-09	0,3
<i>Tapbp</i>	6,81E-09	0,3
<i>Apobec3</i>	1,68E-09	0,3
<i>Slc24a3</i>	5,2E-135	0,3
<i>Irf2</i>	5,48E-09	0,3
<i>Nrn1</i>	8,03E-22	0,3
<i>Cd3d</i>	2,21E-11	0,3
<i>Sdf4</i>	9,09E-10	0,3
<i>Myo1f</i>	5,88E-12	0,3
<i>Gramd1b</i>	6,92E-12	0,3
<i>Tm9sf2</i>	1,31E-12	0,3
<i>Cep112</i>	3,8E-17	0,3

Marker genes for gene expression signatures

9.5. Core Treg signature

gene name	p-value	logFC
<i>Foxp3</i>	0	1,8629989
<i>Ikzf2</i>	0	0.8798949
<i>Tnfrsf4</i>	0	0.7115828
<i>Izumo1r</i>	0	0.6989631
<i>Ctla4</i>	0	0.6113174
<i>Ighm</i>	1,6E-305	0.5452426
<i>Il2ra</i>	0	0.4564178
<i>Tnfrsf18</i>	1,9E-270	0.4989956
<i>Cd74</i>	0	0.5044473
<i>Shisa5</i>	0	0.4761345
<i>Ltb</i>	2E-291	0.5543692
<i>Cd27</i>	8E-283	0.3777700
<i>Tnfrsf9</i>	7E-262	0.4462104
<i>Ifi2712a</i>	3E-257	0.5425519
<i>Rgs10</i>	5E-249	0.4226842
<i>Cd81</i>	3E-234	0.3518428
<i>Tigit</i>	3E-230	0.3949213
<i>Arl5a</i>	1E-216	0.2888677
<i>Tspan32</i>	1E-207	0.3122513
<i>Ypel3</i>	1E-200	0.3499318
<i>Ctss</i>	5E-196	0.3237298
<i>Gimap3</i>	3E-187	0.4178310
<i>Tox</i>	3E-187	0.3884186
<i>Samhd1</i>	3E-181	0.3536239
<i>Ptprcap</i>	4E-180	0.3447317
<i>Limd2</i>	3E-178	0.3630621
<i>Pglyrp1</i>	3E-177	0.2936310
<i>Smc4</i>	8E-168	0.3345896

Marker genes for gene expression signatures

<i>Rhoh</i>	2E-163	0.2989581
<i>H2afz</i>	6E-149	0.3863511
<i>Peli1</i>	2E-146	0.2920431
<i>Cd83</i>	2E-145	0.2667446
<i>Rnaset2a</i>	9E-137	0.2576960
<i>Itm2c</i>	9E-129	0.2825780
<i>AW112010</i>	5E-128	0.4000786
<i>Gimap1</i>	1E-124	0.2783984
<i>Stat1</i>	2E-124	0.3377209
<i>Inpp4b</i>	1E-117	0.3430236
<i>Chd3</i>	3E-107	0.2505315
<i>Hopx</i>	2E-106	0.3166784
<i>Serinc3</i>	4E-101	0.2586610
<i>Gimap4</i>	4E-180	0.2555963

9.6. Regenerative Treg signature

gene name	p-value	logFC
<i>Ikzf2</i>	0	1,9
<i>Tnfrsf4</i>	0	2,0
<i>Areg</i>	0	1,8
<i>Hopx</i>	0	1,9
<i>Ctla4</i>	0	1,7
<i>Foxp3</i>	0	1,2
<i>Tox</i>	1,5E-300	1,2
<i>Cd74</i>	2,7E-295	1,3
<i>Tnfrsf18</i>	3,9E-279	1,1
<i>Nfkbia</i>	2,5E-254	1,3
<i>Itgav</i>	5,1E-237	1,0
<i>Tnfrsf9</i>	2,2E-208	1,2
<i>Ubald2</i>	2,7E-164	1,0
<i>Cd83</i>	4,2E-153	1,1

Marker genes for gene expression signatures

<i>Areg.1</i>	5,6E-139	2,4
<i>Dusp1</i>	6,4E-36	1,1
<i>Srgn</i>	2,08E-72	1,6
<i>S100a11</i>	6,49E-71	1,1
<i>Tigit</i>	2E-68	1,2
<i>Junb</i>	7,6E-50	1,2
<i>S100a6</i>	1,81E-38	1,1

9.7. Suppressive Treg signature

gene name	p-value	logFC
<i>Ctla4</i>	0	1,973488
<i>Tnfrsf4</i>	0	0,732925
<i>Ikzf2</i>	0	0,659215
<i>Foxp3</i>	0	0,542675
<i>Tigit</i>	0	0,503058
<i>Hopx</i>	2,9E-245	0,460024
<i>Tnfrsf9</i>	3,7E-278	0,451821
<i>Maf</i>	0	0,448842
<i>Tox</i>	3,5E-258	0,444689
<i>Tnfrsf18</i>	2,1E-246	0,420139
<i>Cd74</i>	2,3E-230	0,417279
<i>AW112010</i>	1,1E-124	0,381878
<i>Icos</i>	1,2E-163	0,374608
<i>Izumo1r</i>	4,2E-116	0,371708
<i>Arl5a</i>	0	0,364448
<i>Il2ra</i>	2,9E-183	0,32581
<i>Hif1a</i>	2,7E-176	0,312915
<i>Ifi27l2a</i>	1,44E-87	0,309833
<i>Cd83</i>	4,8E-196	0,298909
<i>Nfkbia</i>	4,29E-77	0,295476
<i>Ighm</i>	1E-110	0,289926

Marker genes for gene expression signatures

<i>Malat1</i>	9,28E-97	0,288474
<i>Itm2c</i>	9,2E-137	0,28288
<i>Itgav</i>	7,9E-211	0,266549
<i>Peli1</i>	7,5E-124	0,260765
<i>Serinc3</i>	9,1E-104	0,253019

9.8. Genes upregulated in all tumor tissue

gene name
<i>Plek</i>
<i>Kif22</i>
<i>Ifit3b</i>
<i>Rsad2</i>
<i>Gzmk</i>

9.9. Genes upregulated in the overall DGE analysis and BioMart Database

gene name
<i>Adora2b</i>
<i>Ifi204</i>
<i>Smpdl3b</i>
<i>Gzma</i>
<i>Cd14</i>
<i>Spp1</i>
<i>Lag3</i>
<i>Ticam2</i>
<i>Sell</i>
<i>Lacc1</i>
<i>Ccl2</i>
<i>Cybb</i>
<i>Tlr6</i>

Marker genes for gene expression signatures

<i>Lgals3bp</i>
<i>Tbx21</i>
<i>Pparg</i>
<i>Il12rb2</i>
<i>Gimap5</i>
<i>Gfi1</i>
<i>Ramp1</i>
<i>Aurka</i>
<i>Ifit2</i>
<i>Pdcd1</i>
<i>Slc37a2</i>
<i>Cxcr3</i>
<i>Id1</i>
<i>Tpx2</i>
<i>Nkg7</i>
<i>Klrc1</i>
<i>Aurkb</i>
<i>Psmb10</i>
<i>Tlr2</i>

10. Curriculum vitae

Name Sara Salome Clara Helbich
Birth date [REDACTED]
Address [REDACTED]
Nationality German
Contact helbichs@uni-mainz.de

Education

October 2019 – October 2021	Goethe University of Frankfurt Drug research, Msc
October 2016 – October 2019	University of Lübeck Molecular nutrition medicine, Bsc

Professional Experience

Since October 2021	PhD Student University Medical Center Mainz Institute of Immunology, AG Delacher
March 2021 – October 2021	Master Thesis Max-Delbrück Center Berlin Molecular Medicine, AG Höpken
September 2020 – December 2020	Internship Goethe University of Frankfurt Pharmacology, AG Schmidtko
September 2020 – December 2020	Bachelor Thesis University of Lübeck Neurosurgery, AG Zechel

Publications

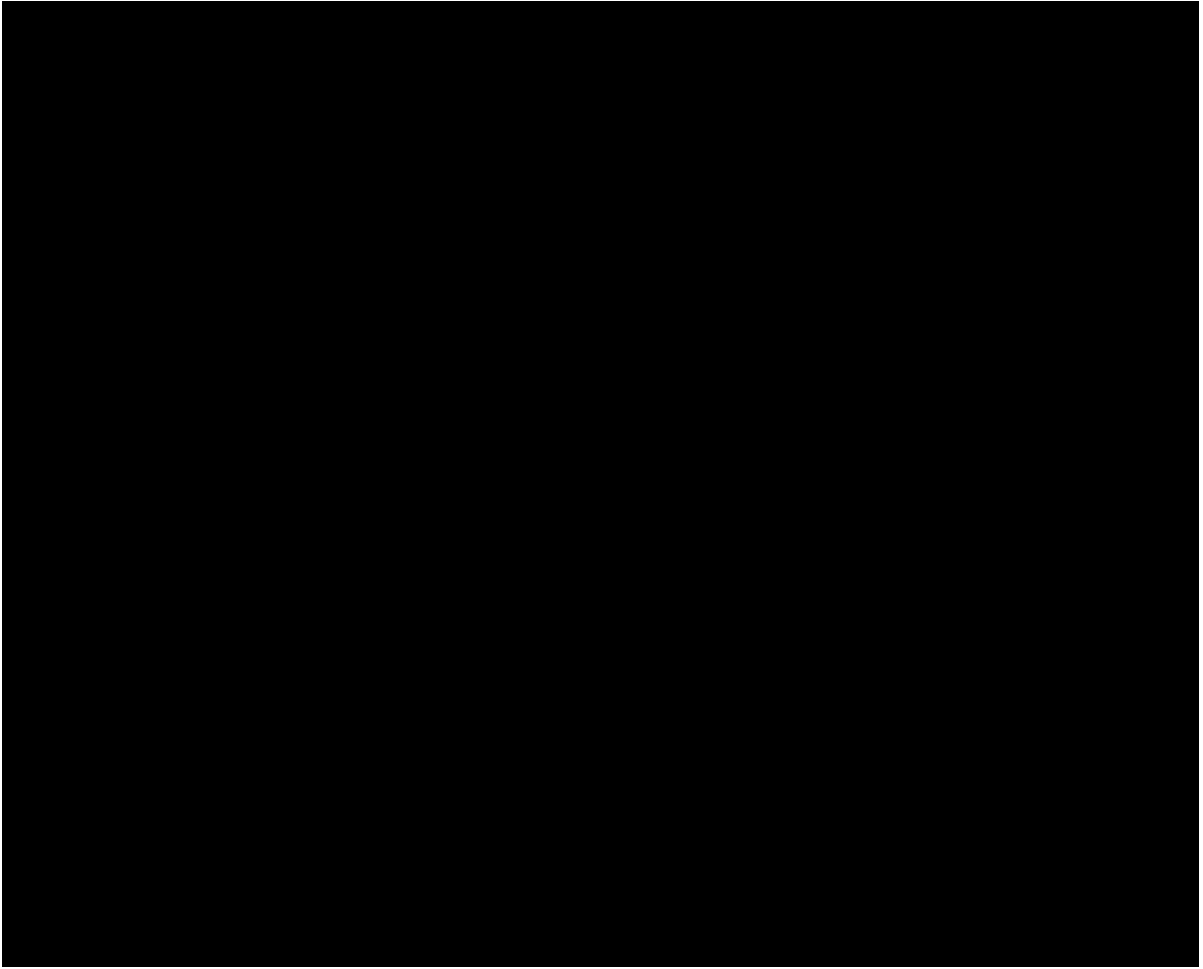
- 2024 Delacher M, Schmidleithner L, Simon M, Stüve P, Sanderink L, Hotz-Wagenblatt A, Wuttke M, Schambeck K, Ruhland B, Hofmann V, Bittner S, Ritter U, Pant A, **Helbich SS**, Voss M, Lemmermann NA, Bessiri-Schake L, Bohn T, Eigenberger A, Menevse AN, Gebhard C, Strieder N, Abken H, Rehli M, Huehn J, Beckhove P, Hehlhans T, Junger H, Geissler EK, Prantl L, Werner JM, Schmidl C, Brors B, Imbusch CD, Feuerer M. The effector program of human CD8 T cells supports tissue remodeling. *J Exp Med*. 2024 Feb 5;221(2):e20230488. doi: 10.1084/jem.20230488. Epub 2024 Jan 16. PMID: 38226976
- 2023 Nedwed AS, **Helbich SS**, Braband KL, Volkmar M, Delacher M, Marini F. Using combined single-cell gene expression, TCR sequencing and cell surface protein barcoding to characterize and track CD4+ T cell clones from murine tissues. *Front Immunol*. 2023 Oct 12;14:1241283. doi: 10.3389/fimmu.2023.1241283. PMID: 37901204; PMCID: PMC10602882.
- 2023 Braband KL, Nedwed AS, **Helbich SS**, Simon M, Beumer N, Brors B, Marini F, Delacher M. Using single-cell chromatin accessibility sequencing to characterize CD4+ T cells from murine tissues. *Front Immunol*. 2023 Oct 16;14:1232511. doi: 10.3389/fimmu.2023.1232511. PMID: 37908367; PMCID: PMC10613658.
- 2022 Klaus T, Wilson AS, Vicari E, Hadaschik E, Klein M, **Helbich SSC**, Kamenjarin N, Hodapp K, Schunke J, Haist M, Butsch F, Probst HC, Enk AH, Mahnke K, Waisman A, Bednarczyk M, Bros M, Bopp T, Grabbe S. Share. Impaired Treg-DC interactions contribute to autoimmunity in leukocyte adhesion deficiency type 1. *JCI Insight*. 2022 Dec 22;7(24):e162580. doi: 10.1172/jci.insight.162580. PMID: 36346673

11. Acknowledgment

[Redacted]

[Redacted]

Acknowledgment



12. Eidesstaatliche Erklärung

Ich, Sara Salome Clara Helbich, [REDACTED] in Kassel (Hessen), erkläre hiermit, dass ich die vorliegende Arbeit selbstständig verfasst und dabei keine anderen als die von mir angegebenen Hilfsmittel benutzt habe. Sämtliche Stellen der Arbeit, die im Wortlaut oder dem Sinn nach aus Publikationen oder Vorträgen anderer Autoren entnommen sind, habe ich als solche gekennzeichnet. Außerdem versichere ich, dass die Arbeit bisher weder gesamt, noch in Teilen einer andern Prüfungsbehörde vorgelegt wurde.